The petrogenesis of the Winddam, Koedoesfontein, and Rietfontein intrusions, Vredefort Dome, South Africa

WAJ Kruger

22891293

Dissertation submitted in fulfilment of the requirements for the degree *Magister Scientiae* in Environmental Sciences at the Potchefstroom Campus of the North-West University

Supervisor: Prof MS Coetzee

May 2017

DISCLAIMER

Although all care was taken to ensure the accuracy of this report, neither the sender and/or the North-West University can be held responsible for any errors or omissions that might have occurred. Although all possible care has been taken in the production of the reports and plans, NWU and/or the sender cannot take any liability for perceived inaccuracy or miss-interpretation of the information shown on these maps.

ACKNOWLEDGEMENTS

I would like to thank the following colleagues and friends for their selfless and willing support during the course of this project:

- My supervisor, Prof Marthie Coetzee, for introducing me to the igneous intrusions in the Vredefort Dome, her mentorship, and for always being kind and willing to listen to and discuss various ideas and subjects on a regular basis.
- Ricart Boneschans, for providing me with thin sections and chemical data for many rock samples from the Koedoesfontein Complex.
- Thato Maake, for always being willing to assist with field work and sample preparation.
- Sascha Roopa, for helping me to significantly improve the quality of some of the maps used in this dissertation.
- Jessica Strydom, for helping me to collect samples in the field and keeping me company when working late nights in the lab and office.
- Jaco Koch, for his innovative assistance with the hand-held rock drill.

I would like to express my gratitude to the owner of the farm Winddam 54, Mr. Geo Olivier, for kindly allowing me to collect rock samples from the Winddam intrusion.

I would like to thank Prof Allan Wilson especially for his kind assistance preparing samples for ICP-MS analysis at the University of the Witwatersrand.

I would like to express my gratitude to Dr. Leenta Grobler for assisting with the editing of this dissertation.

Finally, I would like to thank my parents for their interest in my work and their financial support, without which I would not be able to do what I love most.

ABSTRACT

Three boninitic magmas (labelled B1 to B3) are deemed responsible for the formation of the majority of the Rustenburg Layered Suite (RLS) of the Bushveld Igneous Complex (BIC). A Ti-rich magma, called the Bushveld Uitkomst magma (Bu), is thought to have formed from the same mantle source as B3 but represents a lower fraction melt of the mantle. Bu led to the formation of various satellite intrusions outside the BIC, collectively referred to as the high-Ti igneous suite (HITIS). The chemical evolution of the Bu magma is divided into five stages, labelled A to F.

The current view is that three igneous intrusions (consisting of ultramafic to dioritic rocks) located in the Vredefort Dome, called the Winddam wehrlite (Ww), Koedoesfontein Complex (KC), and Rietfontein Complex (RietC), form part of stage D to E of the Bu magma's evolutionary pathway based on their mineralogy. This hypothesis could not previously be confirmed geochemically as very little information regarding the geochemistry of these intrusions is available.

This study serves to accomplish the following goals with the aid of geochemical data: characterise Ww, KC and RietC in terms of their mineralogical, textural, and geochemical features, propose plausible explanations for variations observed in the mineralogical content across the intrusive bodies of Ww, KC, and RietC, determine whether or not Ww, KC, and RietC are related to one another in terms of their geochemical characteristics, determine their relation with the HITIS using a rare earth element modelling approach, and provide information regarding the mineralogical and geochemical composition of the mantle source from which the intrusions originate.

Ww primarily consist of olivine-hornblende clinopyroxenite and subordinate olivine-hornblende gabbronorite. KC contains an ultramafic sill consisting of wehrlite, olivine-clinopyroxenite, and clinopyroxenite. Other rock types that form part of KC include hornblende gabbronorite, hornblende norite, pyroxene hornblendite with minor quartz, and diorite. Rock types that form part of RietC include olivine (± hornblende) clinopyroxenite, olivine diorite, and magnetite-rich troctolite and dunite.

Rocks from all three intrusions range from fine to medium grained with typically anhedral to subhedral grain shapes. Ultramafic rocks are typically characterised by adcumulate or heteradcumulate textures with interstitial hornblende and plagioclase. Diorite from KC is glomeroporphyritic with augite glomerocrysts with flow textures in its matrix. Flow textures are also present in the magnetite-rich troctolite from RietC and plagioclase grains have lobate grain boundaries where in contact with the magnetite. Deformation textures include

planar deformation features in olivine from Ww, pseudotachylite in some ultramafic samples from KC and RietC, granoblastic textures with polygonal mineral aggregates in Ww and troctolite in RietC, and sutured grain boundaries between augite grains. These textures likely originated during meteorite impact.

Ultramafic rocks from Ww, KC, and RietC are generally rich in MgO, Ni, Cr, and Co, and poor in TiO_2, alkalis, and incompatible trace elements such as Zr, Y, and Rb. Ultramafic intrusions from all three intrusions show significant overlap on Harker diagrams. They commonly display negative high field strength element (HFSE) anomalies and positive Ba and Pb anomalies on multi-element spider diagrams normalised to the primitive mantle. On chondrite normalised rare earth element (REE) diagrams, significant variation in the slopes of LREE are observed while rock samples show comparable HREE patterns. Due to these geochemical similarities, ultramafic rocks from Ww, KC, and RietC are believed to be comagmatic products.

Variation in the abundance of olivine and augite across the Ww intrusion is believed to be a product of preferred nucleation of augite in certain areas of the magma, enriching the surrounding melt in olivine component. The enstatite-bearing rocks from KC and troctolite from RietC typically display contrasting geochemical characteristics compared to the ultramafic rocks, and are inferred to have formed from a different magmatic lineage. It is considered possible to produce the diorite from KC via fractional crystallisation of the parental magma of the ultramafic rocks as it possesses similar incompatible element ratios and higher incompatible element contents. Olivine diorite from RietC display intermediate REE compositions between the troctolite and ultramafic rocks and is believed to have formed through mixing of the parental magmas responsible for the formation of the latter two rock types.

Regarding their geochemistry, ultramafic rocks from Ww, KC, and RietC are geochemically more primitive than any member of the HITIS, and cannot fit into stage D-E of the Bu magma's evolutionary pathway. They do display comparable REE patterns to the most primitive member of the HITIS: the Marble Hall primitive diorite (MHPD). Fractionation of olivine, augite, and plagioclase from an estimated magma parental to KC produces a near identical REE pattern compared to the parental melt of the MHPD. This observation implies that these intrusions are related to the HITIS but represent more primitive members.

Low REE contents and flat HREE patterns of estimated parental melts of Ww, KC, and RietC suggest they formed by large fraction melting (approximately 40 weight percent) of a spinel lherzolite mantle source. Negative HFSE anomalies suggest the mantle was hydrothermally enriched in the vicinity of a subducting oceanic plate before melting occurred.

KEY TERMS

Winddam wehrlite, Koedoesfontein Complex, Rietfontein Complex, high-Ti igneous suite, Bushveld Igneous Complex, Rustenburg Layered Suite, Vredefort Dome.

TABLE OF CONTENTS

TABLE OF CONTENTS (CONTINUED)

TABLE OF CONTENTS (CONTINUED)

TABLE OF CONTENTS (CONTINUED)

TABLE OF CONTENTS (CONTINUED)

LIST OF TABLES

LIST OF FIGURES

CHAPTER 1

CHAPTER 2

LIST OF FIGURES (CONTINUED)

CHAPTER 3

CHAPTER 4

LIST OF FIGURES (CONTINUED)

LIST OF FIGURES (CONTINUED)

LIST OF FIGURES (CONTINUED)

LIST OF FIGURES (CONTINUED)

CHAPTER 5

LIST OF FIGURES (CONTINUED)

LIST OF FIGURES (CONTINUED)

LIST OF FIGURES (CONTINUED)

CHAPTER 6

LIST OF FIGURES (CONTINUED)

LIST OF FIGURES (CONTINUED)

ABBREVIATIONS

ARS: Annas Rust Sheet

Aug: Augite

Atm: atmospheric pressure

b.d.l.: below detection limit

BGU: Basal gabbro unit of the Dullstroom Formation

BIC: Bushveld Igneous Complex

Bu: Busheld Uitkomst magma

BUS: Basal Ultramafic Sequence

Cal: Calcite

Chl: Chlorite

Cpx: Clinopyroxene

D: Partition coefficient

En: Enstatite

HITIS: High in titanium igneous suite

HREE: Heavy rare earth elements

ILG: Inlandsee Leucogranofels

IUGS: International Union of Geological Sciences

KC: Koedoesfontein Complex

LCZ: Lower Critical Zone

LI: Lindequesdrift intrusion

LMI: Layered mafic intrusion

LMZ: Lower Main Zone

LOI: Loss on ignition

ABBREVIATIONS (CONTINUED)

LREE: Light rare earth elements

LZ: Lower Zone

Ma: Mega annum

Mag: Magnetite

MargZ: Marginal Zone

mm: Millimetres

MORB: Mid-ocean ridge basalt

n.d.: Not determined.

OGG: Outer Granite Gneiss

OIB: Ocean island basalt

Ol: Olivine

Opx: Orthopyroxene

PDF: Planar deformation feature

PPL: Plane polarised light

ppm: parts per million

Px: Pyroxene

REE: Rare earth element

RietC: Rietfontein Complex

RLS: Rustenburg Layered Suite

SF: Steynskraal Formation

Tr-Act: Tremolite-actinolite

TTG: Tonalite-trondhjemite-gneiss

UCZ: Upper Critical Zone

ABBREVIATIONS (CONTINUED)

UMZ: Upper Main Zone

UZ: Upper Zone

vol. %: Volume percentage

Ww: Winddam Wehrlite

wt. %: Weight percentage

WUM: Wilson’s ultramafic magma

XPL: Crossed polarised light

CHAPTER 1

INTRODUCTION

1.1 BACKGROUND INFORMATION

Two remarkable geological phenomena are present in South-Africa. They have a close temporal relationship, with their times of formation just ± 30 million years apart. The first, with an approximate age of 2054 Ma (Scoates & Friedman, 2008), is the Rustenburg Layered Suite (RLS) of the Bushveld Igneous Complex (BIC). The RLS is the largest known layered mafic intrusion (LMI) on Earth (Wilson, 2015). It also hosts the largest platinum deposit in the world in the famous Merensky-, UG-2, and Platreefs (Naldrett *et al*., 2009). The second is the 2023 Ma Vredefort Dome (Kamo *et al*., 1996), which contains remnants of the largest and second oldest (Garde *et al*., 2012) confirmed meteorite impact site (Kamo *et al*., 1996; Koeberl *et al*., 1996; Le Roux *et al*., 1994; Martini, 1991) on the planet.

Outcrops of the BIC can be found from Nietverdiend in the west, all the way to Burgersfort in the east, and from Villa Nora in the north to but a few kilometres from Pretoria in the south (Cawthorn *et al*., 2009). In chronological order, it consists of the Rooiberg Group (mafic to felsic volcanic rocks), RLS (intermediate-, mafic-, to ultramafic rocks), Rashoop Granophyre Suite, and the Lebowa Granite Suite (Cawthorn *et al*., 2009; Kruger, 2004). The magmatic activity associated with the RLS appears to have stretched further than the extent of the BIC itself, with similar satellite intrusions occurring near Marble Hall, east of Badplaas, near Heidelberg (De Waal *et al*., 2008) and Fochville (Coetzee & Kruger, 1989), and several locations in the Vredefort Dome (Bisschoff, 1999a; De Waal *et al*., 2008) (see Figure 1.1).

This study is concerned with the petrogenesis of three possibly Bushveld-related (De Waal *et al*., 2008; Stepto, 1990) satellite intrusions, called the Rietfontein Complex (RietC), the Koedoesfontein Complex (KC), and the Winddam wehrlite (Ww). Similar to the RLS, they consist of intermediate- to ultramafic rocks, with some associated felsic intrusive bodies in the case of RietC and KC (Bisschoff, 1999a). All three of these intrusions are situated in the Vredefort Dome, which is located approximately 120 km south-west of Johannesburg (Figure 1.1).

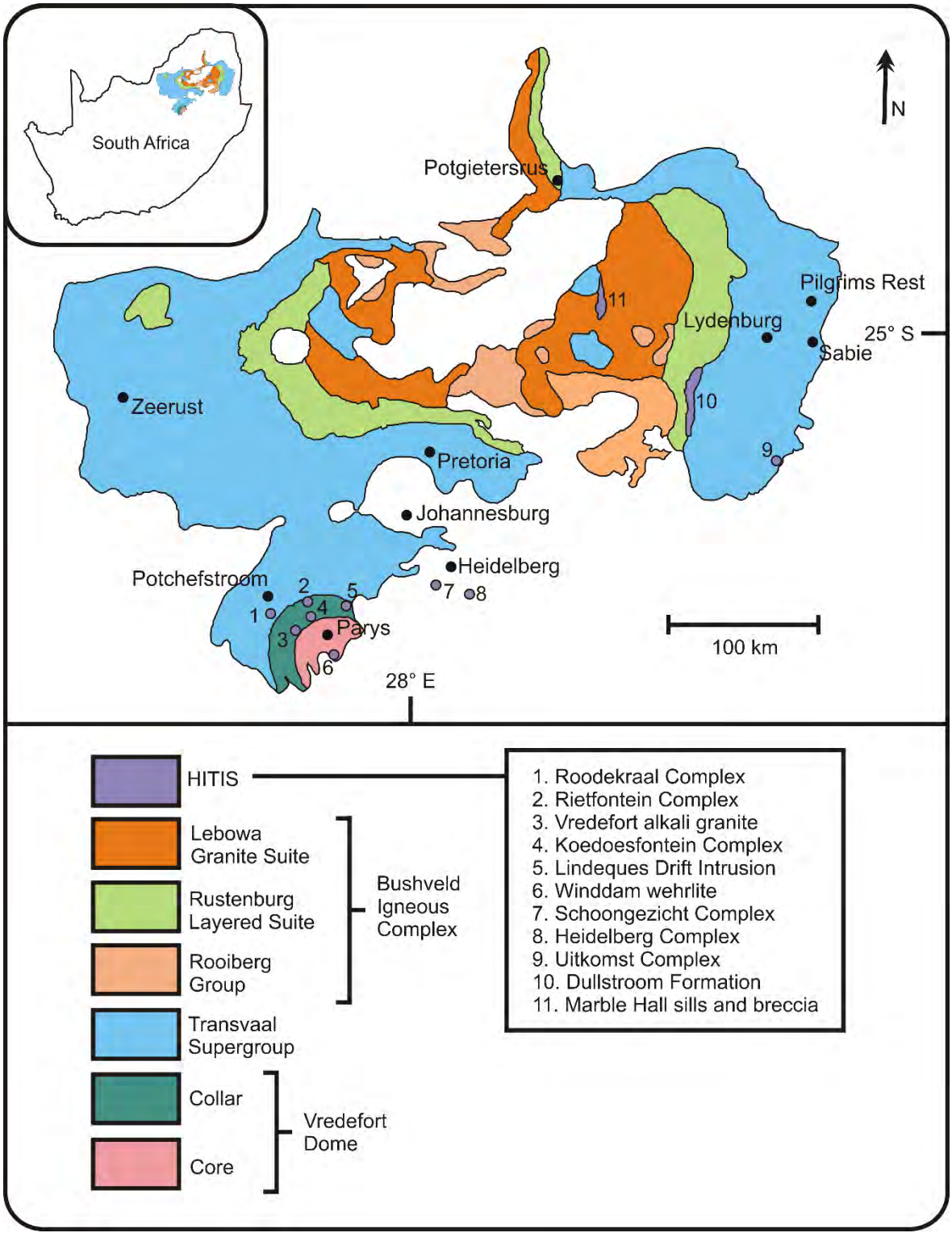

Figure 1.1: Geographic distribution of the Vredefort Dome, Bushveld Igneous Complex, HITIS, and the Transvaal Supergroup. Modified after Davies and Cawthorn (1984), Stevens *et al*. (1997), and Wilson (2015). HITIS localities are from De Waal *et al*. (2008). HITIS: High in titanium igneous suite, which is a group of satellite intrusions presumed to be comagmatic with the Bushveld Igneous Complex.

Although this is a controversial topic, it has been proposed that several mantle-derived boninitic magmas contributed to the formation of the majority of the RLS (reviewed by Eales, 2002). Chronologically, they are labelled as Bushveld magma 1 (or B1) to Bushveld magma 3 (B3). According to De Waal and Armstrong (2000), a different magma type was also produced from the same source as B3. This magma type, called the Bushveld Uitkomst magma (Bu), led to the formation of several igneous bodies outside the RLS, collectively referred to as a high in titanium igneous suite (HITIS) (De Waal *et al*., 2008). The ultramafic to intermediate intrusions of the HITIS have similar lithologies and mineralogies, and primarily consist of clinopyroxene, sodic plagioclase, hornblende, and less commonly olivine and magnetite(-ilmenite) as primary minerals (De Waal *et al*., 2008). Igneous bodies belonging to the HITIS are the:

- Marble Hall Diorite
- Uitkomst Complex
- Dullstroom Formation
- Roodekraal Complex
- Lindeques Drift Intrusion
- Heidelberg Intrusion
- Rooiberg High-Ti lava
- Schoongezicht Complex
- Rietfontein Complex
- Koedoesfontein Complex
- Winddam wehrlite
- Schurwedraai and Baviaanskranz granite (collectively referred to as the Vredefort alkali granite).

Although Ww is not labelled as one of the HITIS of De Waal *et al*. (2008), it is placed here because of its chemical similarity to RietC according to Stepto (1990). The geographical distributions of most of the HITIS intrusions are shown in Figure 1.1.

De Waal *et al*. (2008) devised a model for the evolution of the Bu magma to produce the HITIS intrusions, roughly in the order they are listed above, based on major- and trace elemental concentrations of the intrusions (see section 2.3.2 for details). However, trace element concentrations were unavailable for RietC and KC. Based on their mineralogical composition, De Waal *et al*. (2008) argued that there is a good chance that RietC and KC will fit into their fractionating model.

1.2 PROBLEM STATEMENT

In order to confirm if RietC, KC and Ww are indeed compatible with the model proposed by De Waal *et al*. (2008), trace element concentrations are needed, as it provides a greater insight into petrologic problems than major elemental data alone (Rollinson, 1993). Without trace elemental concentrations, there is still considerable uncertainty regarding whether RietC, KC, and Ww are related in origin, let alone related to the HITIS.

Modern petrologic models describing the variation in the mineralogy of the intrusions (especially the layering observed in RietC, see section 2.5.1) can be constructed once trace elemental compositions are available. Previous models describing the formation of these intrusions (Bisschoff, 1969; 1972; 1973) relied only on the mineralogy, since little major elemental data was available and trace elemental concentrations were too low to be detected by the older X-ray fluorescence (XRF) technology used at the time. A detailed report documenting the geochemistry of RietC, KC, and Ww are thus still lacking.

To make sense of geochemical data, detailed petrographic descriptions of the same samples that are chemically analysed, need to be performed (Vernon, 2004). The petrography of RietC, KC (Bisschoff, 1969; 1972; 1973) and Ww (Stepto, 1990) has been described, but will be repeated in this study to compare with the chemical data and to compare the petrographic characteristics of the intrusions with one another.

1.3 SCOPE OF THIS STUDY

This study is only concerned with the ultramafic, dioritic, and mafic rocks of Ww, KC and RietC, their possible relationship with one another, and to the HITIS. It does not deal with the associated granitic nor lamprophyric rocks of RietC and KC.

1.4 RESEARCH AIM AND OBJECTIVES

The ultimate aim of this study is to determine the petrogenesis of RietC, KC and Ww, their relation to one another, and their relation to the HITIS. To accomplish this, the following objectives need to be completed:

1. Provide detailed descriptions regarding the mineralogical composition and petrographic characteristics of RietC, KC, and Ww.

2. Obtain whole-rock chemical compositions (major and trace elements) of the different rock types from the three intrusions to compile the first detailed report of their geochemistry.
3. Propose viable explanations for variations in the mineralogy and geochemistry observed in RietC, KC, and Ww.
4. Use the geochemical and mineralogical compositions of RietC, KC, and Ww to determine if they are related to one another and to the HITIS using a rare earth element (REE) modelling approach.
5. Use the trace elemental compositions of RietC, KC, and Ww to provide information regarding the mineralogical and geochemical characteristics of their mantle source.

1.5 CHAPTER OVERVIEWS

- Chapter 2: Literature overview

This chapter deals with the magmas responsible for the formation of the RLS, the formation and evolution of the Bu magma to produce the intrusions that form part of the HITIS, the geology of the Vredefort Dome, and the geology of Ww, KC, and RietC.

- Chapter 3: Methodology

In this chapter, the focus falls on describing sample collection strategies for Ww, KC, and RietC, how the samples were analysed and how each analytical method contributes to achieving the objectives set out above.

- Chapter 4: Mineralogy and petrography

Chapter 4 deals with the modal mineralogical compositions of different rock types from Ww, KC, and RietC, how the mineralogical content varies within each intrusion, the classification of rock types according to their modal mineralogical content, and with their petrographic characteristics.

- Chapter 5: Geochemistry

A detailed report is given on the geochemical composition of the intrusions, and how the chemistry varies across the intrusive bodies themselves. Harker plots are used to compare the geochemistry of Ww, KC, and RietC, and to identify trends in their magmatic evolution. Furthermore, chemical classification of the intrusions is performed, followed by

the construction of multi-element spider diagrams and REE diagrams to obtain clues regarding processes at work during the formation of Ww, KC, and RietC.

- Chapter 6: Petrogenesis

Possible explanations are provided regarding the origin of the observed petrographic characteristics of Ww, RietC, and KC along with possible causes of deformation. New petrologic models are proposed to explain the mineralogical and chemical variation seen across Ww, KC, and RietC. The relation between Ww, KC, and RietC is tested using a REE modelling approach, followed by a comparison between the geochemistry of these three intrusions to that of the HITIS to determine if these intrusions fit into the HITIS model as proposed by De Waal *et al*. (2008). In the final section of this chapter, geochemical constraints are placed on the mineralogical and chemical nature of the melting source from which Ww, KC, and RietC originated.

- Chapter 7: Conclusion

The major findings and conclusions made in this study are summarised and suggestions for future research are made.

CHAPTER 2

LITERATURE OVERVIEW

The events leading up to the petrogenesis of Ww, KC, and RietC, as suggested by De Waal *et al*. (2008), are numerous and complex. Currently, it is believed that it started with a mantle melting event that produced the Lower to Main Zones of the RLS. A smaller fraction melt of the mantle from the same source produced the Bu magma that led to the formation of the HITIS. Through deep-seated crystal fractionation, the Bu magma's composition changed until it finally intruded into the rock formations that later formed part of the Vredefort Dome, possibly producing the three intrusions relevant to this study. Sometime after their formation, the intrusions were affected by shock metamorphism due to the Vredefort meteorite impact.

To resolve the uncertainty regarding the petrogenesis of these three intrusions, four important topics need to be reviewed based on the above: the Bushveld magmatic event, the HITIS magmatic event, the geology of the Vredefort Dome, and the geology of RietC, KC, and Ww. The information given in this chapter will serve as the backbone for future interpretations made in this study.

2.1 THE BUSHVELD MAGMATIC EVENT

2.1.1 Overview of the Bushveld Igneous Complex

The BIC was emplaced in sedimentary rocks of the Transvaal Supergroup in South Africa (Barnes & Maier, 2002; Kruger, 2004; McCarthy & Rubdige, 2005; Tankard *et al*., 1982) and outcrops in an area of about 66 000 km^2. The general shape of the RLS is that of a lopolith, with its layers dipping towards the approximate centre of the structure (Kruger, 2004). Its surface area is divided into four limbs, called the Western Limb, Far Western Limb, Northern Limb (also called the Potgietersrus Limb), and Eastern Limb. On a stratigraphic basis, the RLS is divided into, from bottom to top, the Marginal Zone (MargZ), the Lower Zone (LZ), the Critical Zone (CZ), the Main Zone (MZ) and the Upper Zone (UZ). The CZ and MZ are further subdivided into a Lower- and Upper Critical (LCZ and UCZ) and Lower and Upper Main (LMZ and UMZ) Zones (see Figure 2.1).

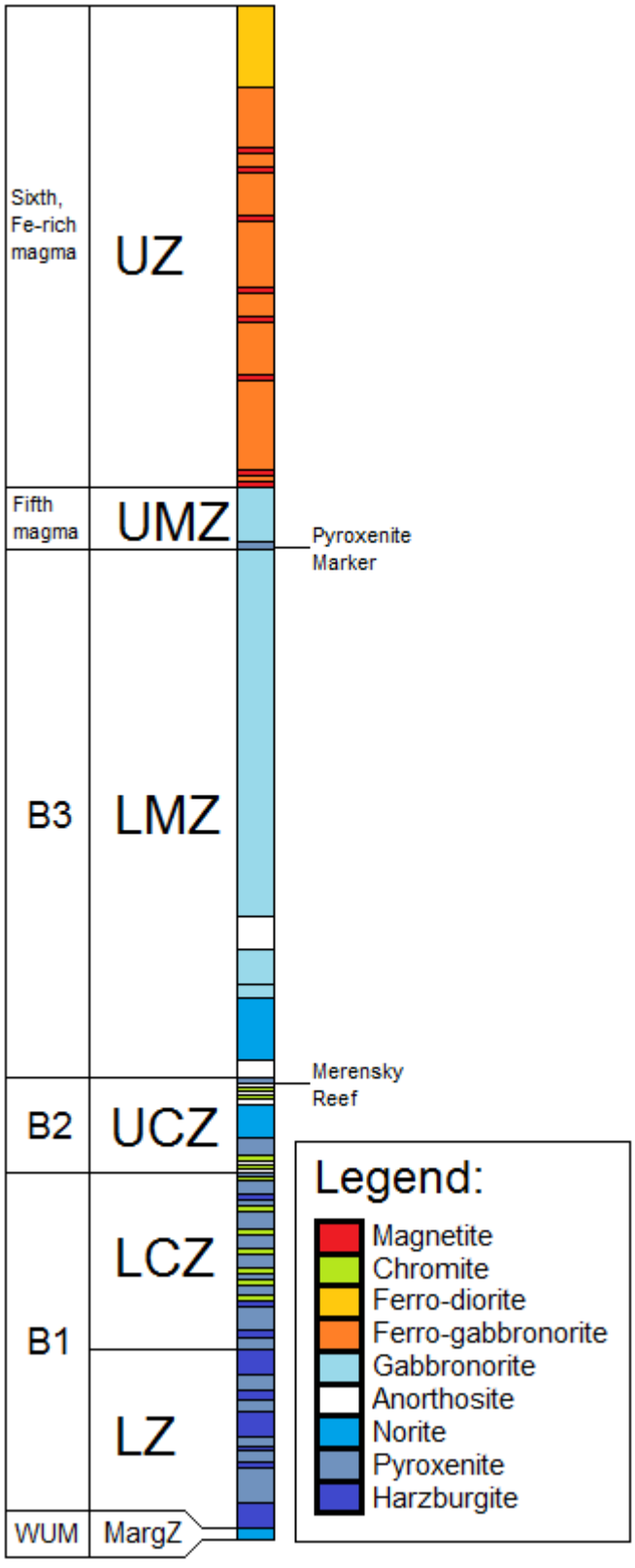

Figure 2.1: Compiled stratigraphic column of the Rustenburg Layered Suite (modified after Kruger, 1994) showing which magma type contributed to which zone in column on the left (Eales, 2002; Scoon & Mitchell, 2012; Wilson, 2015). WUM: Wilson's ultramafic magma. See text for remaining abbreviations.

The thickness of the RLS varies to a maximum of 7 km in the Western- and Eastern Limbs, and decreases to 5 km in the Northern Limb to about 3 km in its most northern section (Barnes & Maier, 2002). According to Hatton (1995), the RLS magmas of the BIC originated from a mantle plume, and estimates by Cawthorn and Walvaren (1998) have shown that the volume of magma produced was in the order of 600 000 km^3, yet it took less than 1 Ma for the entire body to cool below subsolidus temperatures (Zeh *et al*., 2015). During its emplacement and crystallization, the RLS experienced contamination from the country rock as indicated by heterogeneous values in the Sr-isotopic character in plagioclase grains (see Roelofse *et al*., 2015 for details).

2.1.2 Formation of the Rustenburg Layered Suite

A lot of uncertainty still surrounds the issue regarding how many magmas contributed to the formation of the RLS and what their exact compositions might have been. Generally, the literature refers to six compositionally distinct magmas that contributed to the formation of the RLS: an initial ultramafic magma that contributed to the formation of the MargZ, B1 that led to the formation of the LZ and LCZ, B2 contributed to the formation of the UCZ, B3 was responsible for the formation of the LMZ, a fifth magma crystallised to form the UMZ, while a sixth iron-rich tholeiitic magma resulted in the formation of the UZ.

2.1.2.1 The Marginal Zone: the first ultramafic magma

The earliest known magma that contributed to the formation of the RLS is the one identified by Wilson (2012; 2015) referred to in this study as Wilson's ultramafic magma (WUM). This magma, which is more mafic in composition than any of the other Bushveld magmas, intruded at a deeper level than the RLS itself to form what is known as the Basal Ultramafic Sequence (BUS). The BUS contains many alternating layers of the ultramafic rocks dunite, pyroxenite, and harzburgite discovered in a borehole from the Clapham area of the BIC. Evolution of this magma led to the formation of norites containing minor quartz and biotite at the top of the magma chamber, which is referred to as the Marginal Zone of the RLS (Wilson, 2015).

2.1.2.2 The Lower Zone and Lower Critical Zone: the B1 magma

This magma initially crystallised in the crust to produce several micropyroxenite sills that have presumably preserved the original composition of B1 (Sharpe & Hulbert, 1985; Godel *et al*., 2011). Further upward movement of B1 caused it to intrude on top of the

Marginal Zone, which was still in a partially liquid state (Wilson, 2015). This intrusion of the more primitive B1 magma is evident as a reversal (increase) in the Mg# (Mg/(Mg+Fe)*100) of the mafic minerals across the interface of the MargZ and LZ (Wilson, 2015). Subsequent crystallisation of B1 produced the cyclic layering of alternating dunite, harzburgite, pyroxenite, and chromite of the LZ and LCZ.

However, the B1 magma alone was not chemically suited to crystallise the large amounts of olivine observed in the LZ, nor does it have enough chromium to produce the amount of chromite in the LZ and LCZ (Eales, 2002). Furthermore, crystallisation of a single injection of B1 into the magma chamber cannot explain the LZ's modal layering (Cawthorn & Walraven, 1997). Eales (2000) proposed that during the crystallisation of B1, magma was injected into the chamber from a deeper seated source, carrying olivine crystals and microphenocrysts of chromite. Eales (2002) points to the existence of peridotite sills at the footwall of the RLS as the possible source of these additional magmas. Frequent injection of this magma would also explain the origin of the LZ's modal layering (Eales, 2002; Cawthorn *et al*., 2009). The B1 magma should thus not be considered the only parent of the LZ and LCZ.

2.1.2.3 Formation of the Upper Critical Zone: the B2 magma

A sudden discontinuity in the original Sr^{87}/Sr^{86} isotopic character (before the decay of Rb^{87} to Sr^{87}) is observed as one crosses the boundary of the LCZ to the UCZ (Eales, 2002; Kruger, 1994; Winter, 2010). Strontium isotopes do not mass fractionate during magmatic crystallisation, and the original Sr^{87}/Sr^{86} should remain constant in a single body of magma (Winter, 2010). Therefore, the conclusion was made that a different magma, called B2, led to the formation of the UCZ.

The basal unit of the UCZ is defined as the appearance of cumulate plagioclase to form a layer of anorthosite (Barnes & Maier, 2002). The existence of the B2 magma was based on the composition of a chill margin adjacent to the UCZ (Harmer & Sharpe, 1985). Godel *et al*. (2011) and Latypov (2015) warn that chill margins can experience changes in its chemical composition during the assimilation of the country rock, or during equilibration with the slower-cooling adjacent magma from which it formed. This can render them unreliable to represent the composition of the parent magma. Eales (2002) points out that incompatible trace element ratios in B2 do not match those in the rocks of the UCZ. For example, Zr/Rb ratios in B2 are up to eight times higher than those recorded in the CZ, while the CZ contains Ce/Sm ratios that are two times higher than those recorded in B2

(references within Eales, 2002). This serves as a strong argument against the parental potential of B2 to UCZ rocks.

2.1.2.4 Formation of the Lower Main Zone: the B3 magma

A steep rise in the initial $^{87}Sr/^{86}Sr$ character is observed across the boundary from the UCZ to the MZ (Kruger, 1994), which was interpreted as the intrusion of a new type of magma at this boundary. It crystallised to form a major part of the RLS (see Figure 2.1), and the resulting rock types include norites, gabbronorites, with fewer anorthosites and pyroxenite (Clarke-Halkett, 2010; Kruger, 2004). Similar to B2, the B3 magma originally deemed parental to the MZ was also identified as a chill margin to the MZ rocks (Harmer & Sharpe, 1985). Problems pointed out with the parental status of B3 is the inconsistency of incompatible element ratios of B3 and the MZ rocks, as well as the higher Mg# of the MZ compared to B3 (Eales, 2002). Kruger (2004) argued that the B3 magma is a mixture of residual UCZ magma and a different magma, which he called BvMz, and that B3 is not parental to the MZ. Kruger (2004) considered BvMz as the true parent of the MZ, although he states that the existence and composition of this magma requires confirmation. Therefore, as with B2, it appears unwise to consider B3 as one of the magmas parental to the RLS.

2.1.2.5 Formation of the Upper Main Zone: the fifth magma

A sudden reduction in the initial $^{87}Sr/^{86}Sr$ ratio occurs as one crosses from the Lower MZ to the Upper MZ at the pyroxenite marker. This, along with other geochemical and mineralogical data, has served as evidence that a new type of magma has intruded into the Bushveld chamber at this point (Davies & Cawthorn, 1984; Kruger, 1990; 1994). Davies and Cawthorn (1984) have proposed that the UMZ formed from the B2 magma after it experienced a certain degree of fractional crystallisation, depleting this magma in compatible trace elements such as Ni. However, a definite composition of the magma responsible for the formation of the UMZ has not yet been proposed.

2.1.2.6 The Formation of the Upper Zone: the sixth magma

The most prominent feature that distinguishes the UZ from the rest of the RLS is the presence of monomineralic magnetite layers. In between these layers, iron-rich intermediate and mafic rocks are present such as olivine-magnetite diorite, olivine gabbro, and anorthosite (Scoon & Mitchell, 2012). Davies and Cawthorn (1984) believed that the

UZ also crystallised from the same magma responsible for the formation of the UMZ. A more recent study by Scoon and Mitchell (2012) has shown that an entirely different, Fe-rich tholeiitic magma served as the parent for the UZ.

2.2 THE HITIS MAGMATIC EVENT

The focus now shifts away from the BIC to the petrogenesis of the HITIS. The formation of the Bu magma is described here, along with its crystallisation and evolution to produce the HITIS rocks. The lithology and mineralogy of the majority of the HITIS is summarised in Table 2.1.

2.2.1 Formation of the Bu magma

Compared to RLS magmas, Bu typically contains higher concentrations of elements incompatible with mantle minerals (De Waal *et al*., 2008), such as Ti, K, and P (Rollinson, 1993). The most primitive Bu magma composition contains 1.89% TiO_2 (De Waal *et al*., 2008) compared to the 0.41% TiO_2 of the B3 magma (Harmer & Sharpe, 1985). The differences in K_2O and P_2O_5 are just as significant, with the primitive Bu liquid having more than four and seven times the concentrations of the B3 magma, respectively.

During melting of the mantle, incompatible elements are initially released from the solid phase in greater concentrations than compatible elements (Ernst, 2014; Rollinson, 1993; Winter, 2010). This results in a magma that has a higher concentration of incompatible elements versus those produced by higher melt fractions. Using an assumed mantle mineralogical composition of garnet lherzolite, De Waal *et al*. (2008) has shown that a small fraction of melt could have produced the rare earth element (REE) patterns of Bu that later produced the REE patterns of B3 when a larger fraction of melt of the same material was produced.

Relative to the B3 magma, the Bu is also more alkaline in nature, with a higher (Na_2O + K_2O) to SiO_2 ratio. This difference can also be explained by the concept that the Bu is a lower fraction melt than B3. Due to the release of incompatible alkalis and proportionally less silica during lower fraction melting, lower fraction melts tend to be alkaline, while higher fraction melts are more tholeiitic (Green & Ringwood, 1967; Kushiro, 2001; Winter, 2010).

Table 2.1: Summarised lithology and mineralogy of the HITIS intrusions, excluding RietC, KC and Ww, which are discussed in detail in section 2.5.

Geological unit	Lithology and mineralogy
Marble Hall diorite	Dark coloured gabbronorite and diorite make up the bulk of the Marble Hall intrusion. The dioritic rocks consist of sodic plagioclase (An_{2-45}), clinopyroxene, amphibole, biotite, magnetite(-ilmenite) with smaller amounts of apatite, K-feldspar, zircon and quartz (De Waal and Armstrong, 2000).
Basal Gabbro of the Uitkomst Complex	The lower (basal) part of the Uitkomst Complex consists of gabbro which contains clinopyroxene, smaller amounts of orthopyroxene, plagioclase with an andesine to labradoritic composition, amphibole, and minor amounts of magnetite, biotite, and quartz (De Waal and Armstrong, 2000).
High-Ti and FeTiP Rooiberg lavas	Basaltic rocks consisting of clinopyroxene, plagioclase (An_{55}), with minor K-feldspar and titanite (Buchanan *et al*., 1999).
Lindeques Drift Intrusion	The rock types range from spessartite, syenodiorite to syenite with some pegmatitic schlieren (Bisschoff, 1999a). Amphibole phenocrysts are present in the spessartite within a matrix of clinopyroxene, oligoclase, biotite, amphibole, magnetite(-ilmenite), and apatite (Bisschoff, 1969).
Heidelberg Intrusion	Mineralogy and lithology are similar to the spessartite of the Lindeques Drift intrusion but with more abundant amphibole (De Waal *et al*., 2008).
Roodekraal Complex	Alkali-rich andesitic lava (hawaiite), smaller amounts of diorite and olivine diorite. In some parts of the lava, andesine phenocrysts occur in a matrix consisting of clinopyroxene, amphibole, plagioclase, magnetite(-ilmenite), biotite and apatite. The mineralogy of the diorite is similar to the lava but contains small amounts of olivine and K-feldspar (Bisschoff, 1999a; De Waal *et al*., 2006). The olivine diorite contains abundant olivine, magnetite, clinopyroxene, orthopyroxene, and plagioclase (An_{41}) (Clark, 1972 cited by De Waal *et al*., 2008).
Schoongezicht Complex	An ultramafic complex that primarily consists of magnetite(-ilmenite) rich (up to 24% modal composition) clinopyroxenite with little orthopyroxene. The complex also contains smaller quantities of amphibole, biotite, and sulphides (De Waal *et al*., 2008 and references within).
Vredefort alkali granite	As the name implies, the Vredefort alkali granite consists primarily of albite, K-feldspar and quartz. In some localities, it classifies as syenite due to a lower modal abundance of quartz (Bisschoff, 1999a; Graham *et al*., 2005).

Thus, on the grounds of alkalinity, incompatible major elements, and trace element concentrations it was argued that the Bu and B3 magmas likely share their origins in the same place in the mantle. This provides a possible link between the HITIS and BIC magmatic events. However, because of problems associated with the parental status of B3 (see section 2.2.2), this statement has to be re-evaluated.

Another aspect that De Waal *et al*. (2008) used to link the HITIS and Bushveld magmatic events is the fact that absolute ages of dated HITIS rocks are indistinguishable from those obtained for the RLS (see Figure 2.2). Although absolute ages are still lacking for the majority of the HITIS rocks, their relative ages to the country lithologies of known age overlap the time of formation of the RLS (see section 2.5 and De Waal *et al*., 2008 for details).

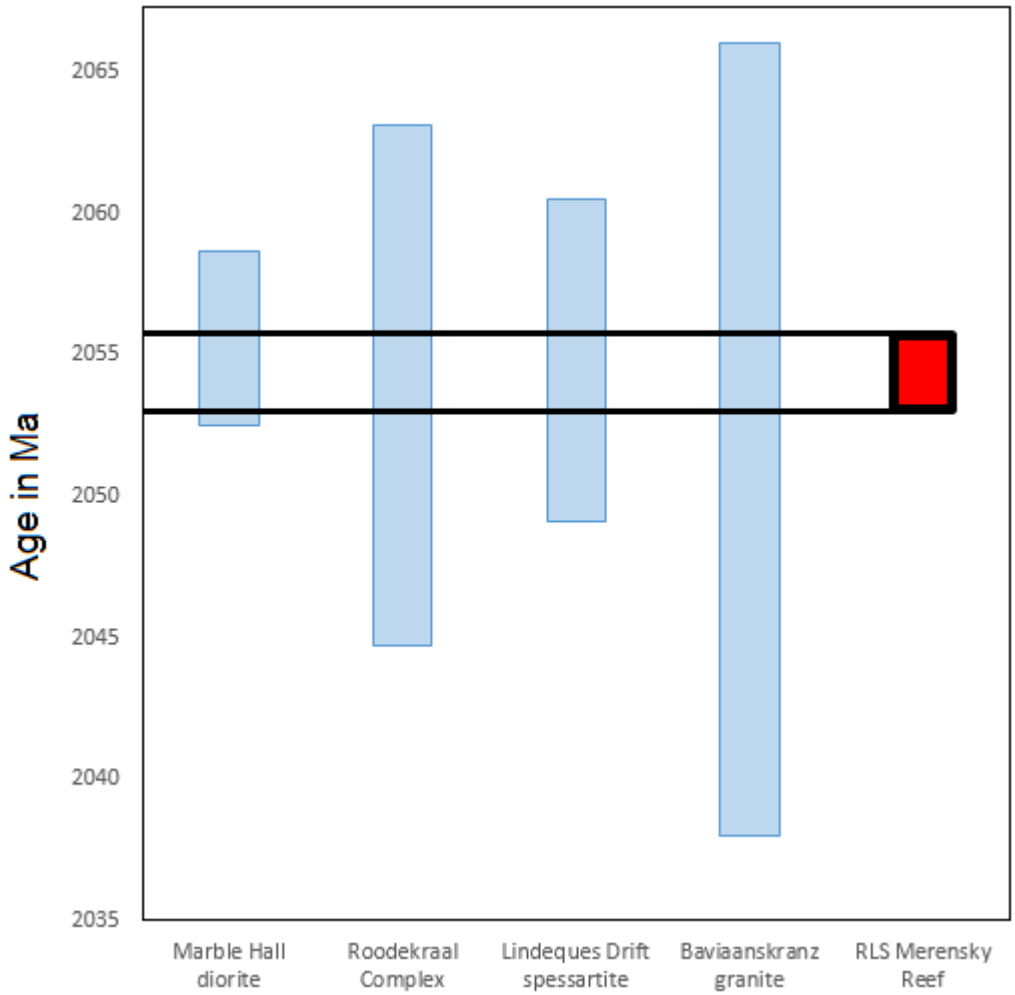

Figure 2.2: The range of absolute ages determined for the Marble Hall diorite (De Waal & Armstrong, 2000), the Roodekraal Complex (De Waal *et al*., 2006), the Lindeques Drift spessartite (De Waal *et al*., 2006), the Baviaanskranz granite (Graham *et al*., 2005), and the Merensky Reef of the RLS (Scoates and Friedman, 2008). The ages of the HITIS are indistinguishable from that of the RLS because they bracket the age of the Merensky Reef (which is extended across the graph using black lines).

2.2.2 Crystallisation and evolution of the Bu magma

During the course of magmatic evolution of Bu, De Waal *et al*. (2008) identified five changes (inflection points) in the slope (labelled A to F) of the SiO_2/MgO ratio of the magma, which represents a change in the fractionating phases (see Figure 2.3). Five stages are defined based on these inflection points; the stage from A to B, B to C, and so forth. This section will focus on describing the evolution and crystallisation of the Bu magma. It does not serve to provide in-depth descriptions of all the resulting HITIS intrusions, of which proper descriptions can be found in references provided by De Waal *et al*. (2008). Refer back to Table 2.1 for a summary of the lithology and mineralogy of the majority of the HITIS and Figure 1.1 for its geographic distribution.

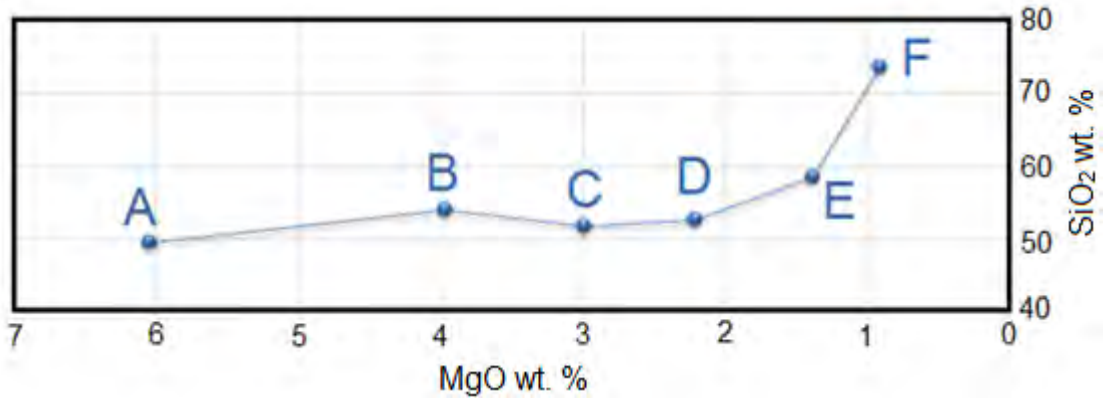

Figure 2.3: Harker diagram for the average compositions of the Bu magma. Inflection points are labelled as A to F and indicate a change in the fractionating phase(s). Magmatic evolution proceeds from left to right (notice the MgO scale from 7 wt. % left to 0 wt. % right) as MgO is depleted in the melt during crystal fractionation. Modified after De Waal *et al*. (2008).

- Stage A to B

After the intrusion and subsequent crystallisation of the B1 magma to produce the LZ of the BIC, the most primitive Bu magma was emplaced in an area approximately 150 km north-east of present day Pretoria. During its rise into the crust, the magma cut discordantly into the foliation planes of the Malmani dolomite of the Transvaal Supergroup. This led to the formation of more than 30 individual diorite sills, as discovered in a borehole just south of the town of Marble Hall, called the Marble Hall diorite (De Waal & Amstrong, 2000). Outcrops of these diorite sills can be seen just east and about 5 km north of Marble Hall. Extrusion of the Bu magma in the same area led to the formation of volcanic breccia which contains fragments of LZ RLS rocks. According to De Waal *et al*. (2002), this serves as evidence that the formation of the Marble Hall diorite succeeds the formation of the LZ of the RLS.

The relatively primitive Bu magma also intruded into more Transvaal rocks 200 km east of Pretoria to form the lower part of the Uitkomst Complex, called the Basal Gabbro Unit (BGU). The BGU formed as a sill beneath ultramafic rocks that are probably related to the B1 magma of the RLS (Gauert *et al*., 1995).

Extrusion of HITIS liquid occurred in an area between the BGU and the Marble Hall diorite (De Waal & Amstrong, 2000). These lavas were classified as part of the Dullstroom Formation of the Rooiberg Group of the BIC. The Dullstroom Formation is divided into low-Ti (TiO_2 < 1.0 wt. %), high-Ti and FeTiP-rich lavas (TiO_2 > 1.0 wt. %) (Buchanan *et al*., 1999), with the latter two forming part of the HITIS (De Waal *et al*., 2008).

As of yet, the Marble Hall diorite, the BGU of the Uitkomst Complex, and the FeTiP/High-Ti lavas of the Dullstroom Formation are the only known igneous rocks that crystallised during stage A to B. However, approximately 53% of the Bu magma appears to have crystallised during this stage, fractionating only amphibole (De Waal *et al*., 2008). If this is the case, one would expect to encounter an abundance of hornblendites as the crystallised products of Bu during stage A to B.

A possible explanation of why this is not the case is that dehydration of amphibole would occur in shallower regions of the crust. This would prevent amphibole crystallisation at near-surface conditions of the Earth (see Figure 2.4). Prograde metamorphism of amphibole typically produces orthopyroxene, clinopyroxene, plagioclase and ilmenite (Buckley *et al*., 2006), which is similar to the mineralogies of the rocks that formed during stage A to B (see Table 2.1).

- Stage B to C

The derivative Bu liquid that formed after amphibole fractionation served as the parental magma to three known igneous bodies representative of stage B to C; the Lindeques Drift diorite, the Roodekraal mugearite, and diorite, and additional high-Ti lava from the Dullstroom Formation (De Waal *et al*., 2008).

Bu-liquid extruded onto the surface of the Earth approximately 8 km SSE from present day Potchefstroom (De Waal *et al*., 2006) to produce the alkaline, andesitic (mugearite) volcanic rocks now known as the Roodekraal Complex (Bisschoff, 1999a), with additional lava from the same stage also extruding to form part of the Dullstroom Formation (De Waal *et al*., 2008). An intrusive, dioritic variety from the same magma is present at the Lindequesdrift Intrusion.

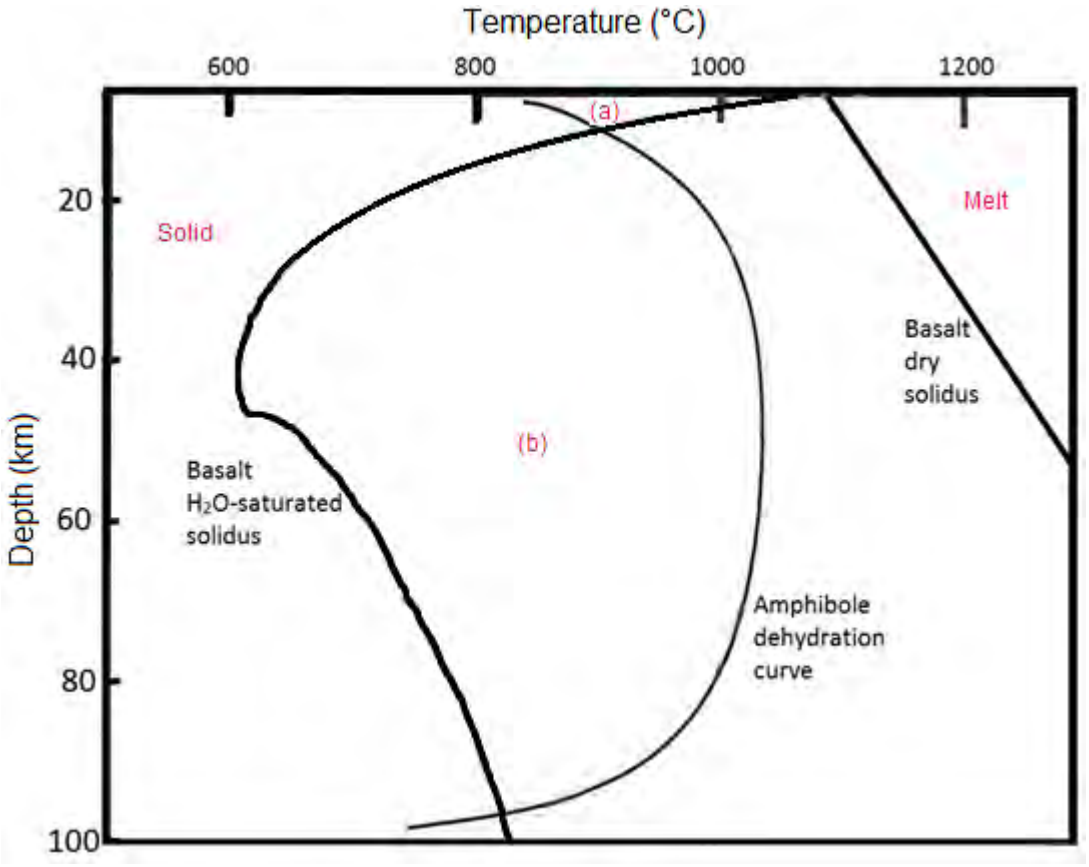

Figure 2.4: Location of the dry- and H_2O-saturated basalt solidus (Murphy, 2006) and the amphibole dehydration curve (Millholen *et al.,* 1974 cited by Winter, 2010) relative to temperature and depth of the crust and upper mantle. Amphibole cannot crystallise in the upper crust (a) from a H_2O-saturated basaltic melt because its solidus lies to the high-temperature side of amphibole's dehydration curve. At deeper levels of the crust and mantle (b), amphibole can crystallise because the H_2O saturated solidus lies to the low-temperature side of the amphibole dehydration curve.

- Stage C to D

Further expulsion of the HITIS liquid occurred from the Roodekraal volcano during this stage. Intrusive plutonic diorite also crystallised to form the Roodekraal diorite, Lindequesdrift diorite and more evolved (compared to stage A to B) Marble Hall diorite. The Bu magma experienced a decrease in Fe and Ti concentrations due to oxide (magnetite and ilmenite) formation (De Waal *et al*., 2008). Removal of dense oxide minerals probably led to the rapid increase of the SiO_2 content (as observed in Figure 2.3) of the magma during this stage.

- Stage D to E

Unique to stage D to E is a dramatic decrease in the V content of the magma due to magnetite crystallisation (De Waal *et al*., 2006), which adds to the Ti and Fe depletion experienced during stage CD. Additional clinopyroxene crystallisation occurred, along with smaller amounts of olivine, apatite, and orthopyroxene. These fractionating products are observed in the cumulate rocks of KC and RietC, along with those of the Lindequesdrift and Heidelberg intrusions (De Waal *et al*., 2008) as shown in Table 2.1.

- Stage E to F

The final 3% of the Bu magma crystallised during this stage. SiO_2 concentrations have increased dramatically from inflection point E (see Figure 2.3), which caused the melt to have a more granitic composition. This led to the formation of the Schurwedraai alkali granite and the Baviaanskranz granite, collectively referred to as the Vredefort alkali granite. More granitic rocks also occur as part of RietC and KC, which are also believed to have formed during this final stage of HITIS crystallisation (De Waal *et al*., 2008; Graham *et al*., 2005).

2.3 THE VREDEFORT DOME

Most of the HITIS intrusions believed to have formed during stages D to E and E to F intruded into the Vredefort Dome, as described in the previous section. This includes RietC, KC and Ww. To understand the geological setting, time relations, metamorphic textures, and possible alteration of these intrusions, the geology of the Vredefort Dome needs to be discussed. This section thus serves to give a summarised explanation of the lithologies in the dome, and how the meteorite impact event influenced the local geology. An overview of the Vredefort Dome (see Figure 2.5) is provided first, followed by brief descriptions of the rock types found within.

In chronological order of formation, the dome primarily consists of Archaean granites, the Dominion Group, the Witwatersrand Supergroup, the Ventersdorp Supergroup, and the Transvaal Supergroup. The Archaean granites form the hub of the Vredefort Dome, while the latter units form the collar strata (Bisschoff, 1999a). The southern and eastern parts of the Vredefort Dome are covered by younger rocks of the Karoo Supergroup.

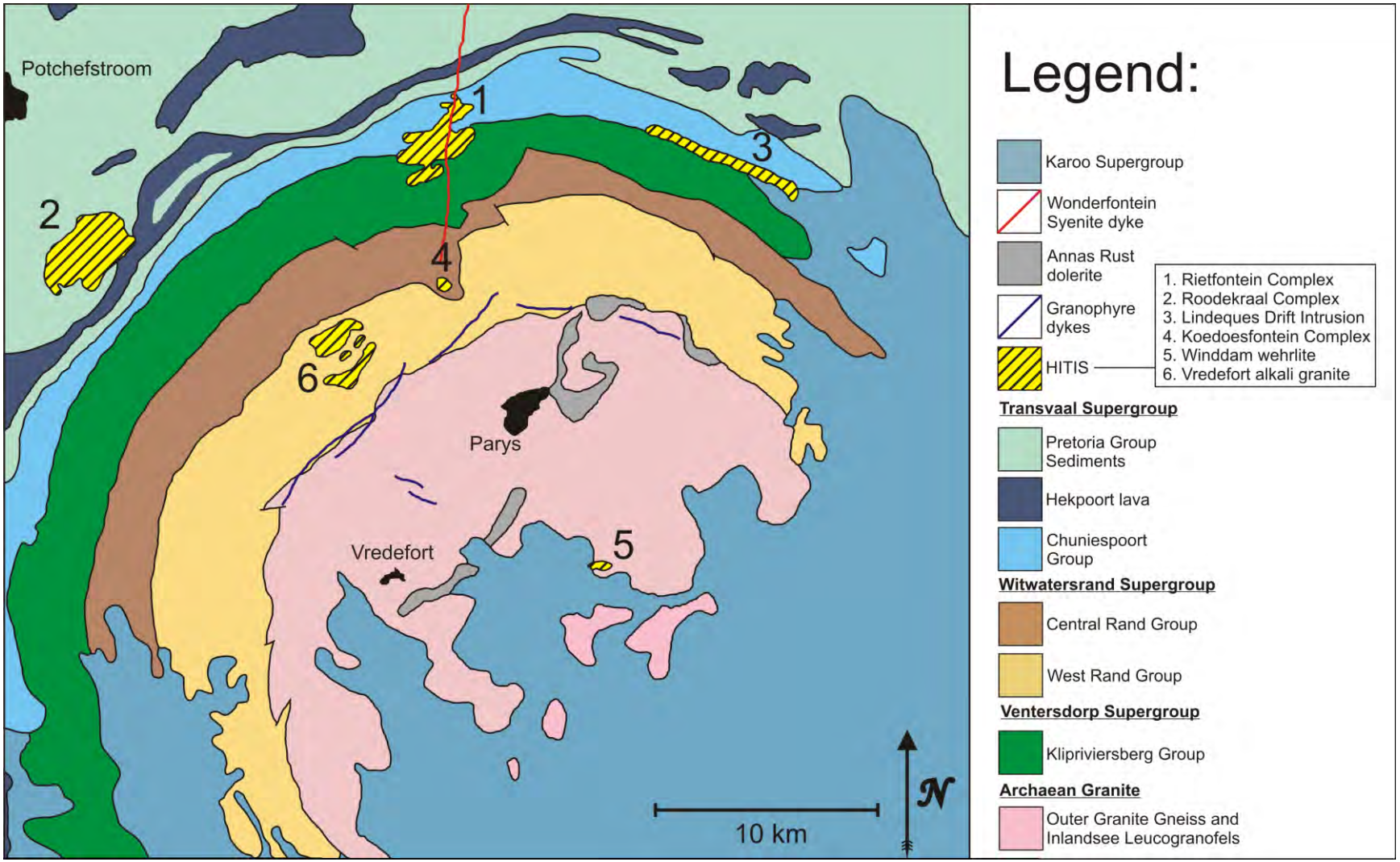

Figure 2.5: Simplified geological map of the major lithologies of the Vredefort Dome (modified after Bisschoff, 1982) and those belonging to the HITIS.

2.3.1 Archaean basement

Stepto (1990) divided the core of the Vredefort Dome into the Outer Granite Gneiss (OGG), the Inlandsee Leucogranofels (ILG) and the Steynskraal Formation (SF). The OGG and ILG formed part of a tonalite-trondhjemite-gneiss (TTG) suite (Lana *et al*., 2004) similar to many other granitic intrusions in South Africa that came about during the early crustal formation of the Kaapvaal Craton (Tankard *et al*., 1982).

The OGG consists of massive granitic rocks, which are, in some localities, metamorphosed to gneiss due to local shearing (Stepto, 1990). Small greenstone remnants can frequently be found within the OGG (Lana *et al*., 2004; Robb *et al*., 2009; Stepto, 1990). The OGG experienced amphibolite facies metamorphism (Bisschoff, 1982), and a transition to the granulite facies occurs at the outer boundary of the ILG (Fagereng *et al*., 2008; Lana *et al*., 2004). The presence of orthopyroxene in the ILG is a testament of granulite facies metamorphism, although the ILG's mafic content is generally less than 5%. Garnet and cordierite are also present in some localities of the ILG (Stepto, 1990), which points to a high-pressure origin typically experienced in the upper levels of Earth's mantle or deep sections of continental crust (Deer *et al*., 2013).

The protolith of both the OGG and ILG appears to be a mixture of sedimentary and igneous rocks, but now has a uniform crystalline appearance due to metamorphism (Fagereng *et al*., 2008). Approximately 30 to 40 million years prior to impact, the rocks of the core experienced intense thermal metamorphism, which Stevens *et al.* (1997) attributed to the emplacement of ultramafic, Bushveld-related magmas.

Within the ILG, several outcrops occur that are grouped together as the SF. They are much more diverse than the ILG and OGG, and consist of several metasedimentary and metamorphosed igneous rocks including mafic granulite, garnet paragneiss, migmatites and amphibolite (Stepto, 1990).

2.3.2 Dominion Group

Within the Vredefort Dome, the Dominion Group occurs at the contact of the OGG and the Witwatersrand Supergroup (Bisschoff, 1999a) and has an age of about 3100 to 3074 Ma (Armstrong *et al*., 1991; Marsh, 2009). The group formed in an ancient basin that probably came into existence due to continental subsidence associated with rifting, which led to the deposition of sandstone (now quartzite) and conglomerate (Marsh *et al*., 1989; McCarthy & Rubidge, 2005; Tankard *et al*., 1982). This was followed by volcanic activity that

produced extrusive rocks with rhyolitic, andesitic, and basaltic compositions (Bisschoff, 1999a; McCarthy & Rubidge, 2005; Tankard *et al*., 1982). Subsequent retrograde metamorphism (involving primarily a reaction between clinopyroxene and H_2O to produce hornblende) in the Vredefort Dome has altered these volcanic rocks to epidiorite (Bisschoff, 1999a), which was caused by the intrusion of Bushveld-age magma (Jackson, 1994). Baking of some of the Dominion Group sedimentary rocks during the same event led to the formation of hornfelses (Jackson, 1994). These hornfelses contain a variety of metamorphic minerals such as garnet, cordierite, amphibole and plagioclase (Bisschoff, 1982).

2.3.3 Witwatersrand Supergroup

Approximately 100 million years after the formation of the Dominion Group, the sedimentary rocks of the Witwatersrand Supergroup were deposited (Agangi *et al*., 2015). Sedimentation occurred in a large basin that formed during further rifting-induced continental subsidence which caused the Kaapvaal Craton to be submerged below sea level (McCarthy & Rubdige, 2005).

The Witwatersrand Supergroup is divided into the older West Rand- and younger Central Rand Group. The West Rand Group consists of alternating layers of quartzite and hornfels with a pelitic protolith, while the Central Rand Group primarily consists of quartzite and conglomerates. The hornfels of the West Rand Group commonly contain garnet, andalusite, and cordierite as metamorphic porphyroblasts (Bisschoff, 1999a).

2.3.4 Ventersdorp Supergroup

The Ventersdorp Supergroup is divided from bottom to top into the Klipriviersberg Group, the Platberg Group, the Bothaville Formation and the Allanridge Formation (Van der Westhuizen *et al*., 2009). After diagenesis and lithification of the Witwatersrand sediments, widespread volcanic activity covered these rocks to form the Klipriviersberg Group, the lowermost unit of the Ventersdorp Supergroup (Van der Westhuizen *et al*., 2009) approximately 2700 Ma ago (Armstrong *et al*., 1991). The origin of these Ventersdorp lavas is believed to be mantle melts formed during upper-mantle decompression that is attributed to extension of the lithosphere (White, 1997). This led to the formation of a mantle diapir than intruded into and extruded onto the overlying crust (Hatton, 1995).

Only the Klipriviersberg Group is encountered in the Vredefort Dome (Bisschoff, 1999a). Bisschoff (1999a) states that it originally consisted of plagioclase and pyroxene with an intermediate (andesitic) composition that has been subjected to low-grade metamorphism. This has altered the mafic minerals of the Klipriviersberg volcanics to primarily chlorite and actinolite. In some localities the plagioclase is present as larger phenocrysts set in an aphanitic groundmass.

Several sills and dykes of epidiorite also occur within the dome, primarily within the strata of the Witwatersrand Supergroup. Bisschoff (1999a) believed that these rock types are comagmatic with the overlying Klipriviersberg Group, and could represent conduits for the lava flows. They originally consisted of pyroxene and plagioclase, but hydration metamorphism after their formation converted the pyroxene to hornblende, producing the plagioclase-hornblende bearing epidiorite.

2.3.5 Transvaal Supergroup

The processes responsible for the generation of the Ventersdorp lavas caused subsidence and basin formation on the Kaapvaal Craton between 2700 and 2450 Ma (Sumner & Beukes, 2006). This led to the deposition of siliclastic and chemical sedimentary rocks of the Transvaal Supergroup in the resulting basins.

The lowermost unit of the Transvaal Supergroup in the Vredefort Dome and adjacent Potchefstroom synclinorium is the 20 m thick Black Reef Formation. Outcrops of this unit in the Vredefort Dome are rare, but are well exposed in the vicinity of RietC. Lithologies that make up the Black Reef Formation include both arenite (now quartzite), and conglomerate (now meta-conglomerate) (Bisschoff, 1999a). The Black Reef Formation is overlain by the much thicker (1200 to 1500 m) Malmani Subgroup of the Chuniespoort Group and primarily consists of dolostone with minor chert (Bisschoff, 1999a). Where the dolostone is in contact with the younger RietC, it has recrystallised to marble, while the accompanying chert has undergone metamorphism to a medium-grained quartzite (Bisschoff, 1982).

2.3.6 Other igneous intrusions in the Vredefort Dome

Several mafic intrusions of apparent Bushveld-age, which Bisschoff (1969; 1972; 1973) grouped into either a tholeiitic- or alkaline suite, are present in the Vredefort Dome. Intrusions belonging to the alkaline suite include the Roodekraal Complex, Lindequesdrift intrusion (see Table 2.1), RietC, KC, and the Ww, (discussed in section 2.5).

Tholeiitic intrusions include the Wittekopjes norite, Reebokkop dolerite and the Parsons Rust dolerite-norite (Coetzee, 2001; Coetzee *et al*., 2006). They primarily occur as sills that had intruded conformably into the sedimentary succession of the Witwatersrand Supergroup, with a few outcrops also present within the core of the Vredefort Dome. It has been shown that the tholeiitic suite could represent satellite intrusions that crystallised from a derivative B1 magma that formed the LZ of the RLS (Coetzee, 2001; Coetzee *et al*., 2006).

More ultramafic rocks were uncovered in a borehole near the centre of the Vredefort Dome that primarily consist of altered harzburgite (Hart *et al*., 1990). Hart *et al*. (1990) believed that these rocks formed part of the upper mantle that was uplifted during the meteorite impact event. In contrast, Merkle and Wallmach (1997) argued that these lithologies, like the tholeiitic suite, also formed during the Bushveld magmatic event based on geochemical evidence.

The Annas Rust dolerite (also as the Annas Rust sheet or ARS) and has intruded the Dome in several localities (see Figure 2.5). The age of the ARS is approximately 1000 Ma and thus younger than the meteorite impact event (Reimold *et al*., 2000). The ARS consists primarily of plagioclase, pigeonite, augite, and olivine (Coetzee *et al*., 1995; Bate, 1995).

2.3.7 Impact-related features

Geological features that originated from impact are pseudotachylite, the Vredefort granophyre, shatter cones, planar deformation features (PDFs), the presence of high-pressure silica polymorphs, and the dramatic overturning of the collar strata. Each one of these features is briefly discussed here.

- Pseudotachylite

When a large meteorite hits the surface of the crust, the surrounding rocks undergo intense deformation during a process called shock metamorphism (Winter, 2010), which leads to a change in the structural arrangement of the affected lithologies (Langenhorst & Deutsch, 2012). A common product of shock metamorphism in the Vredefort Dome is a glassy material called pseudotachylite (Figure 2.6) (McCarthy & Rubidge, 2005), which is formed because of heat generated due to friction in the affected rocks. This heat causes melting of the host material, and fast solidification of the melt leads to the formation of pseudotachylite veins (Harris *et al*., 2013; Vernon, 2004; Winter, 2010). More voluminous pseudotachylite with a massive habit occurs in the core of the Vredefort Dome and,

Figure 2.6: Dark-coloured and yellowish (due to alteration) pseudotachylite veins (arrows) in a boulder of granite from the Inlandsee Leucogranofels, Vredefort Dome.

contrary to the above, is thought to originate due to melting caused by shock decompression (Harris *et al*., 2013). Zircon crystals found within Vredefort Dome's pseudotachylite had their atomic clocks reset during recrystallisation, and provided an age of 2023 Ma for the impact event (Kamo *et al*., 1996).

- The Vredefort granophyre

The Vredefort granophyre occur as nine dykes (between 10 to 50 meters wide) that cross-cut the pseudotachylite (Bisschoff, 1982; 1996). The granophyre dykes (also referred to as impact melt breccia, Vernon & Clarke, 2008) are thought to have originated from melt draining into fractures of the underlying crust from an upper impact melt sheet (Hart *et al*., 2004; Lieger & Riller, 2012). Impact melt sheets form due to superheating of the crust that occurs during meteorite impact events (Lieger & Riller, 2012), as can be observed in the well-preserved Orientale impact structure on the Moon (Spudis *et al*., 2014).

The granophyre dykes are contaminated by mafic country rock adjacent to the original impact sheet (Lieger & Riller, 2012), as well as a small fraction of chondritic material from the meteorite itself (Koeberl *et al*., 1996). The emplacement of the granophyric dykes from the melt sheet could have taken thousands of years (Lieger & Riller, 2012 and references within). This explains why the granophyre would crosscut the pseudotachylite even if both these features formed due to meteorite impact.

- Shatter cones

The presence of shatter cones in the Vredefort Dome was first described by Hargraves (1961). All shatter cones found in geological materials have been produced by only two known processes: nuclear detonation and meteorite impact (Reimold & Jourdan, 2012). Shatter cones are generally described as quasi-conical structures, which consist of V-shaped striations (see Figure 2.7) (Baratoux & Reimold, 2016; Koeberl, 2002; Sagy *et al.*, 2004), with the tip of the "V" pointing in the direction of impact (Sagy *et al*., 2004).

Figure 2.7: V-shaped shatter cone in quartzite from the Witwatersrand Supergroup, Vredefort Dome.

- Planar deformation features

In the Vredefort Dome, crystallographically oriented linear features of small, spherical dots are commonly observed in quartz grains (in thin sections) resident in the Archean granites, referred to as planar deformation features (PDFs) (Schreyer, 1984). These structures can be identified optically, and serve as diagnostic indicators of lithologies affected by the meteorite impact (for example, De Olivera *et al*., 2014; Kamo *et al*., 1996). PDFs form when movement occurs along several planes in a crystal structure, causing friction and subsequent melting of the mineral, leading to the formation of small spherical glass inclusions (Goltrant *et al*., 1992). In the case of the Vredefort Dome, Schreyer (1984) has determined that the spherical inclusions are not glass but consist of small, CO_2-rich fluid inclusions, trapped in the PDFs during their formation.

- High-pressure polymorphs of silica

The shockwave generated by the meteorite impact event has led to the vitrification of quartz grains associated with quartzites in the Witwatersrand Supergroup of the Vredefort Dome. This was followed by recrystallisation of the diaplectic silica glass to both coesite and stishovite, which are both high-pressure polymorphs of SiO_2 (first recognised by Martini, 1978). Because of the high pressures required for their formation, coesite and stishovite are almost exclusively found in areas affected by meteorite impact (Deer *et al*., 2013). This led Martini (1978) to conclude that the Vredefort Dome structure is a product thereof.

- Overturning of the collar strata

Due to the rebound effect that occurred after the initial impact (Brink *et al*., 1997), the collar strata have been overturned from a near-horizontal position to verical and, in some instances, the rocks are now upside down and dipping towards the centre of the Vredefort Dome at steep angles of about 70° to 80° (Brink *et al*., 1997; McCarthy & Rubidge, 2005). Subsequent erosion resulted in a cross-section from the Earth's upper to lower crust (Slawson, 1976) (see Figure 2.8). In contrast, Fagereng *et al*. (2008) argued that the overturned section only extends to the mid-crustal levels based on $\Delta^{18}O$ values. Whatever the case may be, the implications of Slawson's (1976) "crust on-edge" model is that the closer a lithological unit occurs to the centre of the Vredefort Dome, the deeper it was buried prior to impact.

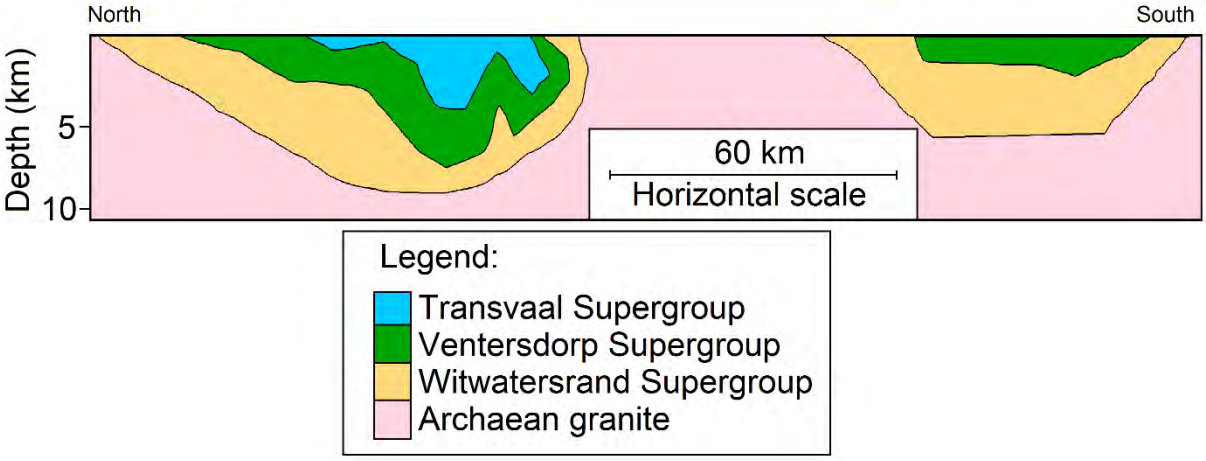

Figure 2.8: North-north-west trending cross-section of the Vredefort Dome to demonstrate its internal structure (modified after Jahn & Riller, 2009)

2.5 THE GEOLOGY OF THE RIETFONTEIN COMPLEX, KOEDOESFONTEIN COMPLEX, AND WINDDAM WEHRLITE

This section aims to provide further details regarding the age, lithology, and mineralogy on the three intrusions relevant to this study. All three intrusions share the common rock type wehrlite (or olivine clinopyroxenite in samples with a lower modal olivine abundance), while dioritic, troctolitic, lamprophyric, and felsic rocks are also present. Refer back to Figure 2.5 for the localities of the three intrusions in the Vredefort Dome.

2.5.1 Winddam wehrlite

Ww is intrusive into rocks of the ILG and lies close to the centre of the Vredefort Dome, approximately 11 km SSE of Parys. The surface outcrop of Ww is oval in shape and has a surface area of about 1.6 x 0.6 km (see Figure 2.9). Stepto (1990) described Ww as consisting of primarily clinopyroxene and olivine with similar grain sizes. Hornblende with a skeletal habit is also abundant (Bisschoff, 1999a). Accessory minerals with a generally smaller grain size are plagioclase and various sulphides, which include pyrite, pyrrhotite, chalcopyrite, bornite and pentlandite (Stepto, 1990).

By comparing the major elemental data of ultramafic rocks from RietC and Ww, Stepto (1990) has made the conclusion that the two intrusions are probably related to each other due to their chemical similarities. However, in contrast to RietC, Ww shows no signs of the typical shock metamorphic features found in the Vredefort Dome like pseudotachylite or shatter cones, suggesting that it might have intruded after the meteorite impact event. Because this would cause an age discrepancy between RietC (see section 2.5.3) and Ww, it would render a coeval relationship between the two intrusions invalid (Stepto, 1990). Bisschoff (1999a) stated that the apparent absence of pseudotachylite in Ww might be due to the poor exposure of the intrusion, or perhaps due to the relative scarcity of pseudotachylite near the centre of the Vredefort Dome (Bisschoff, 1999a; Stepto, 1990).

2.5.2 Koedoesfontein Complex

KC is the smallest of the three intrusions referred to with a lateral extent of about 300 m. It is located approximately 10 km NNE of Parys and consists of several overturned sills of

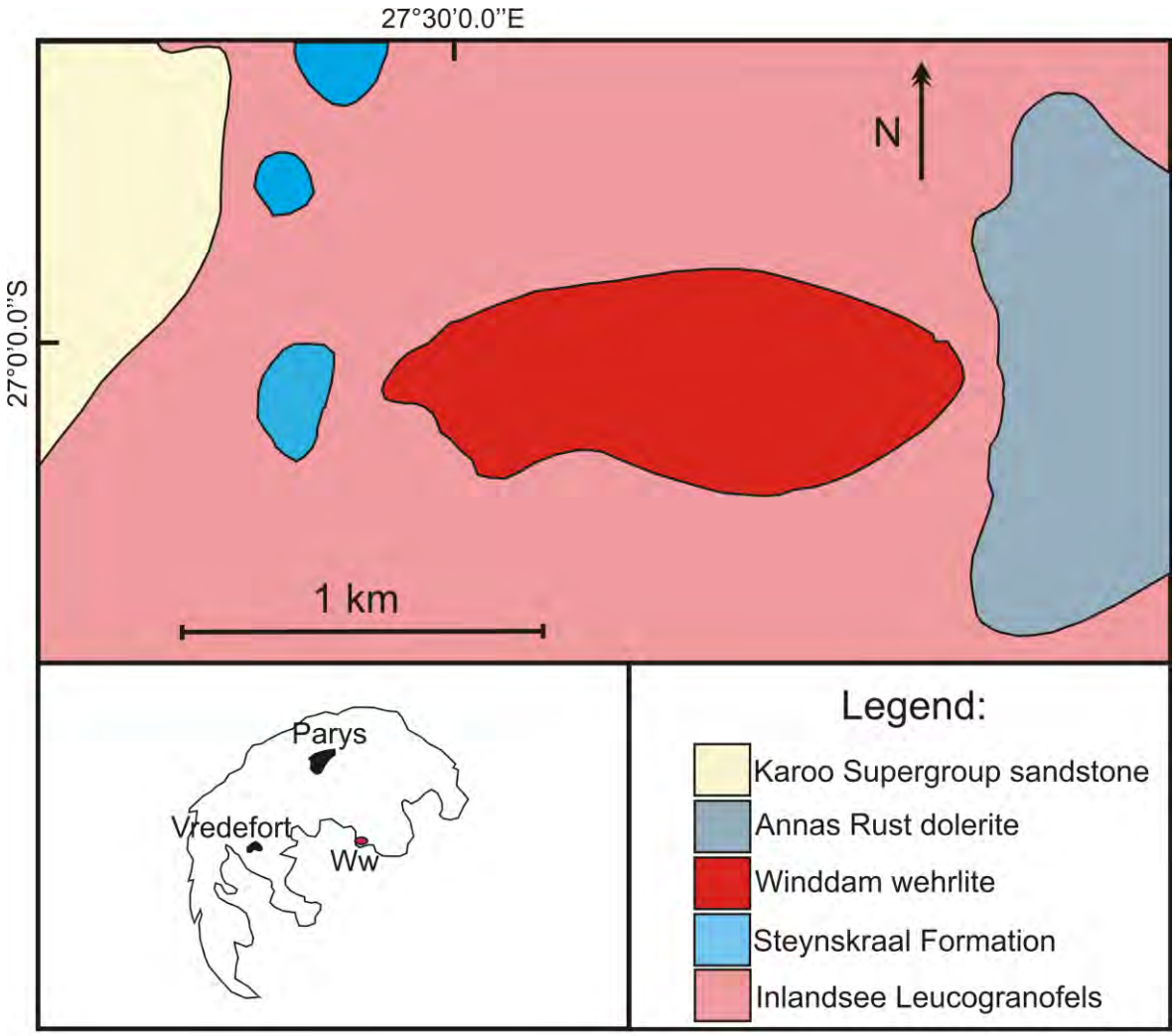

Figure 2.9: Geological map to show the shape of the Ww intrusion and the surrounding geology (after Bisschoff, 1999b). The locality map shows the outline of the core of the Vredefort Dome.

mineralogically distinct igneous intrusions (Boneschans *et al*., 2015) (see Figure 2.10). Bisschoff (1969; 1999a) reports on the presence of a wehrlite intrusion, which is dominated by olivine, clinopyroxene, and minor hornblende and magnetite, porphyritic spessartite that contains hornblende phenocrysts set in a finer matrix of plagioclase and clinopyroxene, and felsic rocks that are modally classified as alkali granite to quartz alkali syenite, all of which form part of KC. Bisschoff (1999a) proposes that the felsic rocks are comagmatic with the Vredefort alkali granite that De Waal *et al*. (2008) propose is part of the HITIS. In addition, Boneschans *et al*. (2015) report on the presence of an unmapped diorite sill, which primarily consists of hornblende, clinopyroxene, and sodic plagioclase.

KC has intruded into sedimentary rocks of the West Rand Group of the Witwatersrand Supergroup in close proximity to an epidiorite sill presumed to be comagmatic with the Ventersdorp Supergroup (Bisschoff, 1969; 1999a). While Bisschoff (1969) described the wehrlite intrusion as a dyke that cuts across the country rock, Boneschans *et al.* (2015)

state that the wehrlite ‘dyke’ is an overturned sill which is aligned sub-parallel to the country rocks. The igneous rocks of KC are situated near the foot of a small hill, and due to coverage of KC by primarily quartzitic colluvial material, outcrops of the intrusion are scarce and difficult to find (Bisschoff, 1969). The presence of pseudotachylite and the intrusion of KC and its intrusion in Witwatersrand Supergroup strata brackets its age between approximately 3000 Ma (age of the onset of Witwatersrand sedimentation) and 2023 Ma (age of the meteorite impact event). Although this provides a large range for a possible age for KC, it is significant to note that this range overlaps with the absolute ages determined for the BIC (2054 ± 0.5 Ma, Scoates & Friedman, 2008) and HITIS (2055.6 ± 3.1 Ma, De Waal & Armstron, 2000).

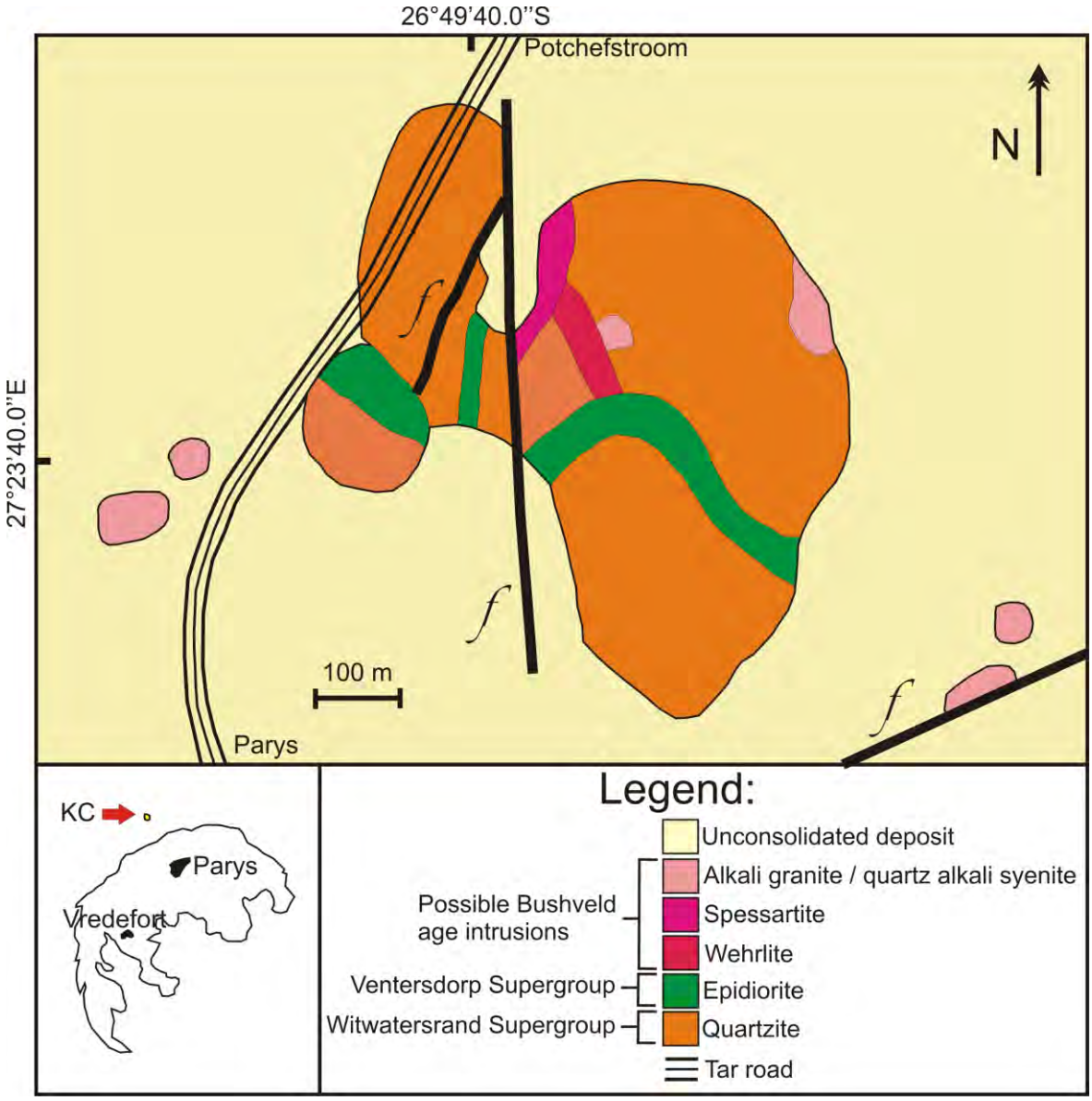

Figure 2.10: Geological map of the Koedoesfontein Complex according to Bisschoff (1999b). The locality map shows the outline of the core of the Vredefort Dome.

2.5.3 Rietfontein Complex

Of the three intrusions relevant to this study, RietC has been mapped (Figure 2.11), and described in the most detail (Bisschoff, 1969; Bisschoff, 1973; Mayer & Bate, 1994). RietC can be divided into a layered, intermediate to ultramafic portion and an upper felsic portion which crosscuts the layered portion. RietC intruded unconformably into the older Ventersdorp Supergroup, the Black Reef Formation, and Chuniespoort Group of the Transvaal Supergroup. The majority of RietC appears to be covered by younger, unconsolidated alluvial deposits that were formed during the flooding of the Vaal River, leading to the poor exposure of the Complex (Bisschoff, 1999). Furthermore, RietC is cut by the Wonderfontein syenite dyke that is probably related to the 1200 Ma (Verwoerd, 2006) Pilanesberg Alkaline Complex (Bisschoff, 1969).

The presence of a shatter cone in the alkali granite (Mayer & Bate, 1994) and the presence of thin pseudotachylite veins in the olivine clinopyroxenite (Bisschoff, 1969) have shown that RietC is older than the meteorite impact event. Thus, RietC would have been overturned along with the collar strata and the igneous layering is now vertical, so that the southern portion represents the lowermost observed section of the complex, while the northern part of the central portion represents the uppermost segment of the layered section. Layers that lie further south are thus inferred to be older than those that lie further north (Bisschoff, 1969). The intrusive nature of RietC into the country rock and the presence of pseudotachylite brackets the age of RietC between approximately 2400 Ma (age of the Chuniespoort dolomite) and 2023 Ma (age of the meteorite impact event). This makes the relative age of RietC indistinguishable from KC, HITIS, and BIC.

In this study, visible outcrops of the layered portion are divided into the southern portion, the western portion, the central portion, and the eastern portion, which are all separated from one another by alluvium (Figure 2.11). The southern and central portions primarily consist of alternating layers of olivine clinopyroxenite and olivine diorite. Bisschoff (1969; 1973) originally classified the olivine clinopyroxenite and olivine diorite as wehrlite and olivine sodagabbro, respectively. Based on mineralogical data from the same author and Kruger (2014), the former terms are more appropriate according to the modern IUGS classification system (Le Bas & Streckeisen, 1991; Winter, 2010). The olivine clinopyroxenite primarily consists of olivine, augite, smaller amounts of hornblende, and accessory magnetite, whereas the olivine diorite is dominated by olivine, augite, sodic plagioclase, and accessory magnetite and biotite.

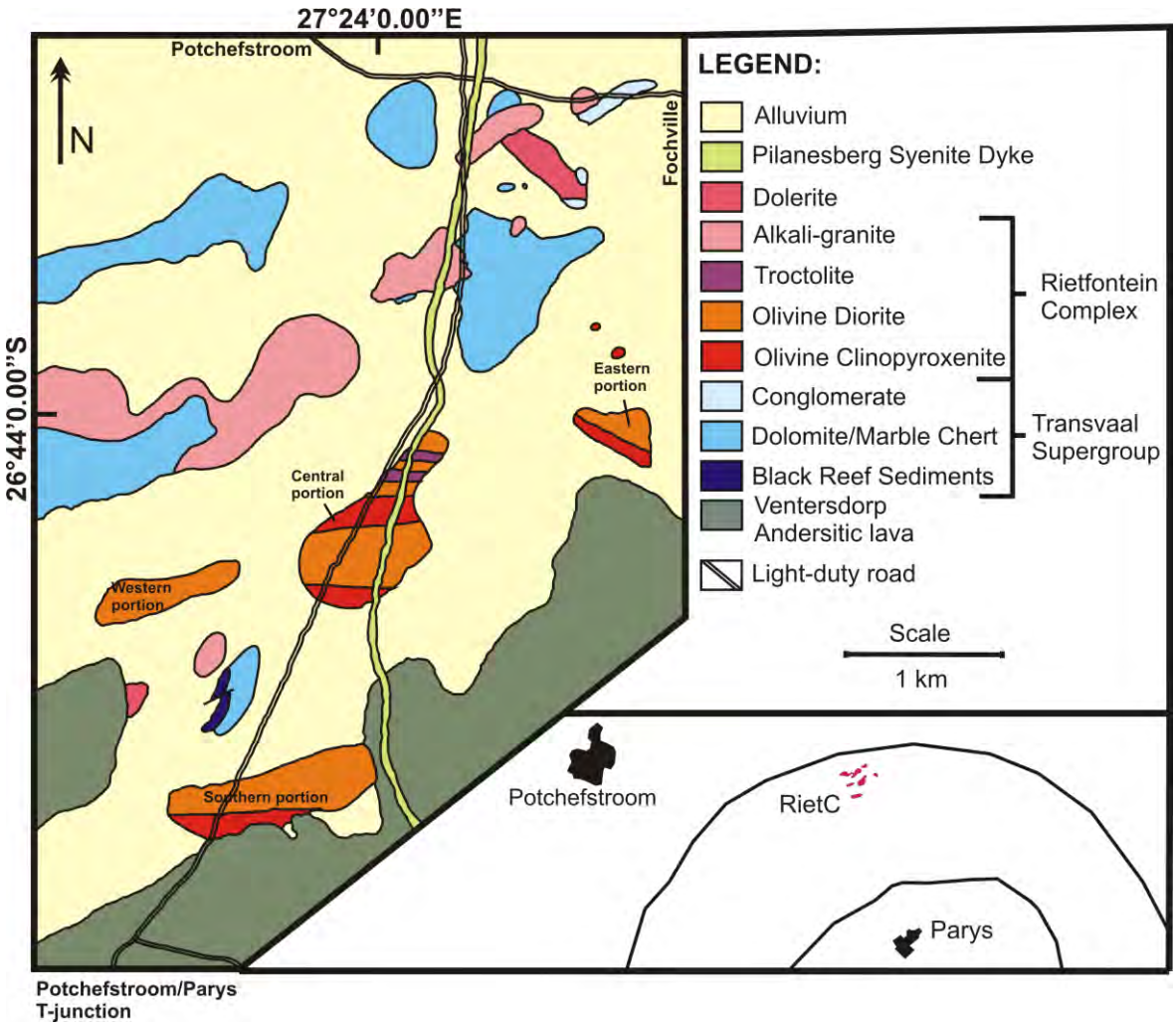

Figure 2.11: The geology of the Rietfontein Complex (modified after Bisschoff, 1969). The locality map shows the outline of the core and collar of the Vredefort Dome.

In the upper (northern) part of the central portion, alternating layers of troctolite and olivine diorite are present (Bisschoff, 1969). The troctolite contains abundant olivine, sodic plagioclase, and magnetite that vary from an accessory phase to highly abundant (up to 37 vol. %) in the northern troctolite layer (Bisschoff, 1969; Kruger, 2014). Accessory biotite is present in all these rock types. The western portion of RietC consists of olivine diorite (Bisschoff, 1973), while the eastern portion consists of both olivine diorite and olivine clinopyroxenite.

Bisschoff (1973) believed that the olivine diorite of the central- and western portion are connected at depth. Mayer and Bate (1994) showed, by making use of a magnetometer, that the southern- and central portions were connected by a thin neck underneath the alluvium cover.

Bisschoff (1969) has proposed that the layering observed in RietC can be explained by considering the addition of several pulses of magma saturated in olivine and augite.

Accumulation of olivine and augite at the bottom of the magma chamber would lead to the formation of an olivine clinopyroxenite layer. As the crystallisation of olivine and augite proceeds, the melt would be depleted in Ca, Mg, and Fe. This would invariably lead to the enrichment of Al and Na in the remaining melt until the magma also becomes saturated in sodic plagioclase. This results in the simultaneous crystallisation of plagioclase along with olivine and augite, leading to the formation of an olivine diorite layer. The addition of a more primitive magma saturated in olivine and augite during this stage would prevent further crystallisation of the plagioclase, and another layer of olivine clinopyroxenite will form on top of the layer of olivine diorite. Once the magma becomes saturated in plagioclase once more, another layer of olivine diorite will accumulate, leading to the cyclic layering observed in RietC. The troctolite would have crystallised from a magma with a different composition that would be oversaturated in olivine and plagioclase. As crystallisation proceeds, this magma would become saturated in clinopyroxene, leading to the presence of olivine diorite layers in between the troctolitic layers. However, Bisschoff (1969) could not test this hypothesis geochemically due to the absence of chemical data for RietC.

Spessartite fragments are scattered over RietC, although Bisschoff (1969) reports that no outcrops of the spessartite could be found. Kruger (2014) reports on the presence of thin veinlets of a rock with a similar appearance to that of the spessartite that cross-cuts the most southern layer of olivine diorite from the central portion, implying that the spessartite is younger in age than the layered portion of RietC. The spessartite is commonly composed of green hornblende phenocrysts set in a matrix of finer sodic plagioclase. The alkali granite makes up the northern parts of the Complex, and crosscuts the layered, dioritic to ultramafic portion in some localities (Bisschoff, 1999a).

CHAPTER 3

METHODOLOGY

This chapter serves to describe the methods used to obtain the data necessary to achieve the research objectives set out in section 1.4. It starts off by giving a description of how and where rock samples were collected and how the rock samples were analysed to obtain data regarding their mineralogical composition, mineral chemistry, and whole-rock major- and trace element geochemistry. Data analysis is dealt with in appropriate sections in the chapters that follow.

3.1 SAMPLE COLLECTION

Samples were collected from Ww, KC, and RietC in such a way as to obtain a good spread of samples across the igneous bodies. This was done to assess how their mineralogical, petrographic, and geochemical characteristics vary on a spatial scale. A list of samples studied is given in Appendix A, along with their identity, sampling location, and the type of analysis performed on each sample. The sampling strategy for each intrusion is dealt with separately below.

3.1.1 Winddam wehrlite

Samples were collected at approximately 100-meter intervals along two traverses over Ww; one over its longest east to west trending direction and one over its shorter north to south trending direction (see Figure 3.1). The traverses were chosen where the Ww intrusion appeared to be at its widest for that particular direction. Each sampling position was recorded using a hand-held GPS device. In areas where rock outcrops were scarce, some deviation from the original traverse occurred, or the sampling point was omitted if no outcrops could be found. As it proved difficult obtaining fresh samples using a rock hammer alone, samples were removed from the outcrop using a hand-held petrol drill with a hollow diamond-coated core bit. Outcrops with visible joints and fracturing were avoided during sampling. All samples collected from Ww during the course of this study are labelled with the prefix W followed by a number indicating the order in which they were collected. An additional 21 samples, collected by MS Coetzee and MD Bate, from the North-West University's Andries Bisschoff Geology Museum rock library were also included in this study to increase the size of the geochemical data set. These samples are labelled CB44 to CB68 although their exact sampling localities in the field are unknown.

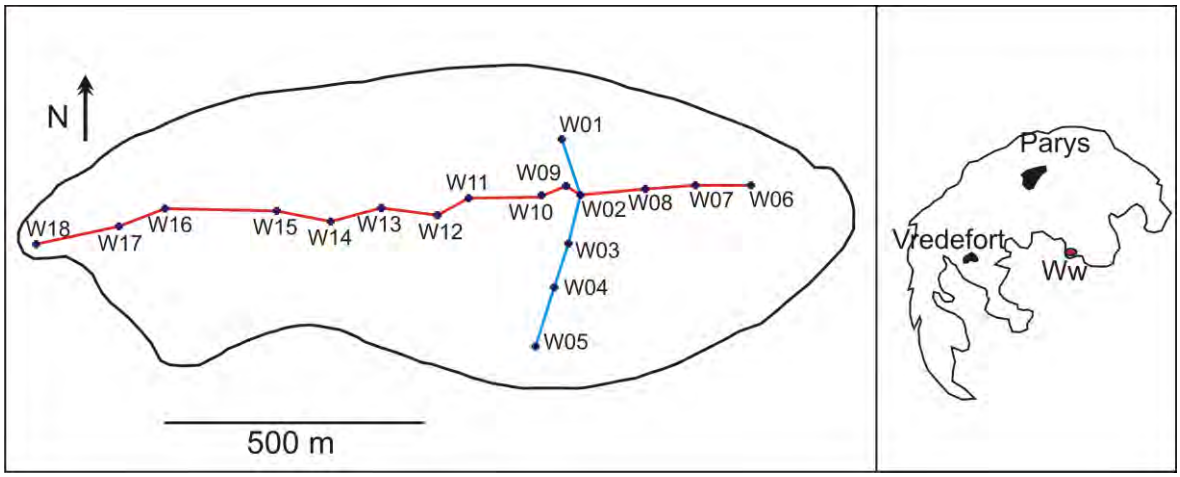

Figure 3.1: (a) Map to indicate the sampling collection sites from Ww. The blue line indicates the north to south transect and the red line indicates the east to west transect along which samples were collected. The black line indicates the extent of the Ww outcrop as mapped by Bisschoff (1999b). The locality map shows the outline of the core of the Vredefort Dome.

3.1.2 Koedoesfontein Complex

The majority of samples from KC are those collected by AA Bisschoff, MS Coetzee, and RB Boneschans, from the North-West University's Andries Bisschoff Geology Museum rock library. Samples of which the exact sampling site is known are labelled as RB, while samples of which the exact sampling locality is unknown are labelled as MSC and a single sample as 304. RB samples include one sample (RB3) that was identified as diorite by Boneschans (2015), while sample 304 and the remaining RB and MSC samples are all of ultramafic composition.

Additional samples were collected to obtain a greater spread of samples across the complex and to improve the sampling density (see Figure 3.2 for sampling localities). The position of each sampling site was recorded using a hand-held GPS device. During field visits to KC, the ultramafic wehrlite dyke could not be followed in a north to south direction as it was originally mapped by Bisschoff (1999b). Instead, the ultramafic intrusion is spread out in a west to east/north-east trending direction, as shown in Figure 3.2. All samples were collected from outcrops with the exception of a single dioritic sample (WK36) due to the difficulty in finding exposures of the mafic/dioritic rocks.

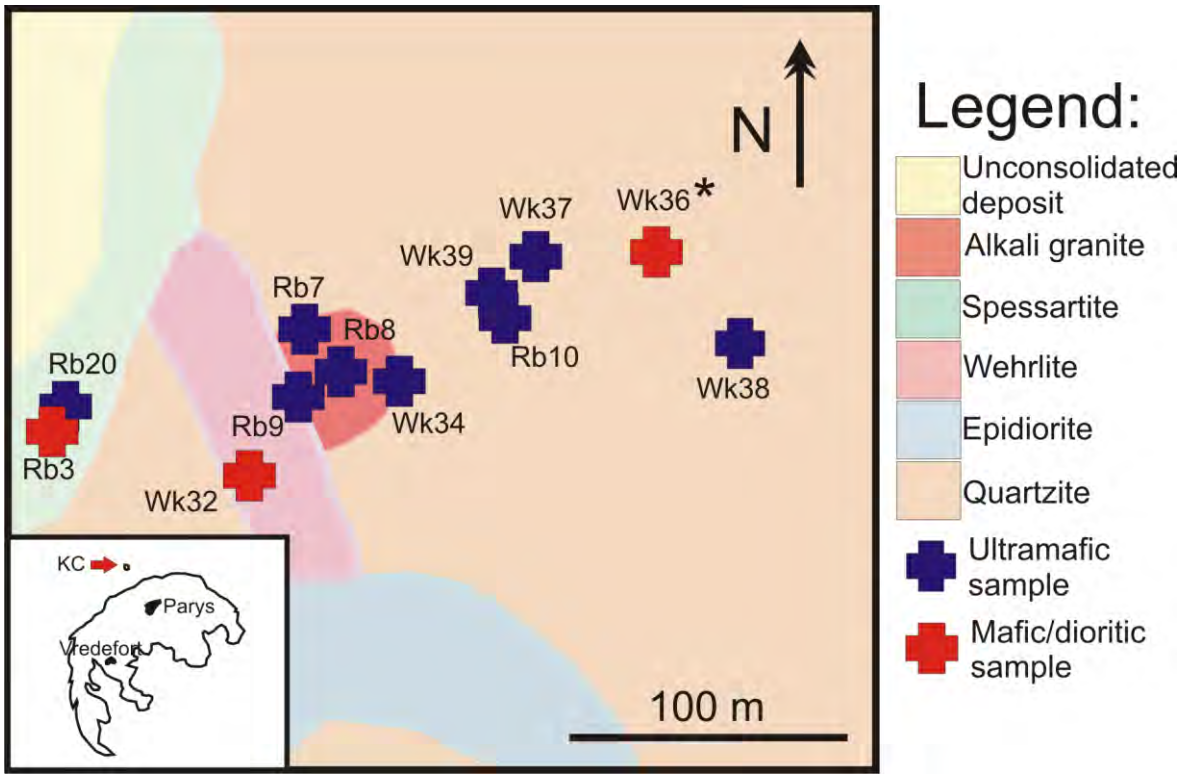

Figure 3.2: A sketch map to indicate the sample collection sites from KC and the boundaries of lithological units as mapped by Bisschoff (1999b). * = Sample WK36 is a loose fragment that was not collected from an outcrop. The locality map shows the outline of the core of the Vredefort Dome.

3.1.3 Rietfontein Complex

The majority of samples studied from the RietC include those collected by MS Coetzee and MD Bate, and stored at the North-West University's Andries Bisschoff Geology Museum rock library and are labelled with the prefix CB, and MB19a. The mineralogy and chemical analysis of three samples (labelled 51, 52 and 54) are those of Kruger (2014). The localities of all samples used are indicated on the stratigraphic column in Figure 3.3.

3.2 PETROGRAPHY

Rock samples collected in the field were studied in thin sections using a polarising, petrographic microscope to accomplish two primary goals: determine the modal mineralogy of the different rock types and to study the textural characteristics of the different rock samples. Modal mineralogy is necessary to classify the rocks according to the modern IUGS classification system for plutonic igneous rocks. The modal mineralogy is also useful to help explain variations in the chemistry of different rock types, which is essential when compiling reports on their geochemical characteristics.

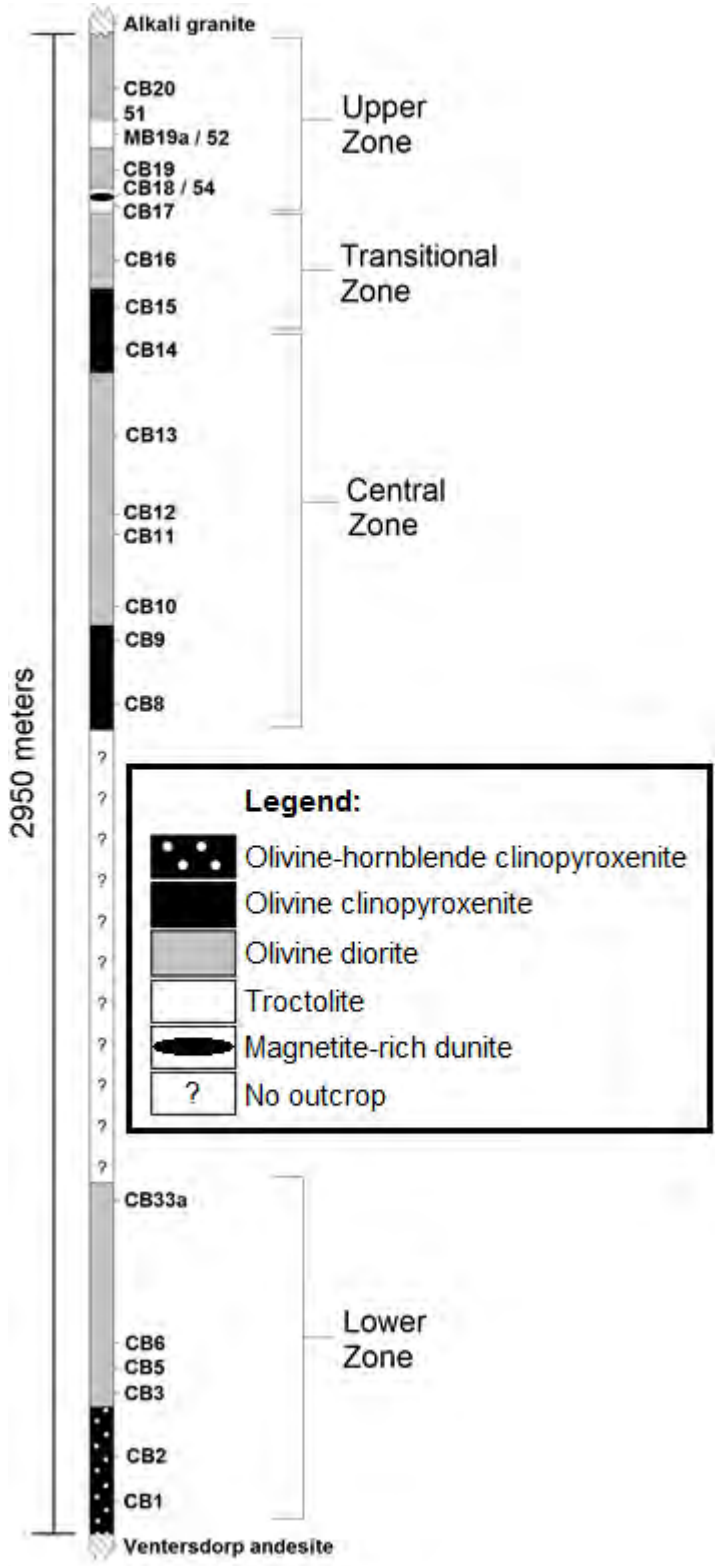

Figure 3.3: Stratigraphic profile of RietC, along with sampling locations and arbitrary stratigraphic subdivisions for ease of reference to different sections of RietC.

Along with geochemical data, the modal mineralogy can be used to estimate liquid compositions of igneous rocks, which can be exceptionally useful to determine whether or not different igneous intrusions are related in origin (discussed in section 6.5.1). Studying

the textural characteristics of rocks can provide valuable clues regarding their crystallisation, metamorphic, and deformational histories, which are essential for unravelling the origin of the rock itself.

3.2.1 Thin section preparation

Four centimetres of the deeper end of the Ww drill cores were used to prepare polished thin sections. For all other samples, visible weathering surfaces were removed using a diamond saw. Samples were polished with diamond-impregnated resin polishing wheels to flatten the surface of the rock. The flattened surface was then glued to a frosted glass slide using an epoxy resin. After a 12 hour waiting period to cure the epoxy, a Struers Accutom-50 precision cut-off machine was used to remove excess sample from the glass slide using a diamond cutting wheel, followed by grinding and polishing until the sample had a final thickness of 30 microns.

3.2.2 Determination of modal mineralogy

After thin sections were prepared, the mineralogical composition in volume percentage (vol. %) of the majority of thin sections were recorded using a point count technique implementing a semi-automatic Swift point counter. Minerals recorded were those underneath the crosshairs of the microscope on each position of the grid. When the crosshairs fell precisely on the boundary of two adjacent minerals, the one that occupies the most space in the lower left quadrant of the crosshairs was counted to avoid any bias. After 500 point counts were performed per thin section, it was found that performing any further counts does not significantly alter the recorded modal mineralogy of the thin section (a variation of less than 2 vol. % for minerals exceeding 20 vol. % was observed, and a variation of less than 1 vol. % for minerals below 20 vol. % was observed). Variations this small from the true modal mineralogy is unlikely to affect the outcome of conclusions made. In order to ensure the accuracy of the point counting method, 800 points were counted per thin section on a millimetre-sized grid. The modal mineralogy of each sample determined via this method is reported in Appendix B.

3.3 WHOLE-ROCK CHEMICAL ANALYSIS

Chemical analysis was performed to accomplish several objectives as set out in the introductory chapter. First of all, chemical analyses are essential in order to provide a report regarding the geochemical composition of the intrusions and to determine how the

chemistry varies within the intrusions themselves. Secondly, the whole-rock chemical analysis can be used to determine trends in the magmatic evolution of Ww, KC, and RietC, allowing their geochemical characteristics to be compared to one another, and can assist in determining if they are related in origin. The chemical composition of the intrusions, especially their trace element concentrations, is essential to determine whether the intrusions fit into the HITIS model of De Waal *et al*. (2008). The relative trace element concentrations can also be used to determine other factors related to the origin of igneous intrusions, such as providing constraints on the mineralogy and geochemical characteristics of the melting source.

3.3.1 Sample preparation

A piece of the lower end of the core was removed for chemical analysis of Ww. Pieces with joints, fractures or surface weathering was avoided during sample selection. In order to remove possible contaminants from the drill core bit, the outer surface of the samples was briefly polished against a diamond-impregnated resin polishing wheel. Afterwards, the samples were crushed using a steel hammer, before being placed in a tungsten carbide ring mill to reduce the size of the particles to below 5 microns. Because this would lead to tungsten contamination, tungsten was not considered in the interpretation of data. For ICP-MS analysis, samples were cleaned in an ultrasonic bath for an hour using deionised water before any crushing was performed. Instead of using a tungsten carbide mill, the samples were powdered using a carbon steel mill for ICP-MS analysis.

3.3.2 X-ray fluorescence

X-ray fluorescence (XRF) spectrometry is an analytical technique used to rapidly obtain accurate data regarding the concentrations of major- and trace elements (Holler *et al*., 2007). All XRF data can be found in Appendices C to F. XRF data for samples labelled as MSC, CB, and MB were obtained from the archives stored in the Geology Department of the North-West University, Potchefstroom campus. MSC samples were analysed at the University of the Free State (Appendix C), while CB and MB samples were analysed at the Council for Geoscience (Appendix D). Samples labelled as WK were analysed at the University of the Witwatersrand (Appendix E). Samples labelled RB, and W were analysed at the XRF and XRD laboratory of the North-West University, Potchefstroom campus (Appendix F), of which the method is described below.

The powdered sample was initially dried at 60 °C for a 24-hour period before being placed in a desiccator and allowed to cool to room temperature. Afterwards, 15 grams of the oven-dried powdered sample was heated to a temperature of 1000° C for a duration of six hours. This was done to drive off any structural hydroxide and carbonate, as well as volatile elements like F, Cl, and SO_3 that are too light to be detected by XRF. The samples were cooled in a desiccator once more, weighed again, and the weight loss was reported as loss on ignition (LOI). Twelve grams of rock powder was placed in aluminium cups and compressed using a 2.5 ton press until the samples had a thickness of about 5-6 mm. The pellets were analysed by a PANalytical Axios Max WDS (wavelength dispersive spectrometer) XRF instrument. A rhodium X-ray tube was used as the source of the X-rays to bombard the pressed samples. Elemental concentrations were determined by using the Super Q database and the data were converted to weight percentage (wt. %) for major oxides and parts per million (ppm) for trace elements.

3.3.3 Inductively coupled plasma mass spectrometry

Inductively coupled plasma mass spectrometry (ICP-MS) is generally used to analyse trace elements that occur in low concentration because of the superior detection limit of this method compared to XRF. Samples were analysed for REE at the University of Cape Town. The REE data for these samples were obtained from the archives of the Geology Department of the North-West University, Potchefstroom campus, and the data is given in Appendix G. Several samples were selected for ICP-MS analysis for a wider range of trace elements at the University of the Witwatersrand. The samples analysed, the list of trace elements, and the concentrations determined using this method is provided in Appendix H.

3.4 ELECTRON MICROPROBE ANALYSIS OF MINERAL GRAINS

This study made use of mineral chemistry data of RietC stored in the archives of the Geology Department at the North-West University, Potchefstroom campus. The mineral chemistry of Ww and KC are not available. Mineral chemistry can be exceptionally useful to determine the processes responsible for layering in igneous intrusions (Namur *et* al., 2015; Winter, 2010). This is because major- and compatible elemental concentrations from whole-rock chemical analysis are greatly influenced by the mineralogy of the rock, while observing changes in the mineral chemistry eliminates this effect.

Electron microprobe analysis was performed using a JEOL 733 microprobe at the North-West University, Potchefstroom campus on olivine, clinopyroxene, and plagioclase from several samples collected from the RietC. For these three minerals each, three separate spots on each of three grains were selected for analysis from each thin section. The analysis was performed on each spot for a duration of 20 to 40 seconds using a 15 kV accelerating voltage, a 0.02 µA beam current and a beam diameter of 1 µm. International mineral standards along with the standard ZAF technique were used to determine the composition of each spot analysed. The averages for each mineral from every individual thin section are reported in Appendix I.

3.5 X-RAY DIFFRACTION

A single sample from Ww (CB47) which was too fine-grained to optically distinguish between augite and enstatite grains present in the rock. It was thus analysed using X-ray diffraction (XRD) with Rietveld quantification to obtain its mineralogical composition at the XRF and XRD laboratory of the North-West University. The diffractogram and calculated mineralogical composition is given in Appendix J.

The sample was crushed to a grain size smaller than 5 micron in a tungsten-caribe steel ringmill. The sample was then prepared by using a back loading technique and was placed onto a spinner stage inside a PANanalytical X'Pert Pro XRD instrument. Thereafter it was bombarded with X-rays originating from a cobalt tube. The crystalline mineral phases present are then identified with an X'Pert Highscore plus and an International Centre for Diffraction Data program. A Rietfield analysis is then performed to determine the weight percentage of all the mineral phases present.

CHAPTER 4

MINERALOGY AND PETROGRAPHY

The purpose of this chapter is to provide mineralogical information of the different lithologies of Ww, RietC, and KC, descriptions of their textural features, type and degree of alteration, and to compare the petrographic features of Ww, KC, and RietC with one another. This chapter is divided into four main sections, namely mineralogy (which deals with the mineral contents of the three intrusions), rock texture (which deals with features such as grain shape, size, and distribution), intra-mineral features (which deals with mineral specific characteristics such as exsolution and twinning), and alteration. Mineral abbreviations used in figures in this chapter can be found in the list of abbreviations.

4.1 MINERALOGY

In this section, each intrusion will be dealt with separately in order to discuss how the mineralogical content varies within each intrusive body and how the rock types are classified according to their mineralogical content. Whether the mineralogy of each intrusion is more typical of alkaline or sub-alkaline rocks will also be discussed, as this can have important petrogenetic implications. The average mineralogical composition of different rock types from Ww, RietC, and KC are summarised in Table 4.1.

4.1.1 Winddam wehrlite

Ww is relatively uniform throughout the entire outcrop. Olivine, augite and hornblende are the most common minerals present with smaller amounts of enstatite. Plagioclase is extremely rare, with only two small grains observed in all 38 thin sections studied. Biotite is only observed in sample W17 and had a modal abundance of 3 volume percentage (vol. %). Opaque minerals observed include pyrite, chalcopyrite, magnetite, and pentlandite, although together their modal abundance never exceeded 1 vol. %.

The modal composition in Ww is remarkably consistent as seen along a north (N) to south (S) transect over the Winddam intrusion (see Figure 4.1) for the first four samples that were collected (refer back to Figure 3.1 for sample localities). Along this transect, the abundance of augite varies between 61 and 64 (vol. %), olivine between 7 and 13 vol. %, hornblende between 16 and 21 vol. %, while enstatite never exceeds 2 vol. %. The only exception to this consistent trend is the most southern sample collected,

Table 4.1: Average and standard deviation (where more than one sample is present) of modal mineral compositions for different rock types from Ww, KC, and RietC. If a rock group contains a relative high amount of a certain mineral compared to other groups, the cell is highlighted in grey.

	Ol vol. %	Aug vol. %	En vol. %	Hbl vol. %	Pl vol. %	Mag vol. %	Qz vol. %
Ww olivine hornblende clinopyroxenite	12.9 ± 7.6	60.3 ± 9.7	1.6 ± 1.1	17.6 ± 7.3	0	< 1	0
Ww olivine hornblende gabbronorite (CB47)	11.1	17.0	34.9	11.4	25.6	2	0
Lower Zone RietC olivine hornblende clinopyroxenites	22.9 ± 0.8	55.5 ± 7.6	< 1	20.9 ± 8.3	0	< 1	0
Central and Transitional Zone RietC olivine clinopyroxenite	15.5 ± 5.7	67.1 ± 4.7	0	< 1	6.7 ± 3.1	7.1 ± 4.1	0
RietC olivine diorite	22.9 ± 11.0	39.5 ± 13.5	0	< 1	31.0 ± 6.9	3.9 ± 3.5	0
RietC troctolite	54.8 ± 12.6	< 1	0	< 1	21.8 ± 13.0	22.6 ± 11.2	0
KC wehrlite-clinopyroxenite	33.5 ± 13.5	62.3 ± 13.4	0	< 1	< 1	7.1 ± 4.1	0
KC gabbronorite (RB3)	0	24	10	15	50	< 1	0
KC norite (WK32)	0	0	50	27	19	< 1	0
KC diorite (WK36)	0	24	0	31	33	12	0
KC pyroxene hornblendite (RB20)	0	13	34	49	0	< 1	2.5

W05, which is dominated by a large hornblende oikocryst. It contains approximately 34 vol. % augite, 20 vol. % olivine, 37 vol. % hornblende, and about 3 vol. % enstatite.

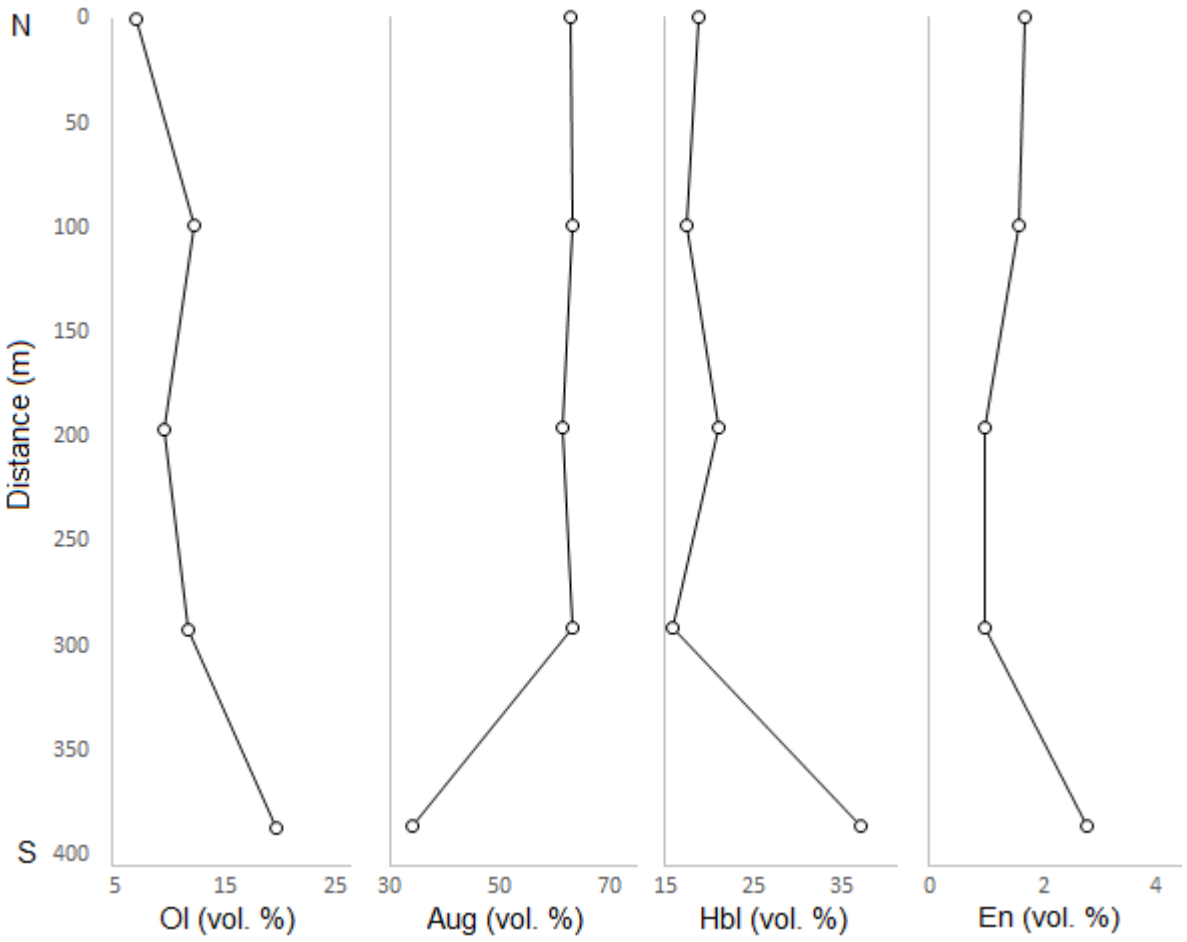

Figure 4.1: Variation in the modal composition of Ww along the north (N) to south (S) transect along which samples (W01 to W05) were collected (refer back to Figure 3.1 in Chapter 3).

The variation in mineral content along the west (W) to east (E) transect is much more variable (see Figure 4.2). However, except for a decrease in the olivine content to the eastern side of the intrusion, no clear trend is apparent in the variation of Ww's modal composition. Once again, augite is by far the most abundant mineral, and its abundance varies from around 48 to 75 vol. %. Hornblende varies from 7 to 29 vol. %, while olivine varies from less than 1% to more than 30 vol. %. Enstatite's abundance never exceeds 4.3 vol. %, and the lowest recorded is less than 0.1 vol. %.

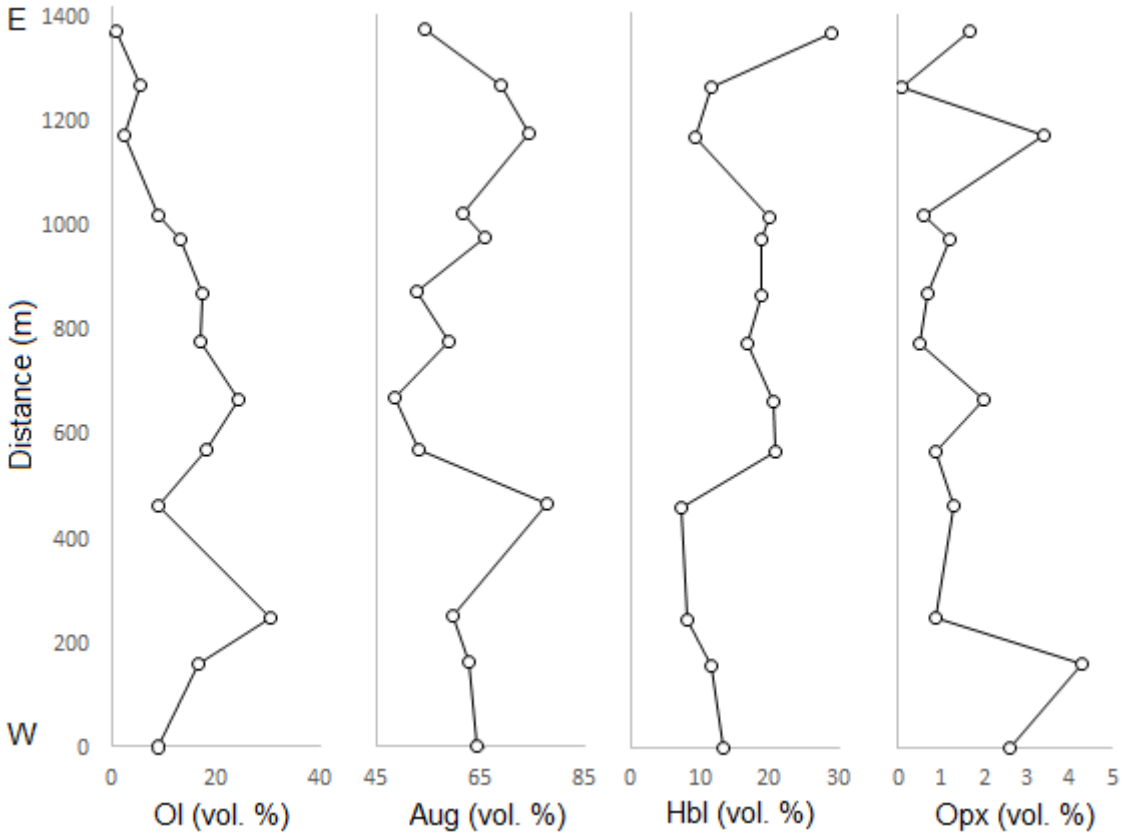

Figure 4.2: Variation in the modal composition of Ww along the west (W) to east (E) transect along which samples (W06 to W18) were collected (refer back to Figure 3.1 in Chapter 3).

The great abundance of augite and relatively low abundance of olivine means that the name wehrlite is inappropriate for the rocks of the Winddam intrusion according to the modern classification scheme of plutonic igneous rocks (Le Bas & Streckeisen, 1991; Philpotts, 1989; Winter, 2010) (see Figure 4.3). Modal compositions from the W-E transect reveal that Ww primarily consists of olivine-hornblende clinopyroxenite, while two samples qualify as hornblende clinopyroxenite and one sample as olivine-clinopyroxene hornblendite. Due to the wide usage of Winddam wehrlite in the literature, it will still be referred to as such. As a whole, ultramafic rocks from Ww will collectively be referred to as olivine-hornblende clinopyroxenite.

A single, relatively fine-grained sample (CB47) (see section 4.3.2) contains much more plagioclase (30 vol. %) than the clinopyroxenite but is not displayed in Figure 4.1 or 4.2 because the exact location of this sample is unknown. In terms of its other constituent minerals, it is comparable to the other ultramafic rocks of Ww with about 10.3 vol. % olivine, 17 vol. % augite, 30.4 vol. % enstatite, 11.5 vol. % hornblende, and 1.7 vol. % biotite. In order to classify this rock type, the anorthite (An) content of the plagioclase was determined via the Michel-Levy statistical method (as described by Heinrich, 1965) and is reported here as An_{57}. This implies that the rock has a mafic mineralogical composition and

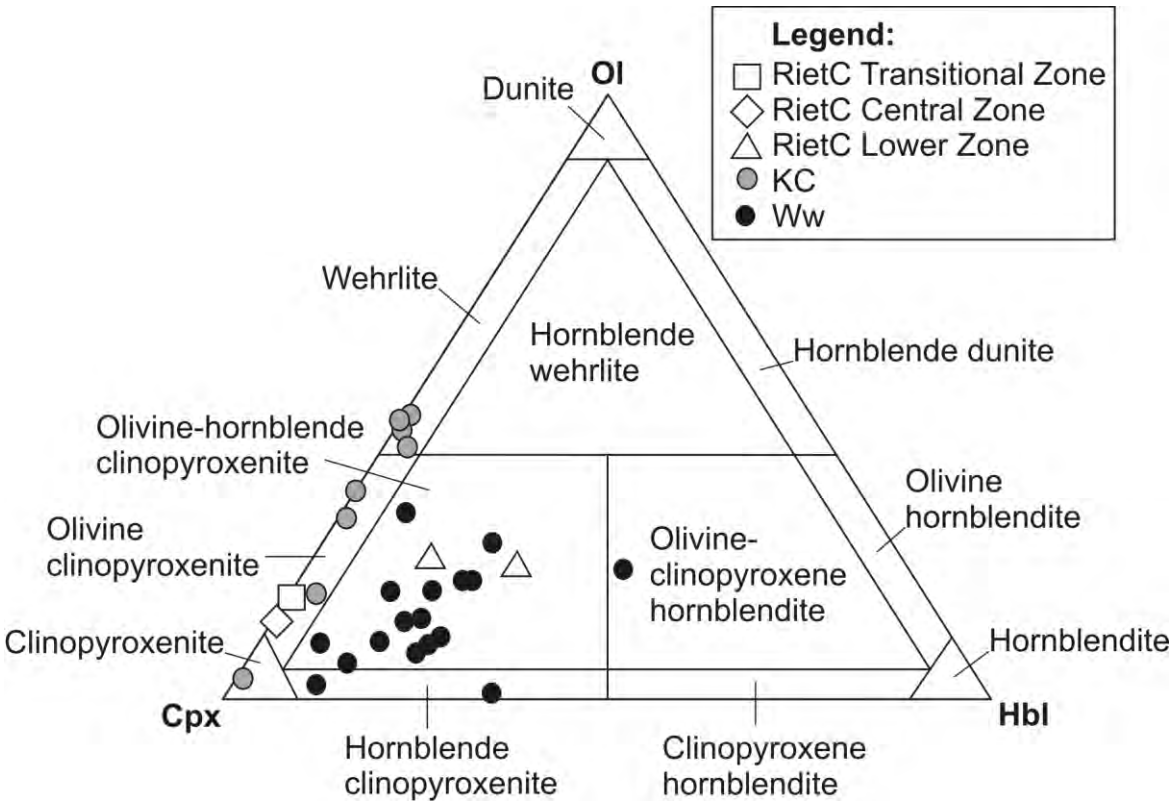

Figure 4.3: Classification scheme used for ultramafic rocks consisting primarily of olivine, clinopyroxene, and hornblende (modified after diagrams in Philpotts, 1989) to demonstrate the classification of ultramafic rocks from Ww, KC, and RietC, and allow for visual comparison of the modal mineralogy of the three intrusions.

classifies as olivine-hornblende gabbronorite according to the IUGS classification scheme (Figure 4.4).

Whether a rock is considered alkaline or not depends on its silica to alkalis ratio (rocks with abundant alkalis relative to silica are said to be alkaline). In order to determine if Ww is alkaline or subalkaline in nature in terms of its mineralogy, it is compared to Yoder and Tilley's (1962) representation of the Di-Fo-Ne-Qz system, shown in Figure 4.5. A rock can only contain the combination of minerals shown in the pyramid in which it lies on this figure. Ww primarily consists of diopside, forsterite, and a small amount of enstatite, which means it would plot in the second pyramid. This suggests that Ww, in terms of its mineralogy, is tholeiitic in nature (see the description underneath Figure 4.5).

4.1.2 Koedoesfontein Complex

The ultramafic rocks of KC classify as wehrlite, olivine clinopyroxenite, and clinopyroxenite (see Figure 4.3), with augite contents that vary from 48 vol. % to as much as 90 vol. %. Olivine contents are comparable to that of Ww and typically vary from 3 to 48 vol. %. In

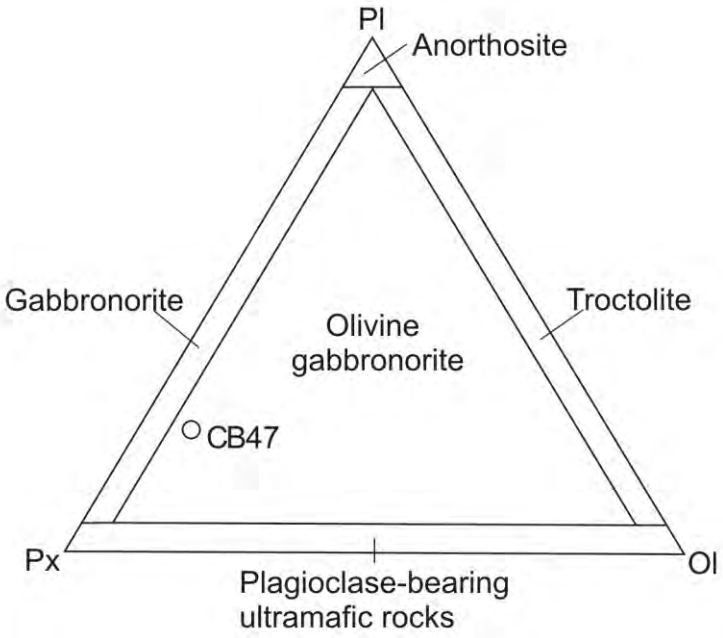

Figure 4.4: Classification scheme used for the classification of mafic rocks consisting of plagioclase, olivine, and a mixture of both clino- and orthopyroxene (modified after Winter, 2010) to classify rock sample CB47 from Ww.

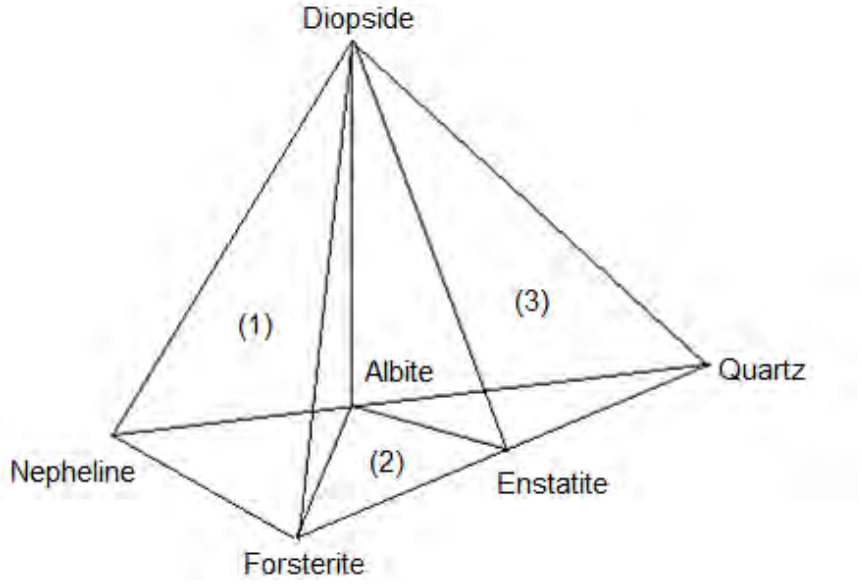

Figure 4.5: Tetrahedron of minerals that will form from a basaltic melt depending on the silica saturation (modified after Yoder & Tilley, 1962). Alkaline rocks tend to be silica-undersaturated and plot in pyramid 1, while sub-alkaline rocks tend to occupy pyramids 2 and 3. If a rock plots in pyramid 1, it can only contain nepheline, diopside, and forsterite, and is said to be silica-undersaturated and alkaline in nature (Wilkinson, 1974). A rock that occupies pyramid 2 contains more silica and nepheline is replaced with albite in the reaction nepheline + SiO_2 = albite (Winter, 2010). In addition, some forsterite will be converted to enstatite in the reaction olivine + SiO_2 = enstatite. If the silica concentration is even higher, all the forsterite would be consumed during this reaction and excess silica would crystallise to form quartz and the rock will plot in pyramid 3. Rocks that plot in the second or third pyramid are said to be sub-alkaline or tholeiitic in nature.

contrast to Ww, the ultramafic rocks of KC contain less hornblende, with the highest abundance recorded being 0.7 vol. %, and no enstatite. Magnetite varied from a fraction of 1 vol. % to as much as 9 vol. %.

The mineralogical variation across a west to east transect of KC's ultramafic sill is shown in Figure 4.6. Olivine contents appear to decrease slightly towards the eastern part of the sill, with one significant drop in olivine content observed in its mid-section. Augite follows the exact opposite pattern of the olivine. Magnetite is relatively abundant in the three most western samples, while no significant modal abundance of magnetite is recorded in the remaining section of the sill. One wehrlite sample from KC (labelled 304) also contains a small fraction of plagioclase (< 2 vol. %).

Samples RB3, WK32, and WK36 differs from the other rocks of KC due to their high modal abundance of plagioclase (between 18 to 50 vol. %) and the absence of olivine. In order to classify these rocks, their anorthite content was determined using the Michel-Levy statistical method (Heinrich, 1965). The results show that the plagioclase in sample RB3, originally classified as diorite (Boneschans *et al*., 2015), has a labradoritic

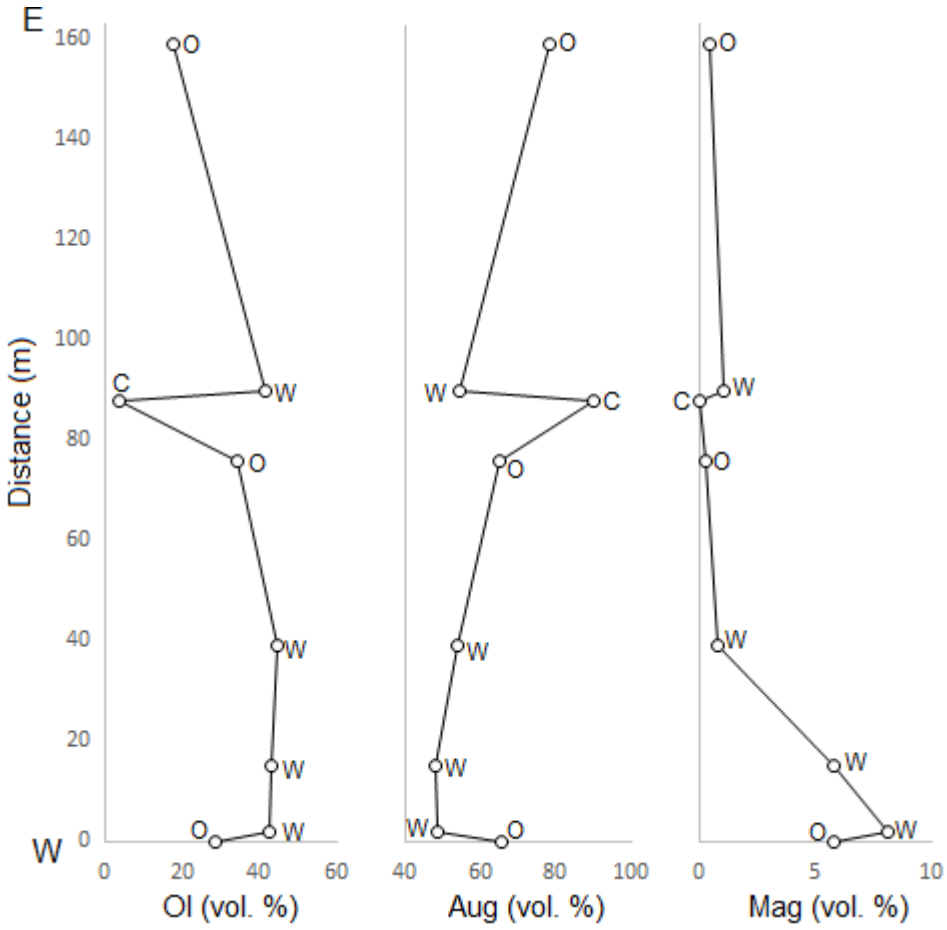

Figure 4.6: Variation in the modal mineral abundance across the wehrlite-clinopyroxenite sill from KC. C: clinopyroxenite; O: olivine clinopyroxenite; W: wehrlite.

composition (An_{62}), implying the rock is mafic in nature. Similarly, sample WK32 has a labradoritic plagioclase composition of An_{54}, while the plagioclase of WK36 is sodic in composition and lies between An_{12} and An_{28}. The exact anorthite content of plagioclase cannot be determined using the Michel-Levy statistical method if the anorthite content of plagioclase is less than An_{37} (Heinrich, 1965).

RB3 consists of approximately 24 vol. % augite, 10 vol. % enstatite, 50 vol. % plagioclase, and 15 vol. % hornblende. Magnetite is present as a minor constituent and makes up less than 1 vol. % of the rock. This mineralogical composition, along with the composition of the plagioclase, indicates that the rock should preferentially be classified as hornblende gabbronorite (see Figure 4.7). With a mineralogical composition of 50 vol. % enstatite, 27 vol. % hornblende, and 19 vol. % plagioclase, sample WK32 classifies as hornblende norite. WK36 contains no enstatite, 24 vol. % augite, 33 vol. % plagioclase, 31 vol. % hornblende, and a significant amount of magnetite (approximately 12 vol. %). Due to the sodic composition of the plagioclase, sample WK36 classifies as diorite. Because of the poor exposure of these rock types, a mineralogical variation diagram such as the one shown in Figure 4.6 could not be constructed.

A unique sample (RB20) classifies as pyroxene hornblendite (see Figure 4.8) and has a distinctive mineral assemblage, with 49 vol. % hornblende, a high enstatite content of about 34 vol. %, a low augite content of approximately 13 vol. %, and also contains a small amount of quartz (± 2.5 vol. %).

The presence of enstatite in the gabbronorite and norite along with the occurrence of both enstatite and quartz in the pyroxene hornblendite means that these samples will plot in pyramids 2 and 3 on Figure 4.5, implying that they are tholeiitic in nature. However, since neither enstatite nor nepheline is observed in the wehrlite/olivine clinopyroxenite, they plot on the plane between pyramid 1 and 2. Thus, whether these rocks are tholeiitic or alkaline in nature has to be assessed chemically (section 5.4).

4.1.3 Rietfontein Complex

The classification of ultramafic rocks from RietC is displayed in Figure 4.3 while the classification of plagioclase-rich rocks from this intrusion are displayed in Figure 4.9. Electron microprobe analysis has revealed that the plagioclase in RietC is sodic in composition (An < 50%) (section 5.3.3). Thus, in contrast to KC and Ww, all plagioclase-rich rocks from RietC are dioritic in nature. For ease of reference, RietC is arbitrarily divided into a Lower Zone, Central Zone, Transitional Zone, and Upper Zone (see Figure 3.3). RietC has

considerable variation in its mineralogical content throughout the intrusion due to its well-developed modal layering (section 2.5.3).

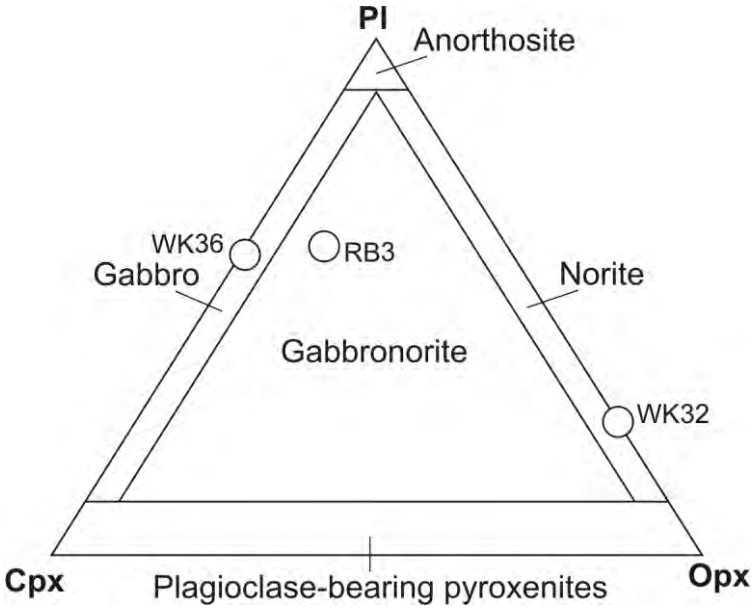

Figure 4.7: Classification diagram for rocks consisting of plagioclase, clinopyroxene, and orthopyroxene (modified after Philpotts, 1989) for the classification of plagioclase-rich rocks from KC.

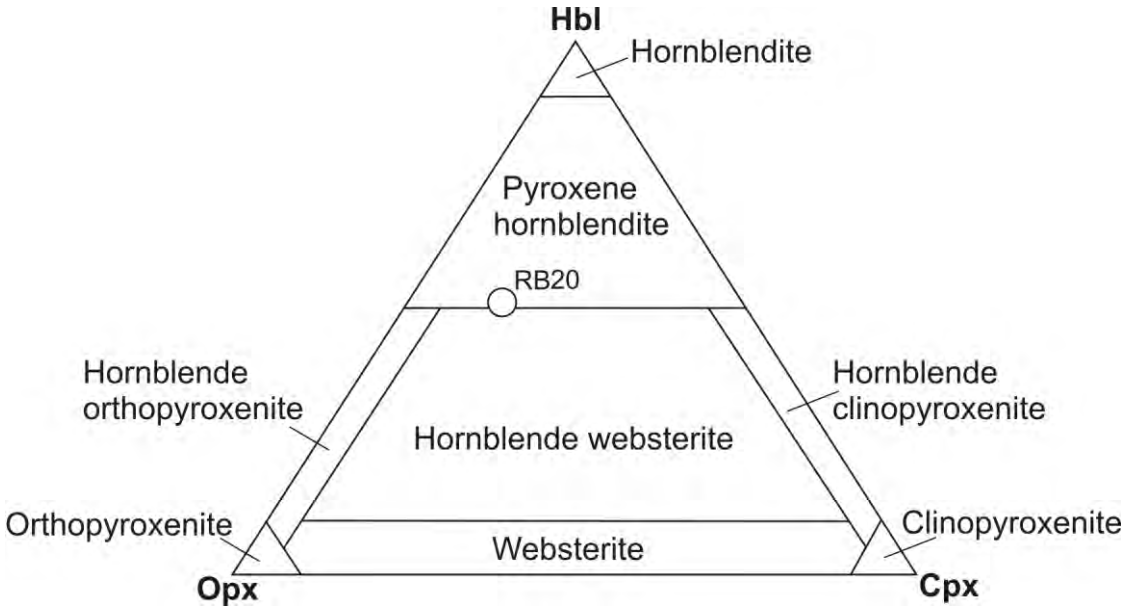

Figure 4.8: Classification diagram for rocks consisting of hornblende, clinopyroxene, and orthopyroxene modified after diagrams in Philpotts (1989) and used for the classification of sample RB20 from KC.

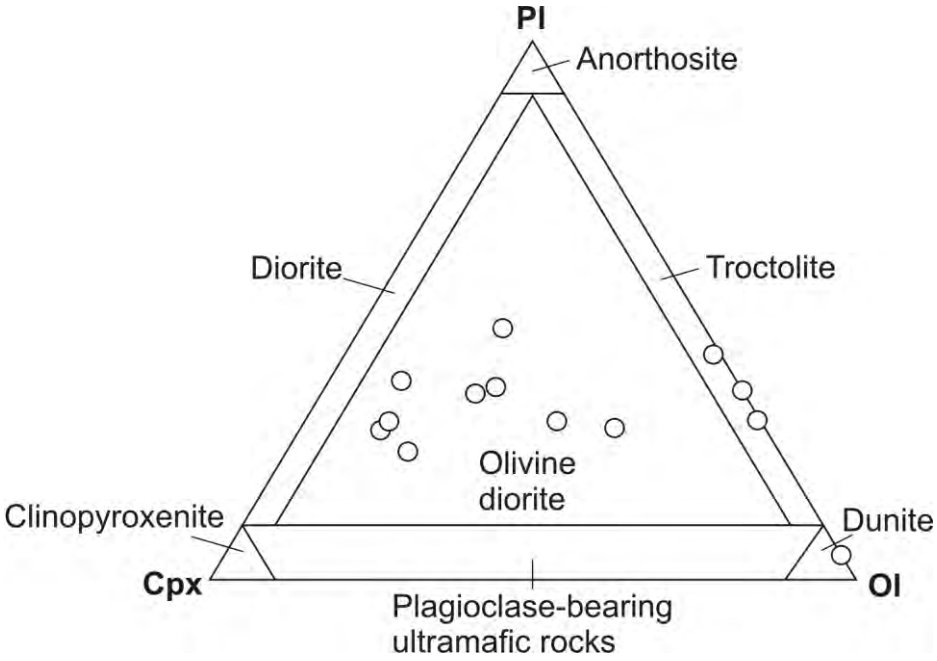

Figure 4.9 Classification diagram for dioritic (An of plagioclase < 50%) igneous rocks that primarily consist of clinopyroxene, olivine, and sodic plagioclase (modified after Winter, 2010) used for the classification of dioritic rocks from RietC.

The variation in the mineralogical content across the southern- and central zones of RietC (Figure 2.11) is shown in Figure 4.10. The mineralogy of the most southern layer of the Lower Zone of RietC is very similar to the rocks of Ww as it is dominated by olivine, augite, and hornblende while it contains little enstatite. Along with the majority of samples from Ww, this layer also classifies as olivine-hornblende clinopyroxenite (see Figure 4.3). The olivine contents of this rock layer appear to be relatively uniform (22 to 23.5 vol. %), while augite vary from 50 to 61 vol. %. A dramatic decrease in hornblende is observed upwards in this layer (from 27 to 15 vol. %), and disappears completely in the overlying layer of olivine diorite. Magnetite was the only opaque phase identified in this rock layer and has an abundance of less than 1 vol. %.

The transition from olivine-hornblende clinopyroxenite to olivine diorite in the Lower Zone is met with the appearance of abundant plagioclase (27 to 45 vol. %) and a small amount of biotite (< 0.5 vol. %). Across this transition, olivine contents vary between 12 to 24 vol. % while the augite content varies from 40 to 56 vol. %. Magnetite is slightly more abundant in the olivine diorite compared to the underlying ultramafic layer and varies from more than 1 to about 4 vol. %.

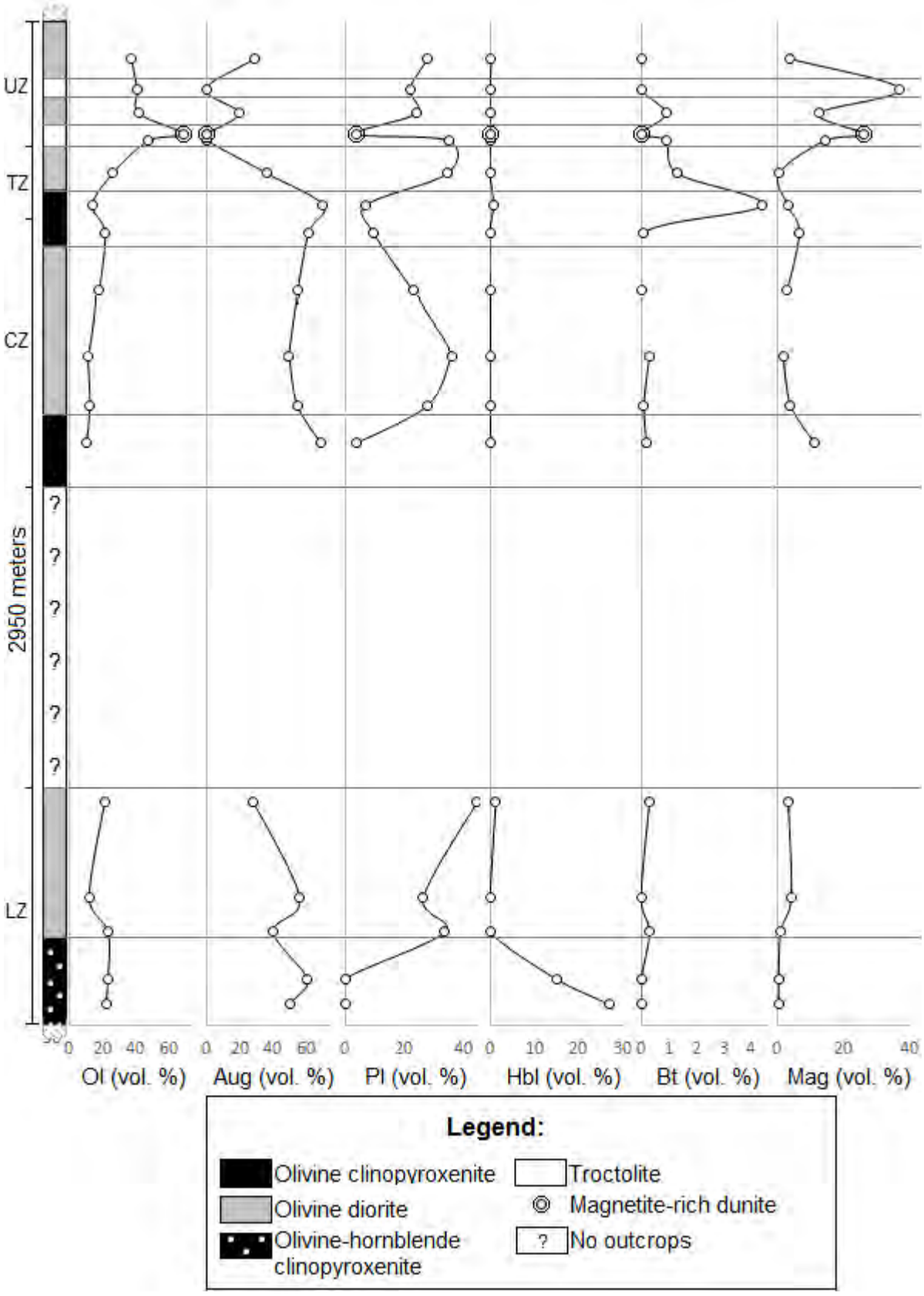

Figure 4.10: Variation in the modal mineral composition across RietC perpendicular to the strike of the layering. LZ: Lower Zone. CZ: Central Zone. TZ: Transitional Zone. UZ: Upper Zone.

The olivine clinopyroxenite of the Central Zone had olivine contents that vary between 10 and 22 vol. %. Augite contents are relatively high and varies from 61 to 70 vol. %. In contrast to the ultramafic layer in the Lower Zone, these rocks have small amounts of plagioclase (between 3 and 10 vol. %) and significant amounts of magnetite (from 6 to 12 vol. %). Hornblende and biotite are virtually absent as both minerals have modal abundances of less than 0.5 vol. %. A total of 4.4 vol. % pseudotachylite was also recorded in sample CB9 from the southern layer of olivine clinopyroxenite in the Central Zone.

The Central Zone olivine diorite contains between 11 and 19 vol. % olivine and 50 to 62 vol. % augite. The plagioclase contents vary from 23 to 36 vol. %, and initially increase upwards in this rock layer before a linear decrease is observed in the central parts of this layer. Plagioclase contents continue to decrease across the transition to the northern olivine clinopyroxenite of the Central Zone. The magnetite contents vary from approximately 2 to 4 vol. %, biotite is less than 0.5 vol. %, and no hornblende is recorded.

The mineralogy of the Transitional Zone olivine clinopyroxenite is recorded as 14 vol. % olivine, 70 vol. % augite, 7 vol. % plagioclase, 3 vol. % magnetite and has the most biotite, compared to any other sample collected, of more than 4 vol. %. The modal hornblende content of this rock layer is less than 1 vol. %. A single sample of olivine diorite (CB16) from the Transitional Zone contained approximately 26 vol. % olivine, 37 vol. % augite, and 35 vol. % plagioclase. It has no hornblende, just more than 1 vol. % biotite and close to 1 vol. % magnetite.

The base of the Upper Zone is defined as a rapid reduction in the augite content of the rock. Troctolite from this section of RietC contained less than 1 vol. % of augite, while olivine contents are high in the troctolite compared to the rest of the intrusion (from 41 to 48 vol. %). The highest olivine content (69 vol. %) is recorded in magnetite-rich dunite samples MB19a and 54 (which are circled in Figure 4.10). These samples contain a low modal abundance of plagioclase (4 vol. %). Overall, the plagioclase content of the troctolite varied from 4 to 35 vol. %. The southern layer of troctolite contains a high modal abundance of magnetite (more than 14 vol. %), while an exceptionally high modal magnetite content is recorded for the magnetite-rich dunite (26 vol. %) and the highest recorded for the Complex is in the northern troctolite layer (37 vol. %). Biotite was scarce in the troctolite and dunite (less than 1 vol. %), and only a small amount of hornblende was detected in the southern troctolite layer (recorded as ± 0.1 vol. %). Upper Zone olivine diorite contain between 37 and 42 vol. % olivine, 19 and 30 vol. % augite, and 24 to 29 vol. % plagioclase. No more than 0.5 vol. % and 1 vol. % hornblende and biotite are recorded in these rocks, while the magnetite content varied from 3 to 13 vol. %.

Due to the presence of enstatite in the Lower Zone ultramafic rocks, this section of RietC appears to be tholeiitic in nature as it falls into pyramid 2 on Figure 4.3. Since neither nepheline nor enstatite was observed in the remainder of the Complex, it occupies the plane between pyramid 1 and 2, and whether it should be considered tholeiitic or alkaline in nature based on its mineralogy is uncertain. This issue is further addressed in section 5.5.1.

4.2 ROCK TEXTURE

During the petrographic investigation of Ww, KC, and RietC, four groups of rocks were identified that share similar textural characteristics namely: (1) olivine hornblende clinopyroxenite from Ww and RietC, (2) wehrlite-clinopyroxenite from KC and RietC, (3) olivine diorite from RietC, and (4) troctolite from RietC, each of which is discussed in individual subsections. Rock samples that do not fit in any of these groups are dealt with separately.

4.2.1 Group 1: Olivine-hornblende clinopyroxenite from Ww and RietC

The typical appearance of rocks that belong to this group is shown in Figure 4.11 for Ww and Figure 4.12 and 4.13 C for the Lower Zone of RietC. In these rocks, the olivine grain shapes are typically equidimensional, oval, to slightly elongated. All of the grains are anhedral and have slightly curved to irregular grain boundaries. Grain diameters of the olivine usually range between 0.5 to 2 mm. The augite varies from a rounded to oval, to slightly elongate grain shape. A feature that distinguishes this group of rocks is the highly irregular, sutured nature of the grain boundaries of the augite (shown in Figure 4.11 and 4.12). The grain diameters of the augite generally vary from 0.5 to 3 mm in length. The lack of intercumulus minerals between augite and olivine grains indicates that these minerals have probably grown after accumulation and that the rock possesses an adcumulate texture.

Enstatite typically encloses olivine and clinopyroxene grains poikilitically (see Figure 4.14), and enclosed olivine grains usually show embayed contacts. Enstatite covers relatively large surfaces in the thin section and varies from 0.3 up to 5 mm in diameter. Its grain shapes are irregular and always anhedral.

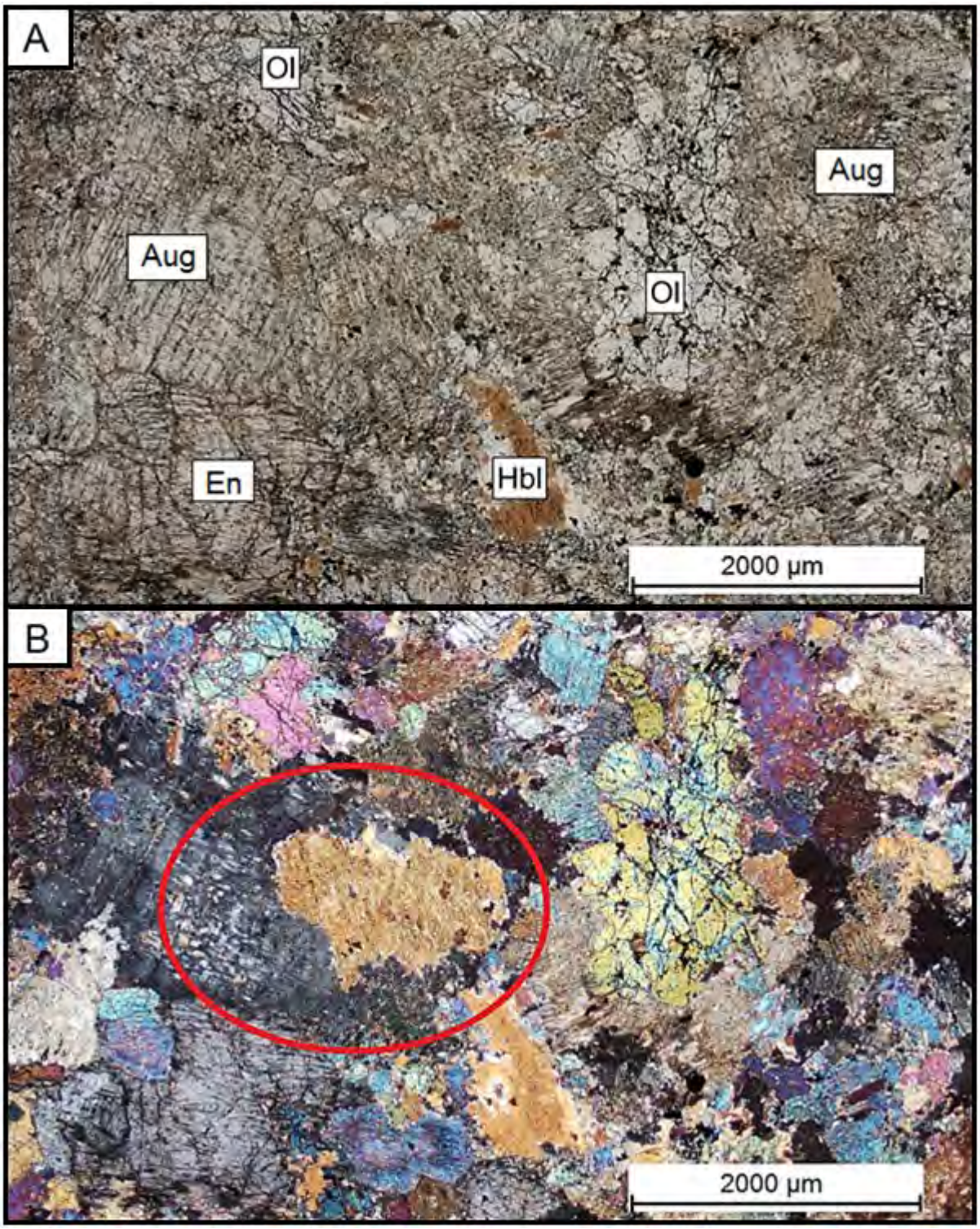

Figure 4.11: Photomicrograph to demonstrate the typical appearance of the Winddam wehrlite (sample WO1). (A) Minerals that make up the majority of Ww can be seen: olivine, augite, enstatite and brown to colourless hornblende. Oxide exsolution has given the augite a clouded appearance using plane polarised light (PPL). (B) Same as A, using crossed polarised light (XPL) to demonstrate the highly irregular, sutured contacts of the augite, circled in red.

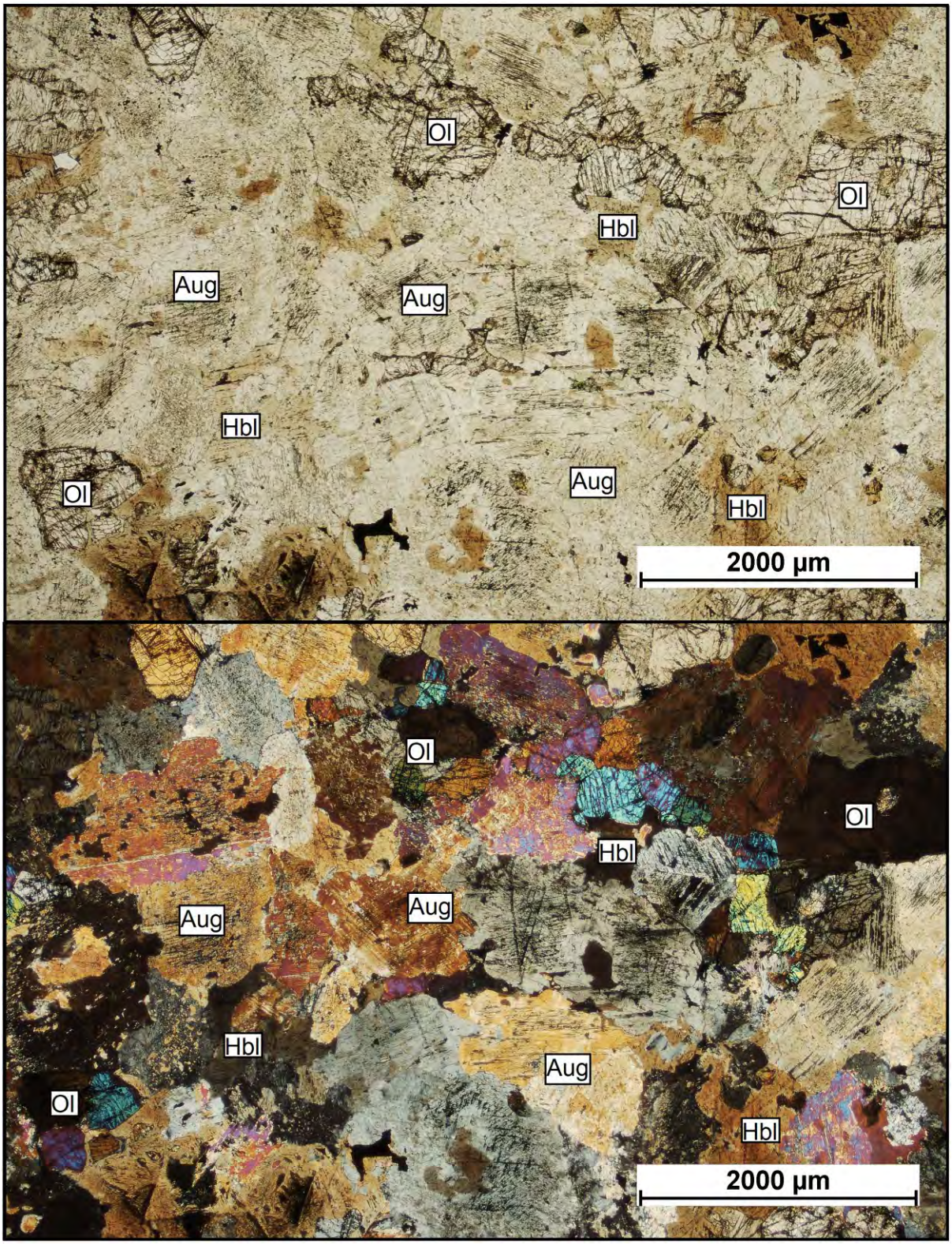

Figure 4.12: Photomicrographs of olivine-hornblende clinopyroxenite in the Lower Zone of RietC (sample CB1). A: Notice the presence of olivine (high relief), clinopyroxene (near colourless) and hornblende (brown) under PPL. B: Same as A, under XPL to demonstrate the highly irregular sutured grain boundaries of the augite.

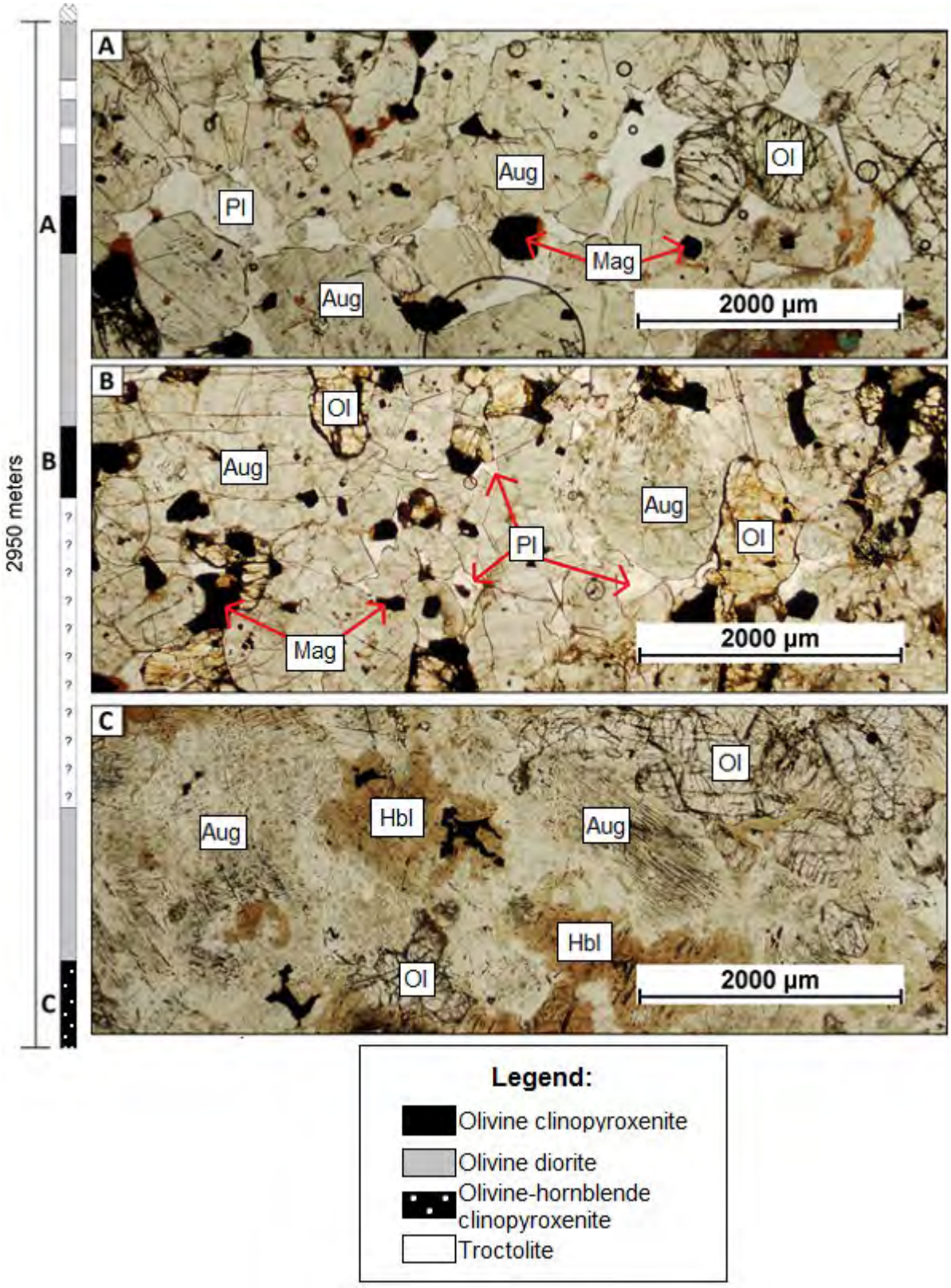

Figure 4.13: Photomicrographs to display the appearance of olivine (±hornblende) clinopyroxenite from the (A) Transitional Zone (sample CB15), (B) Central Zone (sample CB9), and (C) Lower Zone (CB1), from RietC, using PPL. Notice the presence of intercumulus plagioclase in (A) and (B), while the texture is absent in (C). On the other hand, (C) contains a high modal abundance of interstitial hornblende, while this mineral is scarce in the former two samples.

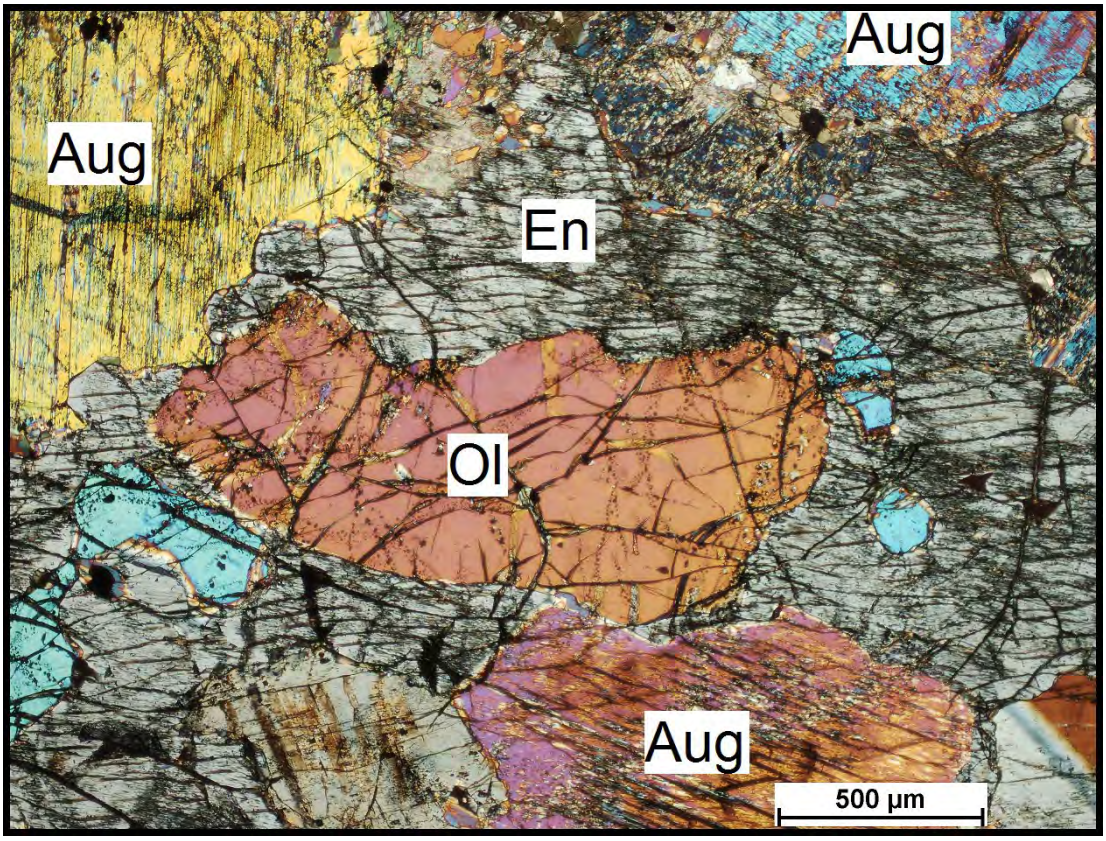

Figure 4.14: A single grain of orthopyroxene (first order interference colour) poikilitically enclosing grains of olivine (W12). The enclosed olivine typically shows embayed contacts, implicating a peritectic reaction relationship between olivine and magmatic silica (see section 6.1.1.3).

Hornblende primarily occurs as an interstitial mineral (Figure 4.15 B), with a highly irregular habit that appears to spread out into interfacial boundaries of the other mafic silicates. Its grain size varies from small specks, but a few microns in diameter, to larger grains that span across large areas of a single thin section. Some of these larger hornblende grains poikilitically include several grains of olivine and augite (Figure 4.15 C). The smaller ones occur as fragments within augite or olivine grains (for example, Figure 4.15 A), or as flakes within the cleavage planes of augite.

An interesting feature of some samples from Ww is the occurrence of small patches or, in other cases, stringers of finer (typically between 100 and 300 µm in diameter), granoblastic mineral grains of olivine, augite, and hornblende, a typical metamorphic texture. The width of these stringers typically varies from 1 to 5 mm, while isolated patches of the texture usually have diameters smaller than 1 mm. The grains that occur within these stringers are usually characterised by planar grain boundaries that intercept to form 120° triple-point grain boundary junctions (see Figure 4.16).

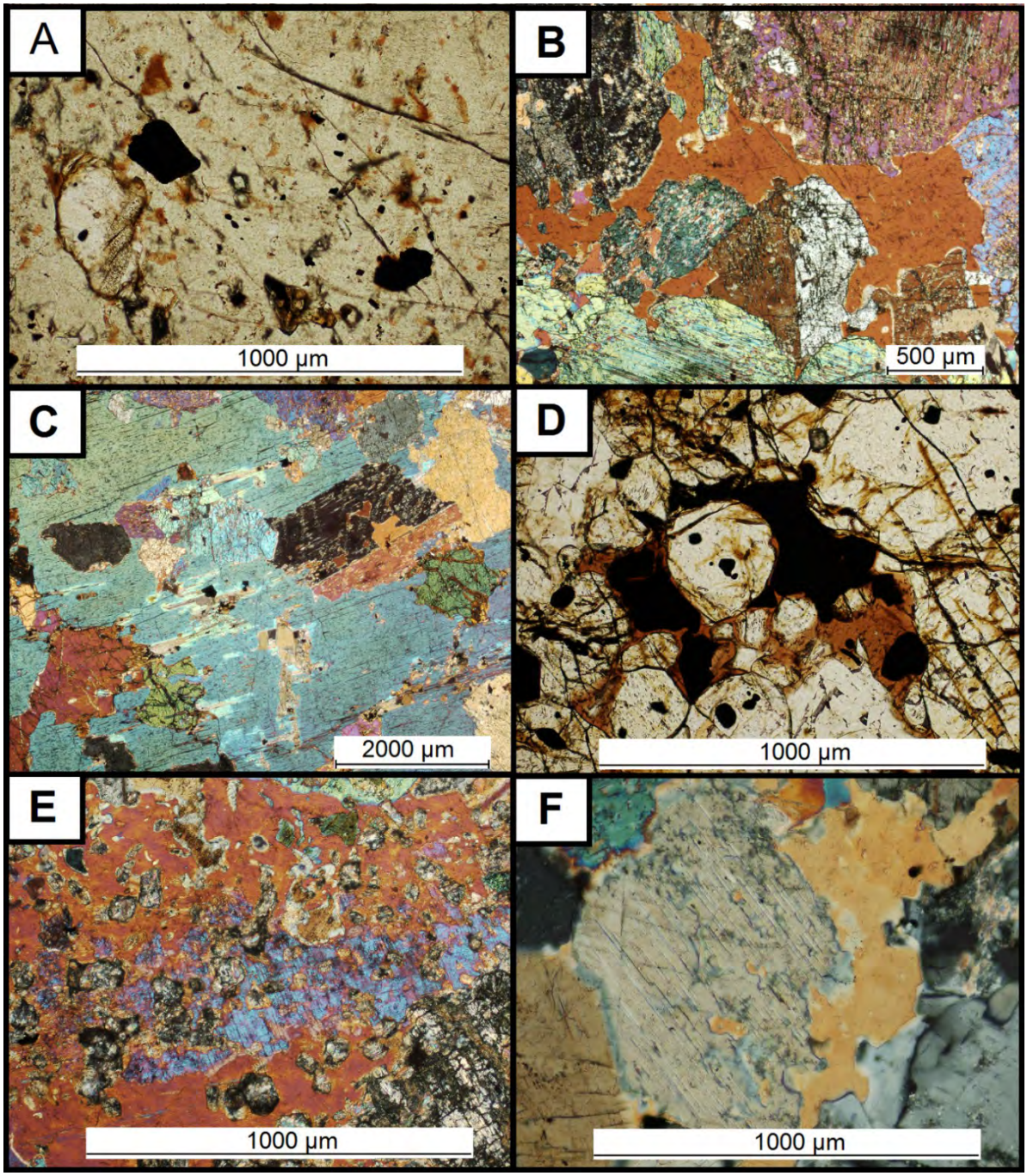

Figure 4.15: Photomicrographs of the occurrence of hornblende from KC, RietC and Ww. (A) Patches of brown hornblende in a grain of augite with a colourless olivine inclusion (left side) from RietC (sample 51, PPL). (B) Interstitial hornblende (orange) that partly envelopes grains of augite from Ww sample W03 (XPL). (C) A large oikocryst of hornblende (2nd order green-blue interference colour) that poikilitically encloses grains of augite and olivine from Ww (sample W05, XPL). (D) Brown hornblende decorating grain boundaries between magnetite and olivine from RietC (sample 51, PPL). (E) Advanced replacement of augite (blue interference colour) by hornblende (reddish) from KC (sample RB20, XPL). (F) Augite (grey interference colour) partly enveloped by hornblende (orange) from KC (sample RB3, XPL).

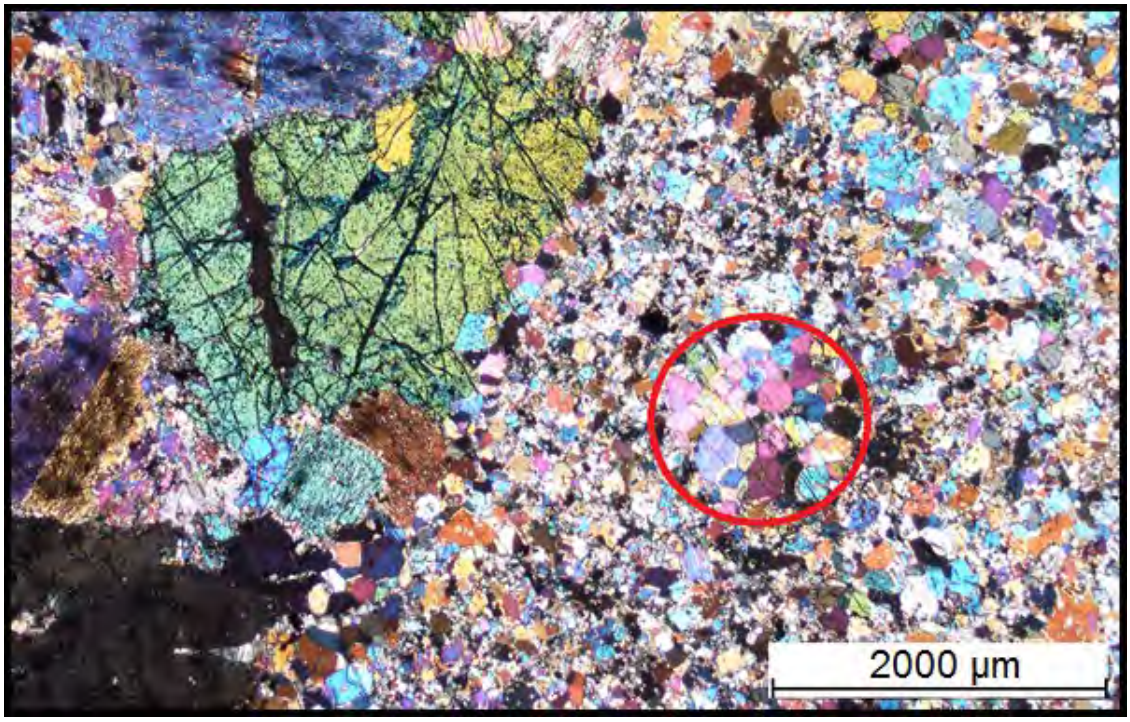

Figure 4.16: A photomicrograph of olivine-hornblende clinopyroxenite (W04, XPL), showing medium-sized grains on the left hand side and fine-sized grains on the right hand side. Inside the red circle grains can be observed with 120° triple-point grain boundary intercept angles.

The sulphides that form part of Ww commonly occur in between the silicates, while some are subpoikilitically surrounded by olivine and pyroxene. They are always anhedral, with highly irregular habits. Magnetite has the same characteristics as the sulphides, although many magnetite grains are also poikilitically included in the silicate minerals.

4.2.2 Group 2: Wehrlite and clinopyroxenite series from KC and RietC

This group includes olivine clinopyroxenite layers from the Central and Transitional Zones of RietC (see Figure 4.13 A and B for its typical appearance) and all wehrlite and (± olivine) clinopyroxenite from KC (Figure 4.17 and 4.18). They primarily differ from Group 1 rocks by their grain boundaries (no dramatic suturing is observed), and the occurrence of intercumulus plagioclase (discussed below).

The augite in Group 2 rocks are mostly rounded to elongated, and typically varies from 0.3 to about 1.5 mm in length. Olivine grains are generally smaller, measuring between 0.3 to 1.2 mm in length. Grain boundaries of both minerals vary from planar to curved, to somewhat sutured. In KC there is a tendency for larger grains of augite to be surrounded by smaller grains of olivine, thus isolating augite grains from one another (Figure 4.17 and Figure 18). This texture is especially well developed in samples that contain more olivine. Bisschoff

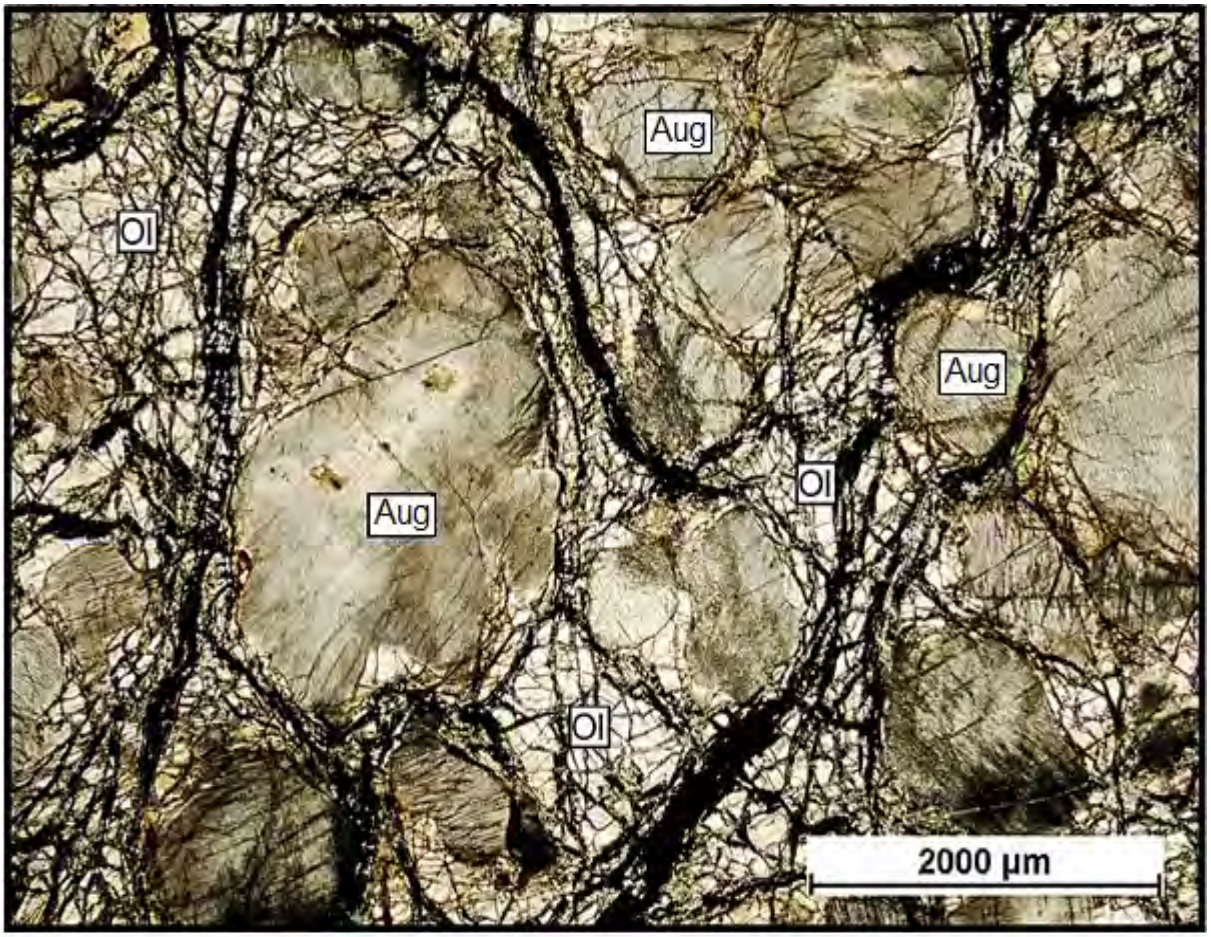

Figure 4.17: Typical rounded grain shapes of clinopyroxene grains (brown), surrounded by colourless olivine in KC (sample RB9, PPL). Opaque veins of magnetite can be observed as a secondary mineral that formed during serpentinisation of olivine. Notice the clouding of the augite which resulted from the exsolution of fine, opaque, rod-shaped needles. A fish-net texture can also be observed where augite grains are surrounded by olivine.

(1969;1973) called this phenomenon a “fish-net” texture, where the augite grains represent the holes in a fishing net while the olivine represents the rope in between.

Plagioclase is only ever observed as an intercumulus mineral in the ultramafic rocks (see Figures 4.13 A and B and Figure 4.19). The interstitial plagioclase habit is controlled by the spaces in between the cumulate minerals and is consequently irregular in shape. Similarly to Group 1 rocks, magnetite has an interstitial occurrence with irregular grain shapes. It is also frequently included in the oikocrystic silicates.

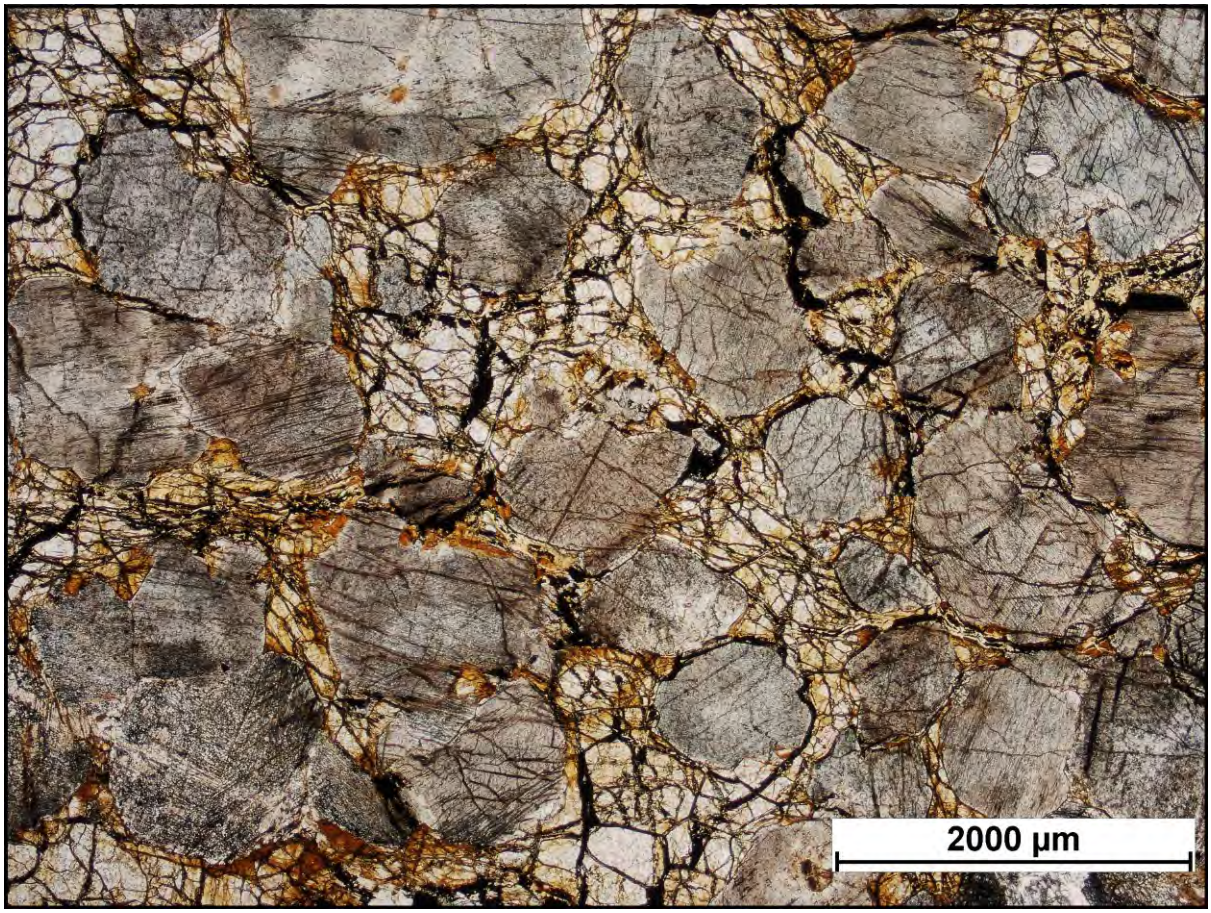

Figure 4.18: Occurrence of a fish-net texture in wehrlite from KC where grains of augite (grey to light brown) are surrounded by smaller grains of olivine (colourless to yellow and orange in colour) (Sample WK34, PPL).

Although rare, biotite and hornblende occur as mantles around some grains of olivine, augite, and magnetite. Many smaller specks of hornblende can also be observed within augite grains (similar to what is shown in Figure 4.15 A). In the northern layer of olivine clinopyroxenite of RietC, some interstitial plagioclase grains are extended over large surfaces, and poikilitically include several grains of olivine and augite to form a heteradcumulate texture.

While pseudotachylite appears to be absent in the northern layer of olivine clinopyroxenite from the Central Zone of RietC, it is a common constituent of the remaining Group 2 rocks from both RietC and KC. Some pseudotachylite veins can be observed with the naked eye, while smaller veins of pseudotachylite can only be observed with the aid of a microscope. When present, pseudotachylite occurs as a dark substance that envelopes several fragments of the affected lithology (see Figure 4.20). The formation of thin pseudotachylite veins is discussed in section 2.4.6.

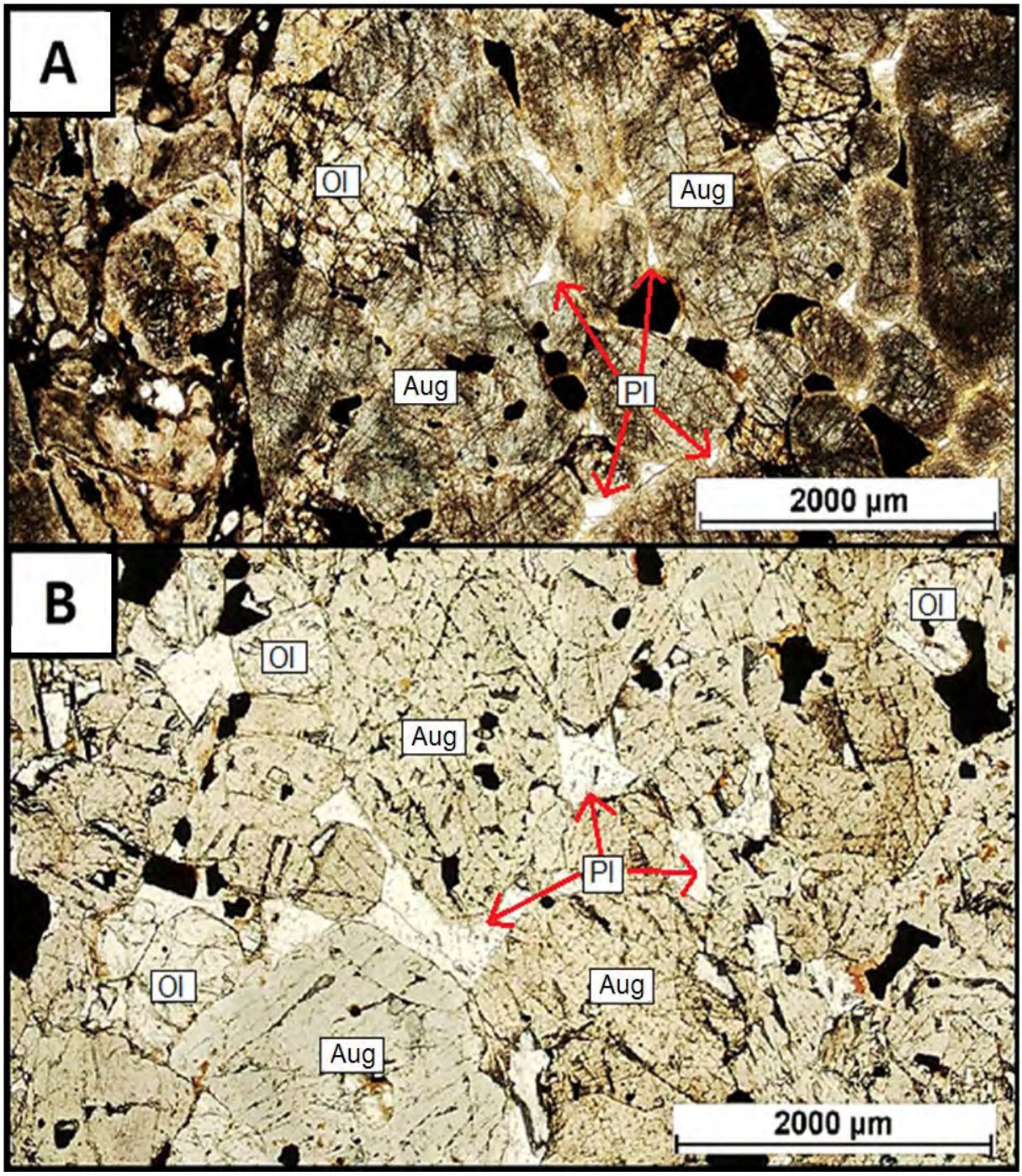

Figure 4.19: Photomicrographs of cumulate textures as it is typically observed in (A) KC (sample 304, PPL) and (B) RietC (sample CB15, PPL). Light brown minerals are augite, with some minor orange-brown hornblende and biotite. Opaque grains are magnetite. Notice the irregular habit of the interstitial post-cumulus plagioclase.

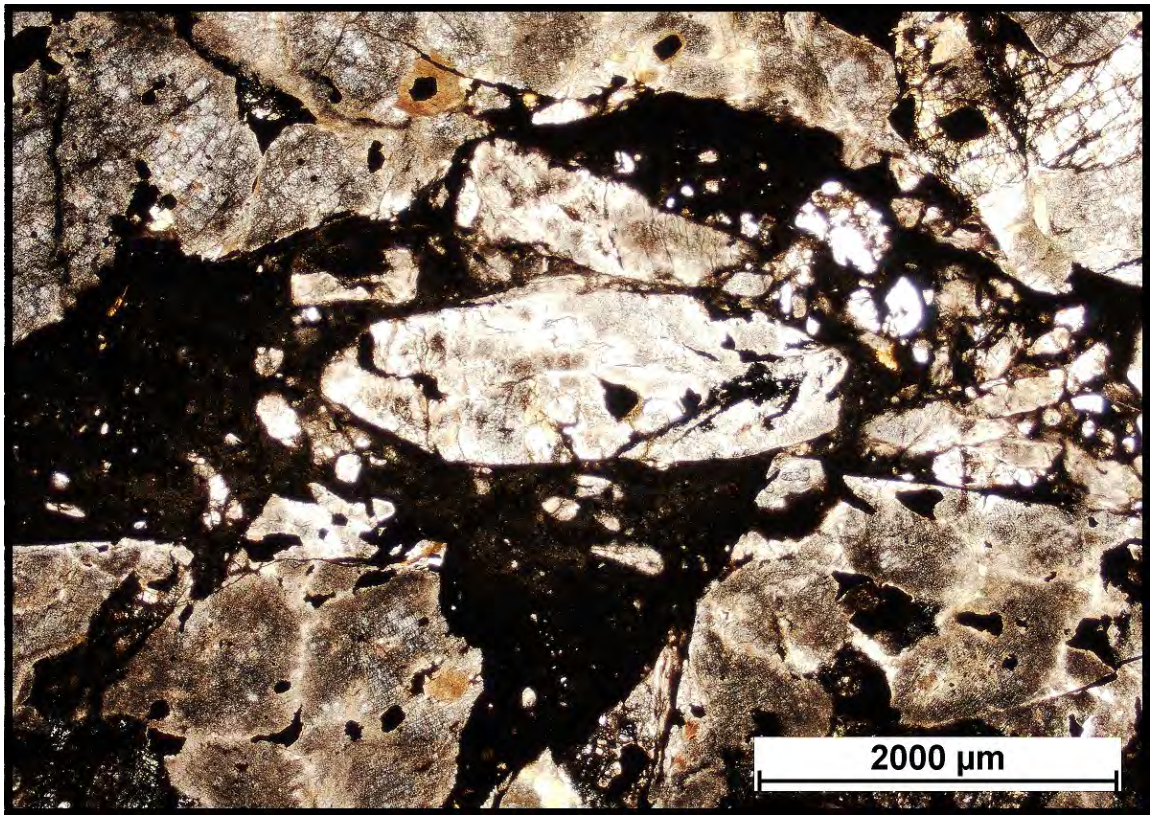

Figure 4.20: Dark coloured pseudotachylite from KC (sample 304, PPL). Notice the presence of abundant inclusions (mainly augite) from the host rock in the pseudotachylite (PPL).

4.2.3 Group 3: Olivine diorite from RietC

Olivine diorite from RietC is similar texturally to olivine clinopyroxenite from the Central Zone. The major difference between the two rock types is that plagioclase does not occur as an intercumulus mineral in the olivine diorite, although it still appears to occur interstitially. The typical appearance of this rock type is shown in Figure 4.21.

In the olivine diorite from RietC, the olivine grains are typically rounded, while augite has rounded to more elongated shapes with typically irregular grain boundaries. The olivine and augite have grain diameters that typically range from 0.5 to 2 mm, and the two minerals appear to have a tendency to cluster together. The grain sizes of the plagioclase typically range from 0.5 to 3 mm in length. Larger plagioclase grains occur near the base and the center of the olivine diorite layer from the Central Zone of RietC, with some plagioclase laths extending up to 5 mm along their c-axis. A gradual reduction in grain size of the feldspar is observed progressing upwards in the olivine diorite layer. As with the mafic minerals, multiple grains of plagioclase tend to occur together to form clusters.

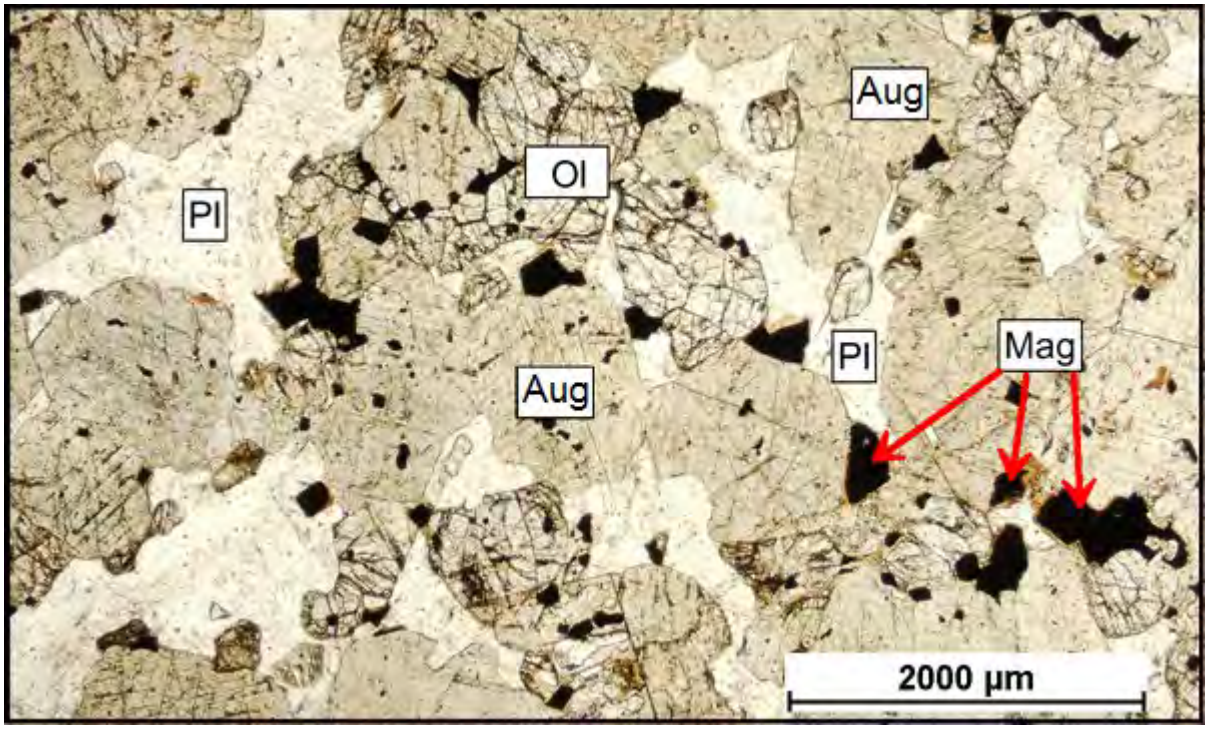

Figure 4.21: Photomicrograph showing the typical appearance of olivine diorite from RietC (sample CB16, PPL), with rounded to slightly elongated grains of augite and olivine, irregular plagioclase, and irregular to cubic magnetite.

Plagioclase grains vary from anhedral to subhedral and have elongated tabular habits. Smaller grains of plagioclase are occasionally poikilitically included in augite oikocrysts. Undulose extinction is a common phenomenon in plagioclase from RietC, which points to bending of the crystal structure of the affected grain during deformation (Winter, 2010).

Biotite and hornblende occur as interstitial minerals, and typically form a mantle with embayed contacts around augite, olivine, and magnetite.

The grain habit of magnetite varies from commonly anhedral and irregular to rarely euhedral and cubic. It usually occurs interstitially between the silicate minerals, but small fragments are also typically enclosed in the silicates.

4.2.4 Group 4: Troctolite and dunite from RietC

Rocks that are classified as troctolite and dunite from RietC are subdivided into three distinct textural groups: the magnetite-rich dunite (samples 54 and CB18), magnetite-rich troctolite (samples 52 and MB19a), and the (relatively) magnetite-poor troctolite (samples CB17 and 51). Each is discussed separately below.

4.2.4.1 Magnetite-rich dunite

The typical appearance of this rock type is shown in Figure 4.22. Olivine grains are typically rounded to oval in shape and are anhedral, and more than ≈95% range in size from 0.1 mm to 1.5 mm in diameter. In some cases, grains that are up to 3.5 mm in diameter have been recorded. When present, plagioclase grains are interstitial between magnetite and olivine with highly irregular habits and tend to include many small olivine and magnetite grains poikilitically. The grain sizes of plagioclase vary from very small (0.1 mm) to up to 2 mm long oikocrysts. Magnetite occurs interstitially between the olivine grains, but also appear to form distinct grains of their own. Biotite and hornblende are rare, and typically occur as mantles surrounding magnetite grains (similar as to what it observed in Figure 4.15 D), especially where in contact with plagioclase.

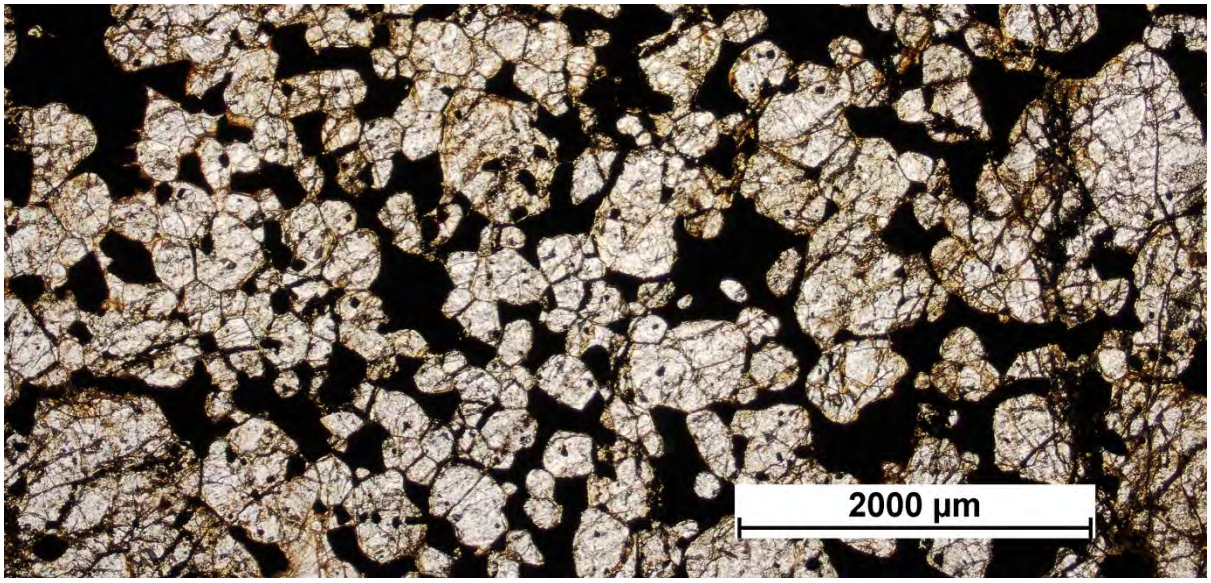

Figure 4.22: Photomicrograph to present the typical appearance of magnetite-rich dunite from RietC (sample 54, PPL). Transparent grains are olivine while opaque grains are magnetite.

4.2.4.2 Magnetite-rich troctolite

Texturally, this rock type shares many similarities with the magnetite-rich dunite. The major difference is the grain shape of the plagioclase, which is no longer interstitial and irregular but more elongated in shape (see Figure 4.23). Grain contacts between plagioclase and magnetite are typically lobate to irregular in the magnetite-rich troctolite (see Figure 4.24). Plagioclase grains are also typically aligned subparallel to one another along their longest dimension.

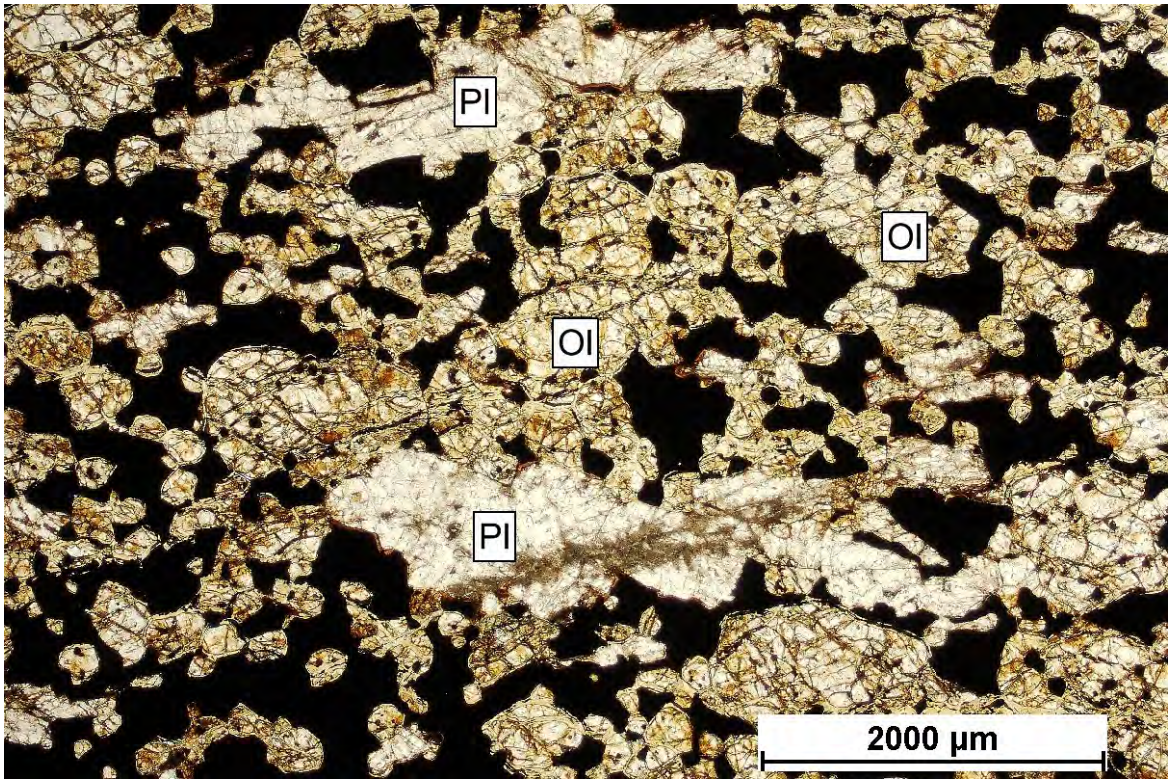

Figure 4.23: Photomicrograph of troctolite rich in opaque magnetite (RietC, sample 52, PPL). Notice the sub-parallel orientation of the plagioclase along their longest dimension.

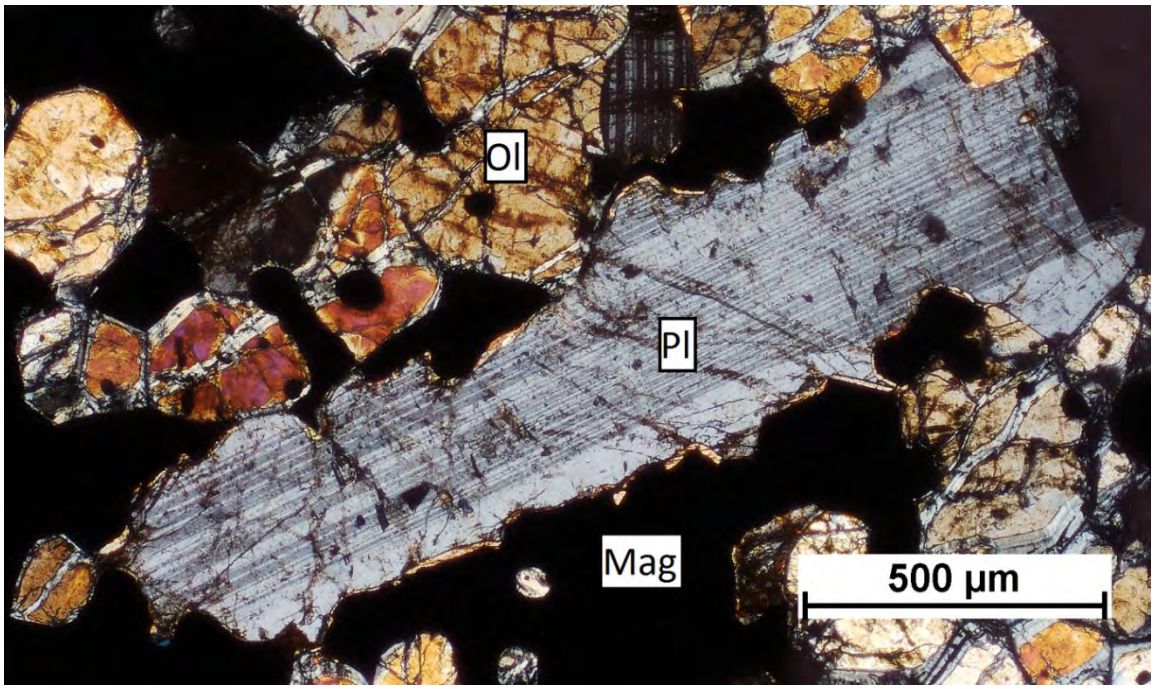

Figure 4.24: Photomicrograph of magnetite-rich troctolite with a plagioclase grain with irregular, lobate grain boundaries where in contact with magnetite (sample 52, RietC, XPL).

4.2.4.3 Magnetite-poor troctolite

Once again, this rock type differs primarily from the previous two by the appearance of the plagioclase. The grain shapes of plagioclase are better developed and ranges from anhedral to subhedral. They are elongated in shape and may reach up to 5 mm in length. Where larger plagioclase grains are present (such as in sample CB17), the rock has a laminated appearance due to the sub-parallel alignment of the plagioclase (compare Figure 4.25 and 4.26). Olivine grains are typically clustered together and contain interstitial magnetite (see Figure 4.25). In some localities, clusters of small (less than 0.3 mm) olivine grains are observed that have 120° triple-point grain boundary junctions (see Figure 4.27), similar to what is observed in olivine-hornblende clinopyroxenite from Ww. Reaction rims of hornblende and more rarely biotite can occasionally be observed around grains of magnetite. When present, augite grains cover large surfaces (up to 5 mm in diameter) and poikilitically includes several grains of mostly olivine and magnetite (see Figure 4.28).

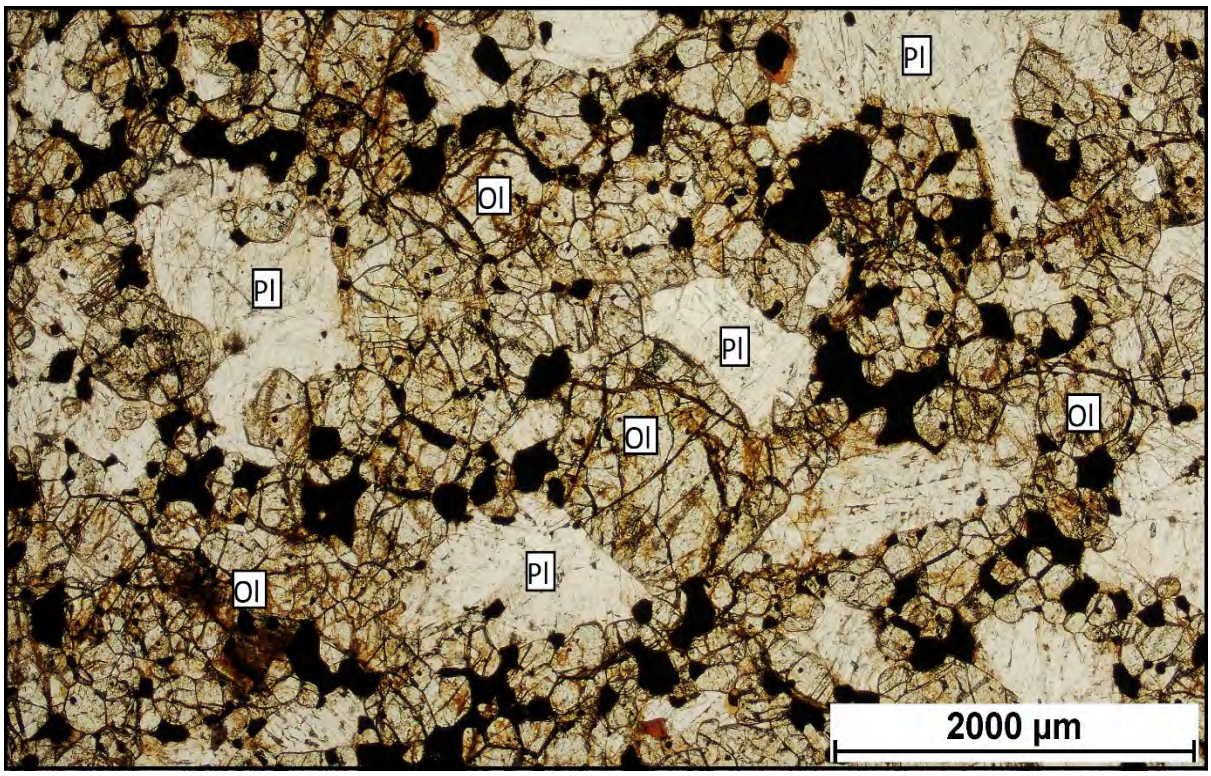

Figure 4.25: Photomicrograph to show the typical appearance of magnetite-poor troctolite from RietC (sample 51, PPL). Olivine grains are usually clustered together and surround separate clusters of plagioclase. Notice the presence of interstitial magnetite (opaque) between the olivine grains.

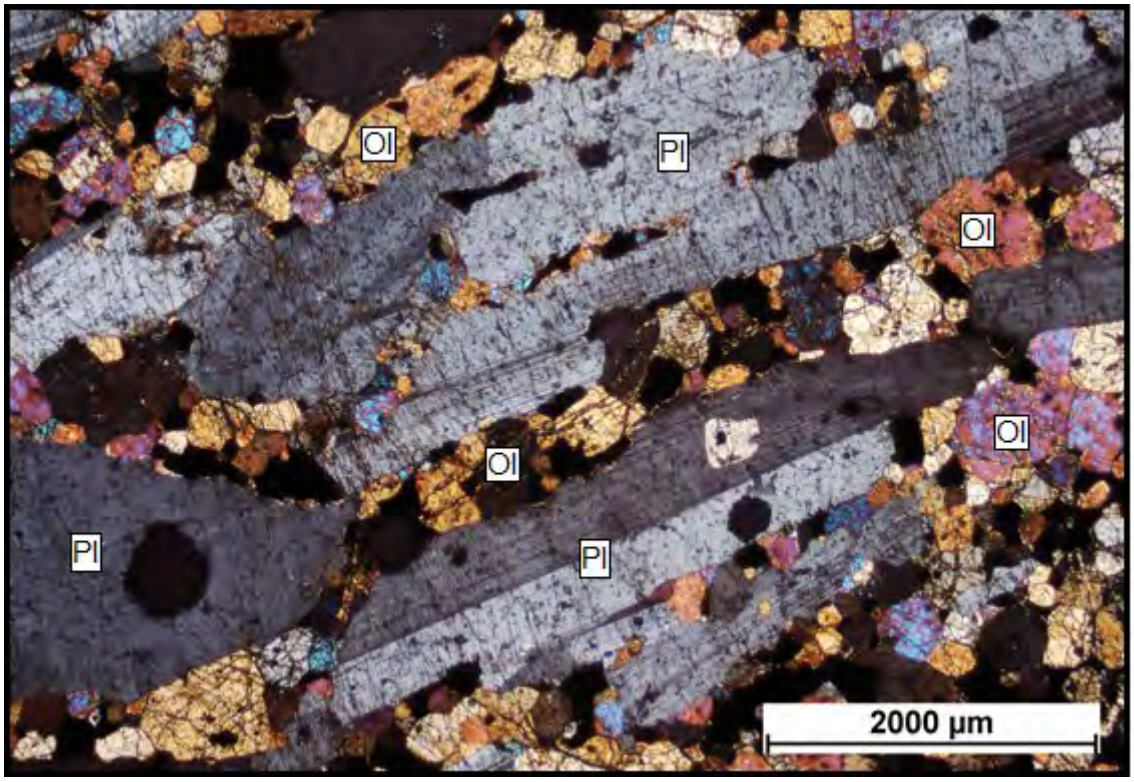

Figure 4.26: Subparallel alignment of plagioclase grains in troctolite from RietC (sample CB17, XPL).

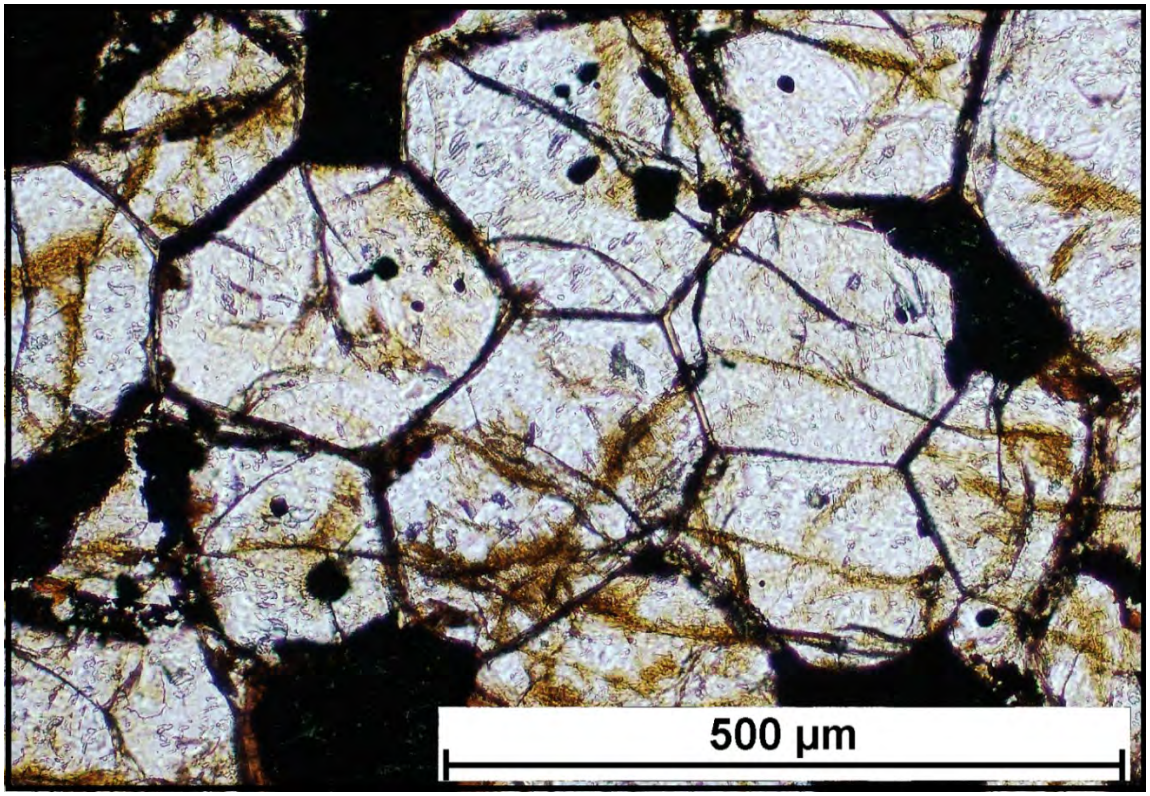

Figure 4.27: Small olivine grains showing approximate 120° grain boundary intercept angles in troctolite from RietC (sample 51, PPL).

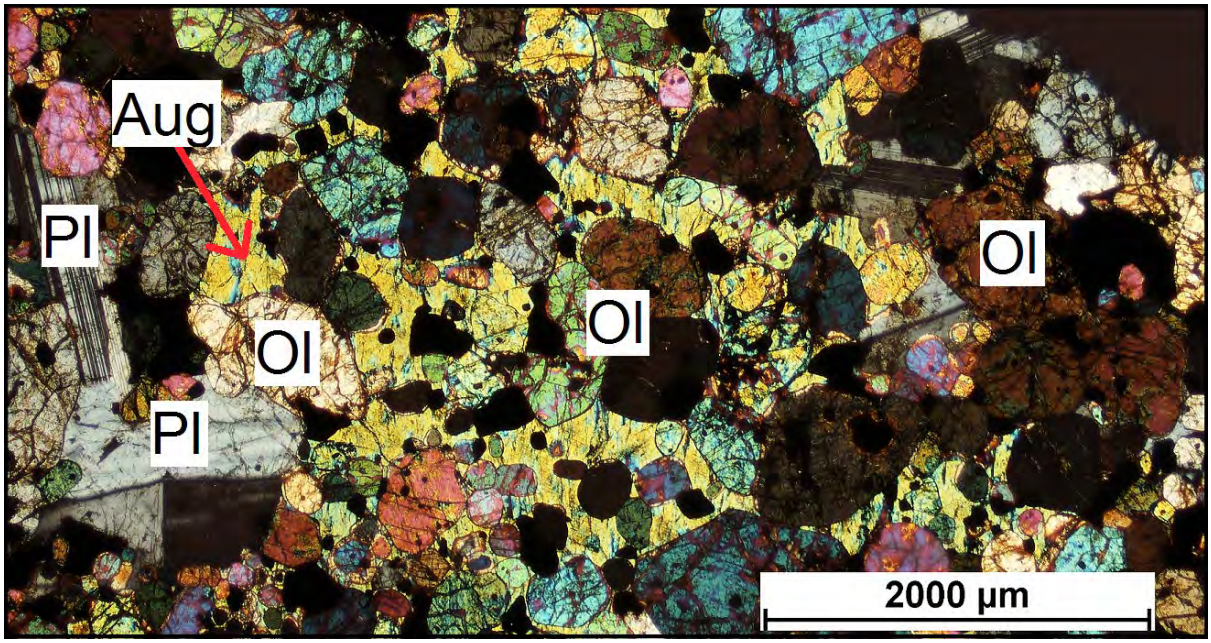

Figure 4.28: Oikocrystic occurrence of augite in troctolite from RietC (sample 51, XPL). Notice the abundance of olivine inclusions in a large grain of augite (blue to yellow-green interference colour).

4.2.5 Hornblende gabbronorite: sample RB3 from KC

The typical appearance of gabbronorite sample RB3 from KC is shown in Figure 4.29. This rock type is similar in appearance to the olivine diorite from RietC; it contains mafic clusters consisting of augite and enstatite while multiple grains of plagioclase tend to form separate clusters of their own. Augite and enstatite are anhedral to subhedral in shape and typically vary in size from 0.3 to 2 mm in diameter. The grain boundaries of the augite vary from planar to irregular, while the grain boundaries of enstatite vary from planar to slightly curved (see Figure 4.29 B). Both the augite and enstatite commonly contain a partial reaction rim of hornblende (see Figure 4.15 F and 4.29 A). Plagioclase grains are rectangular in shape, anhedral to subhedral, and commonly display undulatory extinction. In some cases, grain boundaries of plagioclase appear to intrude into adjacent plagioclase grains, as indicated by the red circle in Figure 4.29 B.

4.2.6 Hornblende norite: sample WK32 from KC

Under PPL, WK32 appears to primarily consist of various small grains of enstatite, plagioclase, and brown hornblende (see Figure 4.30). However, under XPL, it is revealed that many of the enstatite grains are optically continuous, and probably represents fragments of a larger enstatite grain. These grains of enstatite typically span areas of 1 to 9 mm^2 and occasionally display undulatory extinction. The plagioclase grains trapped within the

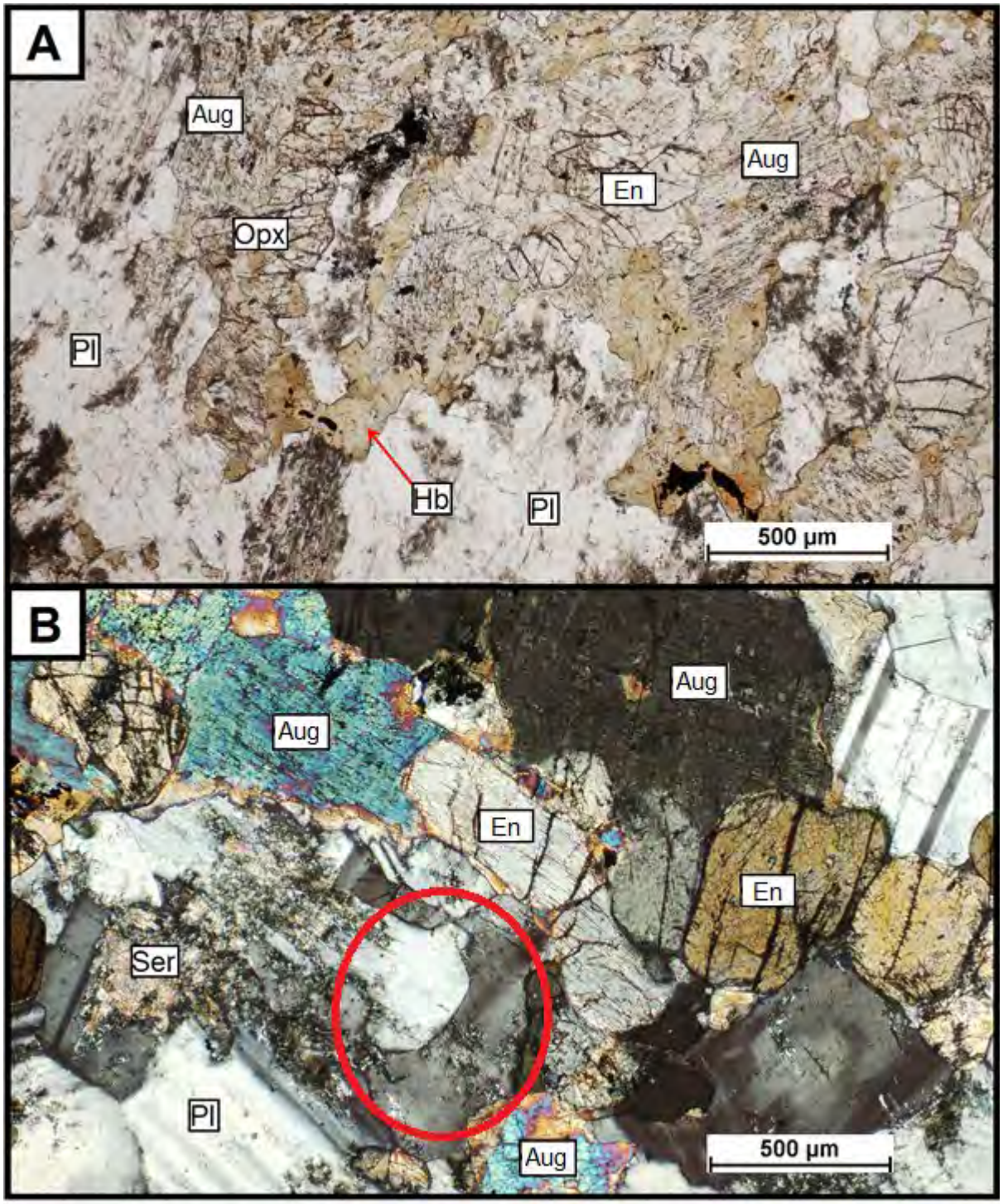

Figure 4.29: Photomicrographs showing the typical appearance of hornblende gabbronorite from KC (sample RB3). (A) Here olivine and augite grains can be seen clustered together, with brown hornblende forming a mantle around these minerals. Colourless plagioclase grains show alteration to sericite which resemble dark-brown dusty specks on the otherwise colourless plagioclase (PPL). (B) An enstatite grain showing 1st order interference colours surrounded by augite, and plagioclase, the latter showing alteration to sericite (second order interference colors) (XPL). An example of grain boundary migration in plagioclase is shown in the red circle.

enstatite fragments are small in size (typically between 0.1 and 0.6 mm in grain diameter), are highly irregular in shape (see Figure 4.30 B), and display undulatory extinction.

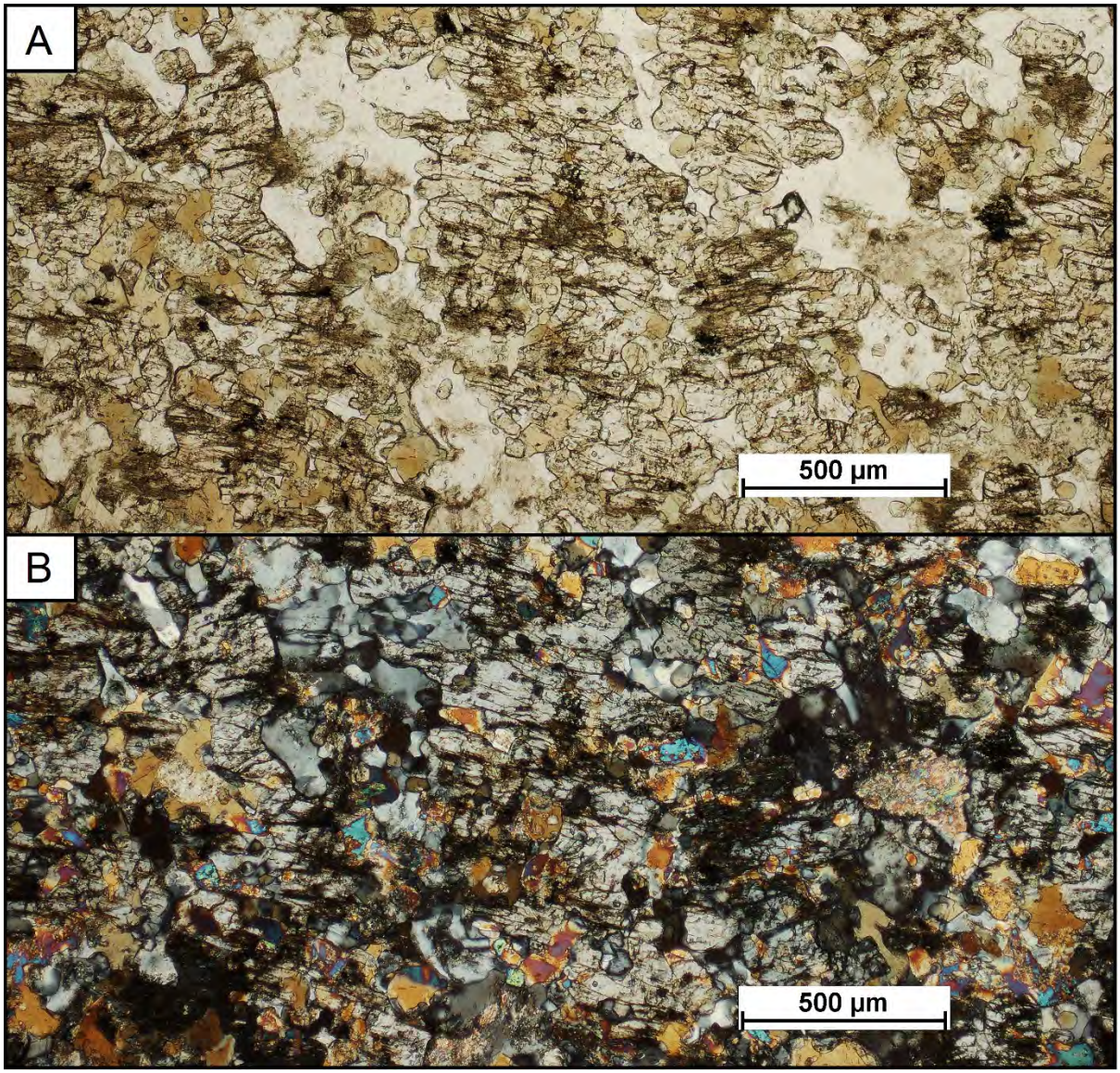

Figure 4.30: Photomicrograph to demonstrate the typical appearance of hornblende norite from KC (sample WK32) using PPL (A) and XPL (B).

4.2.7 Diorite: sample WK36 from KC

KC diorite sample WK36 is characterised by the presence of augite glomerocrysts imbedded within a mixture of smaller grains of augite, plagioclase, hornblende, and magnetite (see Figure 4.31). The augite that makes up the glomerocrysts typically varies from 0.3 to 1.5 mm in diameter, while the diameter of augite, plagioclase, and hornblende in the matrix vary from 0.1 to 0.9 mm. Magnetite grains rarely exceed 0.3 mm in diameter, and are typically clustered together.

Augite varies from rounded to elongated in shape, and are subhedral to anhedral. Hornblende grains are irregular, while the magnetite varies from irregular to cubic. The

plagioclase grains are typically elongated parallel to their c-axis and are aligned subparallel to one another, resembling a trachytic texture (Vernon, 2004; Winter, 2010). The grain boundaries of the plagioclase are oval in shape and no crystal faces are apparent. When in the vicinity of augite glomerocrysts, the plagioclase grains are aligned sub-parallel to the outer boundary of the glomerocrysts.

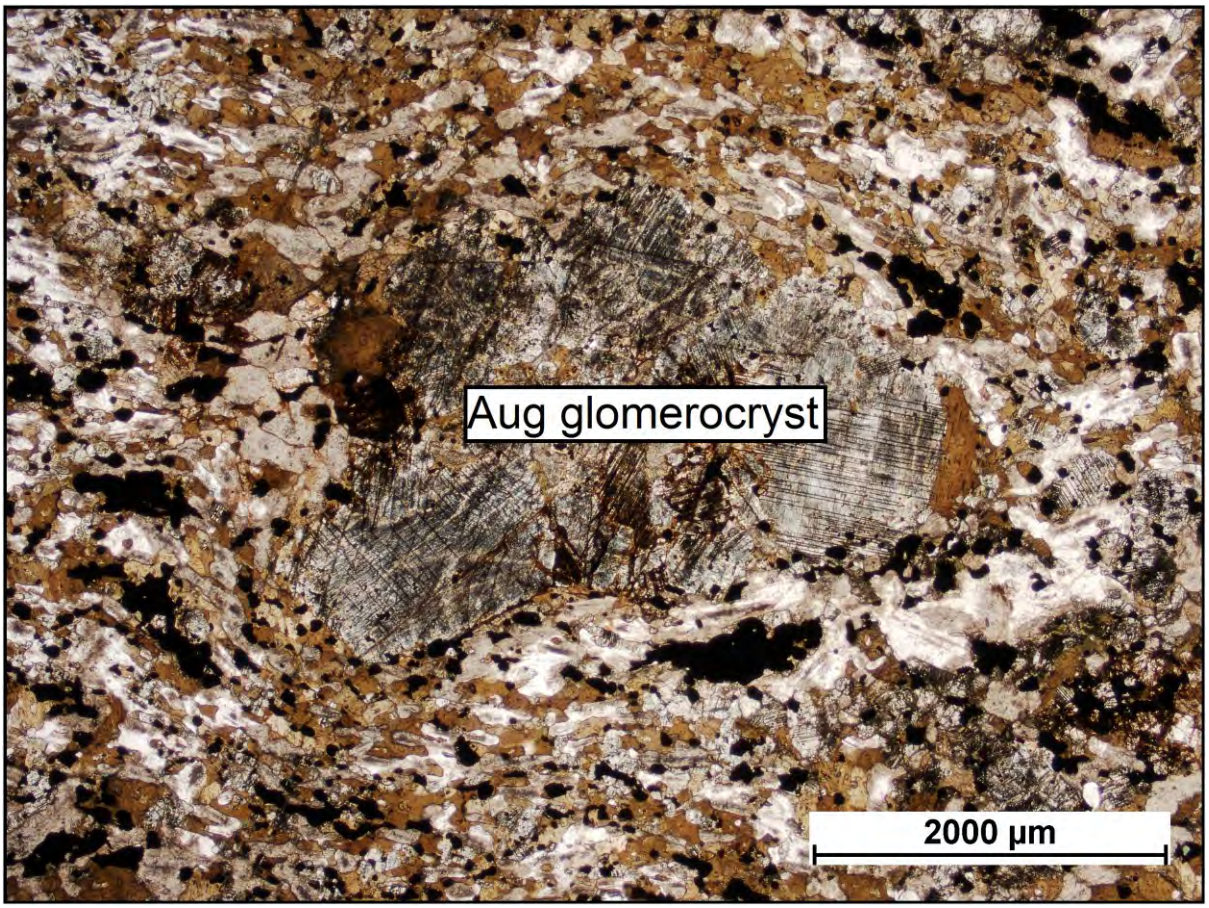

Figure 4.31: Photomicrograph to present the typical appearance of diorite from KC (sample WK36, PPL). Notice the presence of an augite glomerocryst set in a finer matrix of hornblende, magnetite, augite, and plagioclase. The plagioclase grains are aligned sub-parallel to one another and the boundaries of the augite glomerocryst.

4.2.8 Olivine hornblende gabbronorite: sample CB47 from Ww

This rock sample is characterised by a granoblastic texture and consists of a fine, relatively consistent grain sizes (typically between 100 and 300 µm in diameter). Grain shapes are typically rounded to lobate, while planar grain boundaries with 120° triple-point grain boundary junctions are frequently observed, especially in the plagioclase (see Figure 4.32). As with other rock groups discussed previously, hornblende and biotite frequently occur as mantles surrounding the mafic silicates, although distinct grains of these two minerals are also observed.

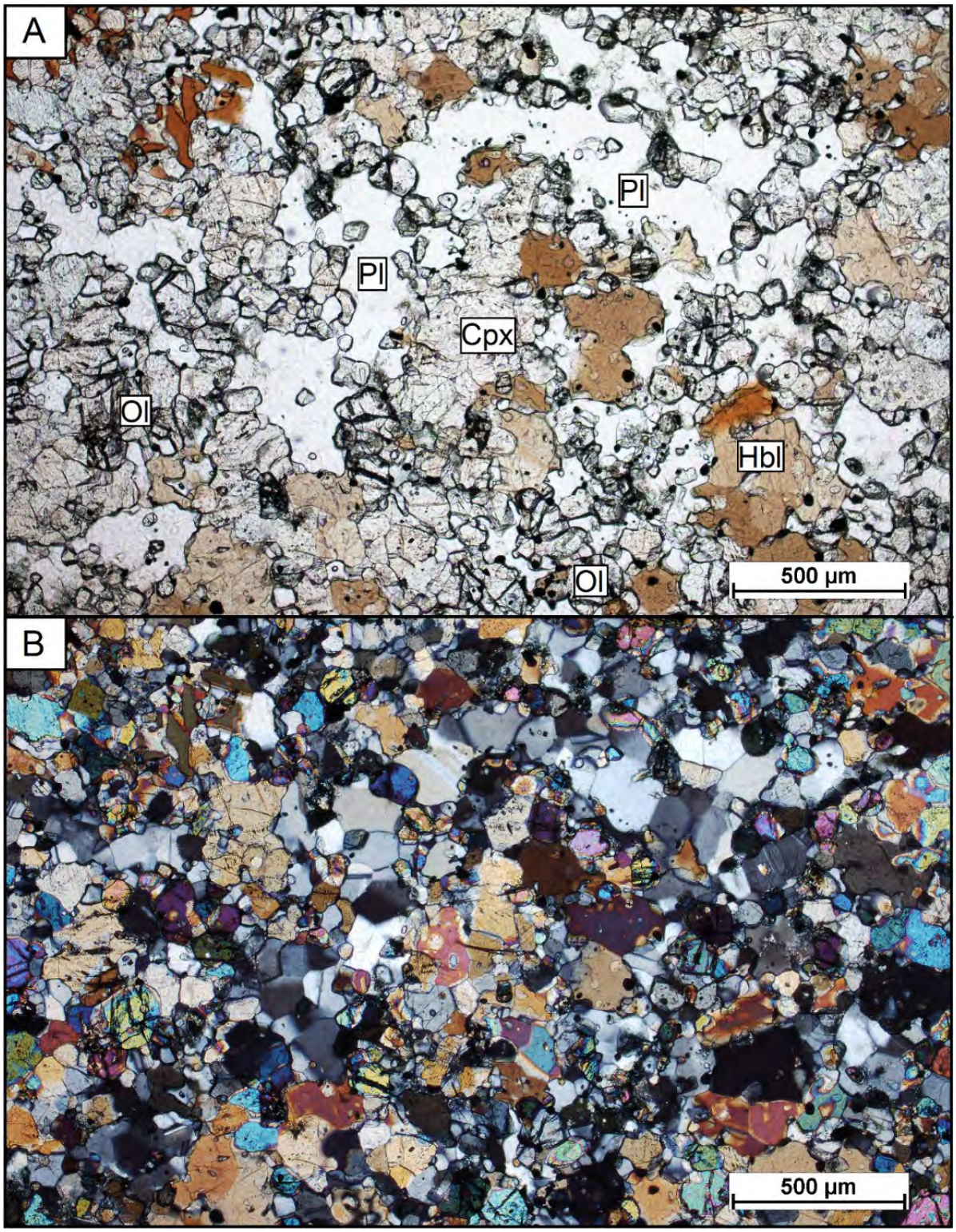

Figure 4.32: Photomicrographs to demonstrate the typical appearance of olivine-hornblende gabbronorite from Ww (sample CB47) using (A) PPL and (B) XPL. Notice the granoblastic texture of the rock in B: relatively consistent grain sizes and 120° triple-point grain boundary intercept angles.

4.2.9 Quartz-bearing pyroxene hornblendite: sample RB20 from KC

In terms of textural criteria, this rock is unique in terms of the degree of replacement of pyroxene by hornblende. Its typical appearance is shown in Figure 4.33. Both augite and enstatite tend to have highly irregular shapes and, in some cases, have a disaggregated appearance when mantled by hornblende (see Figure 4.15 E). Crystal faces can be observed where the pyroxene and hornblende are in direct contact with quartz. The grain diameters of pyroxene typically range from 0.5 to 1.5 mm, while hornblende shows a slightly greater range and tends to vary from 0.2 to 1.5 mm in diameter. Both hornblende and pyroxene vary from equigranular in shape to elongated. Contacts between hornblende grains tend to be lobate. Quartz appears to occur as an anhedral, interstitial mineral that varies from 0.3 to 0.7 mm in diameter and possess planar to curved grain boundaries where in contact with pyroxene and hornblende.

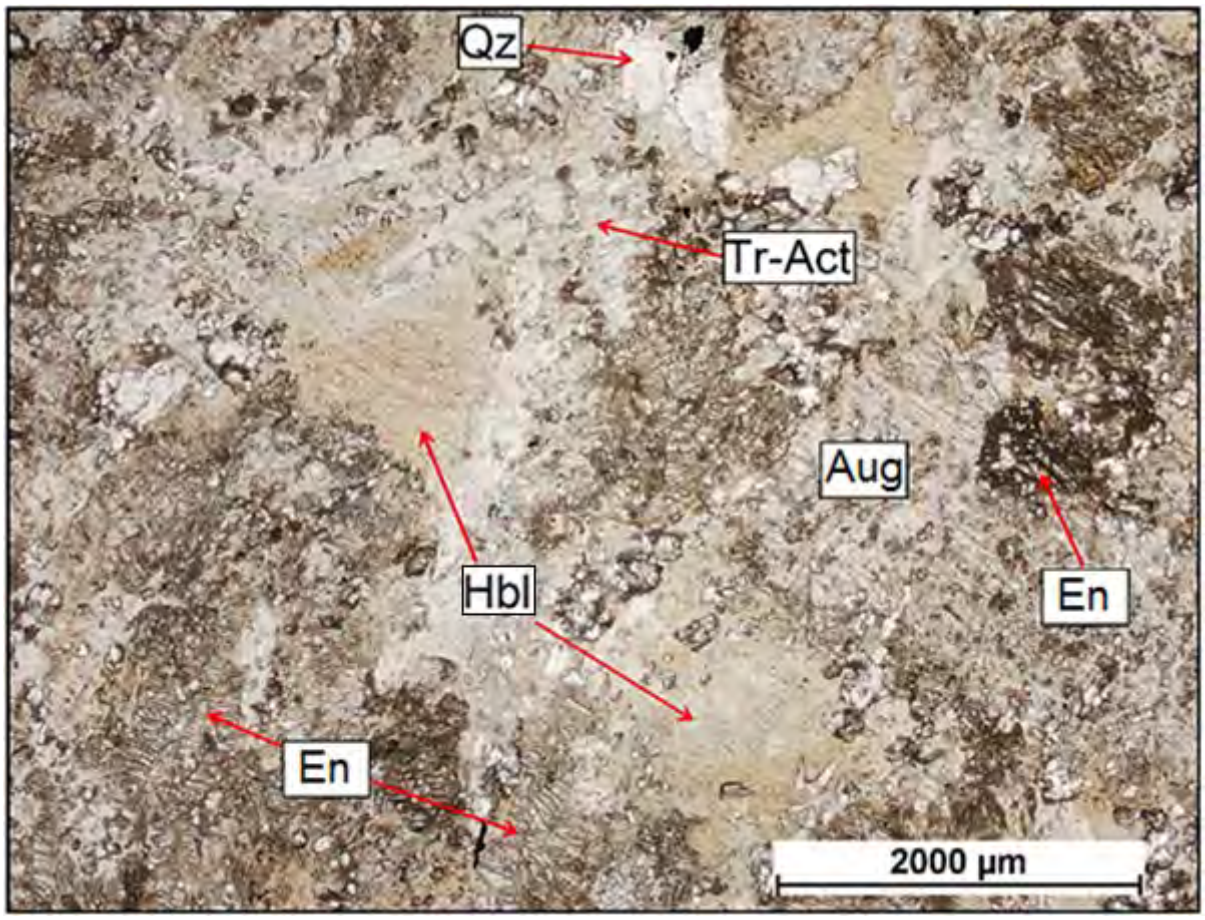

Figure 4.33: Photomicrograph of quartz-bearing pyroxene hornblendite from KC (sample RB20, PPL). Tr-Act: Tremolite-actinolite.

The distinguishing petrographic characteristics of all the groups discussed above is summarised in Table 4.2.

Table 4.2: Summary of the distinguishing characteristics of texturally and/or mineralogically distinct rock types from Ww, RietC, and KC.

	Lithological members	Distinguishing characteristics
Group 1	Ww olivine (±hornblende) clinopyroxenite; Lower Zone RietC olivine clinopyroxenite	Highly sutured grain boundaries between augite; abundant interstitial hornblende; presence of enstatite oikocrysts enclosing embayed olivine; absence of plagioclase.
Group 2	KC wehrlite, olivine clinopyroxenite and clinopyroxenite; Central- and Transitional Zone RietC olivine clinopyroxenite.	Presence of pseudotachylite in some samples; presence of cumulate olivine and augite with intercumulus plagioclase; enstatite absent; hornblende rare.
Group 3	Olivine diorite from RietC	Contains abundant olivine, augite, and sodic plagioclase; no cumulate textures; hornblende rare and orthopyroxene absent.
Group 4	Troctolite and dunite from RietC	Abundant olivine and plagioclase; magnetite is abundant in some layers; augite rare and occurs as large oikocrysts; subparallel alignment of plagioclase; lobate grain boundaries of plagioclase where in contact with magnetite.
RB3	Gabbronorite from KC	Similar to group 3 but contains enstatite instead of olivine.
WK32	Norite from KC	Contains large, fragmented grains of enstatite that enclose multiple smaller grains of highly irregular plagioclase with undulose extinction.
WK36	Diorite from KC	Glomeroporphyritic rock with augite glomerocrysts set in a finer matrix of plagioclase, augite, hornblende, and magnetite. Plagioclase laths are aligned sub-parallel to one another.
CB47	Gabbronorite from Ww	Fine-grained rock with enstatite, augite, olivine, hornblende, and plagioclase. Has a granoblastic texture.
RB20	Quartz-bearing pyroxene hornblendite from KC	Advanced replacement of pyroxenes by hornblende; contains interstitial quartz.

4.4 INTRA-MINERAL FEATURES

All three intrusions will be discussed together in the section on intra-mineral features, since these features commonly occur throughout all the rocks studied during the course of this project.

4.4.1 Zonation and exsolution

Although it occurs in the minority of augite grains, exsolution of enstatite from augite can be observed in all the augite-bearing thin sections. The exsolution is laminar and occurs along one crystallographic orientation. Fine-scale augite exsolution is also observed in some of the enstatite grains and occurs as multiple thin laminae.

A feature commonly present in augite from all three intrusions (and enstatite in hornblende gabbronorite sample RB3 from KC) is the presence of fine, rod-shaped opaque inclusions (Figure 4.34). The texture is especially common in the ultramafic rocks of Ww, KC, and the Lower Zone of RietC. The identity of these exsolved phases could, however, not be established optically, and establishment of their identity should await further research. It has been suggested that opaque inclusions of this nature can form in two ways; (1) they can crystallise directly from the melt and become trapped in late pyroxene (Low *et al*., 2009), or (2) it can be exsolved from the pyroxene itself (Harlow & Klimentidis, 1980; Low *et al*., 2009). Because of the parallel alignment of the rods hints at a crystallographic relationship with the augite (see Figure 4.34 B and Figure 4.35), the latter explanation seems more probable.

Exsolution of opaque phases may occur during subsolidus cooling of the rock. Some elements (a noteworthy example being Ti, see Bèdard, 2014) are incorporated with ease in the crystal lattice of magmatic phases at high temperatures but become incompatible with decreasing temperature. The incompatible elements are then expelled from the crystal structure of the host and might form their own separate phases (Harlow & Klimentidis, 1980; Klein & Dutrow, 2008).

Notice in Figure 4.34 that the density of the exsolved phases show significant oscillation in a near-concentric pattern and appear to preserve earlier crystal faces of the growing pyroxene crystal. According to Low *et al*. (2009), the oscillatory nature of this texture arises due to fluctuating chemical and/or physical conditions in the magma chamber during crystallisation. These can include changes in oxygen fugacity, fluctuations in temperature, or variations in the chemical make-up of the melt. This leads to oscillatory zonation in the

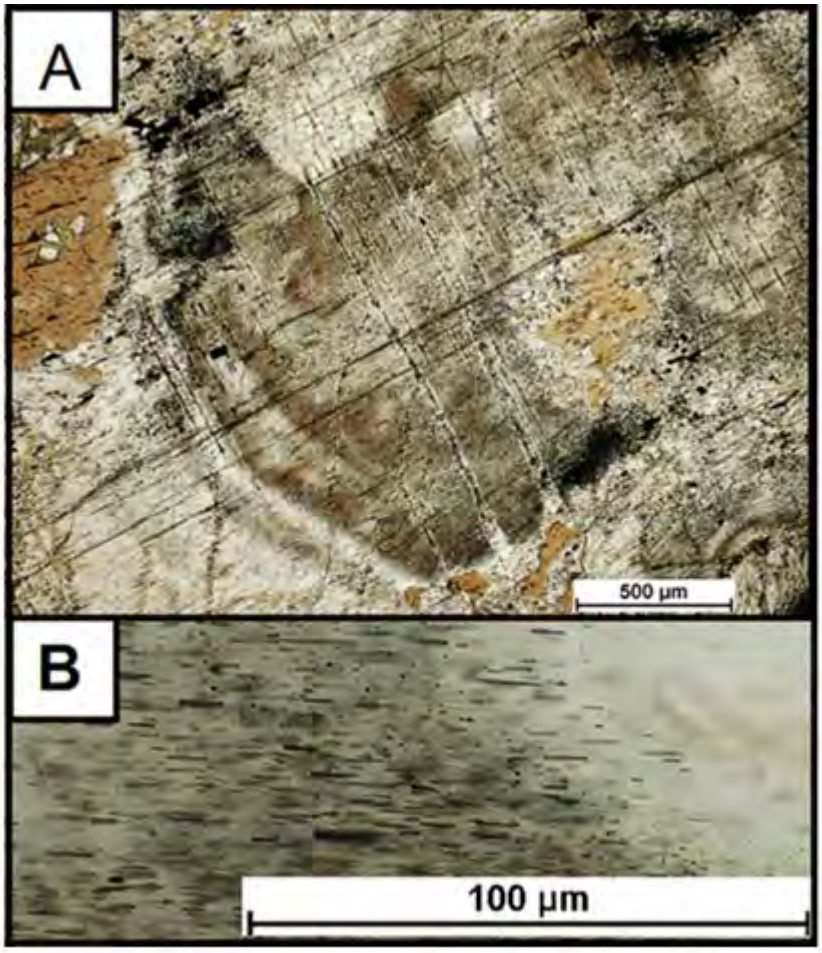

Figure 4.34: (A) Zoning in augite emphasized by exsolution of opaque minerals from Ww (sample W06). Brown patches are hornblende grains (PPL). B: Larger magnification of the opaque minerals in A reveals their acicular habit and parallel orientation that hints at a crystallographic relationship with the augite.

affected mineral grain, whereby the now-exsolved elements are incorporated at varying concentrations for the duration of the grain's crystallisation.

Chemical zonation can also be observed in hornblende as a change in colouration of this mineral from brown near its centre to green and colourless near its grain boundaries (see Figures 4.11 A, Figure 4.30, and especially Figure 4.33). In metamorphic rocks from the Sør Rondane Mountains, East Antarctica, Adachi *et al*. (2010) have found that a change in hornblende colouration from brown to green correlates with a decrease in titanium content of the grain. Higher concentrations of Ti is typically incorporated in hornblende at higher temperatures, which can lead to brown, Ti-rich cores that typically form at high temperatures and green, Ti-poor margins that typically form at lower temperatures. Heinrich (1965) states that the variation in the Ti concentration of hornblende are usually not solely responsible for the variation in colouration, and that the green variety of hornblende is also characterised by a lower alkali content, lower Al_2O_3 concentration and a higher concentration of SiO_2.

Hornblendes that form in magmas with a higher oxygen fugacity are also typically brown in colour while those that form at low oxygen pressures tend to be green (Heinrich, 1965).

4.4.2 Twinning

Simple twinning in augite is common in all the augite-bearing rocks of Ww, RietC, and KC (Figure 4.35). In contrast, simple twinning in hornblende is completely absent, despite the fact that simple twinning in hornblende is common in rocks of igneous origin (Philpotts, 1989). An exception is simple (Figure 4.36) and multiple (Figure 4.37) twinning observed in hornblende in pyroxene hornblendite sample RB20 from KC. Multiple twinning in hornblende is a sign of deformation (Rooney *et al*., 1970; Vernon, 2004), while simple twins appear to be inherited from augite during the formation of hornblende through the replacement of the former mineral by the latter.

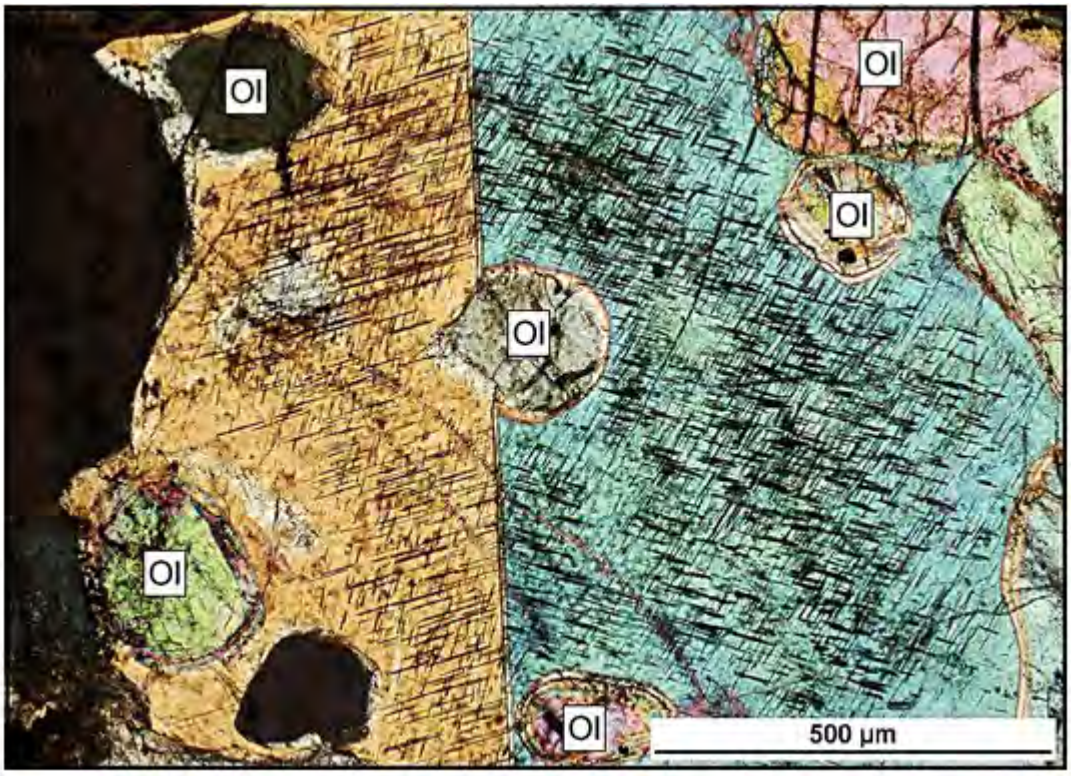

Figure 4.35: A photomicrograph of twinning in augite in troctolite from RietC (sample 51, XPL). Several olivine inclusions are visible in the clinopyroxene. Notice how the orientation of the exsolved opaque needles changes across the twin interface, indicating a crystallographic relationship between the needles and the augite.

When present, plagioclase grains always have abundant albite twinning, with Pericline- and Carlsbad twinning less common. Some plagioclase grains show twin lamellae that fail to extend through the entire crystal and taper off in sharp terminations (Figure 4.38). These twins are formed during deformation of plagioclase and are thus called deformation twins

(Winter, 2010). Twins like these in plagioclase are common in localities that have experienced shock metamorphism, although the texture more commonly arises due to endogenic deformation mechanisms such as orogeny or faulting (Pickersgill *et al*., 2015).

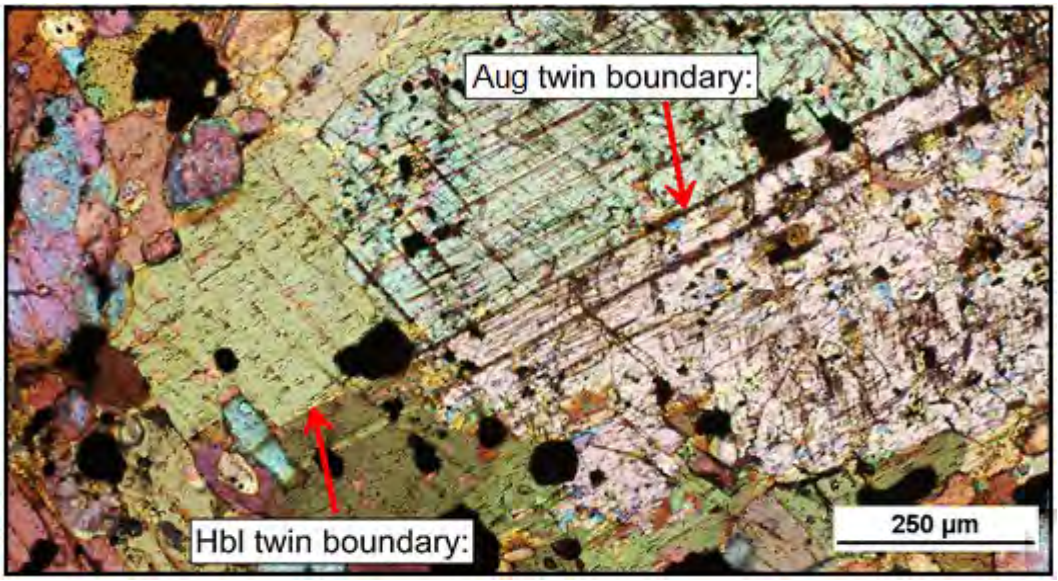

Figure 4.36: A photomicrograph of a twin boundary in clinopyroxene that has been adopted by hornblende (sample RB20, XPL with inserted gypsum accessory plate to enhance the colour difference across the twin interface).

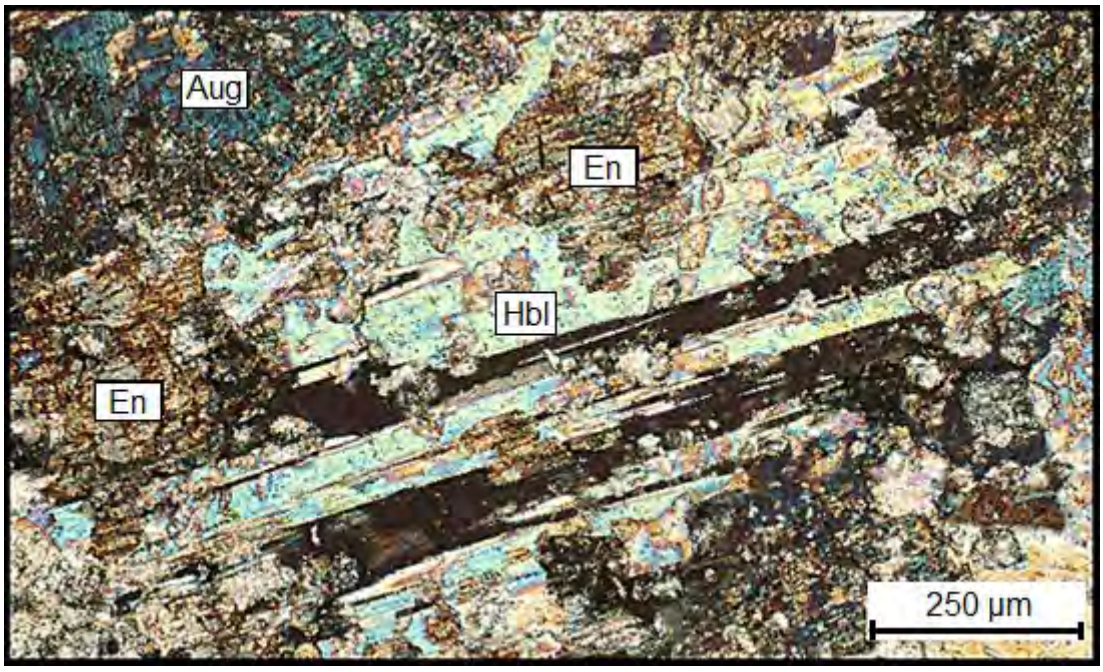

Figure 4.37 Photomicrograph of deformation twins in hornblende (second order green-blue) with alternate twin lamellae in their extinct position (KC, sample RB20, XPL).

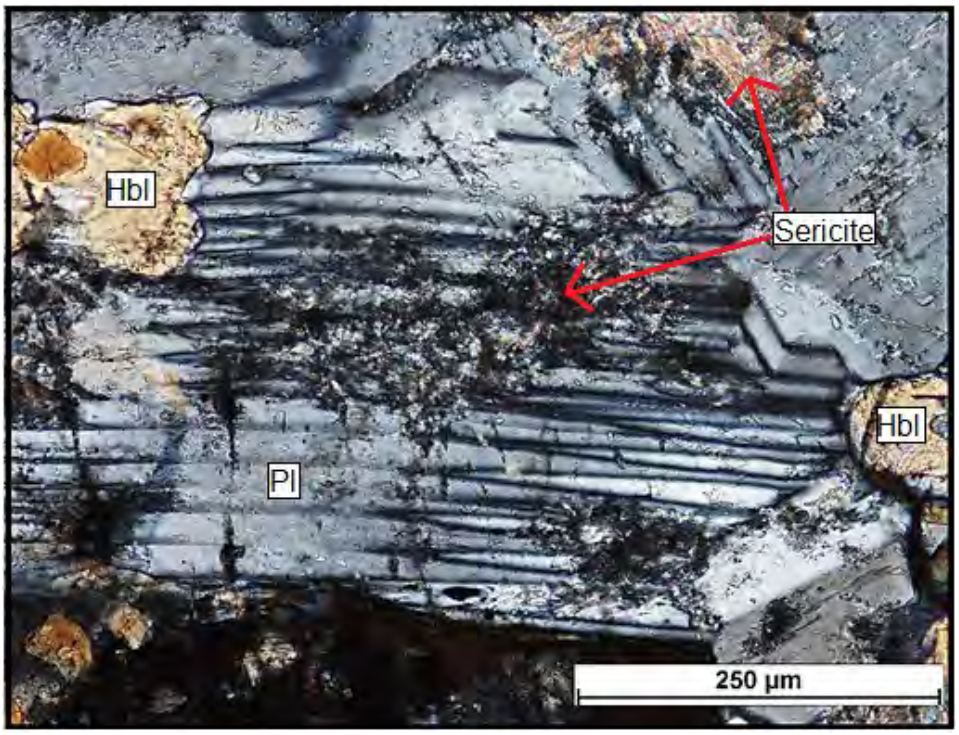

Figure 4.38 Photomicrograph of a plagioclase grain in hornblende gabbronorite from KC showing deformation twins (sample RB3, XPL). Alteration to sericite of plagioclase is common. A more advanced degree of sericitisation displaying second order interference colours can be seen in the upper right corner of the image.

4.4.3 Possible fluid inclusions in planar deformation features

An interesting feature present in the majority of olivine grains in Ww are slightly bent trails of small, spherical inclusions. These features are shown in Figure 4.39 under high magnification, but they can also be observed in olivine grains shown in Figures 4.16 and 4.43. These are similar to descriptions provided by Schmitt and Langenhorst (1996), who noticed tiny glass inclusions in olivine that also occur along curved trails from experimentally shocked chondrites. These glass inclusions formed during partial melting of the olivine along planar deformation features (PDFs). Despite their curved nature, Schmitt and Langenhorst (1996) have noted that the glass inclusions tend to occur parallel to three crystallographic directions, namely (100), (010), and (110).

An attempt was made to compare the crystallographic orientation of these structures observed in Ww with those observed by Schmitt and Langenhorst (1996). Because olivine crystallises in the orthorhombic system, olivine grains will extinguish under a polarising microscope if the polarisers are parallel to (100) and (010) when viewed from (001) as they also correspond to the vibration directions of polarised light passing through olivine crystals (Klein & Dutrow, 2008; Nesse, 2004). The mineral grain should thus be extinct if the vibration

directions of the polarisers of the petrographic microscope are parallel to PDFs that lie in the (100) and (010) crystallographic planes. The extinction angles of olivine were measured in thin sections of Ww in 30 different grains where two directions of the PDFs could be observed that intercept each other at a 90° angle. Extinction angles varied from 0° to 23° from these PDFs, with an average of 10°. This shows that there is a tendency for the PDFs to lie in the planes proposed by Schmitt and Langenhorst (1996).

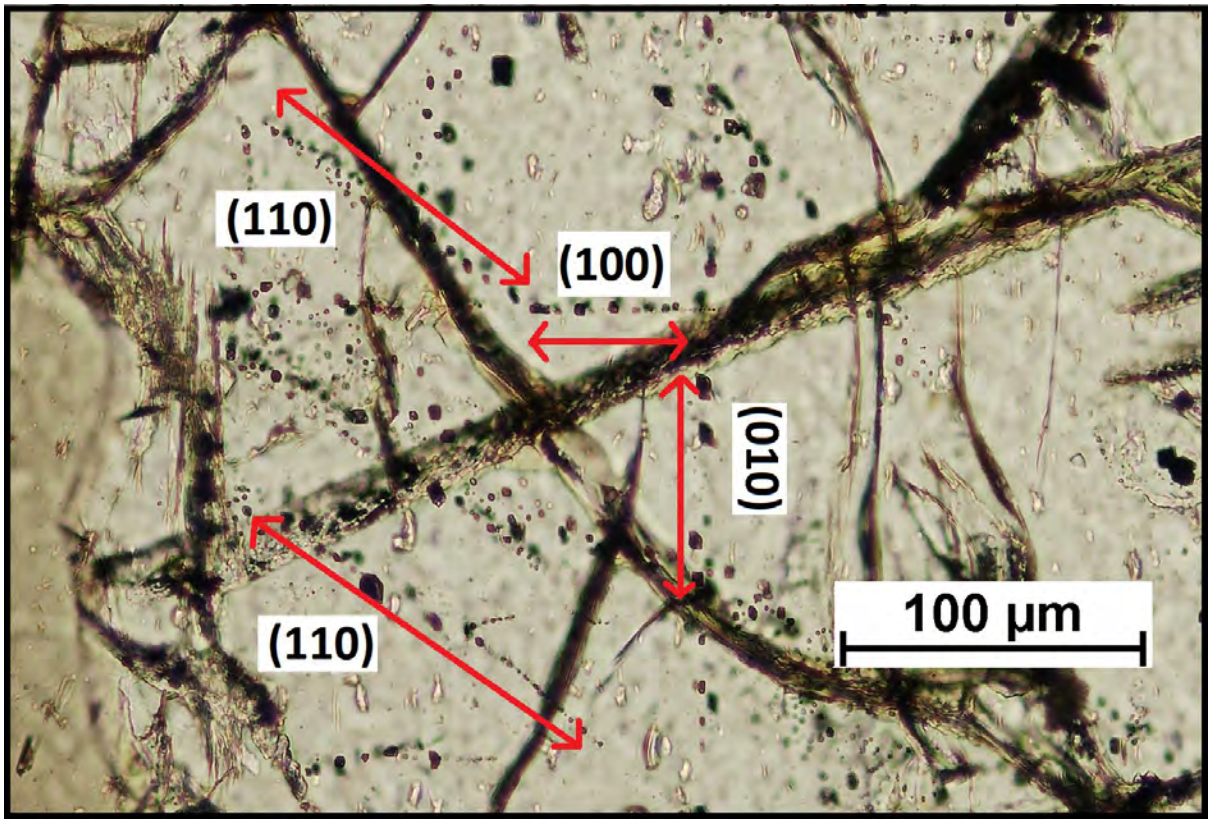

Figure 4.39: Photomicrograph of planar deformation features in olivine and their associated crystallographic orientations.

In the grain shown in Figure 4.39, the two perpendicular trails of inclusions lie perfectly in the (100) and (010) planes of the olivine (extinction angles equal zero). This allows for the determination of the crystallographic orientation of the PDFs as (010) lies parallel to the vibration direction of the slow ray (Z) and (100) lies parallel to the vibration direction of the fast ray (X). One other PDF direction, (110), that cuts across the previous two could also be observed. The crystallographic orientations thus correspond well to the PDFs observed by Schmitt and Langenhorst (1996).

However, the identity of the inclusions themselves is uncertain at this stage. As described in section 2.3.7, Schreyer (1984) observed that inclusions in now-annealed PDFs in quartz

from the centre of the Vredefort Dome are, in fact, CO_2-rich fluids, which might also be the case for Ww.

4.4.4 Symplectite intergrowth in clinopyroxene

A texture observed in the ultramafic rocks of Ww and KC, but absent in RietC, is a symplectic, colourless intergrowth in augite (Figure 4.40). The abundance of this texture is highly variable, with only a couple of instances observed in Ww, to very common in wehrlite sample RB8 and olivine clinopyroxenite RB9 of KC. The fine nature of the intergrowth makes it difficult to identify optically, but in one instance of Ww, some spots of the intergrowth are coloured light brown and have a similar appearance to that of hornblende. Hornblende intergrowths in clinopyroxene has been attributed to exsolution (Isaacs *et al*., 1981; Veblen & Buseck, 1981), pyroxene hydration (Papike *et al*., 1969), hornblende rims on clinopyroxene that grows into the latter mineral, or the exsolution of an originally homogeneous pyroxene to form lamina of two chemically distinct pyroxenes; one of which is more susceptible to replacement by hornblende (Isaacs *et al*., 1981). However, the current petrographic investigation does not yield any conclusive evidence regarding the formation or identity of the intergrowth.

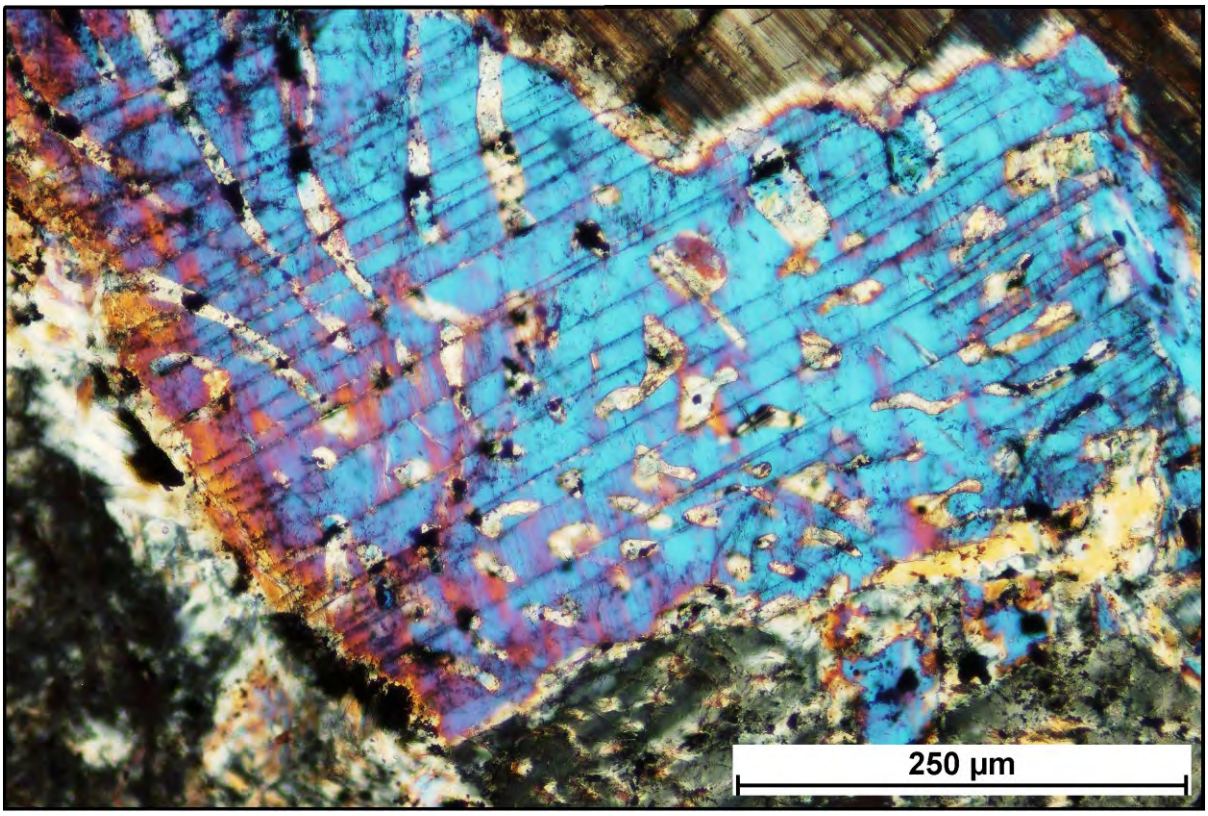

Figure 4.40 Photomicrograph of some type of symplectite intergrowth in augite from KC (sample RB8, XPL).

4.5 ALTERATION

Alteration products present in Ww, KC, and RietC, which are identifiable with the petrographic microscope, include tremolite-actinolite, calcite, chlorite, serpentine, saponite, talc, sericite, and iddingsite. The presence and relative abundance of these alteration products in the three different intrusions are summarised in Table 4.3.

Alteration appears to have been more pronounced along fractures and veins within the affected lithologies (see for example Figure 4.41 and 4.42). Etheridge *et al*. (1984) have provided evidence that fluids present during metamorphism can exert forces that exceed the lithostatic and/or other compressive pressures at work on the rock, which can lead to fracturing. Alternatively, it is possible that the fractures existed prior to alteration, and simply served as conduits for hydrothermal fluids to travel through.

Serpentine is present as an alteration mineral of olivine. It is common throughout the majority of the olivine in KC and RietC, but can only be observed in certain patches of Ww. Serpentine is usually formed during hydrothermal alteration of mafic minerals (Deer *et al*., 2013; Hicks *et al*., 2014; Klein & Dutrow, 2008). Iron and nickel from the olivine grain are rejected by the crystal structure of serpentine which leads to the formation of secondary magnetite (Vernon, 2004) (see Figures 4.17 and 4.41) and iron-nickel alloys (Morrison *et al*., 2015). The serpentine from Ww (and some samples from KC and RietC, although it is less prominent) deviates from its typical colourless nature and is usually coloured yellow to brown. This can, according to Delvigne (1998), be attributed to a second phase of alteration that produced saponite clay minerals and iron oxides as the colouring agent. This also raises the interference colours of the impure serpentine.

Tremolite-actinolite and chlorite usually occur together, and is sometimes seen to occur in a texture that is analogous to a miarolitic texture in appearance, with chlorite in the centre surrounded by needle-shaped tremolite-actinolite that points to the centre of the texture (Figure 4.43). The texture has likely arisen during the replacement of either olivine or augite. Viable nucleation of the amphibole probably occurred at the margin of the now-replaced grain, and started growing inwards during the metamorphic reaction, while the remainder of the grain was replaced by chlorite. Possible intermediates of this texture are also observed as tremolite-actinolite needles that partly project into olivine grains (Figure 4.42 A), some of which are also partly replaced by chlorite along grain fractures (Figure 4.42 B).

Table 4.3: The different alteration minerals observed in Ww, KC, and RietC, along with their relative abundance in each intrusion.

Alteration mineral	Winddam wehrlite	Koedoesfontein Complex	Rietfontein Complex
Actinolite-tremolite	Abundant as a replacement product of hornblende	Common	Rare
Calcite	Rare; present in hornblende	Apparently absent	Scarce
Chlorite	Common as a replacement product of all mafic minerals	Common in sample RB20; replaces mafic minerals	Absent
Serpentine	Common in olivine	Abundant in olivine	Abundant in olivine
Saponite	Rare	Rare	Rare
Talc	Common; associate with orthopyroxene	Rare; associated with orthopyroxene	Rare; associated with orthopyroxene
Sericite	Rare due to low abundance of plagioclase.	Abundant	Abundant
Iddingsite	Rare; replaces olivine.	Common in olivine	Rare

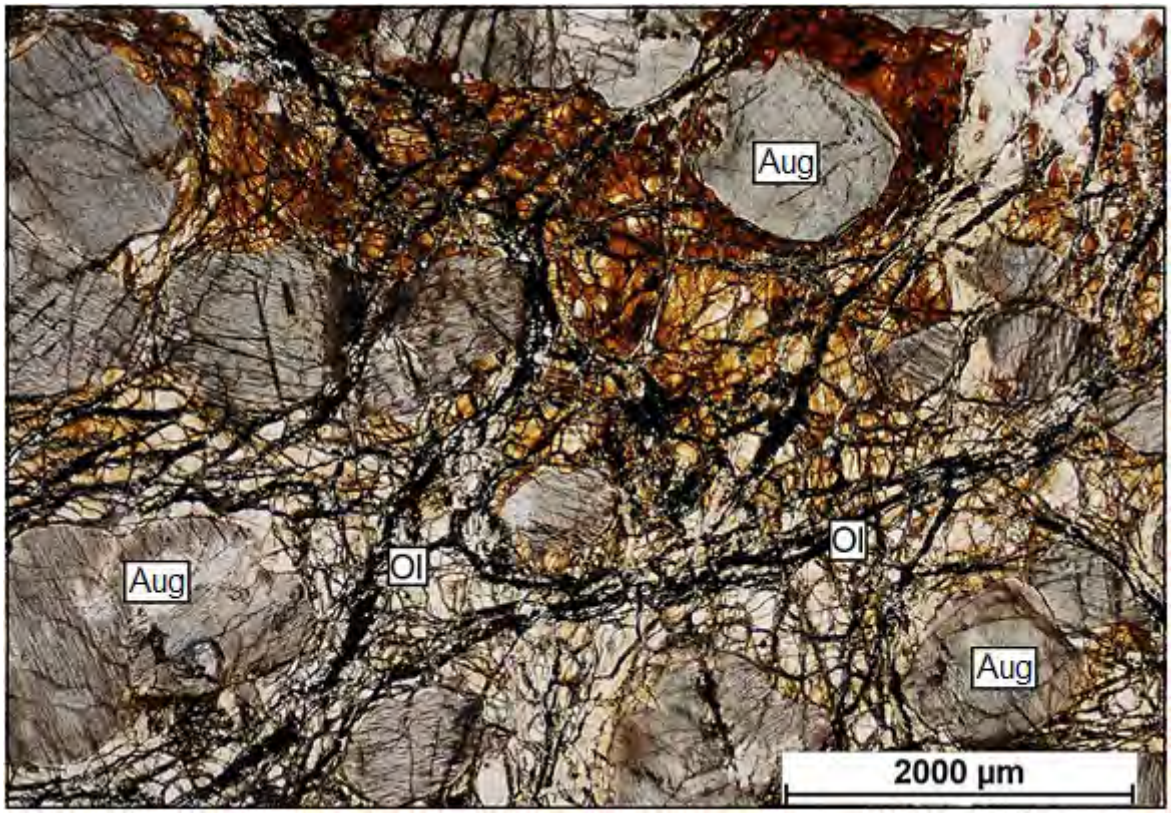

Figure 4.41: Alteration of olivine to dark brown iddingsite to the side of the grain that was exposed to the atmosphere from KC (sample RB7, PPL). Secondary veins of magnetite are present that formed during serpentinisation of olivine.

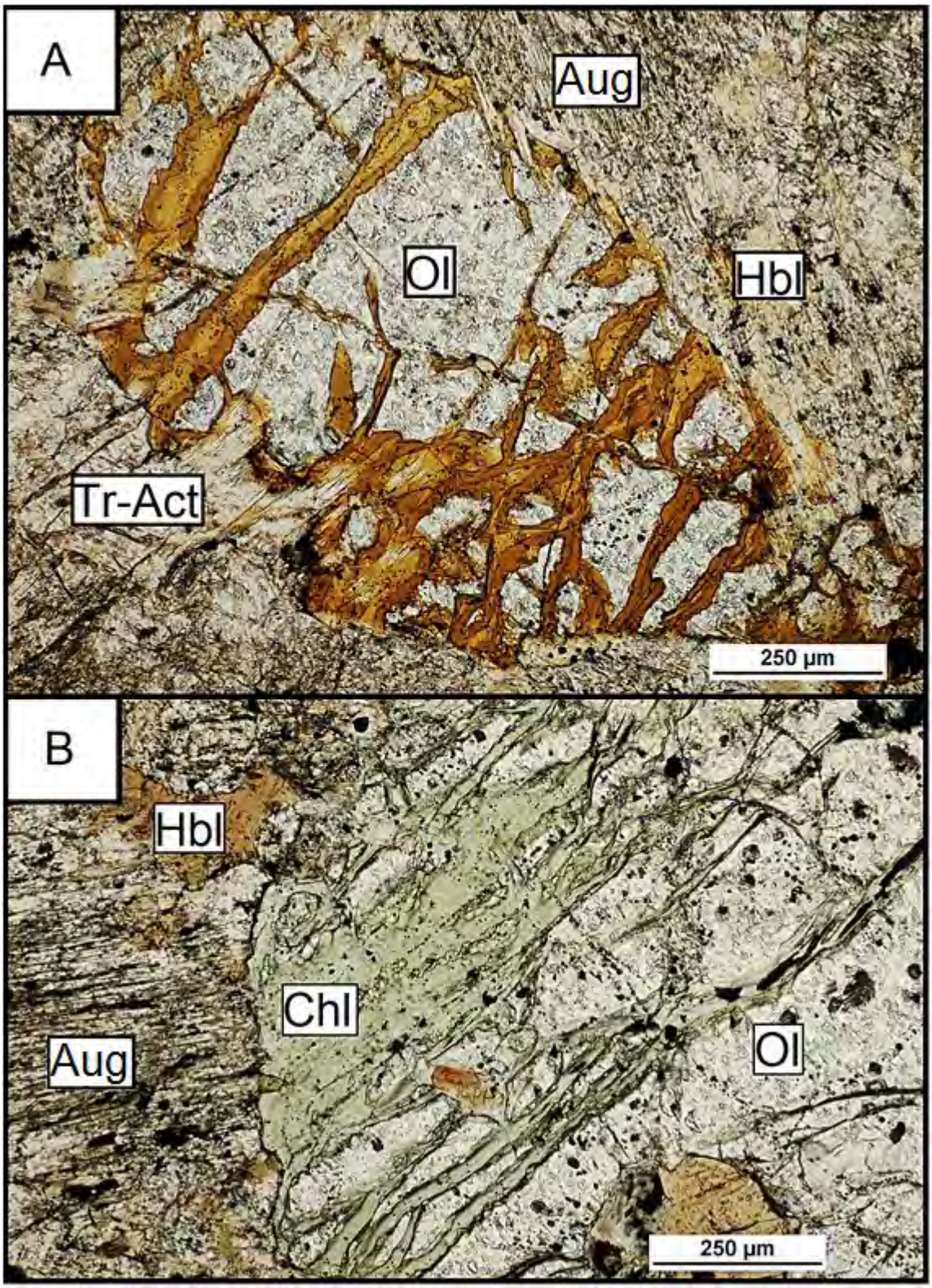

Figure 4.42: Photomicrograph showing alteration of olivine to serpentine and chlorite. A: Serpentine that has been stained to a brownish colour by saponite clay minerals present in fractures of olivine from Ww (sample W03, PPL). Notice the tremolite-actinolite needles protruding into the olivine at the lower left side of the grain. B: Chlorite present in olivine factures from Ww (sample W02, PPL).

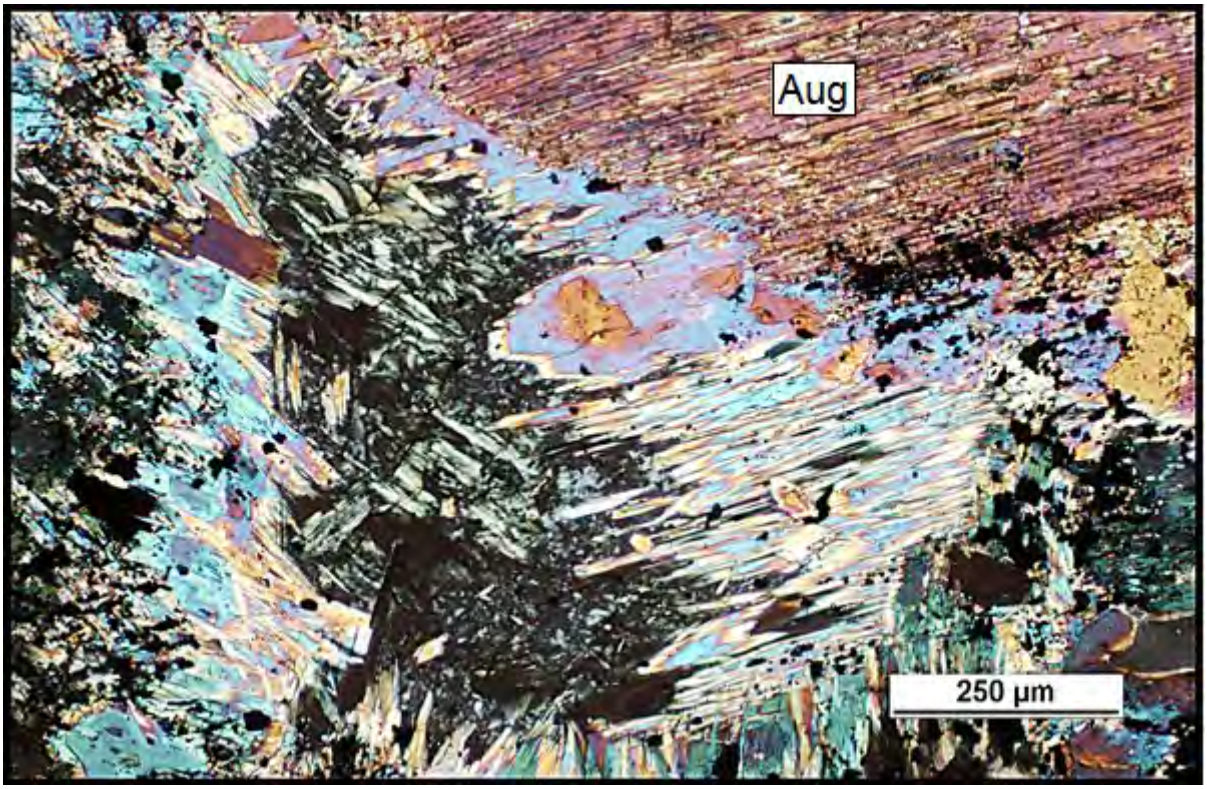

Figure 4.43 Chlorite (black - dark grey first order interference colours) with surrounding tremolite-actinolite needles (second order blue) projecting into the chlorite (sample W01 from Ww, XPL).

Sericite is a very common alteration product of plagioclase in all the rocks of KC and RietC (see Figures 4.29 and 4.38). In some of the olivine clinopyroxenite of both KC and RietC, plagioclase has been completely pseudomorphed to sericite, giving the replaced plagioclase a brownish, dusty appearance. Sericite, which is a fine-grained variety of white mica (including muscovite, phengite, illite, and smectite group clay minerals), forms during low-grade hydrothermal alteration of plagioclase (Deer *et al*., 2013; Delvigne, 1998) and leaching of the alkalis sodium and potassium (Rollinson, 1993).

Some olivine grains in KC have undergone alteration to red to brown iddingsite (Figure 4.41). Iddingsite is defined as a mixture of several minerals like quartz, montmorillonite, chlorite and iron oxides and hydroxides like hematite and goethite that form during the alteration of olivine (Keary, 2001). The formation of iddingsite can occur via a reaction of olivine with atmospheric water (Lee *et al*., 2015) or during both low- (Haraguchi *et al*., 2014) and high-temperature (Clément *et al*., 2007) metamorphism. The concentration of iddingsite in KC increases towards the part of the sample that was exposed to the atmosphere, which leads to the conclusion that atmospheric agents were responsible for its formation. Thus, it can be ascribed to chemical weathering.

In olivine clinopyroxenite from both KC and RietC, some of the mafic minerals (augite, hornblende, and especially olivine) have been partly pseudomorphed by a mixture of serpentine and ferromagnesian clay minerals, which is most likely a mixture of minerals such as vermiculite, smectite, and montmorillonite (Delvigne, 1998). Secondary opaque magnetite that originated during serpentinisation can also be seen within the matrix of the alteration products. Alteration of mafic minerals to ferromagnesian clay minerals like vermiculite is attributed to incipient weathering at atmospheric conditions (Delvigne, 1998). Its colour varies from faint yellow to slightly greenish, and under crossed polarised light it displays a mixture of low (serpentine) and higher (secondary clay minerals) interference colours. A brownish rim of oxidised material can also be observed at the weathering front (see Figure 4.44). Although some of the alteration can be seen in grain fractures, this type of alteration is centripetal (progresses from the surface of the grain inwards towards its centre) and more pronounced around grain boundaries, which stands in contrast to the observed alteration products discussed earlier (see Figure 4.42). Perhaps this is to be expected because fluid pressures at near-surface conditions might not be high enough to penetrate mineral fractures.

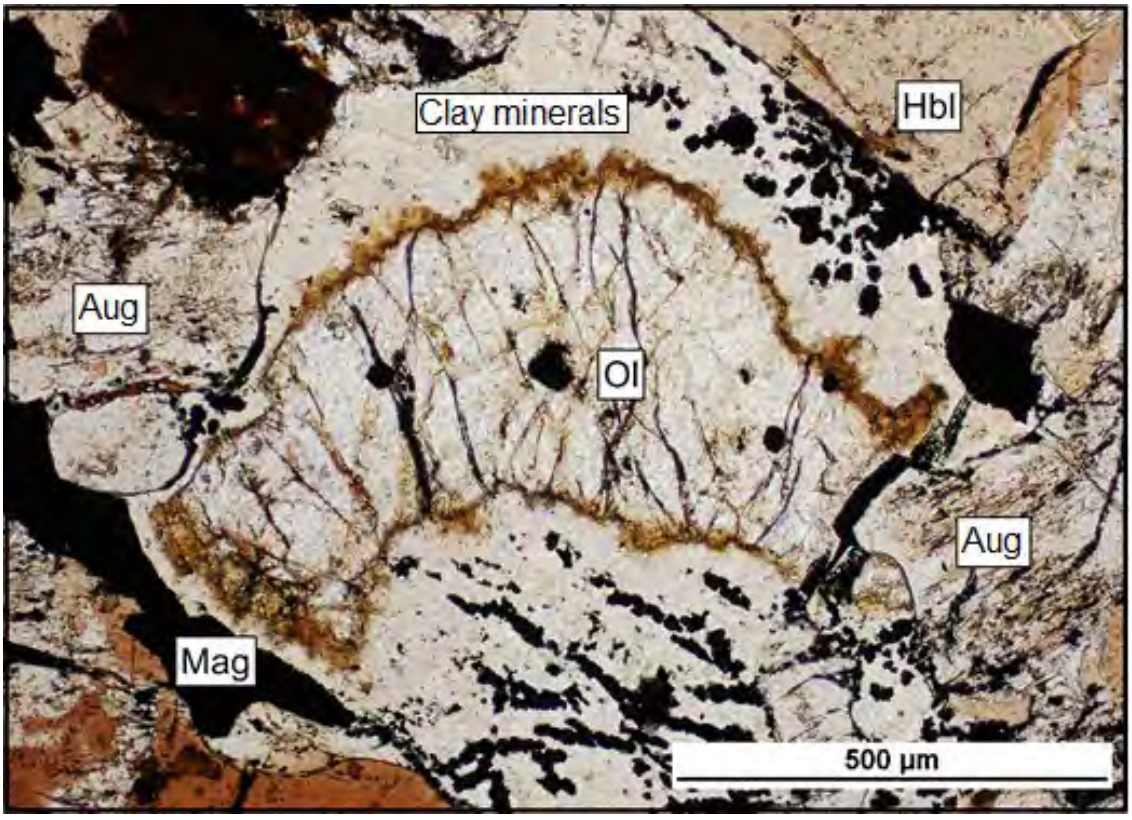

Figure 4.44 Photomicrograph of a grain of olivine that has been partly pseudomorphed by a mixture of serpentine (colourless) and ferromagnesian clay minerals (brownish yellow) (PPL).

Calcite is present in small quantities as an alteration mineral in both Ww and the olivine clinopyroxenite of RietC. When present, it occurs in the cleavage planes of hornblende and augite, and in rarer cases it also occurs as an interstitial mineral (Figure 4.45). The presence of calcite in mafic/ultramafic rocks points to low temperature hydrothermal alteration of the affected lithology, and involves the exposure of the rock to CO_2-bearing fluids (Bjerga *et al*., 2015; Evans & Baltuck, 1988).

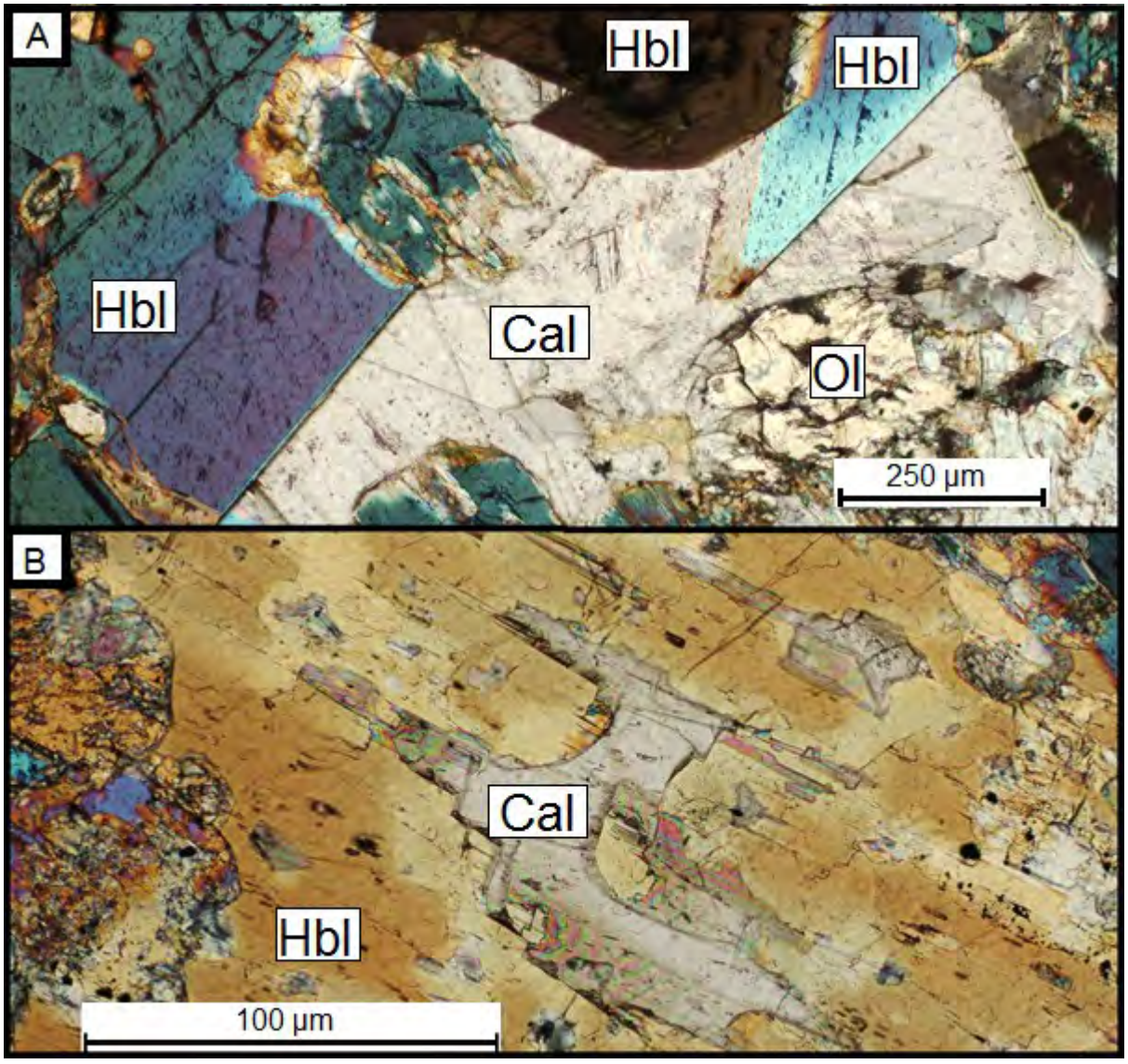

Figure 4.45: The occurrence of calcite in Ww. (A) Here calcite (high-order white interference colour) can be seen as an interstitial mineral. (B) In most cases, calcite appears as inclusions in hornblende. The calcite is generally elongated parallel to the hornblende's cleavage planes (sample W05, PPL).

Finally, talc is typically associated with enstatite in Ww and gabbronorite and norite of KC. It usually occurs in the cleavage planes of the orthopyroxene. Talc is a common alteration mineral of orthopyroxenes, and is frequently observed in mafic complexes such as the RLS of the BIC (Lotter *et al*., 2008). As is the case with all the other alteration minerals discussed

in this section, talc is also a common product of low-grade, hydrothermal alteration of mafic igneous rocks (Deer *et al*., 2013).

CHAPTER 5

GEOCHEMISTRY

As is tradition in petrology, the geochemical characteristics of igneous rocks are usually discussed after petrographic investigations. This is because geochemical data is usually easier to explain if mineralogical data is available. In this chapter, the focus will fall on the whole-rock compositions of the intrusions, searching for patterns of geochemical evolution, geochemical classification, and the examination of multi-element spider and chondrite-normalised rare earth element (REE) diagrams. Once these aspects have been addressed (along with the information obtained in the previous chapters), the stage will be set to construct a petrogenetic model for Ww, KC, and RietC in the chapter that follows.

Before delving into the geochemistry of Ww, KC, and RietC, it is important to clarify the following concepts that are used in this chapter and the remainder of this dissertation. The first is the concept of a primary magma, which refers to a magma that has not undergone any differentiation since its formation and still has the same composition it had before its separation from its place of origin (such as the mantle). These magmas are said to be primitive in composition and they usually contain relatively high concentrations of compatible elements and low concentrations of incompatible elements. When a primary magma undergoes fractional crystallisation, it is said to become more evolved in its chemical composition. This implies that the crystallising magma experiences enrichment and depletion in incompatible and compatible elements, respectively.

5.1 GEOCHEMICAL PROFILES AND COMPOSITION

This section serves to provide average chemical compositions for Ww, KC and RietC, along with the variation in their chemical make-up across the intrusive bodies. To gain a deeper understanding of what chemical variations within the intrusions might imply, it is also important to provide a brief review of the geochemical behaviour of major oxides and trace elements. This involves the behaviour of these elements between ultramafic to mafic melts and the common minerals present in Ww, KC, and RietC (namely olivine, augite, enstatite, hornblende, plagioclase, and magnetite). When assessing a trace element's geochemical behaviour, reference is usually made to its partition coefficient (or D-value), calculated as:

$$D = C_{mineral} / C_{melt} \qquad (5.1),$$

where C refers to the weight concentration of a particular element. If a value of D exceeds one (1) for a particular mineral and chemical element, it means that element is incorporated into the mineral at a greater concentration than what is present in the melt, and the concentration of this element will decrease in the melt during fractionation of this particular mineral. The opposite holds true if D has a value of less than one (McIntire, 1963; Rollinson, 1993; Winter, 2010). Although the behaviour of major elements are not expressed with equation 5.1, the same principle holds that, if the crystallising phases incorporate a higher concentration of a chemical element than what is present in the melt, the concentration of that element will decrease in the remaining melt (and vice versa).

Because the exact locations from which CB samples were collected from Ww are unknown, only W-labelled samples of Ww will be used in this section. In the case of KC, only RB and WK samples will be used while MSC samples will be left out for the same reason. RietC samples used in this section are those indicated on Figure 3.3.

Since RietC contains various types of rocks that differ in terms of their geochemistry, averages will be reported for the olivine (±hornblende) clinopyroxenite, the dioritic rocks, and the troctolite-dunite separately. The chemical make-up of the ultramafic rocks and olivine-hornblende gabbronorite sample CB47 from Ww will also be reported on separately. In the case of KC, wehrlite, olivine clinopyroxenite, and clinopyroxenite samples will be dealt with as one group (referred to as the wehrlite-clinopyroxenite). Enstatite-bearing rocks (which include hornblende gabbronorite RB3, pyroxene hornblendite RB20, and norite WK32) from KC will also be dealt with separately, as they share similar chemical compositions that differ from the wehrlite-clinopyroxenite group. For the same reason, the chemical composition of diorite sample WK36 will be reported on separately. Because of the scarcity of outcrops, a geochemical profile for the enstatite-bearing rocks and the diorite could not be constructed.

5.1.1 Major oxides

The average chemical composition of the different rock types of Ww, KC, and RietC are shown in Table 5.1. Variation in the concentration of the major oxides across the intrusive bodies are indicated on Figure 5.1 for a north to south transect across Ww, Figure 5.2 for a west to east transect across Ww, Figure 5.3 for a west to east transect across the wehrlite-clinopyroxenite sill of KC, and Figures 5.4 and 5.5 for a transect perpendicular to the strike of the layering of RietC.

Table 5.1: Averages and standard deviation (where applicable) of the concentration of major oxides of different rock types from Ww, KC, and RietC. FeO(t) = total iron calculated as FeO.

	Winddam wehrlite		Koedoesfontein Complex			Rietfontein Complex		
Major oxides (wt. %)	**Ultramafic rocks**	**Olivine-hornblende gabbronorite**	**Wehrlite-clinopyroxenite series**	**Enstatite-bearing rocks**	**Diorite**	**Ultramafic rocks**	**Olivine diorite**	**Troctolite and dunite**
SiO_2	43.4 ± 1.0	47.6	45.5 ± 2.3	48.5 ± 2.7	45.1	45.7 ± 1.9	47.8 ± 1.0	33.0 ± 13.2
TiO_2	0.40 ± 0.13	0.47	0.33 ± 0.08	0.44 ± 0.06	2.3	1.2 ± 0.5	0.8 ± 0.2	3.2 ± 2.5
Al_2O_3	2.0 ± 0.6	8.4	1.03 ± 0.19	12.3 ± 3.3	10.7	3.5 ± 0.6	9.2 ± 1.8	5.2 ± 3.0
FeO(t)	11.8 ± 1.7	10.7	12.9 ± 2.1	8.4 ± 1.5	18.0	15.9 ± 2.6	13.1 ± 1.1	30.5 ± 16.3
MnO	0.23 ± 0.02	0.19	0.23 ± 0.02	0.20 ± 0.06	0.28	0.25 ± 0.02	0.20 ± 0.02	0.27 ± 0.06
MgO	19.6 ± 1.3	21.3	23.1 ± 2.8	12.8 ± 4.1	7.0	16.3 ± 2.6	14.9 ± 1.9	18.1 ± 4.8
CaO	14.3 ± 1.2	7.9	12.1 ± 2.2	10.0 ± 2.2	10.1	13.1 ± 0.6	11.2 ± 1.2	4.8 ± 5.0
Na_2O	0.75 ± 0.18	1.52	0.32 ± 0.09	1.3 ± 0.8	3.6	0.99 ± 0.30	2.5 ± 0.5	1.5 ± 0.8
K_2O	0.07 ± 0.02	0.29	0.02 ± 0.01	0.88 ± 0.50	0.52	0.09 ± 0.03	0.12 ± 0.07	0.08 ± 0.03
P_2O_5	0.03 ± 0.01	0.06	0.02 ± 0.01	0.07 ± 0.03	0.54	0.09 ± 0.03	0.08 ± 0.03	0.05 ± 0.02

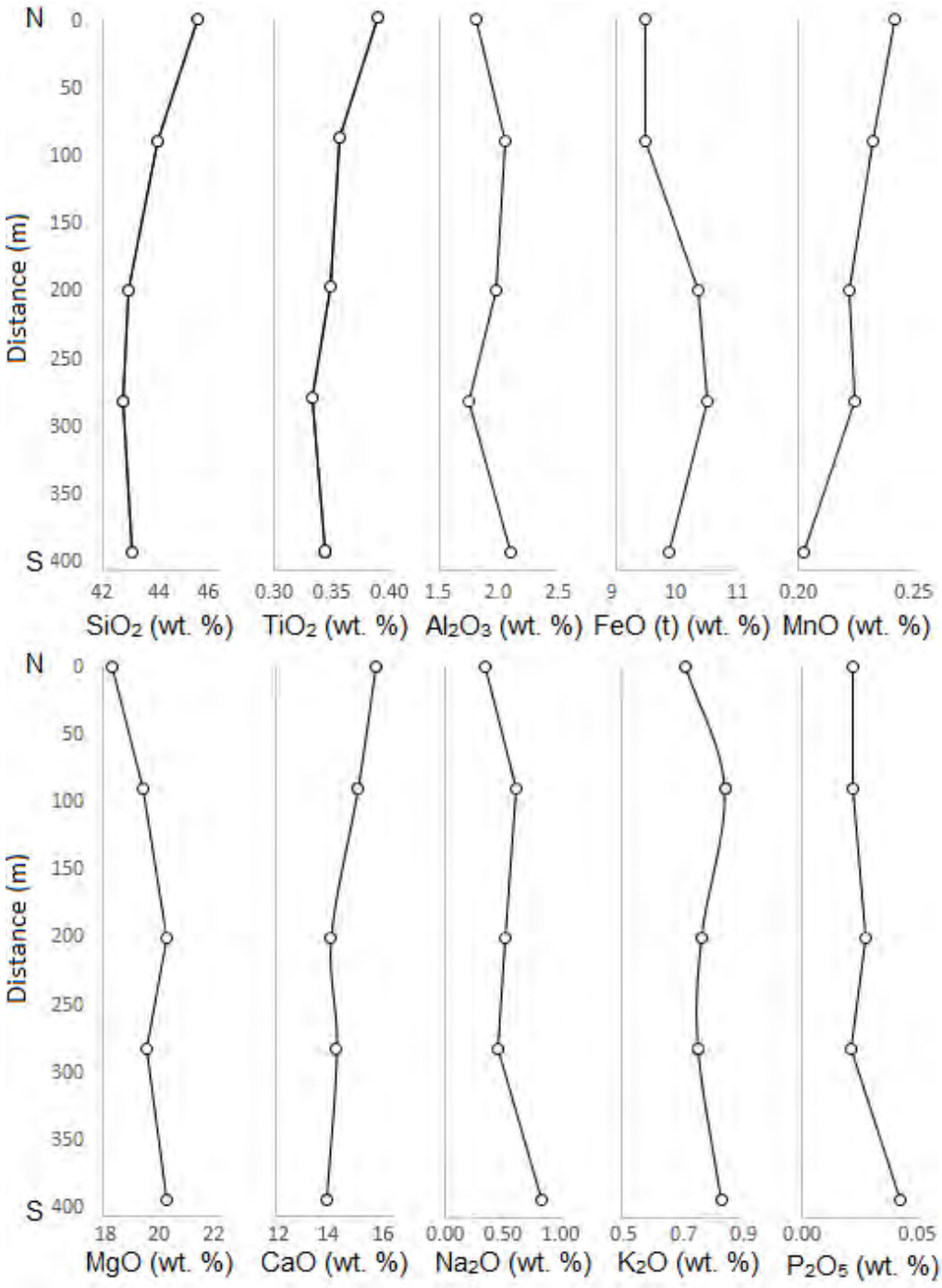

Figure 5.1: Variation of concentration of the major oxides along a north (N) to south (S) transect across Ww. FeO(t) = total iron calculated as FeO.

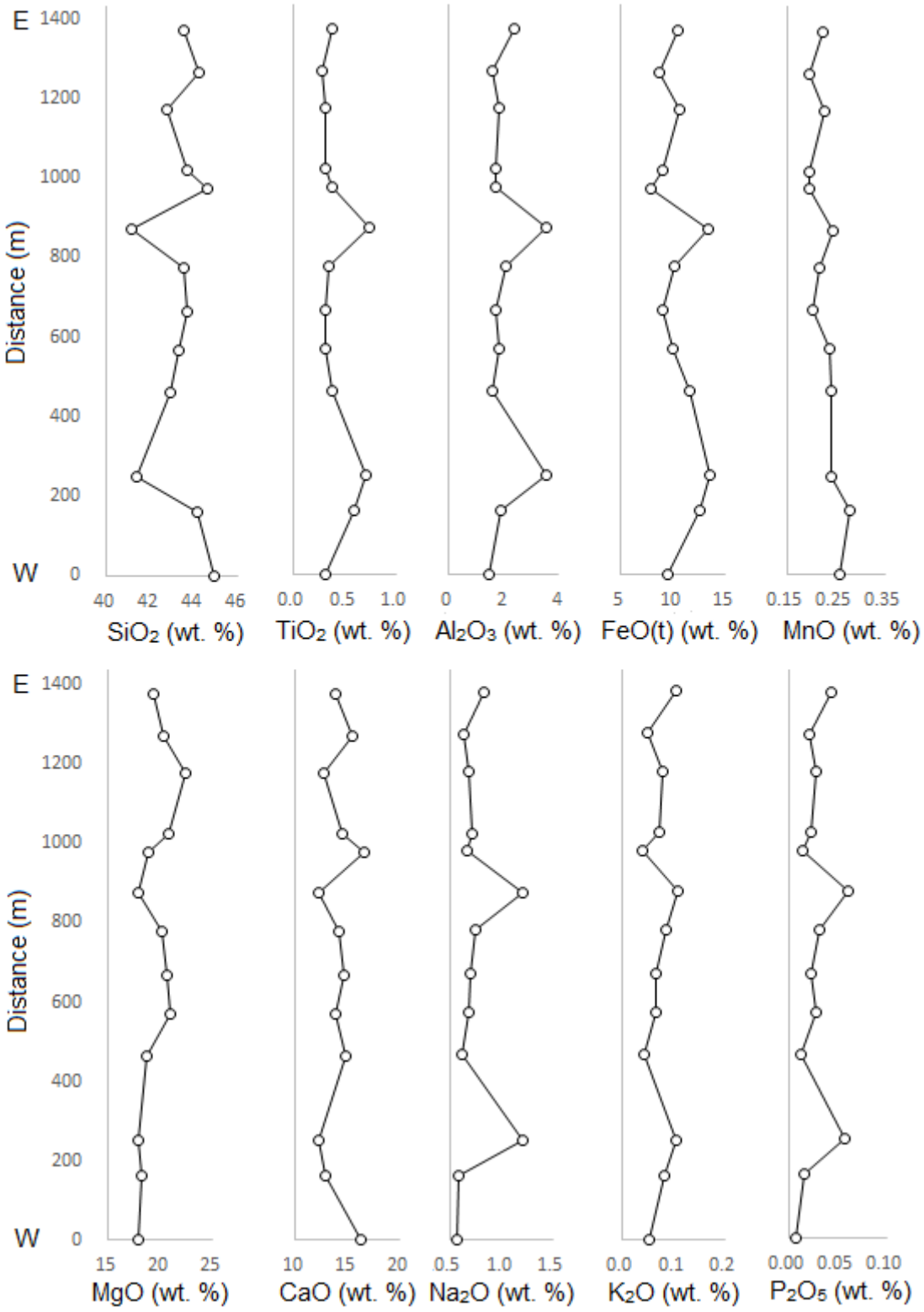

Figure 5.2: Variation of concentration of the major oxides along a west (W) to east (E) transect across Ww. FeO(t) = total iron calculated as FeO.

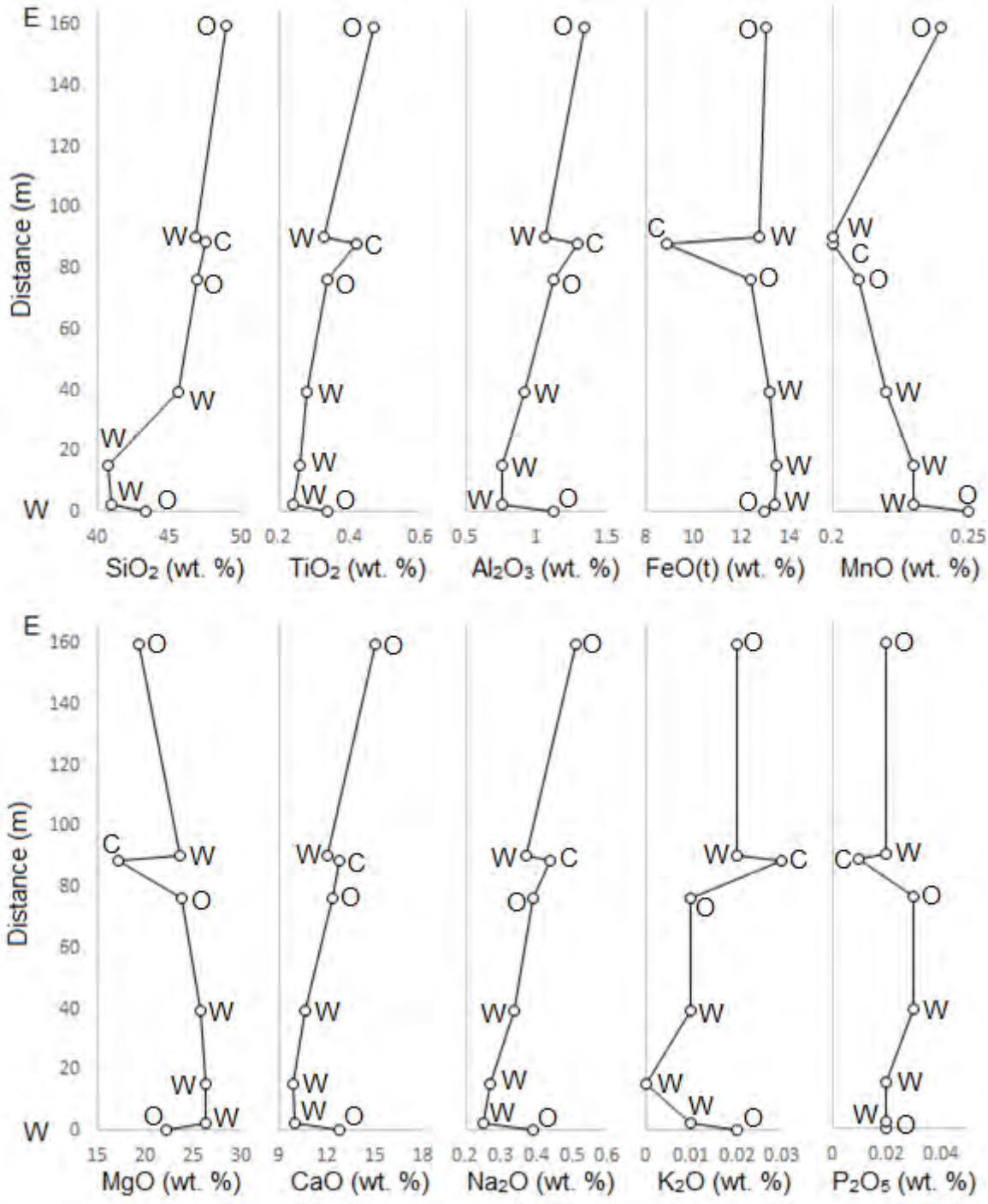

Figure 5.3: Variation of concentration of the major oxides along a west (W) to east (E) transect across the wehrlite-clinopyroxenite sill of KC. FeO(t) = total iron calculated as FeO. C: clinopyroxenite; O: olivine clinopyroxenite; W: wehrlite.

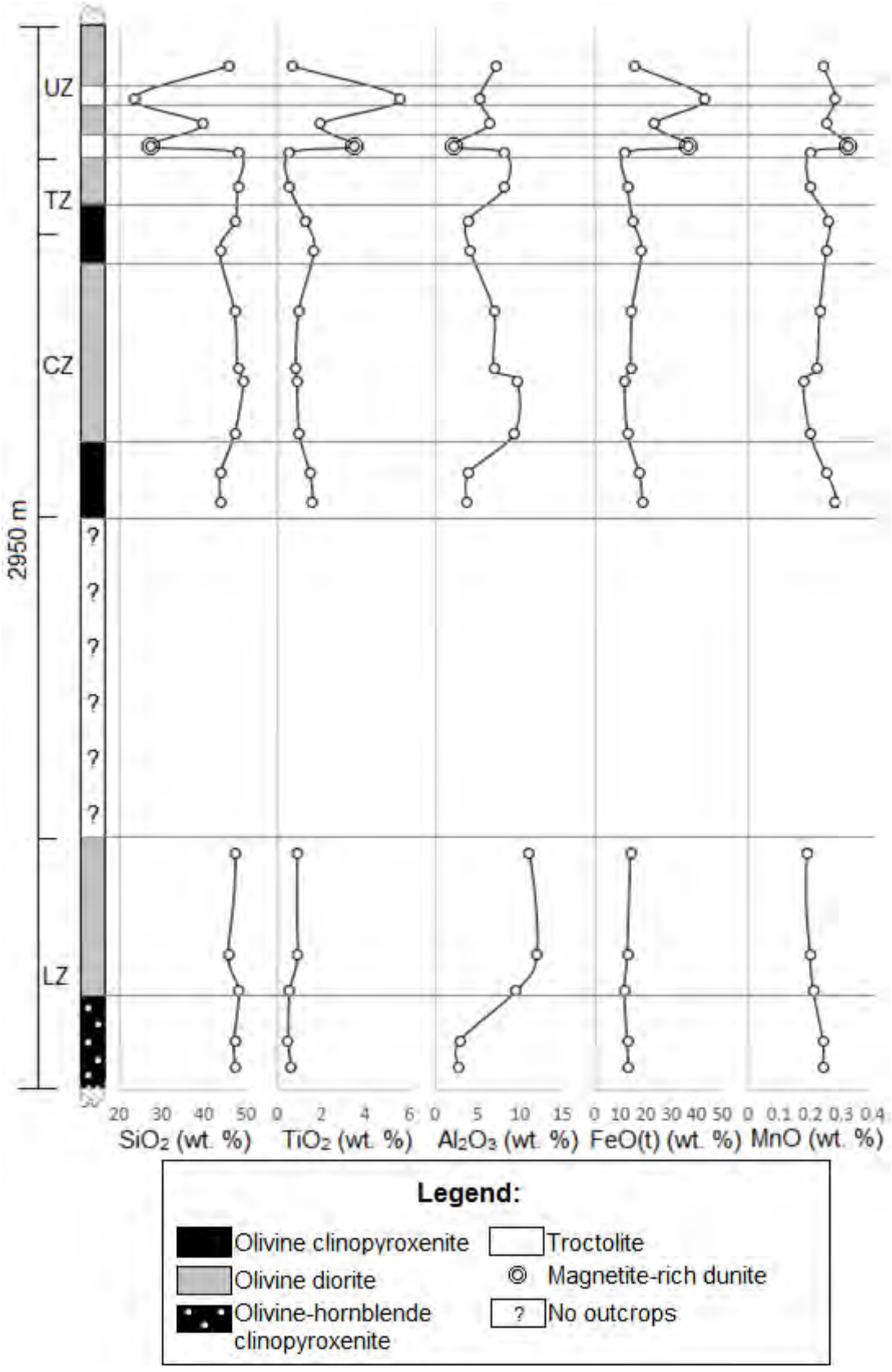

Figure 5.4: Chemical profile perpendicular to strike of the layering in the Rietfontein Complex, showing the variation in concentration of some of the major oxides. FeO(t) = total iron calculated as FeO. LZ: Lower Zone; CZ: Central Zone; TZ: Transitional Zone; UZ: Upper Zone.

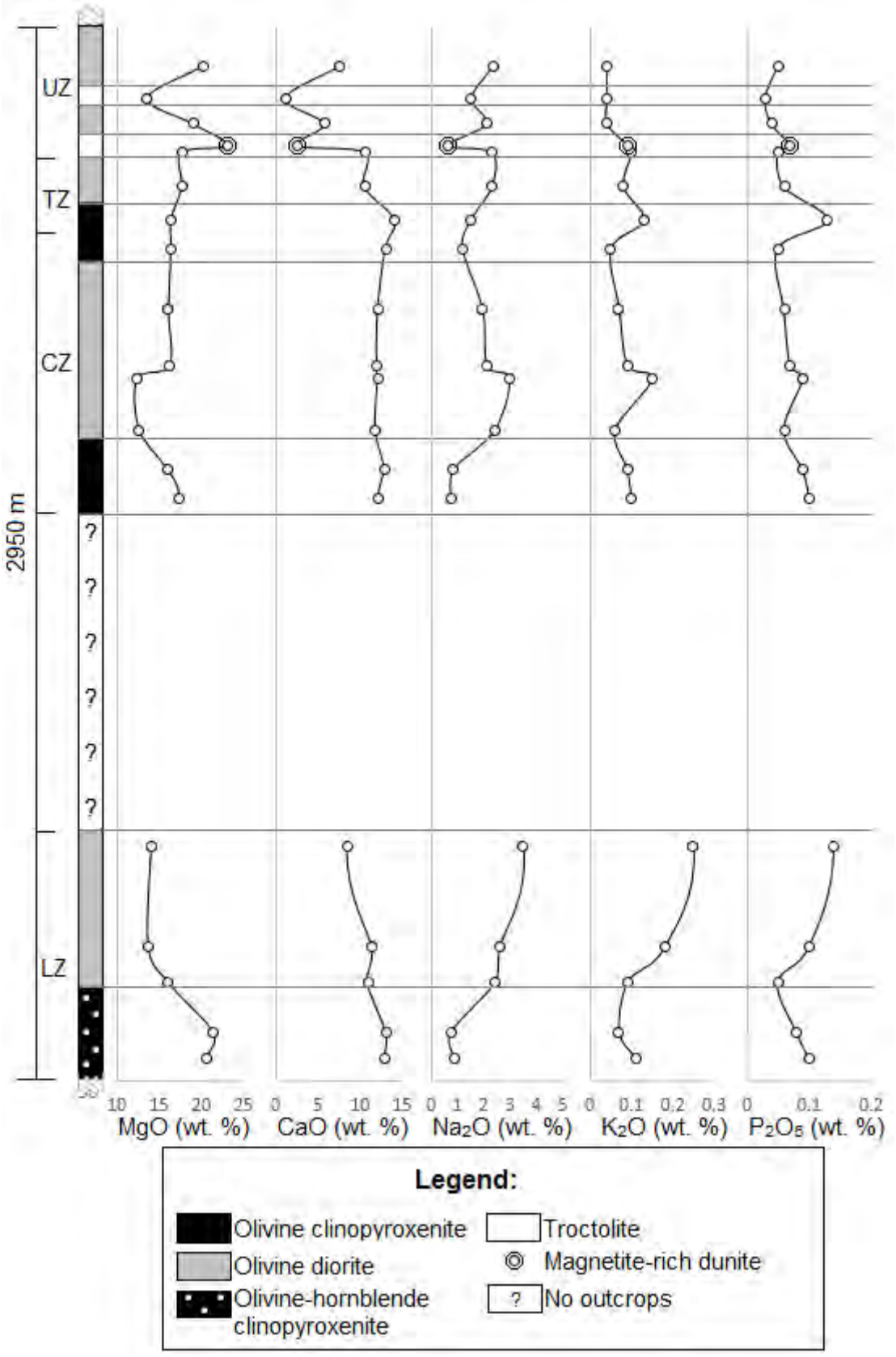

Figure 5.5: Chemical profile perpendicular to strike of the layering in the Rietfontein Complex, showing the variation in some of the major oxides. FeO(t) = total iron calculated as FeO. LZ: Lower Zone; CZ: Central Zone; TZ: Transitional Zone; UZ: Upper Zone.

5.1.1.1 SiO_2

In most cases, SiO_2 is the most abundant oxide present in magmas and is used to build the majority of minerals in igneous rocks (Albarède, 2003; Deer *et al*., 2013; Klein & Dutrow, 2007; Winter, 2010). However, a lower concentration of silica is typically used to construct early forming minerals (for example olivine) than what is present in the melt. This leads to a generally gradual increase in silica in the melt during crystal fractionation of mafic- to ultramafic liquids (Winter, 2010).

- Winddam wehrlite (Figures 5.1 and 5.2)

The average SiO_2 concentrations of ultramafic rocks from Ww are recorded as 43.4 ± 1.0 weight percentage (wt. %) and this low concentration is a testament to the rocks' ultramafic nature. A slight decrease is observed in the silica content from north to south, while two dips are observed in the silica content (at approximately 250 and 900 meters on Figure 5.2) over the west to east transect. These variations in silica content are very small (negligibly so), and no pattern in the mineralogical data could be found to explain these variations. Because of its more mafic nature, the olivine-hornblende gabbronorite has a higher SiO_2 concentration of 47.6 wt. %.

- Koedoesfontein Complex (Figure 5.3)

In KC's wehrlite-clinopyroxenite samples the average SiO_2 concentration is 45.5 ± 2.3 wt. %. From west to east across the wehrlite-clinopyroxenite sill, SiO_2 concentrations initially decrease, followed by a gradual increase across the remainder of the sill. The SiO_2 concentration is generally a bit higher where the olivine content is lower as olivine is the SiO_2-poorest silicate within the intrusion.

The enstatite-bearing rocks have a higher average SiO_2 concentration of 48.5 ± 2.7 wt. % owning to the more mafic nature of these samples. The diorite has a slightly lower concentration of 45.13 wt. %, probably because of its higher modal magnetite content.

- Rietfontein Complex (Figure 5.4)

Average SiO_2 concentrations are 45.7 ± 1.9 wt. % for the olivine (± hornblende) clinopyroxenite and 47.75 ± 1.04 wt. % for the olivine diorite. A very low average concentration of 33.0 ± 13.2 wt % is recorded in the troctolite-dunite. SiO_2 concentrations remain relatively constant across the RietC transect but generally increases across the boundaries from olivine (± hornblende) clinopyroxenite to olivine diorite. An exception to the general constant SiO_2 concentrations is seen when abundant magnetite crystallises in the

Upper Zone, which leads to sudden and dramatic decreases in silica content due to the dilution effect of abundant iron.

5.1.1.2 TiO_2

Generally, TiO_2 is excluded in olivine and clinopyroxene relative to mafic melts but can become compatible with these minerals in extremely high-temperature systems (Bèdard 2005; 2014). TiO_2 is highly incompatible with plagioclase (Bèdard, 2006), while it tends to be compatible in hornblende in most magmatic systems (Rollinson, 1993). In many igneous rocks, TiO_2 tends to concentrate in oxide minerals such as magnetite (Rollinson, 1993) and ilmenite (Deer *et al*., 2013), and the abundance of these minerals can have a dramatic effect on the whole rock TiO_2 concentration (see, for example, Mehdilo & Irannajad, 2010; Wang *et al*., 2014).

- Winddam wehrlite (Figures 5.1 and 5.2)

The average TiO_2 concentration in the ultramafic rocks is low (0.40 ± 0.13 wt. %) and, although it varies slightly more than silica, it still varies very little over both transects. Across the north to south transect, TiO_2 generally appears to be depleted in a southern direction. No consistent trend of TiO_2 enrichment or depletion is observed across the west to east transect. The olivine-hornblende gabbronorite has a similar TiO_2 concentration of 0.47 wt. %.

- Koedoesfontein Complex (Figure 5.3)

Very low average TiO_2 concentrations are also recorded in the wehrlite-clinopyroxenite as 0.33 ± 0.08 wt. %. The variation in the TiO_2 concentration across the sill follows a very similar pattern as the SiO_2 concentration. Because TiO_2 is generally more abundant where the augite content is higher, it might indicate that this oxide is preferentially included in augite versus olivine during crystallisation.

In the case of the enstatite-bearing rocks, the average TiO_2 concentration is slightly higher (0.44 ± 0.06 wt. %) while the diorite has a high TiO_2 concentration of 2.3 wt. % which is attributed to its higher magnetite content.

- Rietfontein Complex (Figure 5.4)

Overall, average TiO_2 concentrations are low for RietC (1.2 ± 0.5 wt. % in the olivine (± hornblende) clinopyroxenite and 0.8 ± 0.2 wt. % in the olivine diorite) while high concentrations are recorded in the troctolite-dunite (3.2 ± 2.5 wt. %).

In the Lower Zone, TiO_2 increases across the olivine clinopyroxenite to olivine diorite boundary. Over the second boundary of this nature in the Central Zone, the concentration falls. Across the olivine diorite to clinopyroxenite boundary in the upper parts of the Central Zone, the concentration increases. In the Transitional Zone, an increase in TiO_2 occurs from the olivine clinopyroxenite to the olivine diorite. The TiO_2 concentration remains relatively constant further upwards across the first layer of troctolite in the Upper Zone, after which the concentrations suddenly increase, which is attributed to the crystallisation of abundant titano-magnetite. Variation in the TiO_2 concentration correlates well with the amount of magnetite in each rock type (compare Figure 4.10 with Figure 5.4).

5.1.1.3 Al_2O_3

High concentrations of Al_2O_3 occur in plagioclase while smaller amounts may be present in pyroxene and amphibole (Albarède, 2003; Deer *et al*., 2013; Klein & Dutrow, 2008).

- Winddam wehrlite (Figures 5.1 and 5.2)

As with the previous two oxides discussed above, the ultramafic rocks have a low average Al_2O_3 concentration (2.0 ± 0.6 wt. %) which can be ascribed to the virtual absence of feldspar (section 4.1.1). Over the north to south transect, Al_2O_3 varies very little. No clear trend of enrichment or depletion of Al_2O_3 is seen across both transects (Figure 5.1 and 5.2). The olivine-hornblende gabbronorite has a much higher average Al_2O_3 concentration (8.4 wt. %) due to the abundance of plagioclase in this rock type.

- Koedoesfontein Complex (Figure 5.3)

The average Al_2O_3 concentrations in the wehrlite-clinopyroxenite is very low in KC due the absence of Al_2O_3-rich phases and is recorded as 1.03 ± 0.19 wt. %. The variation in the Al_2O_3 concentration across the sill is very similar to the variation in SiO_2 and TiO_2. Its pattern is comparable with the augite content of the rock, indicating that Al_2O_3 might be preferentially incorporated into augite versus olivine.

Compared to the wehrlite-clinopyroxenite, the enstatite-bearing rocks had a much higher average concentration of 12.25 ± 3.3 wt. % Al_2O_3 due to the presence of plagioclase feldspar. The diorite also had a high Al_2O_3 concentration of 10.7 wt. %.

- Rietfontein Complex (Figure 5.4)

Al_2O_3 shows a lot of variation across RietC, and has an average concentration of 9.2 ± 1.8 wt. % in the olivine diorite, 3.5 ± 0.6 wt. % in the olivine (± hornblende) clinopyroxenite, and 5.2 ± 3.0 wt. % in the troctolite-dunite. The higher concentration of Al_2O_3 in the olivine diorite compared to the ultramafic rocks is ascribed to the crystallisation of plagioclase in the former rock type. In the Upper Zone troctolite and olivine diorite of RietC, Al_2O_3 concentrations are relatively constant. An exception is the magnetite-rich dunite, which has a very low Al_2O_3 concentration. It is also interesting to note that this oxide is somewhat more abundant in the Main- and Transitional Zone olivine clinopyroxenite when compared to the same rock type in the Lower Zone. This is attributed to the absence of intercumulus plagioclase in the lowermost layer (section 4.1.3).

5.1.1.4 FeO(t)

Iron is accepted into the crystal structure of all mafic silicates (Deer *et al*., 2013; Klein & Dutrow, 2008). However, at high temperatures or in more primitive melts, Mg is preferentially incorporated into mafic silicates at the expense of Fe (Deer *et* al., 2013; Klein & Dutrow, 2008; Winter, 2010). This leads to the general trend of Fe enrichment as crystallisation proceeds in rocks with a mafic or ultramafic composition (Winter, 2010). In the majority of igneous rocks, iron also crystallises in the form of magnetite (Fe_3O_4) (Deer *et al*., 2013). Both ferric and ferrous iron is reported as ferrous iron and is indicated as FeO(t).

- Winddam wehrlite (Figures 5.1 and 5.2)

FeO(t) concentrations in the ultramafic rocks are also relatively consistent across the intrusion and the average concentration is 11.8 ± 1.7 wt. %. Once again, no trend can be observed of either iron depletion or enrichment across the intrusion. The FeO(t) concentration in the olivine-hornblende gabbronorite is similar to the ultramafic rocks, and is recorded as 10.7 wt. %.

- Koedoesfontein Complex (Figure 5.3)

In terms of FeO(t), the wehrlite-clinopyroxenite from KC has an average concentration of 12.9 ± 2.1 wt. %. The concentration of FeO(t) shows very little variation across the wehrlite-clinopyroxenite sill with the exception of a dramatic drop observed near its centre. In this locality, both the olivine and magnetite content of the sill reaches a minimum and might be responsible for the low concentration of FeO(t) here.

FeO(t) concentrations are slightly lower in the enstatite bearing-rocks due to their more mafic composition with an average of 8.4 ± 1.5 wt. % while the diorite has the highest FeO(t) concentration of 18.0 wt. % due to its higher magnetite abundance.

- Rietfontein Complex (Figure 5.4)

Average FeO(t) concentrations are recorded as 15.9 ± 2.6 wt. % in the olivine (± hornblende) clinopyroxenite, 13.1 ± 1.1 wt. % in olivine diorite, and 30.5 ± 16.3 wt. % in the troctolite-dunite. In the Lower Zone, FeO(t) concentrations are relatively constant, while some deviation occurs in the Central Zone, with olivine clinopyroxenite generally displaying elevated FeO(t) concentrations compared to the olivine diorite. As with TiO_2, FeO(t) shows great variation and very high concentrations in some of the magnetite-rich dunite and troctolite samples (CB18 and MB19a) of the Upper Zone, which is attributed to abundant magnetite crystallisation in some of these layers.

5.1.1.5 MnO

This oxide is usually compatible with olivine, and straddles the boundary between being compatible or incompatible with clinopyroxene (Dunn, 1987). In olivine-rich ultramafic rocks, its concentration is thus expected to decrease as crystal fractionation proceeds, while its behaviour is more difficult to predict in pyroxenite.

- Winddam wehrlite (Figures 5.1 and 5.2)

The average MnO concentration in the ultramafic rocks is 0.23 ± 0.02 wt. % and appeared, with little variation in between, to slightly decrease from north to south and from west to east. Probably due to its lower abundance of olivine and the presence of a large amount of plagioclase, the olivine-hornblende gabbronorite has a slightly lower MnO concentration of 0.19 wt. %.

- Koedoesfontein Complex (Figure 5.3)

An average of 0.23 ± 0.02 wt. % MnO was recorded in the wehrlite-clinopyroxenite of KC. MnO concentrations initially fall from west to east across the wehrlite-clinopyroxenite sill and reaches a minimum near its centre. A higher MnO concentration is recorded in the most eastern sample. The MnO concentration correlates positively with the olivine content of the rock (compare Figure 4.6 with 5.3), which is the principle phase to accept MnO into its crystal structure.

Despite the absence of olivine in these rock samples, the enstatite-bearing rocks from KC only has a slightly lower average MnO concentration of 0.20 ± 0.06 wt. %. The MnO concentration is highest in the diorite (0.28 wt. %).

- Rietfontein Complex (Figure 5.4)

RietC has an average MnO concentration of 0.25 ± 0.02 wt. % in the olivine (± hornblende) clinopyroxenite, 0.20 ± 0.02 wt. % in the dioritic rocks, and 0.27 ± 0.06 wt. % in the troctolite-dunite, and varies little across the intrusion. Generally, a small decrease is observed in the concentration of MnO as one passes across olivine (± hornblende) clinopyroxenite to olivine diorite boundaries. The higher concentration of MnO in the ultramafic layers is ascribed to the greater abundance of olivine and augite. In the Upper Zone of RietC, the concentration of this oxide spikes in the magnetite-rich dunite, probably due to the abundance of olivine in this rock type.

5.1.1.6 MgO

MgO is incorporated in mafic minerals (such as, in order of decreasing MgO content, forsterite, enstatite, diopside, and hornblende) in great concentrations during the crystallisation of primitive magmas, causing MgO depletion during magmatic evolution (Deer *et al*., 2013; Klein & Dutrow, 2008; Winter, 2010). As discussed for Fe, ferromagnesian minerals tend to incorporate more Mg and Fe in hot, primitive melts, while the ratio shifts towards greater Fe incorporation as the magma cools (Gasparik, 2013; Winter, 2010).

- Winddam wehrlite (Figures 5.1 and 5.2)

High average MgO concentrations (19.6 ± 1.3 wt. %) are recorded in the ultramafic rocks of Ww. Although an increase is observed in the MgO concentration over the north to south transect, it is considered too small to be of any significance. No dramatic variations are observed in the MgO concentration across the west to east transect. Despite its more mafic composition, the olivine-hornblende gabbronite has a higher MgO concentration (21.3 wt. %) compared to the average of the ultramafic rocks.

- Koedoesfontein Complex (Figure 5.3)

Very high average MgO concentrations are recorded in the wehrlite-clinopyroxenite (23.1 ± 2.8 wt. %). This oxide's concentration initially increase from west to east across the wehrlite-clinopyroxenite sill, then stays relatively constant until the approximate centre of the sill where the concentration suddenly drops. This is followed by a sudden increase in the MgO

content, after which it decreases further east. With the exception of the most eastern sample collected, the MgO concentration correlates well with the olivine content of the rock.

The average MgO concentrations in the enstatite-bearing rocks is much lower owing to their mafic character (12.8 ± 4.1 wt. %). As expected, the diorite has the lowest MgO concentration of 7.0 wt. %.

- Rietfontein Complex (Figure 5.5)

A high average MgO concentration is recorded in the olivine (± hornblende) of RietC (16.3 ± 2.6 wt. %). In the dioritic rocks, the average MgO concentration recorded is 14.9 ± 1.9 wt. %. The highest average MgO concentration of the intrusion is recorded in the troctolite-dunite (18.1 ± 4.8 wt. %). MgO concentrations tend to drop across the Lower- and Central Zone olivine clinopyroxenite to olivine diorite boundaries. A sudden increase in MgO content is observed in the centre of the first olivine diorite layer of the Central Zone. Further up it remains fairly constant until a spike in the MgO concentration is observed in the magnetite-rich dunite. Thereafter, a decrease in MgO content is observed as magnetite becomes more abundant, while an increase is observed for the final olivine diorite layer in which magnetite is relatively scarce.

5.1.1.7 CaO

CaO is primarily incorporated in augite and plagioclase in ultramafic to mafic igneous rocks. This oxide is usually more abundant in plagioclase if the rock has a more primitive composition, and is gradually replaced by Na_2O within the feldspar during cooling and magmatic evolution (Klein & Dutrow, 2008; Winter, 2010).

- Winddam wehrlite (Figures 5.1 and 5.2)

CaO averages at 14.3 ± 1.2 wt. % in the ultramafic rocks, and owes its abundance mainly to the presence of augite. CaO concentrations slightly decrease along the north to south transect, and while some inconsistencies occur, remain relatively uniform over the west to east transect. The olivine-hornblende gabbronorite has a lower concentration of 7.9 wt. %, probably due to its lower abundance of calcic pyroxene compared to the ultramafic rocks.

- Koedoesfontein Complex (Figure 5.3)

In the wehrlite-clinopyroxenite, the average CaO concentration is 12.1 ± 2.2 wt. %. The variation in the CaO concentration across the sill is also similar to that observed for SiO_2,

TiO_2, and Al_2O_3. CaO concentrations correlate well with the augite content of the rock (the only mineral to incorporate large quantities of CaO during its crystallisation).

Average CaO concentrations in the enstatite-bearing rocks are comparable to those in the wehrlite-clinopyroxenite with an average of 10.0 ± 2.2 wt. %. In the diorite, the CaO concentration is 10.1 wt. %.

- Rietfontein Complex (Figure 5.5)

CaO concentrations average at 13.1 ± 0.6 wt. % in olivine (± hornblende) clinopyroxenite, 11.2 ± 1.2 wt. % in the olivine diorite, and 4.8 ± 5.0 wt. % in the troctolite-dunite. Because plagioclase is richer in Na_2O than CaO (see section 5.3), CaO is expected to have a more pronounced association with augite. In the Lower Zone, this relationship between CaO and augite is visible, as CaO concentrations drop across the olivine-hornblende clinopyroxenite to olivine diorite boundary. In the Central Zone, this relationship is less apparent, although the highest CaO concentrations are recorded in the upper olivine clinopyroxenite layer. The CaO concentration falls across the olivine clinopyroxenite to olivine diorite boundary in the Transitional Zone. In the Upper Zone, CaO concentrations are much lower in the troctolite due to the low abundance of augite. Because of the reappearance of augite, the Upper Zone olivine diorite contains higher concentrations of this oxide compared to the troctolite.

5.1.1.8 Na_2O

Na_2O is usually incompatible with olivine, augite, and enstatite, while it is relatively scarce in plagioclase in rocks with an ultramafic- to mafic composition. Therefore, this oxide usually increases during magmatic evolution in basaltic magmas. In rocks with a dioritic composition, Na_2O can become abundant as it is incorporated in sodic feldspars.

- Winddam wehrlite (Figures 5.1 and 5.2)

A low average Na_2O concentration is recorded for ultramafic rocks from Ww (0.75 ± 0.18 wt. %) as one would expect for rocks with an ultramafic composition. As with the majority of the oxides discussed above, no trend of Na_2O enrichment is observed for either transect. The Na_2O concentration in the olivine-hornblende gabbronorite is significantly higher (1.52 wt. %) due to the abundance of plagioclase in this rock type.

- Koedoesfontein Complex (Figure 5.3)

The average concentration of Na_2O is very low in the wehrlite-clinopyroxenite from KC (0.32 ± 0.09 wt. %). Na_2O concentrations follow a similar pattern as CaO across the sill and might reflect a greater tendency for Na_2O to be incorporated in augite relative to the other minerals. Because it is generally incompatible with all mineral phases within the sill, an increased Na_2O concentration could also point to a more evolved composition of the parental magma from which that section of KC crystallised.

A significantly higher Na_2O concentration (1.3 ± 0.8 wt. %) is recorded in the enstatite bearing rocks due to the presence of plagioclase. Because of the presence of sodic plagioclase in the diorite, it has the highest Na_2O concentration of 3.6 wt. %.

- Rietfontein Complex (Figure 5.5)

Average Na_2O values are 0.99 ± 0.3 wt. % in the olivine (± hornblende) clinopyroxenite, 2.5 ± 0.5 wt. % in the olivine diorite, and 1.5 ± 0.8 wt. % in the troctolite-dunite. The great variation in Na_2O throughout the Complex is ascribed to modal layering. Because Na_2O is accepted in plagioclase in much greater concentrations compared to the other silicates in RietC, the concentration of this oxide is usually much higher in the olivine diorite compared to the olivine clinopyroxenite. In the troctolite, the concentration of Na_2O is comparable to the olivine diorite of the rest of the intrusion. Naturally, the magnetite-rich dunite has much lower Na_2O concentrations because of the scarcity of plagioclase in this rock type.

5.1.1.9 K_2O

K_2O is only incorporated in very small concentrations in olivine, hornblende, pyroxenes, and plagioclase (Deer *et al.*, 2013). It is, therefore, considered to be incompatible with mafic- to ultramafic rocks, and tends to increase during the crystallisation of primitive melts.

- Winddam wehrlite (Figures 5.1 and 5.2)

Similar to Na_2O, average K_2O concentrations are very low (0.07 ± 0.02 wt. %) owing to the ultramafic nature of Ww. While small variations occur, K_2O shows no considerable increase or decrease across Ww. The olivine-hornblende gabbronorite has a higher K_2O concentration of 0.29 wt. %.

- Koedoesfontein Complex (Figure 5.3)

KC wehrlite-clinopyroxenite samples also possess a very low average K_2O concentration of 0.02 ± 0.01 wt. %. K_2O concentrations show a similar pattern to SiO_2 (and the other oxides as discussed above) across the ultramafic sill. Due to its incompatible nature with all minerals in the wehrlite-clinopyroxenite, areas where its concentration is higher might indicate a more evolved composition of the parental melt from which the rocks crystallised.

In the enstatite-bearing rocks, the average K_2O concentration is significantly higher (0.88 ± 0.5 wt. %) and is probably due to its more evolved nature. In the diorite, the K_2O concentration is 0.52 wt. %.

- Rietfontein Complex (Figure 5.5)

The average concentration of K_2O in the olivine (± hornblende) clinopyroxenite of RietC is very low (0.09 ± 0.03 wt. %), slightly higher in the dioritic rocks (0.12 ± 0.07 wt. %), and typically lowest in the troctolite-dunite (0.08 ± 0.03 wt. %). These values are lower than average for both tholeiitic and alkaline basalts (Philpotts, 1989). No clear trend between K_2O concentration and mineralogy could be observed. In the Lower Zone, K_2O concentrations tend to increase with stratigraphic height. Across the Main and Transitional Zones, K_2O concentrations generally decrease (with some variation in between) with stratigraphic height, and reach a minimum in the Upper Zone.

5.1.1.10 P_2O_5

P_2O_5 is considered to be incompatible with the common minerals present in igneous rocks, and thus tend to increase as magmatic evolution proceeds. In highly evolved or alkaline rocks (usually granites), P_2O_5 crystallises as apatite when its concentration becomes high enough (Winter, 2010).

- Winddam wehrlite (Figures 5.1 and 5.2)

P_2O_5 has the lowest concentration in the ultramafic rocks of all the oxides discussed above, with an average value of 0.03 ± 0.01 wt. %. Although variations in the P_2O_5 content of Ww is negligibly small, an overall increase in the P_2O_5 concentration occurs both along the north to south and west to east transects. The P_2O_5 concentration is slightly higher in the olivine-hornblende gabbronorite and is recorded as 0.06 wt. %.

- Koedoesfontein Complex (Figure 5.3)

A low average P_2O_5 concentration is recorded in the wehrlite-clinopyroxenite of 0.02 ± 0.01 wt. %. The concentration of this oxide stays fairly consistent across the intrusion with the exception of a drop observed near the centre of the sill. No clear mineralogical pattern exists to explain the variation of the P_2O_5 concentration.

As with K_2O, the average P_2O_5 concentration is higher in the enstatite-bearing rocks (0.07 ± 0.03 wt. %) due to its more evolved nature. The diorite has a much higher P_2O_5 concentration of 0.54 wt. %.

- Rietfontein Complex (Figure 5.5)

P_2O_5 concentrations average at 0.09 ± 0.03 wt. % in the olivine (± hornblende) clinopyroxenite, 0.08 ± 0.03 wt. % in the dioritic rocks, and 0.05 ± 0.02 wt. % in the troctolite-dunite. This oxide is incompatible with all mineral phases observed in RietC, and is expected to increase with magmatic evolution. In the Lower Zone, P_2O_5 concentrations initially decrease, followed by an increase in the Lower Zone olivine diorite. Its concentration generally decreases upwards in the Central Zone, followed by a spike in concentration in the Transitional Zone olivine clinopyroxenite. Lower concentrations are observed in samples collected higher up in the Transitional Zone and Upper Zone. No great variation in its concentration is observed across the Upper Zone itself.

5.1.2 Trace elements

The average contents of selected trace elements are given in Table 5.2 for the different rock types from Ww, KC, and RietC. The variation in concentration of these trace elements across the intrusive bodies are shown in Figure 5.6 for a north to south transect across Ww, Figure 5.7 for a west to east transect across Ww, Figure 5.8 for a west to east transect across the wehrlite-clinopyroxenite sill of KC, and Figures 5.9 and 5.10 for a transect perpendicular to the strike of RietC.

5.1.2.1 Chromium

Cr is generally compatible with clinopyroxene (Bèdard, 2014), orthopyroxene, hornblende, and magnetite (Rollinson, 1993), but incompatible with olivine in rocks with similar MgO concentrations such as Ww, RietC, and KC (Bèdard, 2005).

.

Table 5.2: Averages and standard deviation (where applicable) of the concentration of selected trace elements of different rock types from Ww, KC, and RietC.

	Winddam wehrlite		Koedoesfontein Complex			Rietfontein Complex		
Trace elements (ppm)	**Ultramafic rocks**	**Olivine-hornblende gabbronorite**	**Wehrlite-clinopyroxenite series**	**Enstatite-bearing rocks**	**Diorite**	**Ultramafic rocks**	**Olivine diorite**	**Troctolite and dunite**
Cr	2067 ± 709	3042	1700 ± 188	1522 ± 834	113	1081 ± 376	596 ± 195	1332 ± 601
Co	123 ± 15	n.d.	144 ± 24	92 ± 16	128	n.d.	n.d.	n.d.
Ni	395 ± 74	898	512 ± 117	339 ± 186	39	258 ± 100	292 ± 90	974 ± 157
Rb	1.4 ± 0.6	11	0.37 ± 0.29	23 ± 16	6.2	6.2 ± 1.6	5.4 ± 1.7	4.7 ± 0.6
Sr	61 ± 20	78	36 ± 8	167 ± 41	744	288 ± 152	397 ± 87	220 ± 145
Ba	31 ± 18	115	37 ± 16	135 ± 35	1392	133 ± 57	129 ± 23	292 ± 103
Sc	48 ± 4	27	39 ± 9	38 ± 4	39	50 ± 5	36 ± 9	16 ± 4
V	231 ± 50	174	133 ± 35	182 ± 30	442	242 ± 141	272 ± 101	1337 ± 650
Zr	8.5 ± 2.8	29	5.0 ± 1.6	31 ± 14	40	40 ± 36	30 ± 9	15 ± 3
Y	2.9 ± 0.7	12	3.9 ± 1.7	9.8 ± 1.9	23	6.7 ± 4.4	Frequently b.d.l.	b.d.l.

n.d. = not determined

b.d.l = below detection limit

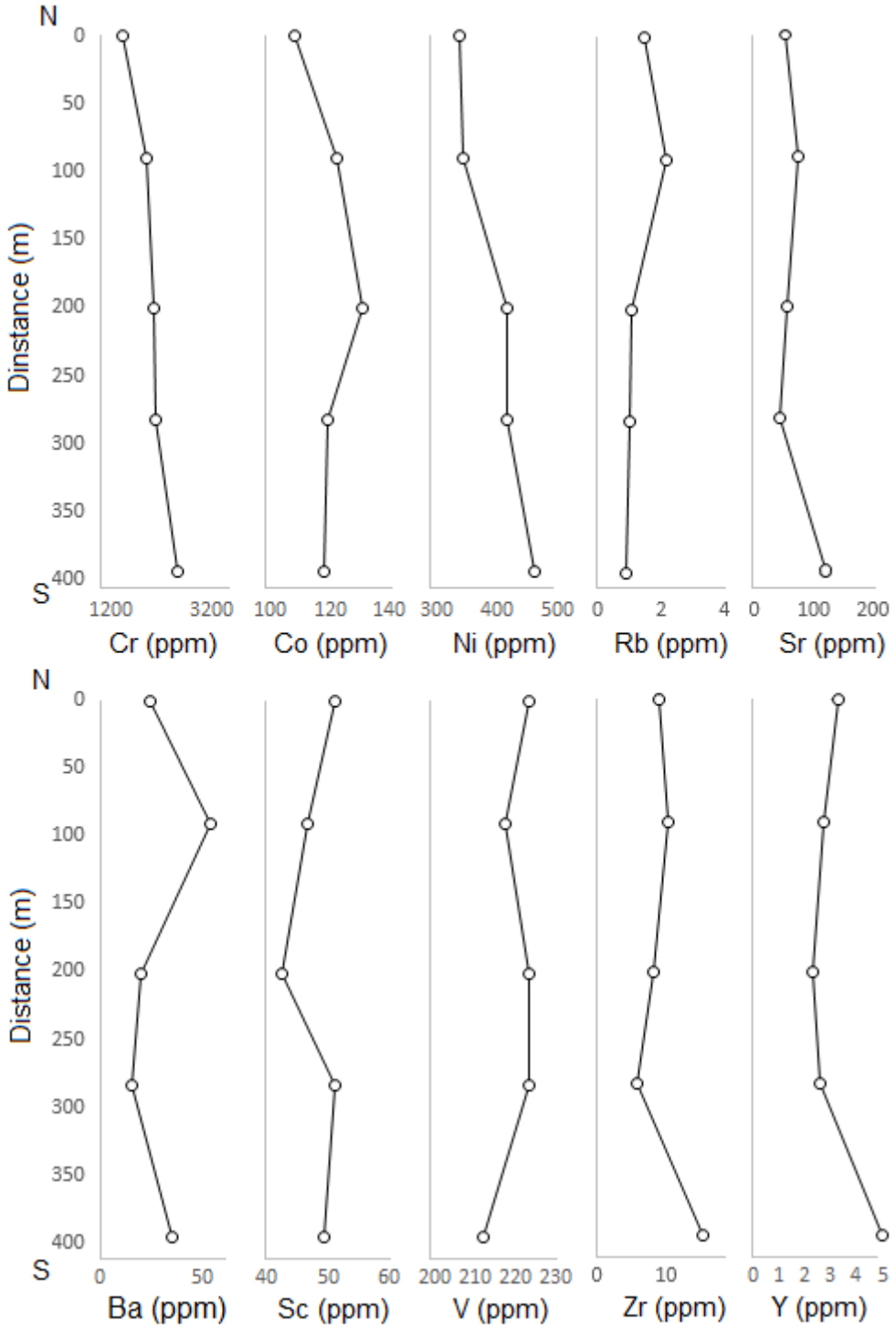

Figure 5.6: Variation in concentration of selected trace elements along a north (N) to south (S) transect across Ww.

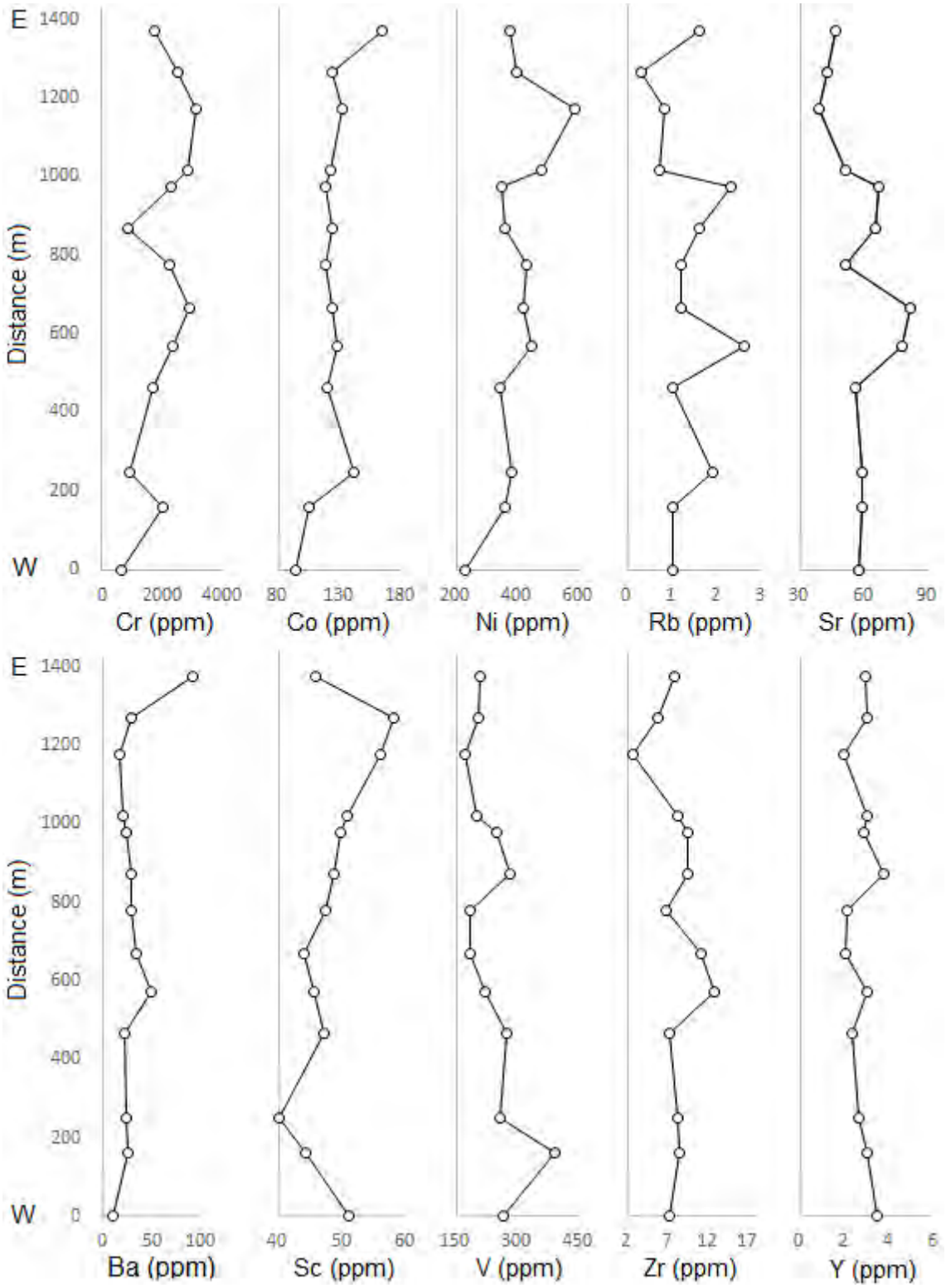

Figure 5.7: Variation in concentration of selected trace elements along a west (W) to east (E) transect across Ww.

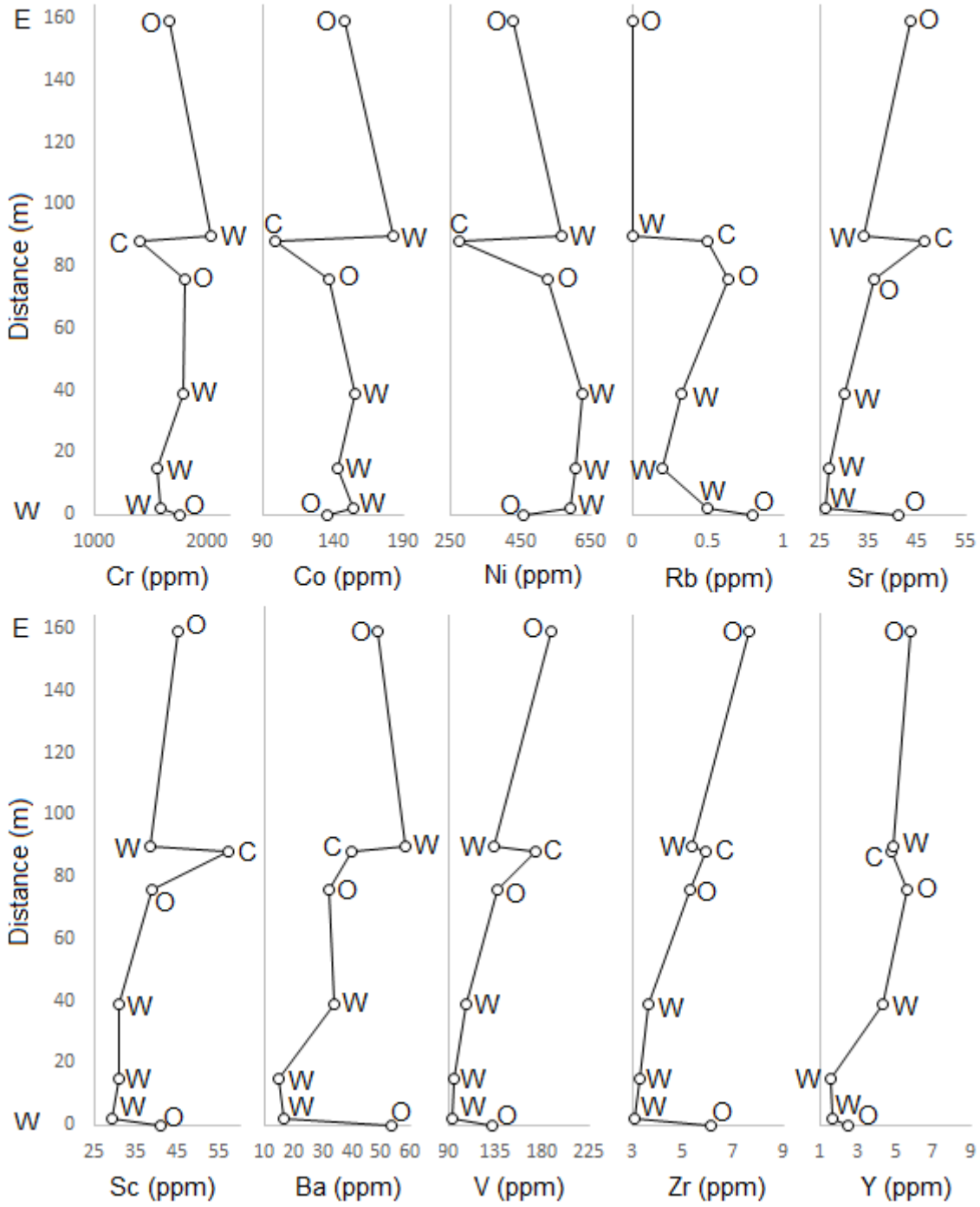

Figure 5.8: Variation in concentration of selected trace elements along a west (W) to east (E) transect across the wehrlite-clinopyroxenite sill of KC. C = clinopyroxenite; O = olivine clinopyroxenite; W = wehrlite.

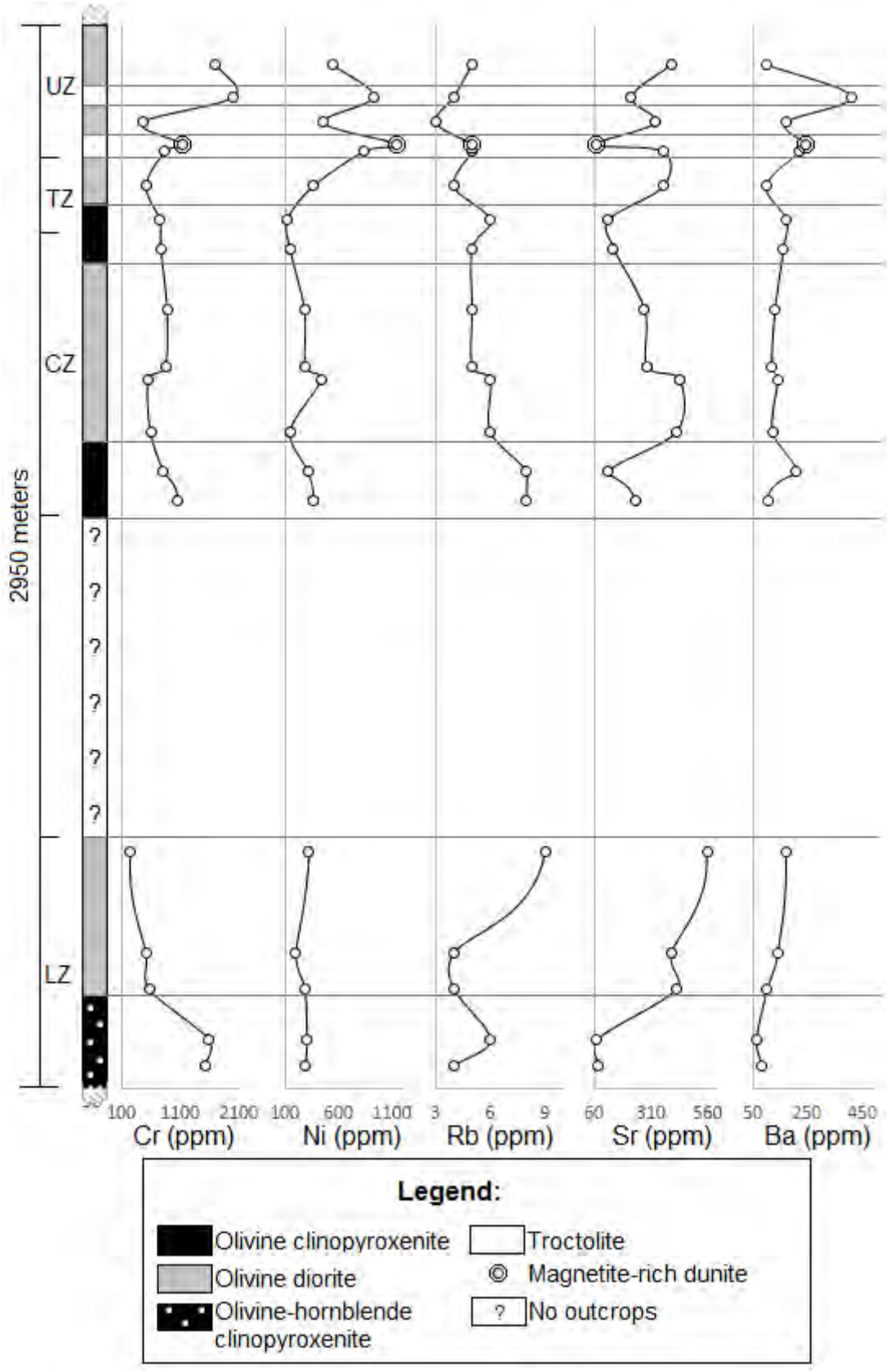

Figure 5.9: Chemical profile perpendicular to strike of the layered RietC, showing the variation in concentration of selected trace elements. LZ: Lower Zone; CZ: Central Zone; TZ: Transitional Zone; UZ: Upper Zone.

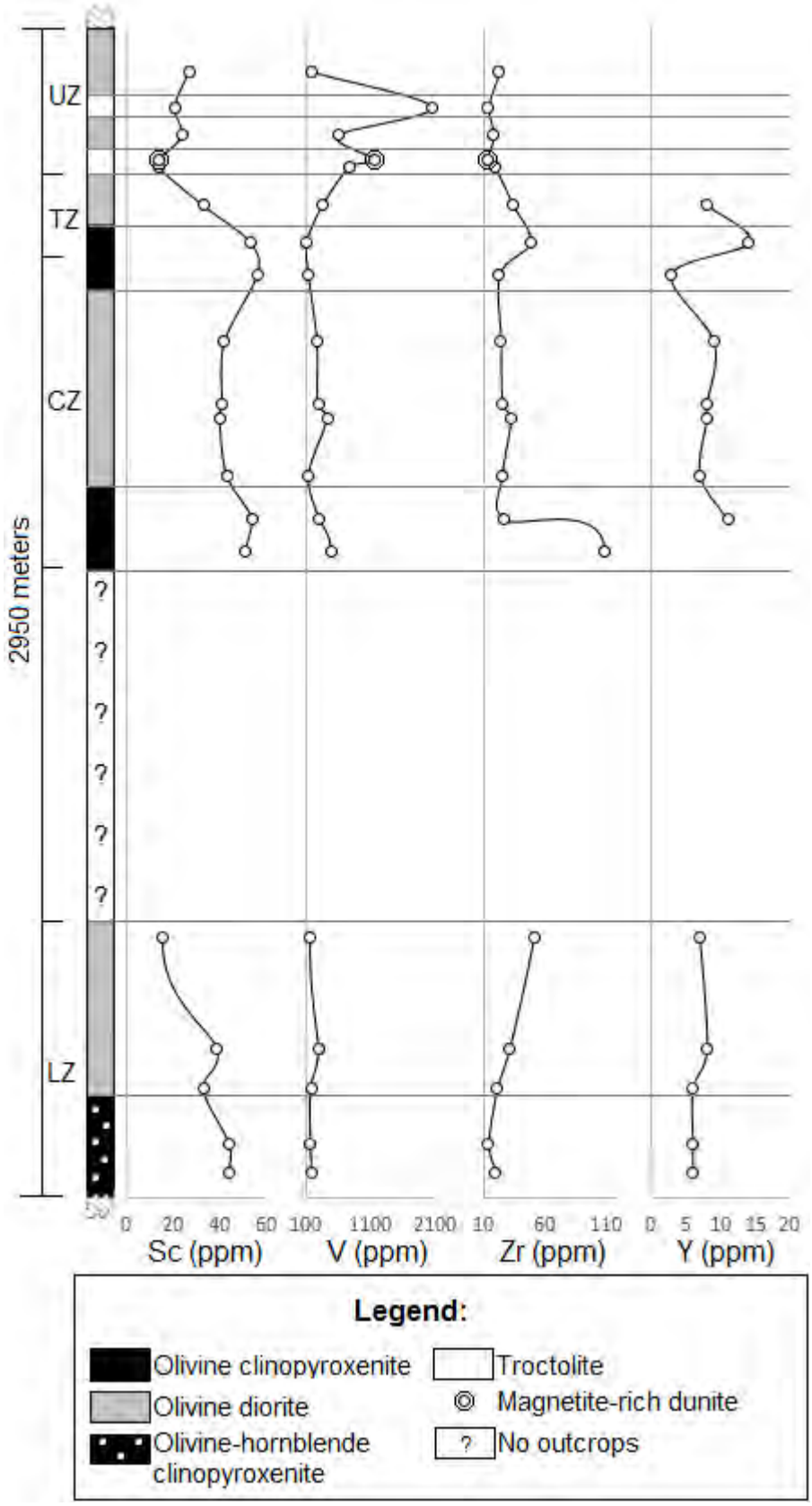

Figure 5.10: Chemical profile perpendicular to strike of the layered RietC, showing the variation in concentration of selected trace elements. LZ: Lower Zone; CZ: Central Zone; TZ: Transitional Zone; UZ: Upper Zone.

- Winddam wehrlite (Figures 5.6 and 5.7)

Cr concentrations are very high with an average of 2067 ± 709 parts per million (ppm). Because augite dominates the modal mineralogy of Ww, Cr should be compatible with the rock. This implies that Cr should decrease during crystallisation. Cr generally increases across the north to south transect, while it generally increases from west to east across the intrusion, with some inconsistencies along the way. The olivine-hornblende gabbronorite had a much higher Cr concentration of 3042 ppm compared to the average of the ultramafic rocks.

- Koedoesfontein Complex (Figure 5.8)

A very high Cr concentration is recorded for the wehrlite-clinopyroxenite from KC with an average of 1700 ± 188 ppm. Cr concentrations are generally consistent across the sill, with a drop in the Cr concentration observed near its mid-section. In contrast to what one might expect, the Cr concentration does not correlate well with the modal abundance of augite. Areas where the Cr concentration is lower, is thus more likely to indicate a more evolved composition of the parental melt and bears little relation to the mineralogy.

A slightly lower Cr average of 1552 ± 834 ppm is recorded in the enstatite-bearing rocks due to its lower abundance of pyroxene. The diorite had a low Cr concentration of 113, reflecting its lower pyroxene content and more evolved nature.

- Rietfontein Complex (Figure 5.9)

The average Cr concentration in the olivine (± hornblende) clinopyroxenite is relatively high (1081 ± 376 ppm), lower in the diorite (596 ± 195 ppm), and highest in the troctolite-dunite (1332 ± 601 ppm). It shows significant variation across the Lower Zone as a sudden decrease in the Cr content is observed across the first olivine clinopyroxenite to olivine diorite boundary due to a decrease in the modal augite content. In the Main and Transitional Zones, its concentration remains relatively constant with some minor variations. In the Upper Zone, the highest concentrations are recorded, which correlates well with the abundance of magnetite in some of these layers.

5.1.2.2 Cobalt

Co is generally incompatible with plagioclase (Bèdard, 2006) and clinopyroxene (Bèdard, 2014) while the D value is close to unity for orthopyroxene (Bèdard, 2007) in Mg-rich rocks. References within Rollinson (1993) state that Co is compatible with olivine and hornblende.

- Winddam wehrlite (Figures 5.6 and 5.7)

Due to contrasting D values mentioned for different minerals within Ww, it is difficult to state with any certainty whether it is compatible with the whole rock. On average, Ww contained 123 ± 15 ppm Co, and the concentration of this trace element remained relatively uniform across both transects. Co was not determined for the olivine-hornblende gabbronorite.

- Koedoesfontein Complex (Figure 5.8)

An average cobalt concentration of 144 ± 24 ppm is recorded in the wehrlite-clinopyroxenite sill from KC. The Co concentration follows a similar pattern as Cr across the sill and is generally more abundant where olivine is more plentiful due to its compatibility with this mineral.

The enstatite-bearing rocks have a lower Co composition of 92 ± 16 ppm due to the absence of olivine in these rock types. Despite the absence of both olivine and enstatite in the diorite, this sample had an intermediate Co concentration of 128 ppm.

- Rietfontein Complex

Co was not analysed for CB samples in RietC.

5.1.2.3 Nickel

Ni is highly compatible with olivine (Bèdard, 2005; Rollinson, 1993), but straddles the boundary between being compatible or incompatible for clino- and orthopyroxene (Bèdard, 2007; 2014). Ni tends to be compatible with hornblende and highly compatible with magnetite in basaltic liquids (Rollinson, 1993).

- Winddam wehrlite (Figures 5.6 and 5.7)

The average Ni concentration is 395 ± 74 ppm. According to its geochemical behaviour, Ni should be compatible with the ultramafic rocks from Ww, and a general decrease in its concentration is expected during crystallisation. Over the north to south transect, Ni increases slightly, while no trend of increase or decrease can be observed over the west to east transect, although some variation does occur within the intrusion. The Ni concentration is significantly higher in the olivine-hornblende gabbronorite (898 ppm).

- Koedoesfontein Complex (Figure 5.8)

A high average concentration of 512 ± 117 ppm is recorded in the wehrlite-clinopyroxenite from KC and owes its abundance to the high modal olivine content some of these rocks possess. The Ni content across the sill follows a similar pattern as the modal olivine abundance (compare Figure 4.6 with 5.8). An initial rise is observed in the Ni content from west to east, after which it generally decreases further east across the sill. Near its centre, Ni concentrations drop which is associated with the low abundance of olivine in this section.

Ni concentrations are lower in the enstatite-bearing rocks with an average of 339 ± 186 ppm due to the lack of olivine. The diorite has a much lower Ni concentration of 39 ppm which attributed to its more evolved composition and absence of olivine.

- Rietfontein Complex (Figure 5.9)

In RietC, the average Ni concentration is 258 ± 100 ppm in the olivine (± hornblende) clinopyroxenite, 292 ± 90 ppm in the olivine diorite, and 974 ± 157 ppm in the troctolite-dunite. Little variation of this trace element in observed in the Lower Zone. In the Central Zone, Ni correlates well with the modal abundance of olivine, which caused the variation observed in Ni concentrations across this part of the Complex. In the Upper Zone, Ni is conserved in both magnetite and olivine, which leads to greater Ni concentrations in the magnetite-rich troctolite layers. The magnetite-rich dunite contains the most Ni due to the great abundance of both magnetite and olivine here.

5.1.2.4 Rubidium

According to Rollinson (1993), Rb is highly incompatible with all the abundant minerals (olivine, orthopyroxene, clinopyroxene, plagioclase, hornblende, and magnetite) that are found in Ww, RietC, and KC, and should increase during crystal fractionation.

- Winddam wehrlite (Figures 5.6 and 5.7)

A low average of 1.4 ± 0.6 ppm Rb is recorded for Ww. Over the north to south transect, variations in Rb is insignificant. From west to east, slightly more variation occurred, but with no clear signs of either enrichment or depletion of this trace element. The olivine-hornblende gabbronorite has a higher Rb concentration of 11 ppm.

- Koedoesfontein Complex (Figure 5.8)

The wehrlite-clinopyroxenite sill from KC possesses a very low average Rb concentration of 0.37 ± 0.29 ppm. Rb concentrations are very low in the eastern part of the sill. Rb concentrations initially decrease in an eastern direction across the three most western samples collected and increase thereafter towards the center of the sill.

The enstatite-bearing rocks have a significantly higher average Rb concentration of 23 ± 16 ppm, while the diorite had an intermediate Rb concentration of 6.2 ppm.

- Rietfontein Complex (Figure 5.9)

The average Rb concentration recorded in RietC is 6.2 ± 1.6 ppm in the olivine (± hornblende) clinopyroxenite, 5.4 ± 1.7 in the olivine diorite, and 4.7 ± 0.6 ppm in the troctolite-dunite. In the Lower Zone, Rb concentrations increase initially in the basal olivine-hornblende clinopyroxenite, but drops across the boundary to the olivine diorite. Thereafter, Rb increases towards the top of the Lower Zone olivine diorite layer. Across the Main and Transitional Zone, Rb concentrations generally decrease, while some variation occurs in between. In the Upper Zone, the highest Rb concentrations are recorded in the first troctolite layer and the magnetite-rich dunite, followed by a drop in concentration across the second, magnetite-rich troctolite. This is followed by a gradual rise in Rb concentrations in the two uppermost samples.

5.1.2.5 Strontium

In mafic igneous rocks, Sr is compatible with plagioclase, while it is incompatible with the mafic minerals olivine, enstatite, augite, and hornblende (Rollinson, 1993).

- Winddam wehrlite (Figures 5.6 and 5.7)

Average Sr concentrations are relatively low (61 ± 20 ppm). Because plagioclase is virtually absent in Ww, it is treated as an incompatible element and its concentration is expected to increase during crystal fractionation. Sr has relatively uniform concentrations across the north to south transect, except for a sudden increase in the most southern sample. This might indicate that the melt was more evolved towards the south of the intrusion. Over the west to east transect, Sr concentrations are also consistent, except for some enrichment in the central region of Ww. The olivine-hornblende gabbronorite has a slightly higher Sr concentration of 78 ppm due to its higher modal abundance of plagioclase.

- Koedoesfontein Complex (Figure 5.8)

A very low average of Sr is recorded in the wehrlite-clinopyroxenite samples from KC of 36 ± 8 ppm. Sr concentrations initially plummet from west to east across the wehrlite-clinopyroxenite sill, after which it gradually increases across the remainder of the intrusion. A spike in the Sr concentration is observed near the centre of the sill. Because Sr is incompatible with all phases present in the olivine-clinopyroxenite, this indicates a more generally more evolved composition of the sill towards its eastern direction.

A significantly higher average Sr concentration of 167 ± 41 ppm is recorded in the enstatite-bearing rocks due to its compatibility with plagioclase. A very high Sr concentration of 744 ppm is recorded in the diorite.

- Rietfontein Complex (Figure 5.9)

In the case of Sr in RietC, the average concentration is 288 ± 152 ppm in the olivine (± hornblende) clinopyroxenite, 397 ± 87 ppm in the olivine diorite, and 220 ± 145 ppm in the troctolite-dunite. Sr is generally more abundant in the olivine diorite due to the presence of plagioclase. The olivine clinopyroxenite in the Central and Transitional Zone typically contains more Sr than those in the Lower Zone. This is due to the presence of intercumulus plagioclase in the ultramafic rocks of the Central and Transitional Zone, while plagioclase is virtually absent in those of the Lower Zone. In the Upper Zone, Sr concentrations are comparable to those observed in the olivine diorite of the Central Zone. An exception is the low Sr concentration of the magnetite-rich dunite, which contains relatively few feldspars.

5.1.2.6 Barium

Ba is highly incompatible with all minerals that make up Ww, KC, and RietC (Rollinson, 1993).

- Winddam wehrlite (Figures 5.6 and 5.7)

The average Ba concentration in ultramafic rocks from Ww is 31 ± 18 ppm. As is the case with many other elements recorded in Ww, no clear increase or decrease in Ba could be observed across either transect, but its concentration was more variable. The most eastern sample collected had a much higher Ba concentration compared to the remainder of the intrusion. In the olivine-hornblende gabbronorite, the concentration is significantly higher (115 ppm), possibly hinting at a more evolved composition of this rock type.

- Koedoesfontein Complex (Figure 5.8)

An average of 37.4 ± 16.1 ppm Ba is recorded in the wehrlite-clinopyroxenite. Its concentration initially decreases from west to east across the sill, after which it increases towards its approximate centre. Thereafter, the concentration decreases slightly towards the most eastern sample collected.

The enstatite-bearing rocks contain a much higher average Ba concentration of 135 ± 53 ppm which is attributed to its more evolved nature. For the same reason, the diorite contains a very high Ba concentration of 1392 ppm.

- Rietfontein Complex (Figure 5.9)

The average Ba concentration for RietC is 133 ± 57 ppm in the olivine (± hornblende) clinopyroxenite, 129 ± 23 ppm in the olivine diorite, 292 ± 103 ppm in the troctolite-dunite. The Ba content generally increases with stratigraphic height across the Lower Zone of the RietC. Over the Main and Transitional Zones, an inconspicuous trend of Ba enrichment is observed, while some variation occurs in between. In the Upper Zone, Ba tends to correlate well with the magnetite content of the rocks, being most abundant in those with the most magnetite.

5.1.2.7 Scandium

Sc is incompatible with plagioclase (Rollinson, 1993), olivine (Bèdard, 2005) and enstatite (Bèdard, 2007), especially at high MgO contents, but generally compatible with augite (Bèdard, 2014) and hornblende (Rollinson, 1993).

- Winddam wehrlite (Figures 5.6 and 5.7)

Average Sc concentrations are relatively high, and are recorded as 48 ± 4 ppm. Since clinopyroxene and hornblende dominate the modal composition of Ww, Sc is expected to be compatible with the whole-rock and should decrease in the melt during crystallisation. However, both the north to south and west to east transect reveals no trend of Sc enrichment or depletion, and is remarkably consistent. A lower Sc concentration of 27 ppm is present in the olivine-hornblende gabbronorite and is most likely a product of its lower augite content compared to the ultramafic rocks.

- Koedoesfontein Complex (Figure 5.8)

A high average Sc concentration of 39 ± 9 ppm is recorded in the wehrlite-clinopyroxenite samples. The variation in the Sc concentration across the wehrlite-clinopyroxenite sill is similar to that observed for Sr. Overall, the Sc concentration follows a similar pattern as the augite content of the sill because of its compatibility with this mineral.

The enstatite-bearing rocks have a similar Sc concentration as the wehrlite-clinopyroxenite samples of 38 ± 4 ppm. The diorite is also indistinguishable in terms of its Sc concentration of 39 ppm.

- Rietfontein Complex (Figure 5.10)

Average Sc concentrations are high in the olivine (± hornblende) clinopyroxenite of RietC (50 ± 5 ppm), slightly lower in the olivine diorite (36 ± 9 ppm), and very low in the troctolite-dunite (16 ± 4 ppm). Its association with augite is clear across the RietC profile, with the ultramafic rocks always displaying higher concentrations of Sc than the olivine diorite. In the Upper Zone, Sc concentrations are lower relative to the rest of the Complex due to the lower abundance of augite in these layers.

5.1.2.8 Vanadium

Mineral phases with which V is compatible are hornblende, augite, and especially magnetite, while it is incompatible with olivine, enstatite, and plagioclase (Rollinson, 1993).

- Winddam wehrlite (Figures 5.6 and 5.7)

Average V concentrations in Ww are 231 ± 50 ppm, which is typical of relatively primitive mafic/ultramafic rocks. Because of its geochemical behaviour, V is expected to be compatible with the whole rock and will be depleted during crystallisation. No such trend is observed over the north to south transect, as V concentrations stay constant. Some depletion in V is observed over the west to east transect, with some variation in between. In the olivine-hornblende gabbronorite, a lower V concentration of 174 is recorded, which is attributed to its lower augite and magnetite content.

- Koedoesfontein Complex (Figure 5.8)

Low V concentrations are recorded in the wehrlite-clinopyroxenite with an average of 133 ± 35 ppm. The variation in the V concentration follows a similar pattern as Sc as well as the augite content of the sill because of this element's compatibility with this mineral.

The enstatite-bearing rocks have a slightly higher average V concentration of 182 ± 30 ppm while the diorite had a high V concentration of 442 ppm, likely because of its higher modal magnetite abundance.

- Rietfontein Complex (Figure 5.10)

The average V concentration in the olivine (± hornblende) clinopyroxenite is recorded as 242 ± 141 ppm, 272 ± 101 ppm, while an exceptionally high V concentration is recorded in the troctolite-dunite of 1337 ± 650 ppm. Probably because of the scarcity of magnetite, V concentrations are relatively low in the Lower Zone and majority of the Central Zone, with no clear sign of either increase of depletion. However, in the Transition Zone, V concentrations rise as the abundance of magnetite increases to yield rocks with very high V concentrations in the Upper Zone. The uppermost sample displayed very low V concentrations as magnetite crystallisation terminates.

5.1.2.9 Zirconium

Zr is highly incompatible with all mineral phases present in Ww, KC, and RietC (Rollinson, 1993).

- Winddam wehrlite (Figures 5.6 and 5.7)

Zr concentrations were low with an average of 8.5 ± 2.8 ppm. Zr shows a small increase towards the south of the intrusion, implying that the melt might have had a more evolved composition in that region. Across the west to east transect, no considerable increase or decrease in its concentration is observed. Zr concentrations are significantly higher in the olivine-hornblende gabbronorite, hinting at a more evolved composition for this rock type.

- Koedoesfontein Complex (Figure 5.8)

A low average Zr concentration of 5.0 ± 1.6 ppm is recorded in the wehrlite-clinopyroxenite sill. The variation in the Zr concentration also follows a similar trend to that of Sr, Sc, and V. Because it is incompatible with all mineral phases of the wehrlite-clinopyroxenite sill, its higher concentration in the eastern parts of the sill indicates that it has a more evolved composition than the western parts.

A much higher average Zr concentration (31 ± 14 ppm) is recorded in the enstatite-bearing rocks, and probably indicates a more evolved composition of the parental magma from which it crystallised. The diorite had the highest Zr concentration of 40 ppm for the same reason.

- Rietfontein Complex (Figure 5.10)

RietC displays an average Zr concentration of 40 ± 36 ppm in the olivine (± hornblende) clinopyroxenite, 30 ± 9 in the olivine diorite, and 15 ± 3 ppm in the troctolite-dunite. From the bottom upwards, Zr concentrations show a general and gradual increase in the Lower Zone. The lowermost olivine clinopyroxenite of the Central Zone displays the highest Zr concentrations near its observable base, which drastically plummets as one progresses to the next sampling point in the profile. Hereafter, Zr concentrations remained relatively constant for the remainder of the Central Zone, but spikes again in the Transitional Zone. From this point upwards, its concentration decreases, with the lowest concentrations of Zr recorded in the Upper Zone.

5.1.2.10 Yttrium

Y is incompatible with all minerals observed in Ww, KC, and RietC (Rollinson, 1993; Bèdard, 2005; 2007; 2014).

- Winddam wehrlite (Figures 5.6 and 5.7)

Average Y concentrations are low at 2.9 ± 0.7. No trend of enrichment or depletion is observed in Y contents over both transects, and while some variation occurs over the west to east transect, its concentration remained very consistent over the north to south one. A higher Y concentration is recorded in the olivine-hornblende gabbronorite, suggesting a more evolved composition.

- Koedoesfontein Complex (Figure 5.8)

The wehrlite-clinopyroxenite sill from KC possesses a low average Y concentration of 3.9 ± 1.7 ppm. Y concentrations generally increase from west to east across the sill. Because of its incompatible nature, this hints at a more evolved composition for the eastern part of the sill than the western part.

A higher average Y concentration of 9.8 ± 1.9 ppm is recorded in the enstatite bearing rocks. The diorite has an even higher Y concentration of 23 ppm. These higher Y concentrations are attributed to a more evolved composition of the magma from which these rocks crystallised.

- Rietfontein Complex (Figure 5.10)

Olivine (± hornblende) clinopyroxenite from RietC have a low average Y concentration of 6.7 ± 4.4 ppm. Average compositions for the olivine diorite, troctolite, and dunite cannot be given, as many samples had concentrations below that of the detection limit of the XRF. In the Lower Zone, Y concentrations tend to increase upwards in the profile. In the Central Zone, Y concentrations fall across the lower olivine clinopyroxenite to olivine diorite boundary. Thereafter it stays relatively constant, but falls again across the upper olivine diorite to olivine clinopyroxenite boundary. The value rises in the Transition Zone, then falls across the next olivine clinopyroxenite to olivine diorite boundary. All remaining samples further up in the profile had Y concentrations that were below the detection limit.

5.1.3 General remarks

- Winddam wehrlite

In general, ultramafic rocks from Ww have very high concentrations of MgO and compatible trace elements, while the rocks possess very low concentrations of incompatible elements, which is a consequence of their ultramafic, cumulate nature. The southern samples from Ww show slightly elevated concentrations of incompatible elements, meaning that this section is more evolved than the northern samples. No clear trend of magmatic evolution can be observed across the west to east transect. The olivine-hornblende gabbronorite appears to be chemically more evolved than the ultramafic rocks as they possess higher incompatible element concentrations. However, its higher compatible element concentrations points to a more primitive composition. It is thus uncertain whether or not the olivine-hornblende gabbronorite should be considered more or less evolved than the ultramafic rocks from Ww.

- Koedoesfontein Complex

Similarly to Ww, ultramafic rocks from KC are characterised by very high compatible element concentrations and low incompatible element concentrations due to their ultramafic and cumulate nature. Although inconsistencies occur, the wehrlite-clinopyroxenite sill appears to be more evolved chemically in its eastern parts due to lower compatible element and higher incompatible element concentrations. The enstatite-bearing rocks and the diorite appear to be chemically more evolved than the ultramafic rocks in terms of possessing higher incompatible element and higher compatible element concentrations.

- Rietfontein Complex

The olivine (± hornblende) clinopyroxenite of RietC is also characterised by high compatible element and low incompatible element concentrations for the same reasons mentioned above. On average, the olivine diorite contains slightly lower incompatible element concentrations than the ultramafic rocks. Whether this points to a more primitive composition of the dioritic rocks compared to the ultramafic rocks is uncertain at this stage, because a significant amount of overlap in the contents of the elements occurs. The troctolite and dunite contain very low incompatible element concentrations, but significantly higher concentrations of FeO(t), TiO_2, Ni, Cr, Co, and V due to the great compatibility of these elements with magnetite.

5.2 MINERAL CHEMISTRY OF THE RIETFONTEIN COMPLEX

This section will focus on the variation in the chemical makeup of minerals from RietC in terms of their solid solution endmembers as well as the compatible trace elements Ni in olivine and Cr in augite because of their usefulness to assess magmatic evolution (see section 6.2). The variation of the solid solution endmember composition of olivine, augite, and plagioclase is shown on Figure 5.11. Variation in the Ni and Cr in olivine and augite, respectively, are shown in Figure 5.12.

5.2.1 Olivine

Olivine is divided into two primary solid solution endmembers, namely its Mg-endmember called forsterite (Fo), which has a chemical composition of Mg_2SiO_4 and a Fe-endmember called fayalite (Fa), with a chemical composition of Fe_2SiO_4 (Deer *et al*., 2013; Klein, 1994; Klein & Dutrow, 2008; Krivolutskaya & Bryanchaninova, 2011).

In RietC, the composition of the olivine varies from approximately $Fo_{64.3}$ to $Fo_{71.4}$. The Fo content in olivine initially increases upwards in the Lower Zone of RietC ($Fo_{67.9}$ to $Fo_{69.8}$) and reaches a maximum just across the olivine-hornblende clinopyroxenite to olivine diorite boundary ($Fo_{71.2}$). A lower Fo content was recorded further upward in the Lower Zone olivine diorite boundary ($Fo_{66.7}$). In the Central Zone, a slight increase in the Fo content is observed across the lowermost olivine clinopyroxenite to olivine diorite boundary ($Fo_{68.1}$ to $Fo_{68.9}$), after which it decreases slightly further upwards in the olivine diorite layer ($Fo_{67.3}$), and appears to increase again in the top olivine clinopyroxenite layer ($Fo_{68.6}$). The shift from the Central Zone to the Transitional Zone is met with a sudden decline in the Fo content ($Fo_{64.3}$),

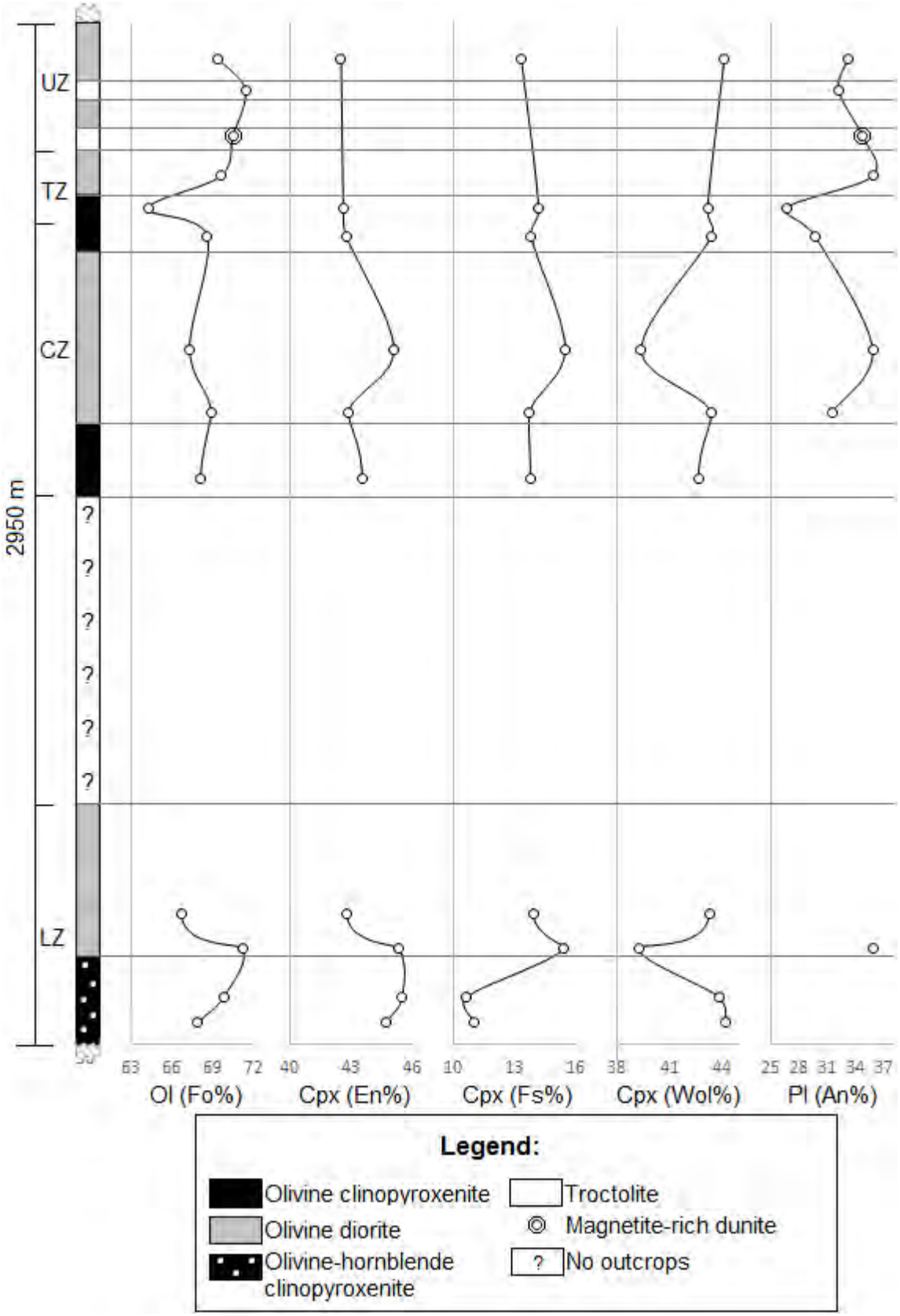

Figure 5.11: Variation in the chemical composition of olivine, augite, and plagioclase in terms of their solid solution endmembers across a profile perpendicular to the strike of the layering of RietC. LZ: Lower Zone; CZ: Central Zone; TZ: Transitional Zone; UZ: Upper Zone.

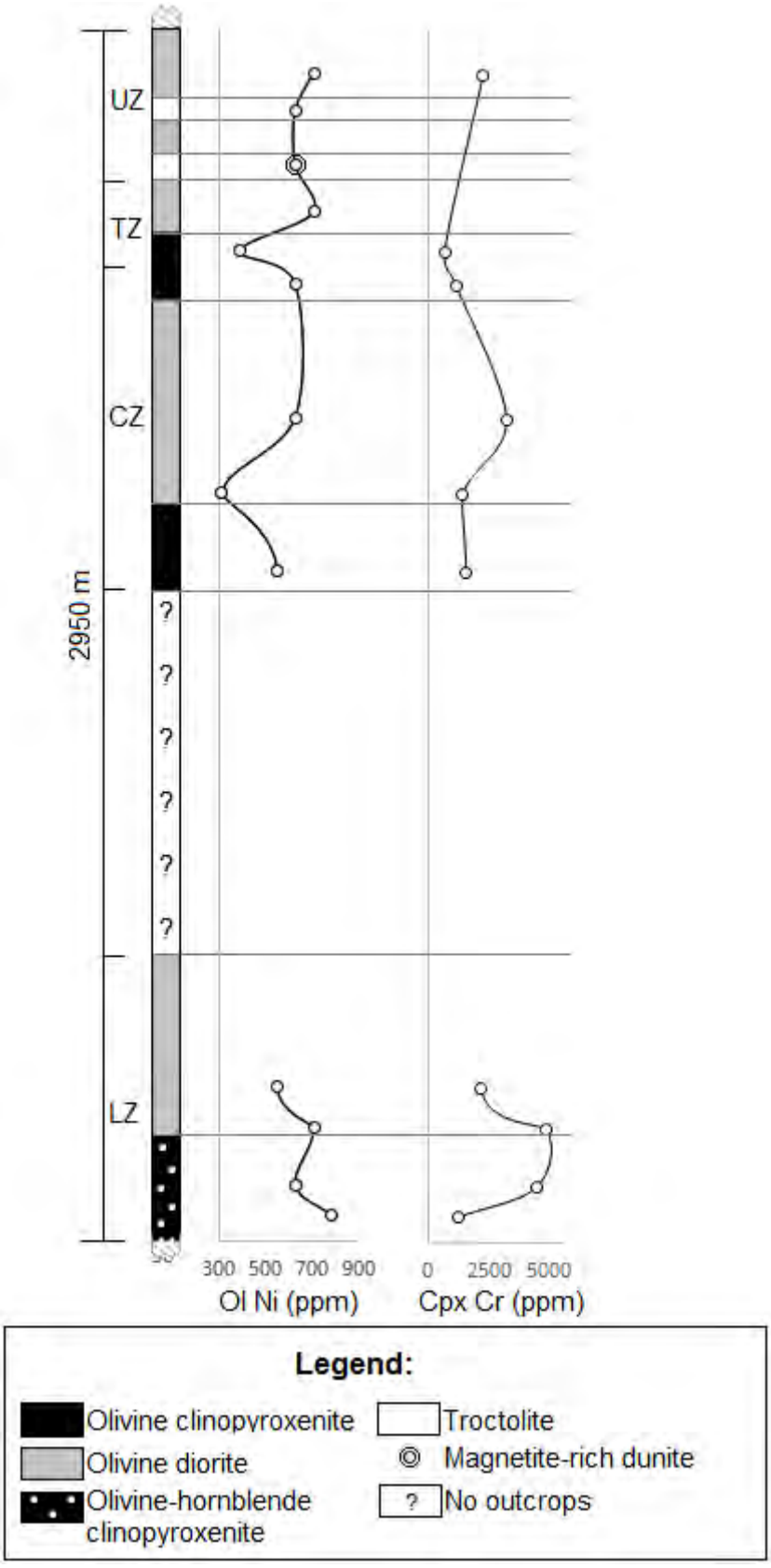

Figure 5.12: Variation in the mineral chemistry of RietC in terms of compatible trace elements detected by the electron microprobe. LZ: Lower Zone; CZ: Central Zone; TZ: Transitional Zone; UZ: Upper Zone.

followed by a rapid rise further upwards in the profile in the Transitional Zone olivine diorite ($Fo_{69.6}$). The Fo content continues to climb through the troctolite of the Upper Zone (from $Fo_{70.5}$ to $Fo_{71.4}$), and decreases slightly in the uppermost layer of olivine diorite in RietC ($Fo_{69.4}$).

Ni concentrations in olivine varied from 314 to 786 ppm (Figure 5.12). The Ni content in olivine appears to decrease upwards in the profile in the Lower Zone olivine clinopyroxenite (785 to 629 ppm), and increases across the olivine clinopyroxenite to olivine diorite boundary (707 ppm). Further upwards in the Lower Zone olivine diorite layer, the Ni concentration decreases (550 ppm). In the Central Zone, Ni concentrations initially fall across the southern olivine clinopyroxenite to olivine diorite boundary (550 to 314 ppm), and then rises further upwards in the olivine diorite layer (629 ppm). Thereafter, it stays more or less constant further upwards in the Central Zone. As with the Fo content, Ni concentrations fall across the boundary to the Transitional Zone (from 629 ppm to 393 ppm), and rises dramatically in the Transitional Zone olivine diorite (707 ppm). Ni concentrations remained relatively constant further upwards through the Upper Zone. The Ni concentrations in the magnetite-rich dunite and northern troctolite layer are both recorded as 629 ppm.

5.2.2 Augite

Augite is divided into three major solid solution endmembers, namely enstatite (En, $MgSiO_3$), ferrosilite (Fs, $FeSiO_3$), and wollastonite (Wo, $CaSiO_3$) (Deer *et al*., 2013; Klein, 1994; Klein & Dutrow, 2008).

The range in composition of augite in RietC is $En_{42.5\text{-}45.5}$, $Fs_{10.7\text{-}15.5}$, and $Wo_{39\text{-}44}$. Similar to the Fo content of olivine, the En content of augite increases upwards in the layer of olivine clinopyroxenite ($En_{44.7}$ to $En_{45.5}$) in the Lower Zone of RietC; remains relatively constant across the boundary to olivine diorite ($Fo_{45.3}$); and decreases further upwards in the olivine diorite layer ($En_{42.79}$). A low Fs content is recorded in the olivine-hornblende clinopyroxenite of the Lower Zone and appears to decrease slightly upward within this rock type ($Fs_{11.0}$ to $Fs_{10.7}$). In the olivine diorite, the Fs content spikes ($Fs_{15.4}$), then continues to decrease further upward in this rock type ($Fs_{13.9}$). In contrast, a high Wo content was recorded in the Lower Zone olivine-hornblende clinopyroxenite, which slightly decreases further upwards in this rock type ($Wo_{44.3}$ to $Wo_{43.9}$), and plummets across the boundary to the olivine diorite ($Wo_{39.3}$). Thereafter, a sharp increase in the Wo content is observed further upwards in the olivine diorite of the Lower Zone ($Wo_{43.3}$).

In the Central Zone, both the En and Fs content of the augite follow a very similar pattern; a very small decrease is observed across the boundary from the southern olivine clinopyroxenite to olivine diorite ($En_{43.6}$ to $En_{42.9}$ and $Fs_{13.8}$ to $Fs_{13.7}$), then it increases in the central part of the Central Zone olivine diorite ($En_{45.1}$ and $Fs_{15.5}$), and decreases again across the northern olivine diorite to olivine clinopyroxenite boundary ($En_{42.8}$ and $Fs_{13.8}$). The Wo content follows a contrasting pattern; it increases slightly across the southern boundary between olivine clinopyroxenite to olivine diorite ($Wo_{42.7}$ to $Wo_{43.4}$), decreases further upwards in the olivine diorite layer ($Wo_{39.4}$), and increases again across the northern olivine diorite to olivine clinopyroxenite boundary ($Wo_{43.4}$).

Across the boundary to the Transitional Zone, the En content stays relatively constant ($En_{42.6}$), while a small increase and decrease is observed for Fs ($Fs_{14.2}$) and Wo ($Wo_{43.2}$), respectively. No data is available to assess the change in clinopyroxene composition across the remainder of the Transitional- and Upper Zones. In comparison to the rest of the complex, the clinopyroxene in the uppermost layer of olivine diorite contained an En content similar to that recorded in the Transitional Zone ($En_{42.5}$), the Fs content was slightly lower ($Fs_{13.}$), while a higher Wo content was recorded in this rock layer ($Wo_{44.1}$).

Cr concentrations in clinopyroxene showed significant variation from 684 up to 4858 ppm. The Cr concentration of clinopyroxene increases upwards in the Lower Zone olivine clinopyroxenite (1232 to 4447 ppm), reaching the highest recorded Cr concentration in RietC just across the boundary to the olivine diorite (4858 ppm), after which it decreases further upwards in the olivine diorite layer (2189 ppm). The southern transition from olivine clinopyroxenite to olivine diorite in the Central Zone is met with a small decrease in the clinopyroxene's Cr concentration (1574 to 1437 ppm). This is followed by a significant increase in the Cr concentration further up in the olivine diorite layer (3216 ppm), while the concentration dramatically decreases across the boundary to the northern olivine clinopyroxenite (1163 ppm). A further decrease is experienced across the boundary to the Transitional Zone (684 ppm). In the uppermost olivine diorite layer, a Cr concentration of 2258 ppm is recorded.

5.2.3 Plagioclase

Plagioclase solid solution series is divided into two major solid solution endmembers, namely albite (Ab, $NaAlSi_3O_8$) and anorthite (An, $CaAl_2Si_2O_8$) (Klein & Dutrow, 2008).

In RietC, plagioclase generally has a sodic composition since its An content varies from $An_{26.7}$ to $An_{35.8}$. No plagioclase grains are present in the Lower Zone olivine-hornblende

clinopyroxenite of RietC, and the variation in the An content in plagioclase of the Lower Zone could not be assessed since only one sample (CB3) was analysed here. Nevertheless, the recorded An content is $An_{35.8}$, one of the two highest An contents recorded in the intrusion.

No data regarding the plagioclase composition is available in the southern olivine clinopyroxenite of the Central Zone. In the Central Zone olivine diorite, An contents appear to increase from the bottom of this layer towards its centre ($An_{31.5}$ to $An_{35.8}$). A decrease in the An content is observed across the olivine diorite to olivine clinopyroxenite boundary ($An_{29.7}$). Across the boundary to the Transitional Zone, a further decrease in the An content is observed ($An_{26.7}$), after which it rises rapidly in the Transitional Zone olivine diorite ($An_{35.8}$). Thereafter, a gradual decrease is observed further upwards across the Upper Zone magnetite-rich dunite ($An_{34.7}$) and to the northern troctolite layer ($An_{32.2}$). A small increase in the An content is observed in the final layer of olivine diorite ($An_{33.2}$).

5.3 TRENDS IN MAGMATIC EVOLUTION

Harker diagrams (also referred to as bi-variate plots) are generally considered an accurate method to identify trends in magmatic evolution (Rollinson, 1993; Wang *et al*., 2014; Winter, 2010). It also provides the opportunity to rapidly and visually compare the chemistry of Ww, KC, and RietC. This can help to determine whether or not they originated from the same primary magma (or magmas) and to assess their relative degree of magmatic evolution (see, for example, Hallis *et al*., 2014). Silica is commonly used on the x-axis of Harker diagrams as silica generally increases during magmatic evolution. However, because the silica contents of all three intrusions are relatively constant, it proved unsuitable.

Other possible choices frequently used are Zr, MgO, and Mg# (100*MgO/(MgO+FeO(t)). Due to its incompatible nature, Zr generally increases during magmatic evolution, while MgO and Mg# usually decrease. Overall, MgO gave the best fit, the clearest trends, and the least amount of scatter against the majority of elements, and is thus used on the x-axis for the majority of Harker diagrams shown below. Near the end of this section, the incompatible trace element Zr is also plotted against selected trace elements for comparison with the MgO Harker plots. In addition to the Harker diagrams, an alkali-iron-magnesium (AFM) diagram was also used to compare and assess trends in magmatic evolution.

Rocks with abundant magnetite are not plotted on the Harker diagrams because the crystallisation of this mineral causes significant deviation from the observed magmatic trends. Diorite and enstatite-bearing rocks from KC are also omitted from the Harker diagrams due to great differences in their geochemistry compared to the ultramafic rocks.

This allows for better visual comparison between the ultramafic lithologies from Ww, KC, and RietC. For the same reason, olivine-hornblende gabbronorite from Ww is not plotted on the Harker diagrams.

5.3.1 Major oxides

For the following discussion refer to Figure 5.13 for MgO and Mg# plotted against Zr and Figure 5.14 for all other major oxides plotted against MgO. Reference will not be made to these figures for the remainder of this section.

- MgO

Because MgO is used on the x-axis of all variation diagrams used in this section, it is important to highlight its features first before examining the trends of the other elements. To assess its behaviour, it was plotted against Zr. In general, MgO decreases from KC to RietC, while Ww typically has intermediate values, although there is some overlap in the MgO content of all three intrusions. In RietC, a gap in the MgO content is visible between the olivine-hornblende clinopyroxenite and olivine diorite due to the differences in mafic mineral content between these two rock types.

- Mg#

In terms of Mg#, Ww generally appears to have the most primitive composition, while KC is intermediate, and the rocks with the most evolved compositions belonged to the RietC. A significant amount of overlap occurs between all three intrusions.

- SiO_2

Little variation is seen in the silica content of all three intrusions relative to the amount of MgO. Overall, a steady increase is observed as MgO falls, which is consistent with the fractionation of Mg-bearing mafic minerals such as olivine. Considerable overlap in the SiO_2 contents of all three intrusions occurs.

- TiO_2

An exponential increase in TiO_2 is observed across all three complexes as MgO is depleted, indicating that the element is generally incompatible with the crystallising phases. While some overlap occurs, KC generally has the lowest concentration of TiO_2, while RietC has the highest in the olivine diorite.

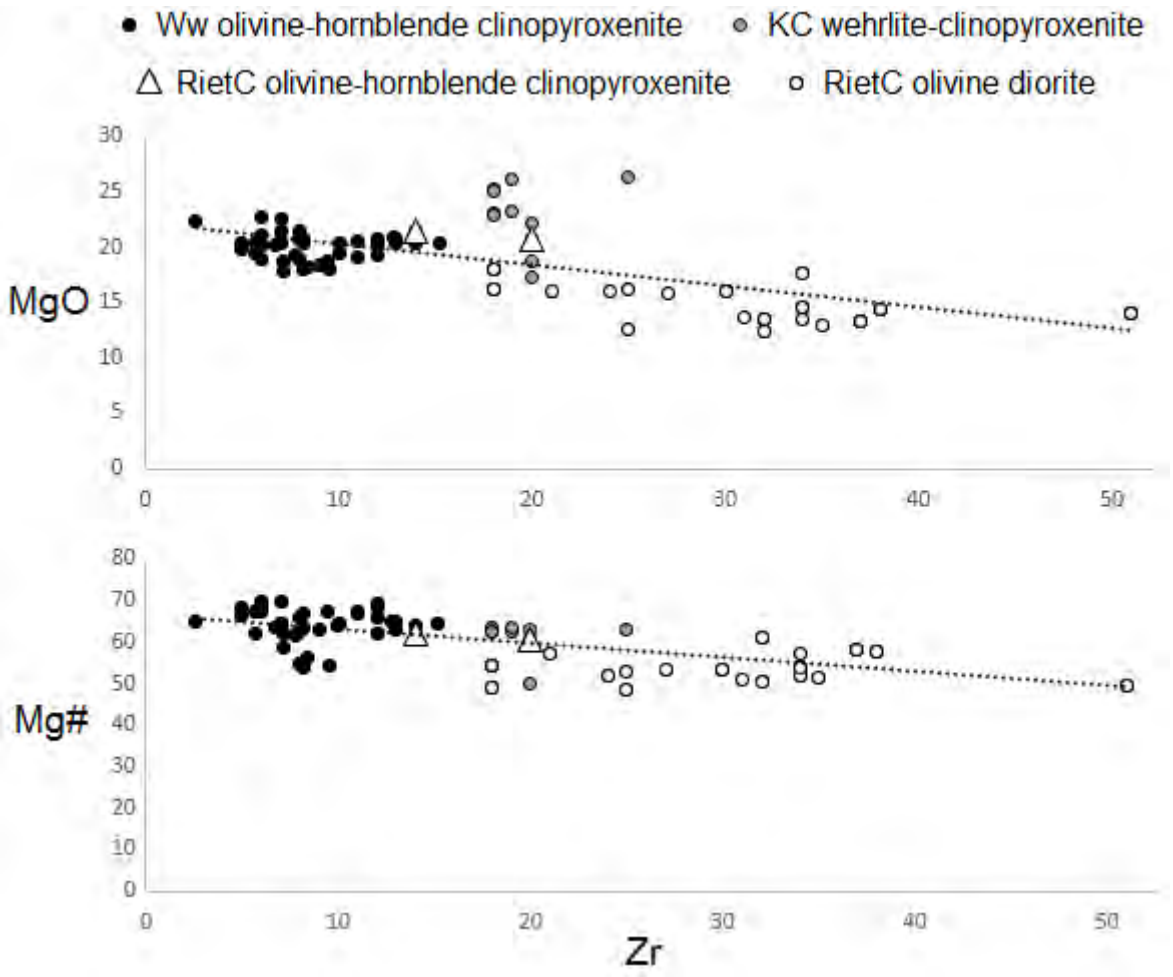

Figure 5.13: Zr plotted against MgO (wt. %) and Mg# (100*MgO/[MgO+FeO(t)]). Trend lines are shown on each Harker diagram.

- Al_2O_3

Al_2O_3's strong association with feldspar is clear on the Harker diagram. All the magnesium-rich, plagioclase-poor ultramafic rocks plot on the lower left-hand side of the diagram. An exponential rise in the Al_2O_3 content is observed as plagioclase start to crystallise in RietC olivine diorite. The presence of plagioclase in the olivine diorite and the virtual absence of this mineral in the ultramafic rocks of the three intrusions leads to the gap observed on the Harker diagram regarding the intrusions' Al_2O_3 contents. Ultramafic rocks from all three intrusions show significant overlap in terms of Al_2O_3.

- FeO(t)

FeO(t) contents show a lot of scatter, but a slight upward trend of FeO(t) enrichment has been identified as MgO is depleted which is consistent with fractional crystallisation. Ww generally show the lowest FeO(t) contents, with KC in between and RietC showing the highest FeO(t) concentrations.

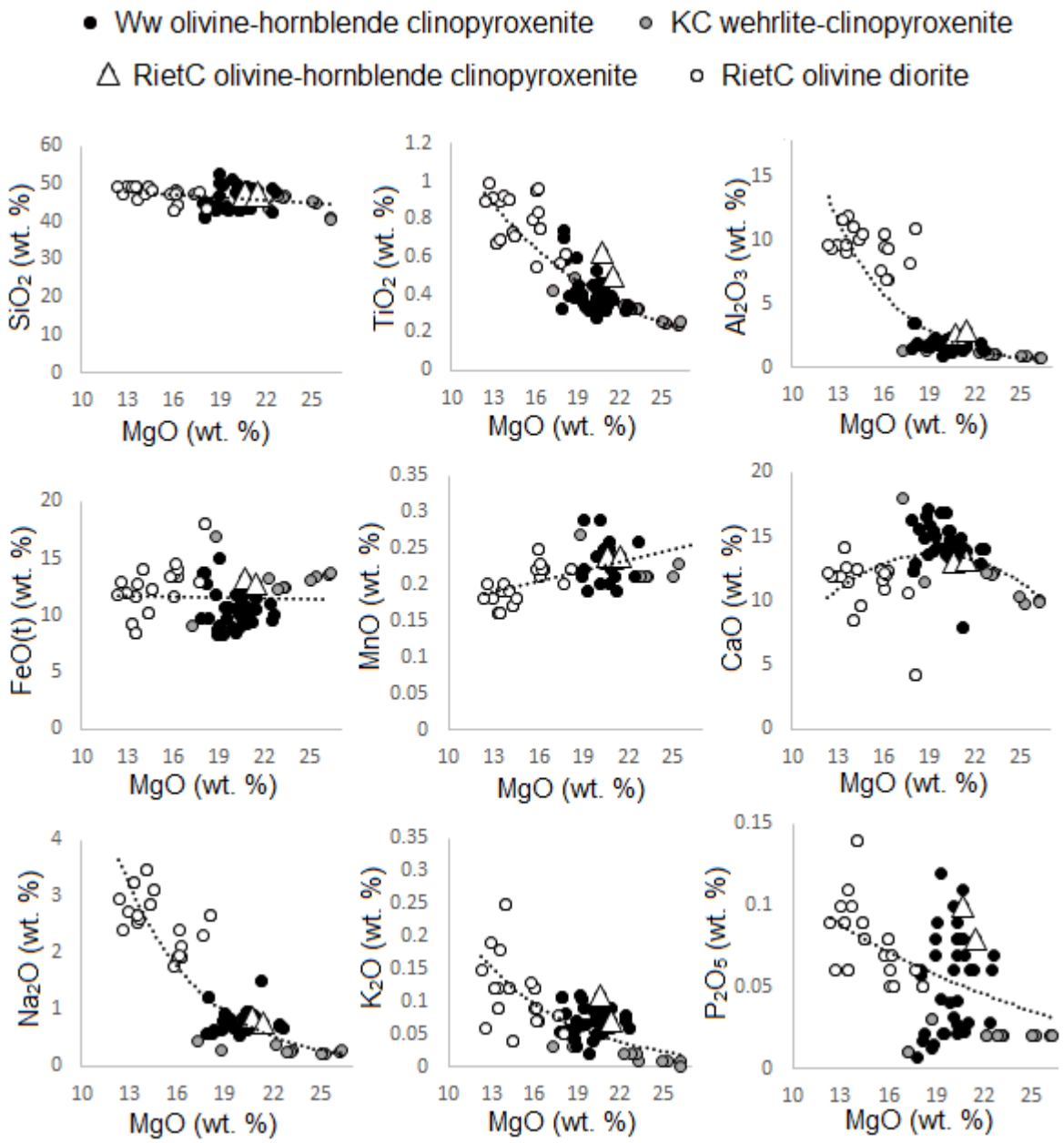

Figure 5.14: Harker diagrams of major oxides plotted against MgO. Trend lines are shown on each Harker diagram.

- MnO

MnO generally follows a linear decrease in concentration as the MgO declines. Significant overlap in the MnO concentration occurs in the three complexes (especially for the ultramafic lithologies), with the highest values of this oxide recorded in Ww, and the lowest values are recorded in the olivine diorite of RietC. Because MnO is primarily incorporated in olivine, conservation of MnO in this mineral probably led to its decrease with magmatic evolution.

- CaO

In KC and Ww, CaO increases as MgO is depleted, while RietC generally follows the opposite pattern. These variations can be explained by referring to the modal content of different rock types from Ww, KC, and RietC. Augite is the principle Ca-bearing phase in the ultramafic rocks of these intrusions. While obvious exceptions are present, the ultramafic rocks from KC generally have a lower augite content compared to ultramafic rocks from RietC and Ww (see Figure 4.3). It, therefore, also has the lowest CaO concentration. Ww generally has the highest augite content, and consequently it also has the highest CaO concentration. The olivine diorite of RietC has less augite, and the sodic composition of the plagioclase explains the low concentration of CaO in these relatively MgO-poor rocks.

- Na_2O

Na_2O increases exponentially from KC, to Ww, and to RietC with decreasing MgO content. The lower Na_2O contents of the ultramafic rocks of KC, Ww, and Lower Zone olivine-hornblende clinopyroxenite of RietC can easily be attributed to the absence of feldspar, because Na_2O would be incompatible with all the major mineral phases present in these rocks. A sudden increase in Na_2O can be seen when plagioclase-rich olivine diorite and troctolite start to crystallise.

- K_2O

K_2O generally shows an exponential increase in concentration across the intrusions as MgO is depleted. This is associated with the incompatibility of K_2O with all the minerals that make up Ww, KC, and RietC, causing it to increase as magmatic evolution proceeds.

- P_2O_5

P_2O_5 shows a significant amount of scatter. It is clear that KC generally have the lowest concentration of P_2O_5, while RietC and Ww generally have similar concentrations of this oxide. Overall, a positive upward trend is recorded for the P_2O_5 when plotted against MgO due to the incompatibility of this oxide.

5.3.2 AFM diagram

AFM diagrams are used to assess magmatic evolution of igneous rocks using three different parameters namely MgO, FeO(t), and total alkalis (Na_2O + K_2O) (see Figure 5.15). During

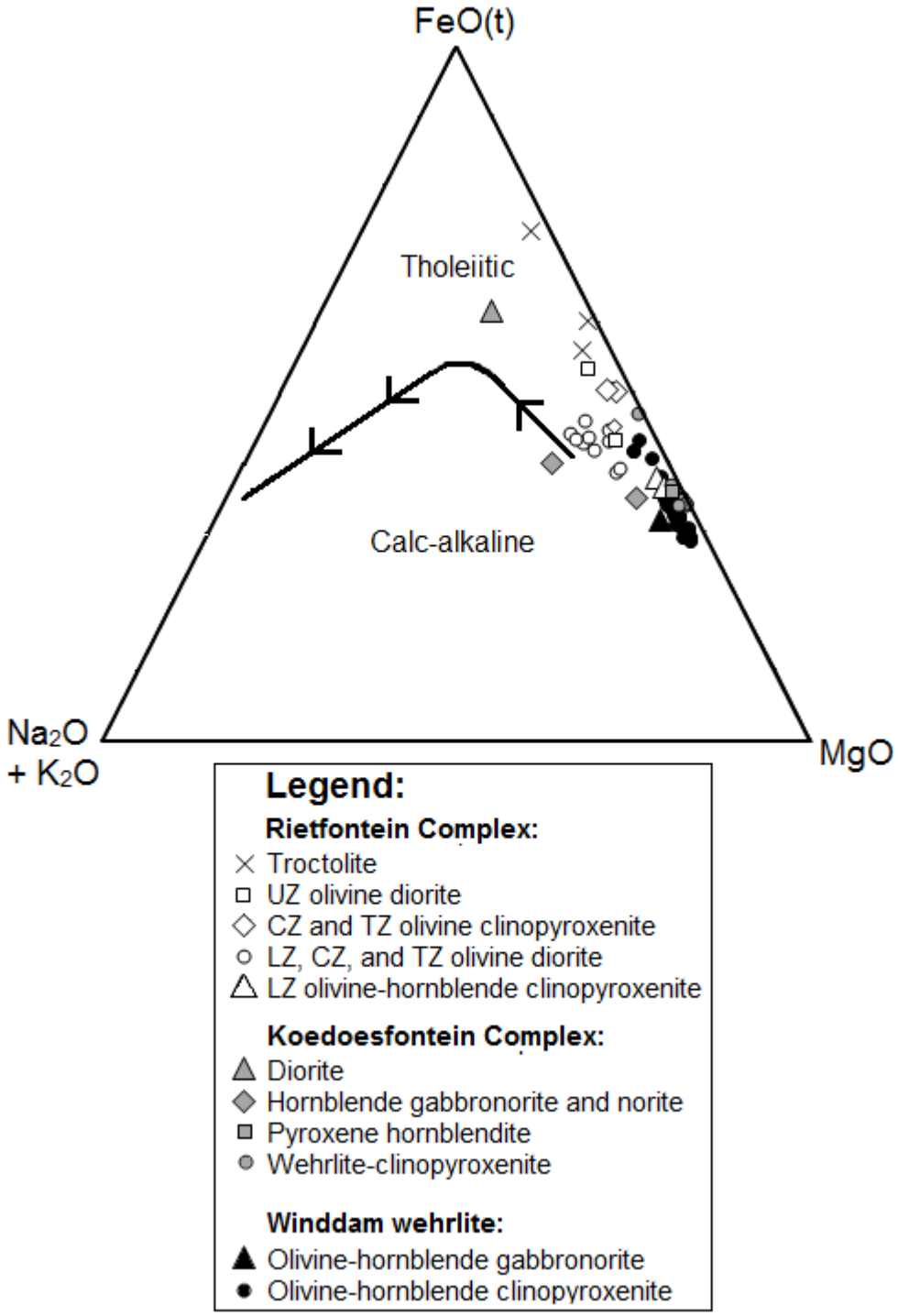

Figure 5.15: AFM ([Na_2O+K_2O]–FeOt–MgO) diagram to discriminate between tholeiitic- and calc-alkaline rocks and to model magmatic evolution.

crystallisation, the whole-rock chemistry typically follow a trend parallel to the curve separating tholeiitic and calc-alkaline rocks. In other words, melts initially experiences iron enrichment and magnesium depletion, followed by both iron and magnesium depletion and alkali enrichment. According to this generalised trend, Ww has the most primitive rocks, as they plot closer to the MgO corner of the diagram. Significant overlap occurs between the ultramafic rocks from KC, the olivine-hornblende clinopyroxenite from RietC, and the

ultramafic rocks from Ww. Overall the ultramafic rocks from all three intrusions plot in a straight line indicating iron enrichment, with the olivine clinopyroxenite from the Central and Transitional Zones of RietC being the most evolved samples. The trend of iron enrichment continues in the form of the troctolite of RietC, which plots closer to the FeO(t) corner due to their high modal abundance of magnetite.

The olivine-hornblende gabbronorite from Ww, the olivine diorite from RietC, and the hornblende gabbronorite and norite from KC have similar FeO(t) to MgO ratios as the ultramafic rocks, but deviates from the trend described above due to their higher alkali content caused by the crystallisation of plagioclase. The diorite from KC is also significantly enriched in FeO(t) and alkalis due to its high magnetite and sodic plagioclase abundance, indicating a more evolved composition.

The majority of rocks display a typical tholeiitic trend of differentiation with significant iron-enrichment that precedes alkali enrichment. The only exception is hornblende gabbronorite (sample RB3) from KC that plots in the calc-alkaline field.

5.3.3 Trace elements

Harker diagrams for selected trace elements plotted against MgO are shown in Figure 5.16. Reference would not be made to this figure for the remainder of this section.

- Cr

In all three intrusions, Cr contents decline with decreasing MgO concentrations, indicating fractionation of augite due to its compatibility with this trace element. RietC has the lowest Cr content on average, while KC is intermediate, and Ww has the highest concentrations. In terms of Cr, KC thus appears to have an intermediate composition, while RietC is generally the most evolved and Ww the most primitive. Significant overlap occurs in terms of the Cr content for the ultramafic rocks from all three intrusions. The lower Cr content of KC relative to its MgO concentration compared to RietC and Ww is attributed to its lower modal abundance of augite in some of its samples (see Figure 4.3).

- Ni

Similar to Cr, Ni is depleted during the evolution of primitive magmas due to its high compatibility with olivine. KC has significantly higher Ni concentrations compared to Ww and RietC due to its higher olivine content in some samples. Because ultramafic rocks from RietC generally had the lowest Ni content, RietC displays the most evolved composition for

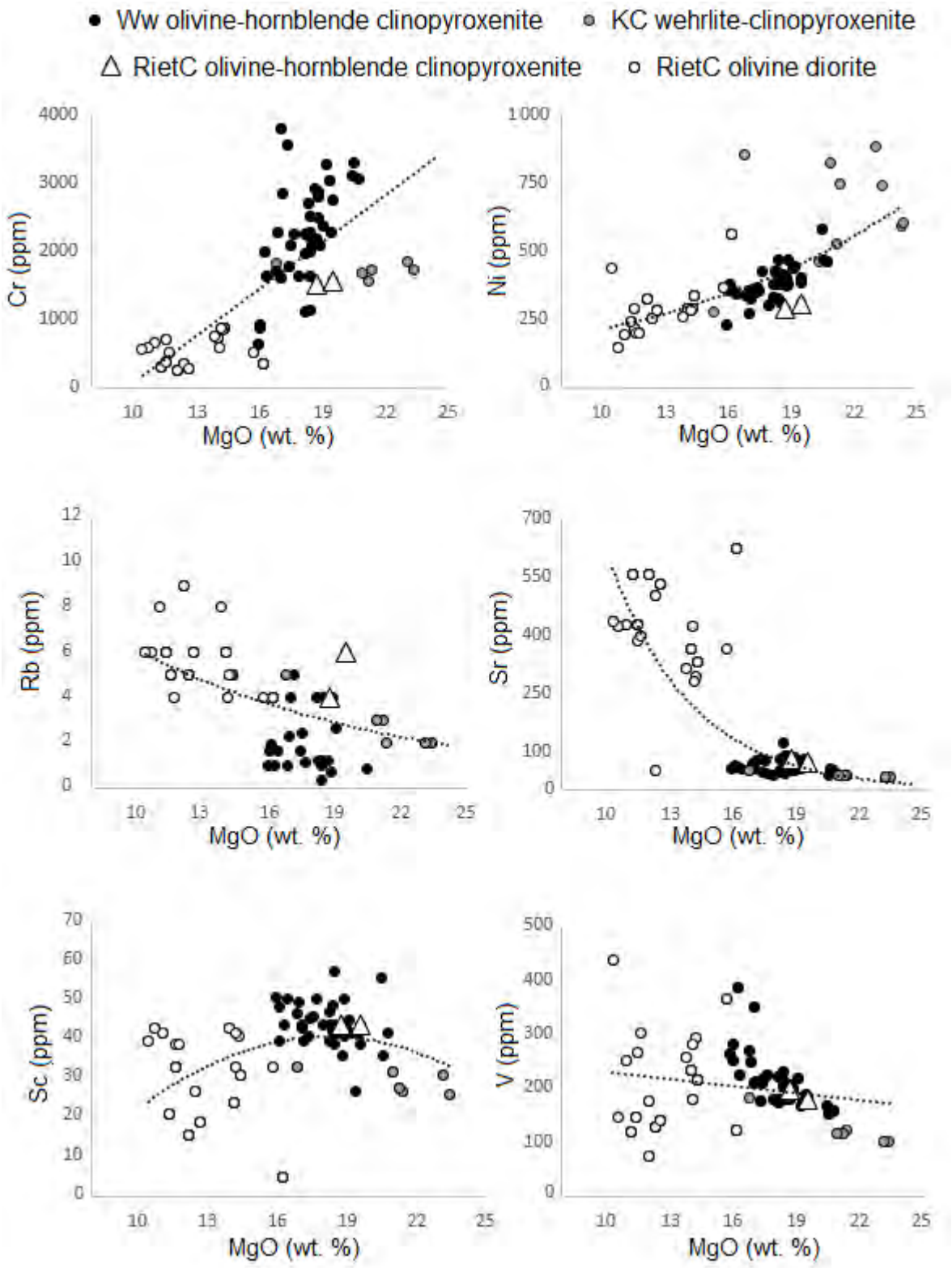

Figure 5.16: Harker diagrams of selected trace elements (Cr, Ni, Rb, Sr, Sc, and V) plotted against MgO of Ww, KC, and RietC. Trend lines are shown on each Harker diagram.

this trace element compared to Ww and KC while Ww is intermediate. Some overlap occurs again in terms of Ni for the ultramafic rocks of all three intrusions.

- Rb

Despite the large amount of scatter of Rb concentrations when plotted against MgO, a general increase in Rb concentrations can be observed with magmatic evolution. Ww contains both the highest and lowest concentrations of Rb. Most RietC samples plot above the general trend of Rb enrichment, and is thus inferred to have the most evolved composition. KC samples generally plot close to this general trend, and it proves difficult to state with any confidence whether it should be considered more or less evolved than Ww in terms of its Rb concentrations.

- Sr

This trace element's association with plagioclase is evident in the Harker diagram provided in this chapter. Because it contains more plagioclase, relatively MgO-poor olivine diorite from RietC show much greater Sr concentrations than the ultramafic rocks from KC, Ww and the Lower Zone olivine-hornblende clinopyroxenite of RietC. Ww generally show intermediate Sr concentrations, while KC has, on average, the lowest Sr values. Once again, some overlap between all three intrusions' Sr contents occurs.

- Sc

Sc shows an almost identical pattern as seen in the CaO/MgO Harker diagram. Since both Sc and CaO are strongly associated with augite, the same explanation for the variation in CaO contents discussed earlier thus applies to Sc.

- V

KC, Ww, and the Lower Zone of RietC shows a general increase in V as MgO is depleted, reflecting its general incompatibility with the common mafic silicates. The olivine diorite of RietC shows a lot of scatter in terms of V concentration, and can be attributed to variations in the modal abundance of magnetite. In terms of V, KC appears to be more primitive, Ww intermediate, and RietC the most evolved.

5.3.4 Zr versus Ni, Cr, Sr, and Y

In addition to the Harker plots discussed above, it was decided to plot the highly incompatible and immobile trace element, Zr, against two other incompatible trace elements

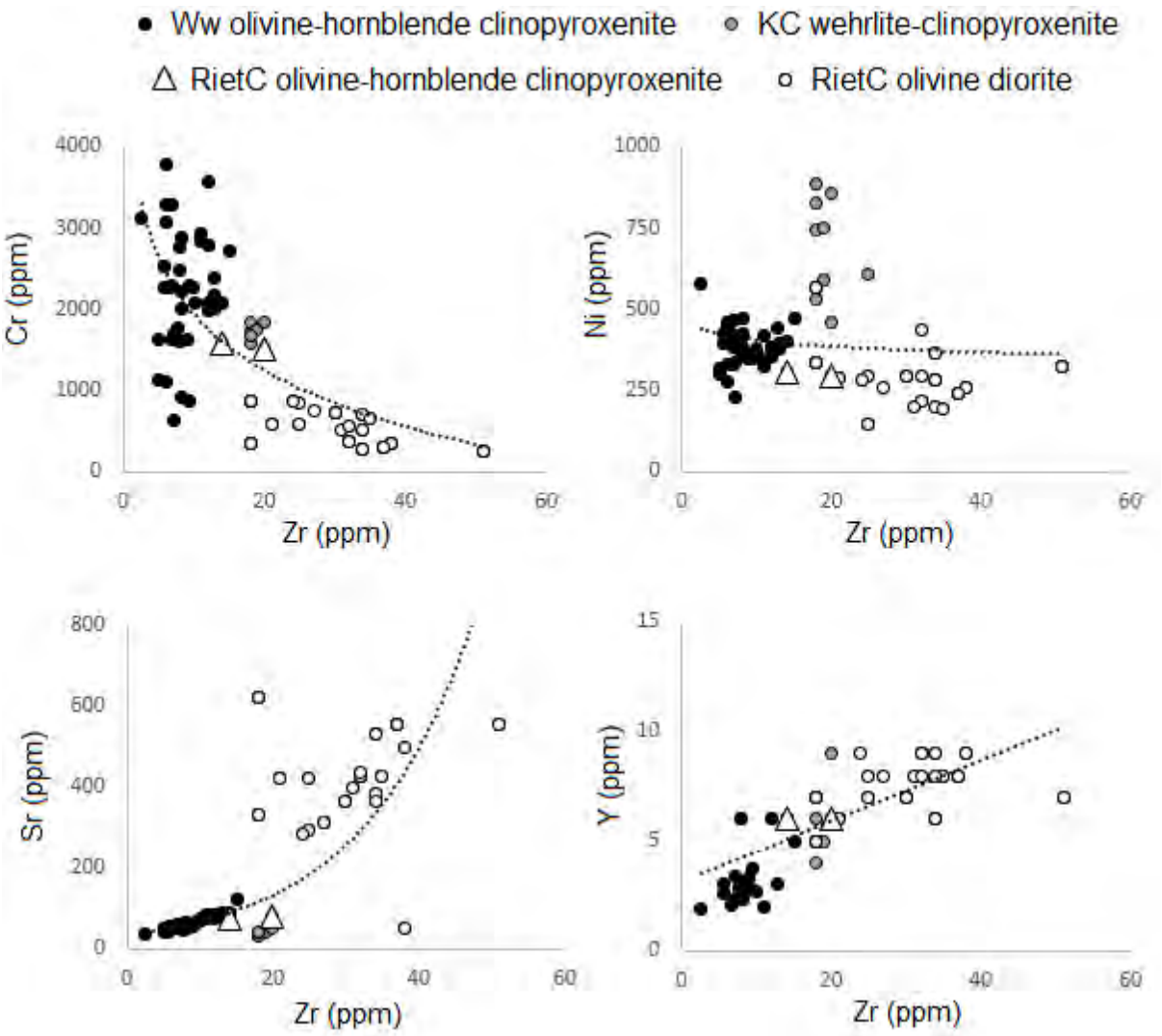

Figure 5.17: Harker diagrams of selected trace elements plotted against Zr. Trend lines are shown on each Harker diagram.

(Sr and Y) and two compatible trace elements (Ni and Cr). This is to further assess trends in magmatic evolution and to determine the relative degree of evolution between Ww, KC, and RietC. See Figure 5.17.

- Cr

Zr is expected to increase as Cr is depleted. In the case of Cr, this trend is not observed in Ww or KC, but can be seen in RietC. When compared to each other, Ww generally had the highest Cr and lowest Zr concentrations, giving it the appearance of the most primitive intrusion of the three. In the main, RietC has the lowest Cr and highest Zr concentrations, making it the most evolved intrusion. KC olivine clinopyroxenite form a tight cluster regarding its Cr and Zr content, and has higher Cr and lower Zr concentrations than RietC in general.

- Ni

Because Ni is also considered compatible, a similar trend of Ni depletion coupled with Zr enrichment as seen for Cr is expected. However, KC contains a much higher Ni content relative to its Zr content due to its high modal abundance of olivine. Significant overlap occurs between the Ni contents of Ww and RietC, but RietC generally has a lower Ni concentration than Ww. This, coupled with its higher Zr concentration, would imply that RietC hosts the most evolved rocks.

- Sr

Because Sr is incompatible with olivine and pyroxenes, its concentration is expected to increase along with Zr during the formation of ultramafic rocks from Ww, KC, and RietC. However, a similar problem in the case of KC is observed as were for Ni in this section; KC has intermediate Zr concentrations, but the lowest (thus most primitive) Sr concentrations. The olivine diorite from RietC has very high Sr contents compared to the ultramafic rocks because of the accumulation of plagioclase. Ultramafic rocks from Ww and RietC show comparable Sr contents and cannot be distinguished from one another. Rocks belonging to Ww show a steady and consistent increase in both Sr and Zr.

- Y

Plotting Zr and Y against each other is exceptionally useful because both elements are incompatible with all mineral phases observed in Ww, KC, and RietC. Thus, they should both show an increase as magmatic evolution proceeds. The ratio between incompatible elements in magmatic systems tend to remain constant (Rollinson, 1993; Winter, 2010), making Zr and Y useful to assess whether or not different igneous intrusions are related to another. A steady and linear increase is observed in both Zr and Y, with Ww plotting as the most primitive intrusion, KC generally intermediate, while RietC contained the most evolved rocks. A significant amount of scatter is observed for all three intrusions, implying that some process other that fractional crystallisation has influenced the ratio between these two elements (perhaps crustal assimilation or alteration). Nevertheless, the three intrusions are indistinguishable in terms of their Zr/Y ratios (samples from all three intrusions plot both above and below the trend line).

5.3.5 General remarks

The whole-rock chemistry of olivine-hornblende clinopyroxenite from the Lower Zone of RietC are, in many cases, indistinguishable from those of Ww (see Harker plots for MgO

versus SiO_2, MnO, CaO, Na_2O, K_2O, P_2O_5, Rb, Sr, Sc and V, and Sr versus Zr – Figures 5.14 and 5.16). This further supports Stepo's (1990) observation that these rock units might have originated from the same magma due to their chemical similarities. However, RietC's Lower Zone olivine-hornblende clinopyroxenite do appear to have generally more evolved composition in terms of higher TiO_2, Al_2O_3, and FeO(t) concentrations.

Of the three intrusions, the ultramafic rocks and olivine diorite from RietC are generally more evolved that the ultramafic rocks from KC and Ww. KC and Ww proved more difficult to distinguish from each other due to overlapping. In terms of MgO, Na_2O, K_2O, Ni, and V, KC appears to have the most primitive composition. On the other hand, Ww appears to be more primitive in terms of Mg#, FeO(t), MnO, Cr, Y, and Zr. If, for reasons stated above, Mg# and Zr are considered to be more accurate indicators of magmatic evolution, then overall Ww should be considered the most primitive intrusion.

5.4 TAS CLASSIFICATION

Based on the alkalis (Na_2O+K_2O) versus silica (TAS), Irvine and Baragar (1971) have divided igneous rocks into two main series; the alkaline- and sub-alkaline series (see Figure 5.18). With the exception of the diorite from KC, all samples from Ww, KC, and RietC plot in the sub-alkaline field. This classification is further supported by the fact that enstatite is observed in Ww, the Lower Zone olivine-hornblende clinopyroxenite of RietC, and the hornblende gabbronorite and norite from KC (section 4.1). Both the mineralogical and geochemical evidence thus show that the three intrusions are sub-alkaline in nature.

5.5 MULTI-ELEMENT SPIDER PLOTS

Multi-element spider diagrams are plotted using trace elements that are considered incompatible with mantle minerals. The concentration of the trace elements are normalised to a different rock type (for example chondrite, primitive mantle, or mid ocean ridge basalts (MORB) are commonly used) and are then plotted on a graph and arranged in order of increasing compatibility from left to right (Rollinson, 1993). In this study, all samples are normalised to an estimated composition of the primitive mantle from McDonough *et al*. (1992) (normalisation values are given in Appendix K).

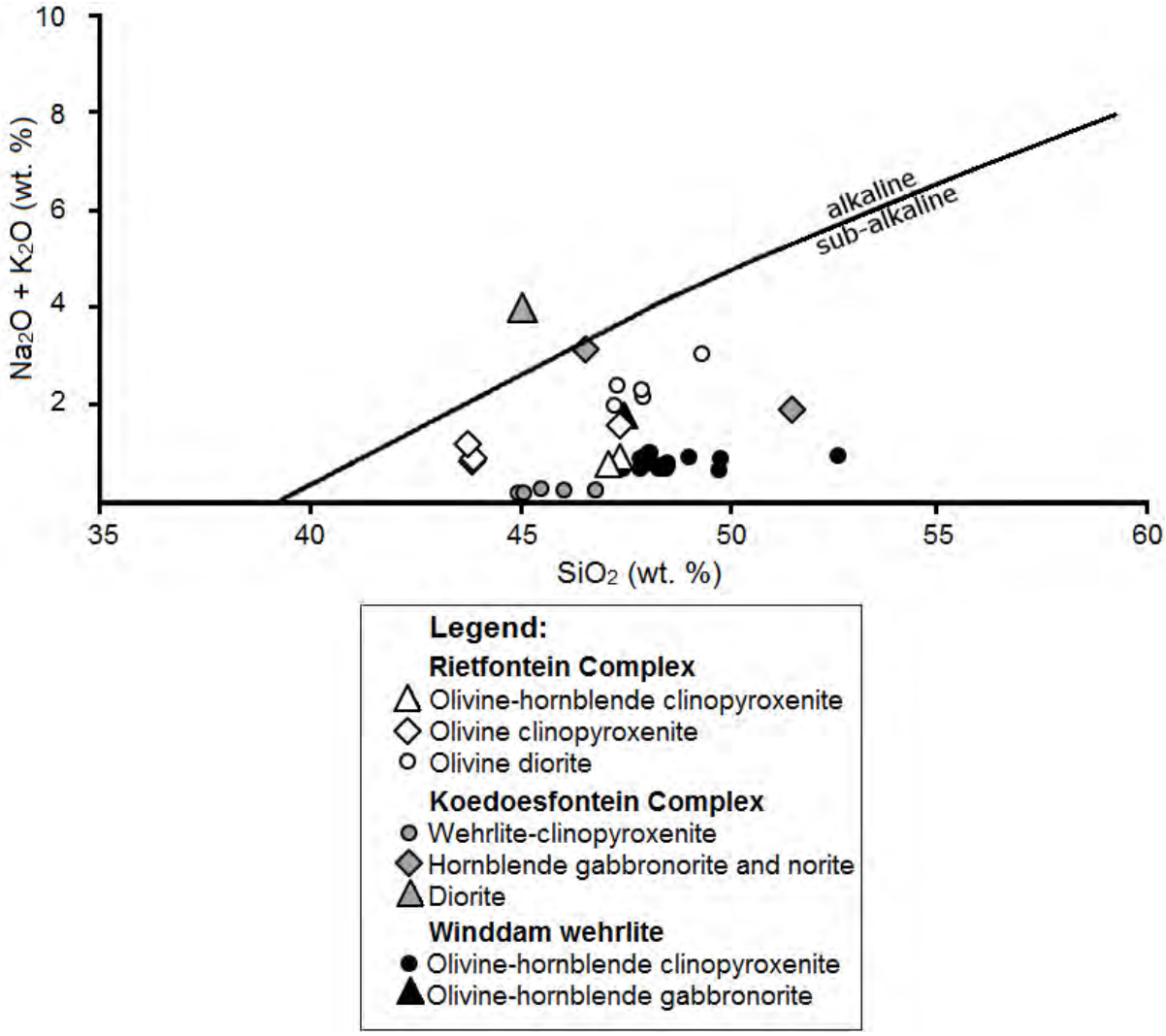

Figure 5.18: Geochemical classification diagram to determine whether rocks are alkaline or sub-alkaline in nature. The line subdividing the alkaline and sub-alkaline series based on total alkalis and silica is from Irvine and Baragar (1971).

Multi-element spider diagrams can be useful to unravel the nature of the mantle from which mafic rocks originate. During partial melting of the mantle, higher concentrations of the more incompatible trace elements are released into the melt compared to elements with higher compatibility (Foulger, 2010; Rollinson, 1993; Winter, 2010). Consequently, basalts that crystallise from partial mantle melts have higher concentrations of incompatible elements than more compatible elements compared to the magma source (Saito *et al*., 2015). This results in overall negatively sloping curves on spider diagrams as is the case of ocean island basalts (OIB) (Rollinson, 1993; Sun, 1980; Winter, 2010). Rocks that form from mantle material that has experienced extensive partial melting (such as MORB) are typically depleted in highly incompatible elements, and produce positive curves on spider diagrams (Husen *et al*., 2016; Rollinson, 1993; Winter, 2010).

Because the ratio of incompatible elements present in mantle-derived igneous rocks are highly dependent on the melting source (especially in the case of immobile elements), rocks that display similar curves on spider diagrams are usually inferred to have formed from the same primary magma (Rollinson, 1993; Winter, 2010). Because these elements also tend to be incompatible with minerals common in mafic rocks, comagmatic rocks that plot higher up on spider diagrams than others are also typically more evolved in nature (see, for example, Coetzee, 2001). However, even in related suites of rocks, some deviation may still occur if a mineral accumulates with a preference for a certain trace element (for example, Sr in plagioclase) or if the magma is contaminated by, for example, continental crust which can lead to an increase in elements such as Rb, K, and Zr (Halim *et al*., 2016; Rollinson, 1993; Winter, 2010).

In other cases, hydrothermal alteration of the rocks themselves or of the melting source (such as the mantle) can cause relative enrichment or depletion of certain elements. Elements that are typically mobile in hydrothermal fluids are the large-ion lithophile elements (LILE), and include elements such as Na, K, Rb, Sr, and Ba (Rollinson, 1993; Winter, 2010). Those that are frequently immobile are referred to as high field strength elements (HFSE), which include Th, U, Nb, REE, Zr, Y and Ti, among others (Rollinson, 1993; Winter, 2010). Spider diagrams can serve as a useful means to contrast the relative abundance of LILE and HFSE.

Elements that are mobile in hydrothermal fluids may be leached from an igneous rock during hydrothermal alteration, leading to negative anomalies of the LILE on multi-element spider diagrams. In other cases, when rocks are exposed to fluids carrying a high LILE concentration, the rocks can become enriched in these elements, leading to the development of positive LILE anomalies compared to the HFSE (for example Baier *et al*., 2008; Onwualo-John, 2016; Woo *et al*., 2014).

This section serves to report on the shapes produced on spider diagrams for different rock types from Ww, KC, and RietC, how these shapes compare to one another, and to report on any anomalies observed on these diagrams and what they might imply.

5.5.1 Winddam wehrlite

Because of the higher accuracy of the ICP-MS analysis, only samples analysed by ICP-MS are discussed here. Because many elements used on the spider diagram are below the detection limit of the XRF analysis performed on olivine-hornblende gabbronorite sample CB47, it is not discussed here. The general slope of Ww samples (Figure 5.19) is that of a

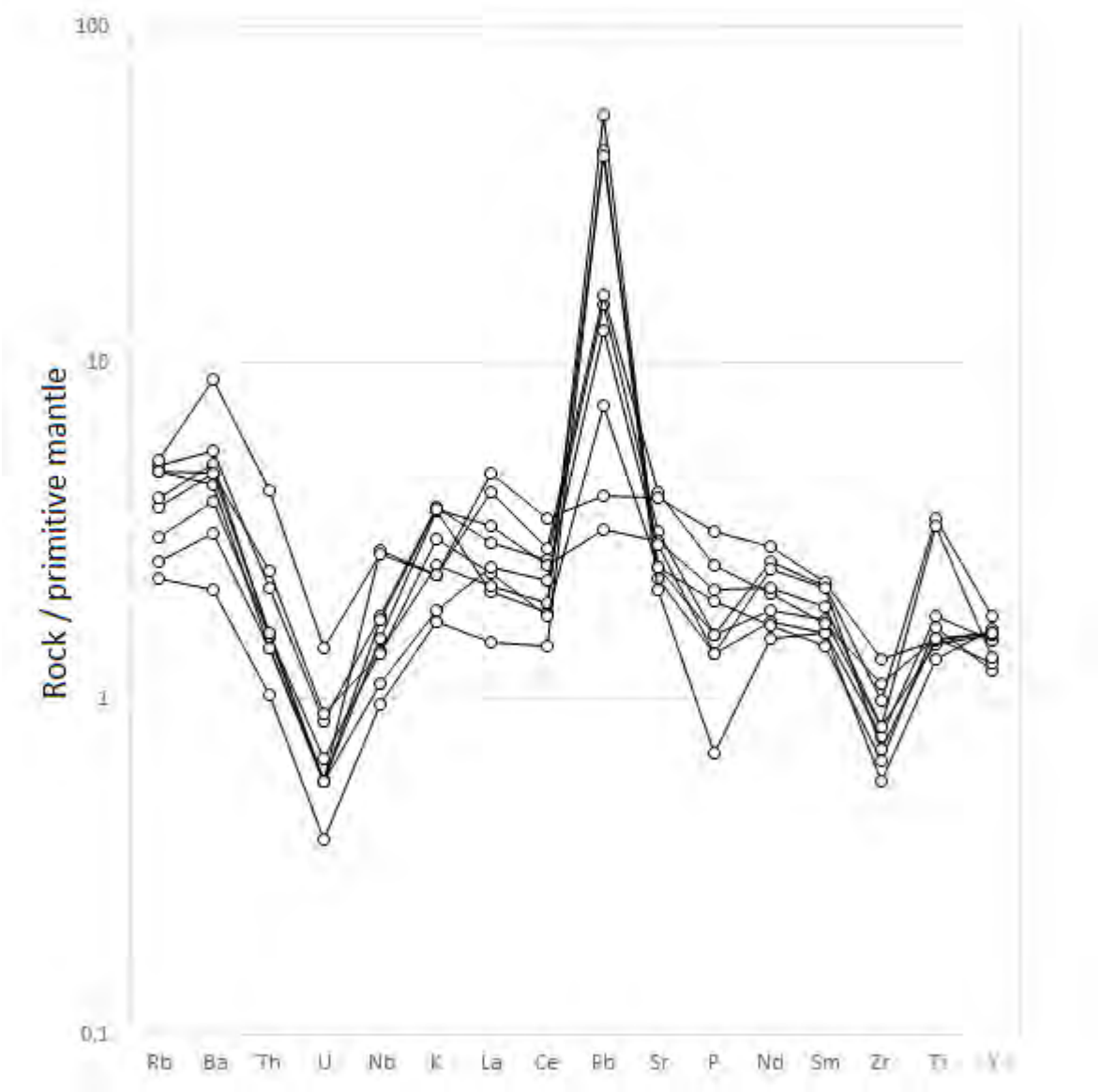

Figure 5.19: Multi-element spider diagram for ultramafic samples from Ww. Normalisation values are from McDonough *et al*. (1992).

decreasing concentration relative to the primitive mantle from left to right on the multi-element spider diagram, indicating that Ww formed from a relatively fertile source. This is especially true considering that the parental melt of Ww is likely to contain higher concentrations of the more incompatible elements than the rock itself.

The majority of Ww samples are further characterised by positive Ba anomalies, negative Th, U, and Nb anomalies (producing a trough at the position of these three elements), very well developed positive Pb anomalies, negative P and Zr anomalies, and positive Ti anomalies. Because of its status as a LILE, Ba was probably introduced to Ww through hydrothermal activity, either at the melting source or later in the rock itself. Because of the high hydrothermal mobility of Pb, positive lead anomalies have been ascribed to the

contamination of magma by Pb-bearing hydrothermal fluids from the country rock during its emplacement in the crust (for example, Onwualo-John, 2016).

In contrast, Nb, Zr, and P all display very low mobility. Low-mobility elements can become depleted relative to more mobile elements when the mantle source is altered by hydrothermal activity, usually in the vicinity of a subducted oceanic plate (Baier *et al*., 2008; Ernst, 2014; Woo *et al*., 2014; Zhang *et al*., 2016). This occurs via transport of hydrothermal fluids from the subducted oceanic sediments to the mantle wedge. The subducted sediment is leached of its more mobile elements which is then transferred to the mantle wedge. The mantle may remain enriched in mobile elements for vast amounts of time even after subduction has terminated (Ernst, 2014).

5.5.2 Koedoesfontein Complex

Only one ultramafic sample from KC (olivine clinopyroxenite RB9) was analysed for trace elements using ICP-MS and is plotted on Figure 5.20. Ultramafic WK samples that were analysed by means of XRF are plotted separately on Figure 5.21 since fewer elements were analysed via this method compared to ICP-MS. Overall, ultramafic rocks from KC show a very flat slope on the spider diagram, but its parental melt is likely to be enriched in the more incompatible elements than the more compatible elements, which would give a negatively inclined slope. Similar to Ww samples, wehrlite-clinopyronite samples from KC show positive Ba anomalies and negative P and Zr anomalies. Positive Pb anomalies is also observed on the majority of samples shown on Figure 5.21, while it is absent in olivine clinopyroxenite sample RB9 on Figure 5.20. The possible causes of these anomalies have already been discussed in the previous section and applies here as well. Negative Rb and K anomalies are also prominent in wehrlite-clinopyroxenite samples in Figure 5.21. Because of high mobility of Rb and K, both of these elements may be leached from the host rock during hydrothermal alteration (for example, Torres-Alvarado *et al*., 2010). Negative Nb anomalies are observed in olivine clinopyroxenite RB9, hornblende gabbronorite RB3, diorite WK36, pyroxene hornblendite RB20, and hornblende norite WK32 while it is absent in the other samples.

Hornblende gabbronorite sample RB3 from KC is plotted on Figure 5.20. It is generally enriched in the less compatible elements, leading to the overall negative slope observed on the spider diagram. It shares positive Ba and Pb anomalies with the wehrlite-clinopyroxenite, while it contrasts with this rock type in terms of well-developed positive K and Rb anomalies. This implies that K and Rb had to be intruduced by an external source such as crustal contamination that had not affected the wehrlite-clinopyroxenite. Although the Pb anomaly

diminishes the visual effect, RB3 also shows a positive Sr anomaly, which is ascribed to the presence of plagioclase in this rock type. Similar to the wehrlite-clinopyroxenite, hornblende gabbronorite RB3 also possesses a negative Zr anomaly. The pyroxene hornblendite sample RB20 has a pattern similar to the hornblende gabbronorite (Figure 5.21), but differs in terms of displaying a positive Zr anomaly and a negative P anomaly.

Hornblende norite sample WK32 has a similar pattern as the wehrlite-clinopyroxenite samples (Figure 5.21), but differs in terms of possessing a positive Zr anomaly and a negative Ti anomaly. The diorite differs from the wehrlite-clinopyroxenites in terms of the absence of a positive Pb anomaly as this element is below the detection limit of the XRF.

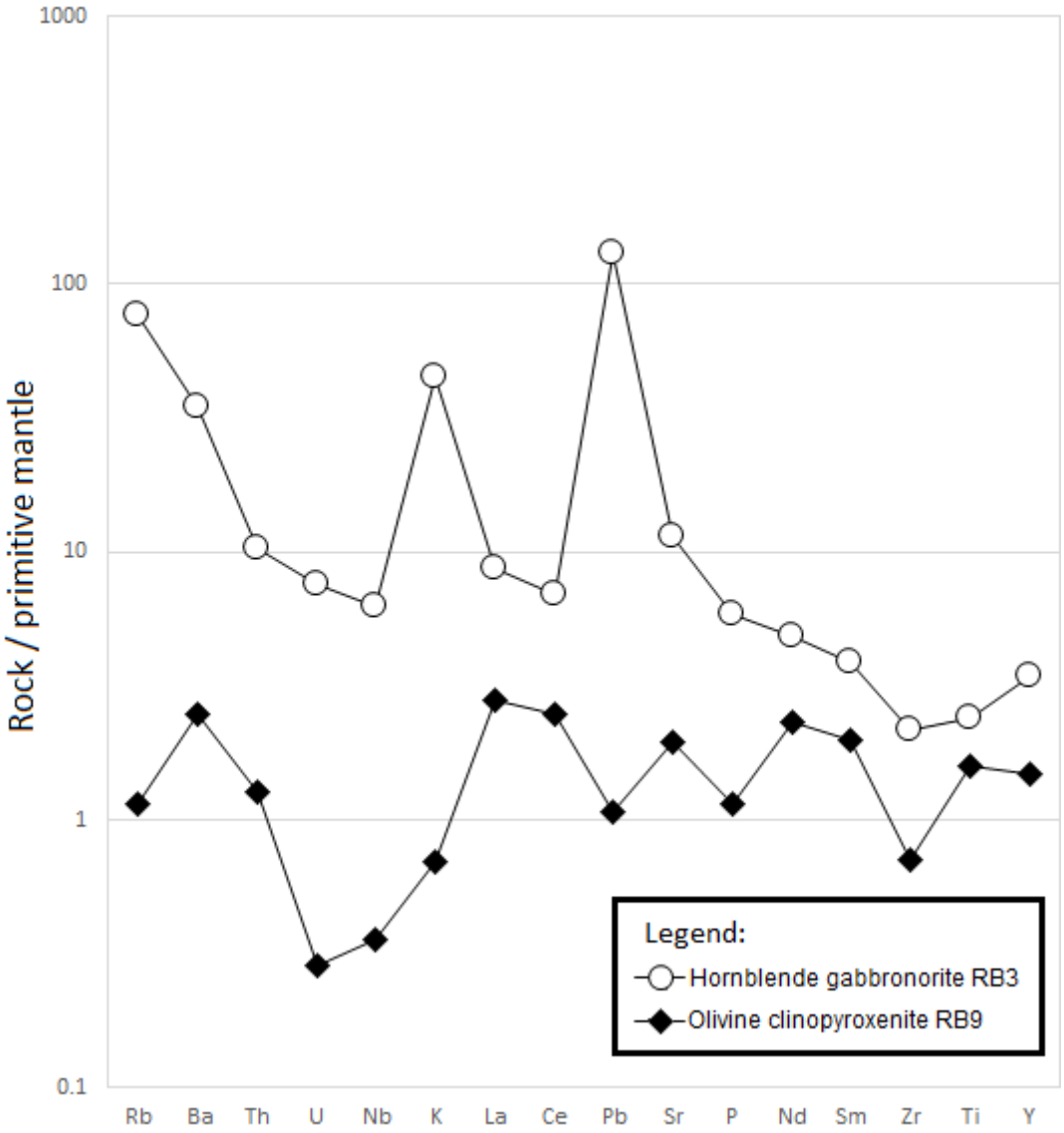

Figure 5.20: Multi-element spider diagram for olivine clinopyroxenite RB9 and hornblende gabbronorite (RB3) from KC. Normalisation values are from McDonough *et al.* (1992).

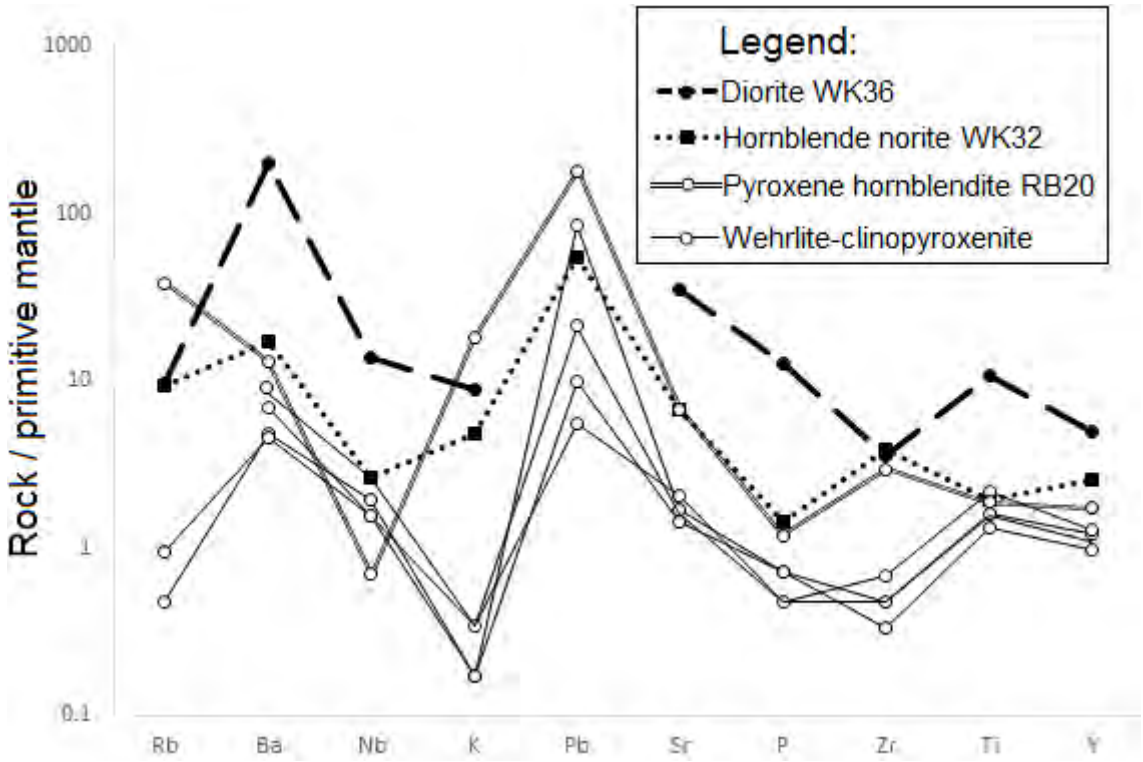

Figure 5.21: Multi-element spider diagram for wehrlite-clinopyroxenite samples, pyroxene hornblendite RB20, hornblende gabbronorite WK32, and diorite WK36 from KC. Normalisation values are from McDonough *et al*. (1992).

5.5.3 Rietfontein Complex

Spider plots of RietC samples are shown on Figure 5.22. Overall, all rock types show a gentle negative slope due to the relative enrichment of highly incompatible elements. With the exception of the troctolite, all rock types display positive Ba, Pb, and Ti anomalies, and negative Th, U, Nb, K, P, and Zr anomalies (similar to ultramafic rocks from Ww and KC). Possible explanations for these anomalies have been provided in the previous two sections.

Interestingly, olivine diorite samples contain lower concentrations of the incompatible elements in the majority of cases when compared to the ultramafic rock layers, hinting at a more primitive geochemical composition. They also differ from the ultramafic rocks by the presence of positive Sr anomalies due to its incorporation in the mineral plagioclase.

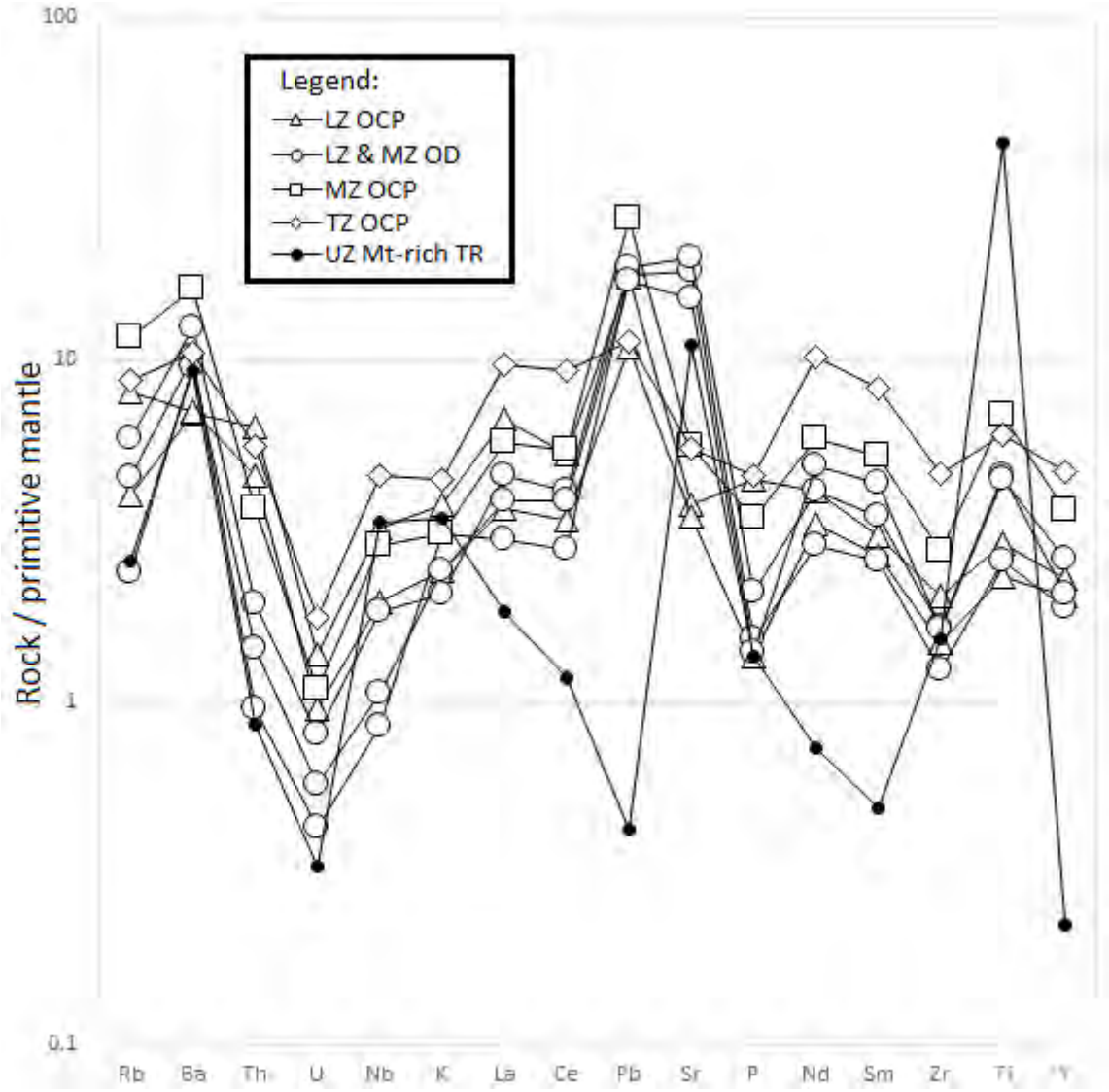

Figure 5.22: Multi-element spider diagram for different rock samples from RietC. Normalisation values are from McDonough *et al*. (1992). LZ: Lower Zone; MZ: Main Zone; TZ: Transitional Zone; UZ: Upper Zone; OCP: Olivine clinopyroxenite; OD: Olivine diorite; Mt: Magnetite; TR: Troctolite.

The troctolite follows a similar pattern as the other rock types for the first four elements on the spider diagram. Thereafter it starts to differ in terms of the absence of a Nb anomaly, negative anomalies for La, Ce, and Pb. It shows a positive Sr anomaly similar to the diorite (once again due to the presence of plagioclase), but negative Nd and Sm, as well as Y, anomalies. It has a very well developed positive Ti anomaly, which is associated with the crystallisation of titano-magnetite.

5.6 CHONDRITE-NORMALISED REE PATTERNS

Perhaps one of the most useful ways to unravel the origin of igneous rocks is through the study of chondrite-normalised REE diagrams (normalisation values used in the section are given in Appendix L). This is because the relative concentration of REE generally stays the same in related suites of igneous rocks, while variations in the REE concentration can be used as petrological indicators for various processes (for example plagioclase accumulation which leads to an increase in Eu concentrations) (Hanson, 1989; McKay, 1989). Due to their large ionic radii, almost all REEs (Eu being a notable exception) are incompatible with the majority of the common silicates found in igneous rocks (Henderson, 1984). D-values tend to increase from the lighter to heavier REEs as their atomic radii decreases (McKay, 1989; Rollinson, 1993; Winter, 2010). Many igneous rocks that originate during partial melting of an undepleted mantle source are thus generally enriched in lighter REEs relative to the heavy REEs. In the case of rocks that originate from a depleted mantle source (such as N-MORB), the heavier REEs might be enriched in comparison to the lighter REEs. Based on this variation in their geochemical behaviour, REEs are traditionally divided into two primary groups for ease of reference: the light REEs (LREEs) which include La, Ce, Pr, Nd, Sm, Eu, and Gd, and heavy REE (HREEs), which include Tb, Dy, Ho, Er, Tm, Yb, and Lu.

The interpretation of chondrite-normalised REE diagrams is usually based on the slopes produced by the LREE and HREE when the elements are plotted in order of increasing atomic weight. This section serves to quantify these slopes for Ww, KC, and RietC, and how the slopes from different samples of the same intrusion compare to one another. Slopes that are frequently quantified in the literature are $(La/Sm)_N$ (subscript N indicates the values have been normalised to chondrite) as representatives of the slope of LREE, and $(Tb/Yb)_N$ as representatives of the slope of the HREE. The smaller the variation between these slopes for different samples is, the higher the likelihood that they are comagmatic products from the same primary magma (Rollinson, 1993; Winter, 2010).

Another aspect of REE patterns typically discussed is Eu-anomalies. An Eu-anomaly refers to a deviation in the concentration of what one would expect for Eu relative to the other REEs and is visible as a positive (upward) or negative (downward) spike at the Eu position on chondrite-normalised REE diagrams. The origin of a positive Eu anomaly is usually ascribed to the accumulation of plagioclase because of the compatibility of Eu^{2+} with this mineral. The absence (or prior fractionation) of feldspar can also be responsible for a negative Eu anomaly. Eu-anomalies are quantified as Eu/Eu*, where Eu is the measured concentration of Eu in the rock, while Eu* is the expected concentration of this element. Eu* is calculated as $(Sm_N + Gd_N)/2$ because Eu lies between these two elements on the periodic

table. Thus, an Eu/Eu* value of more than one indicates a positive Eu anomaly, while a value of less than one indicates a negative Eu anomaly (Rollinson, 1993). $(La/Sm)_N$, $(Tb/Yb)_N$, and Eu-anomaly values are given in Appendix M for individual samples.

5.6.1 Winddam wehrlite

Chondrite-normalised REE patterns for Ww are displayed on Figure 5.23. Overall, the ultramafic rocks of the intrusion show comparable patterns in terms of the HREE, with $(Tb/Yb)_N$ having an average value of 1.36 and a standard deviation of 0.07, indicating that all these rock samples originated from the same primary magma. Although obvious exceptions exist, Ww is generally fractionated in terms of its LREE (contains higher LREE concentrations compared to HREE). The LREE patterns of this intrusion are highly variable with $(La/Sm)_N$ ratios ranging from 0.97 to as high as 2.52. Average $(La/Sm)_N$ are recorded as 1.58 with a high standard deviation of 0.46. No Eu anomalies are apparent in the rocks from Ww as Eu/Eu* varies from 0.95 to 1.04.

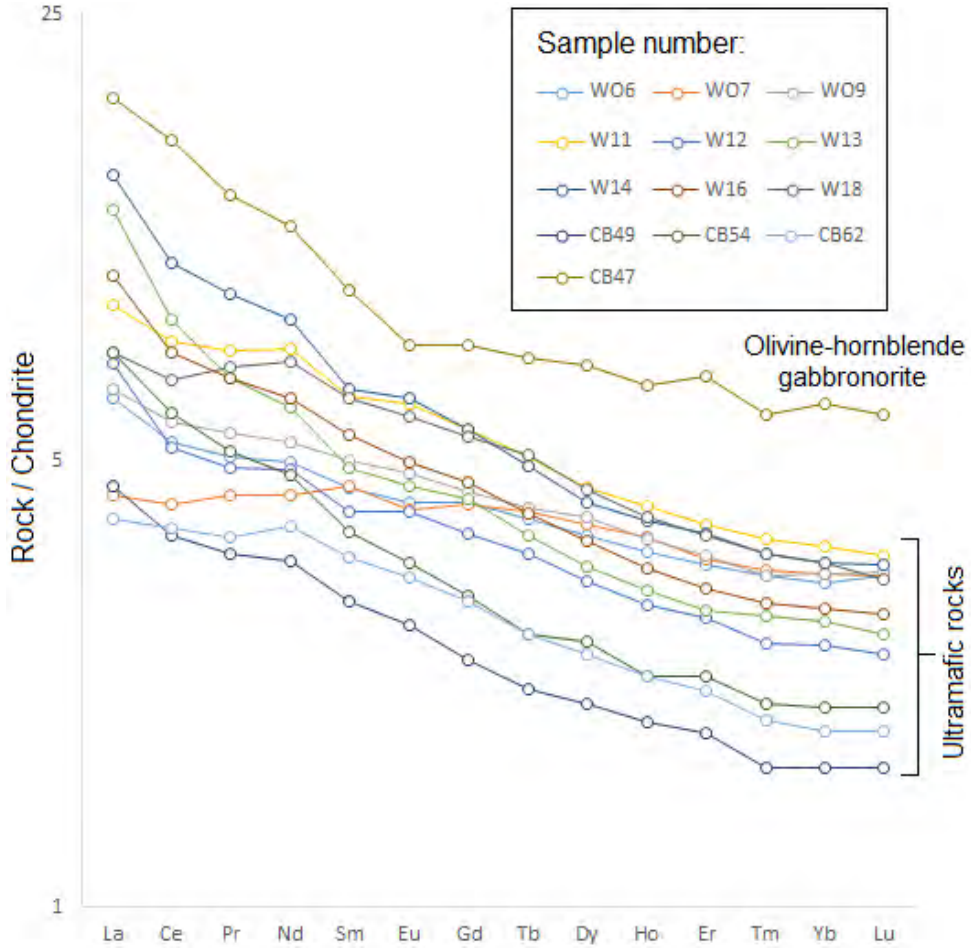

Figure 5.23: Chondrite-normalised REE patterns of rock samples from Ww. Normalisation values are from the C1 chondrite of Sun and McDonough (1989).

The single sample of olivine-hornblende gabbronorite CB47 has a $(La/Sm)_N$ slope that is indistinguishable from the ultramafic rocks of 2.01. However, it differs from the ultramafic rocks in terms of a $(Tb/Yb)_N$ slope of 1.18, lower than any other value recorded in Ww. Despite the fact that it contained abundant plagioclase, it displays a negative Eu anomaly (0.90), implying than plagioclase fractionation have occurred prior to the crystallisation of this rock.

5.6.2 Koedoesfontein Complex

As with Ww, KC shows significant variation in the chondrite-normalised REE slopes produced by its ultramafic lithologies (see Figure 5.24). All three olivine clinopyroxenite samples are weakly fractionated in terms of its LREE. Samples MSC268 and MSC272 display near identical REE patterns, and produce low $(La/Sm)_N$ values of 0.80 and 0.81, respectively. Their $(Tb/Yb)_N$ differed slightly from each other, and values of 1.70 and 1.65 were produced, respectively. Olivine clinopyroxenite sample RB9 produces a much higher value of 1.46 for $(La/Sm)_N$, and a slightly lower value of 1.46 for $(Tb/Yb)_N$ All three samples display weakly negative Eu anomalies (0.92 to 0.94) due to the absence of plagioclase. A

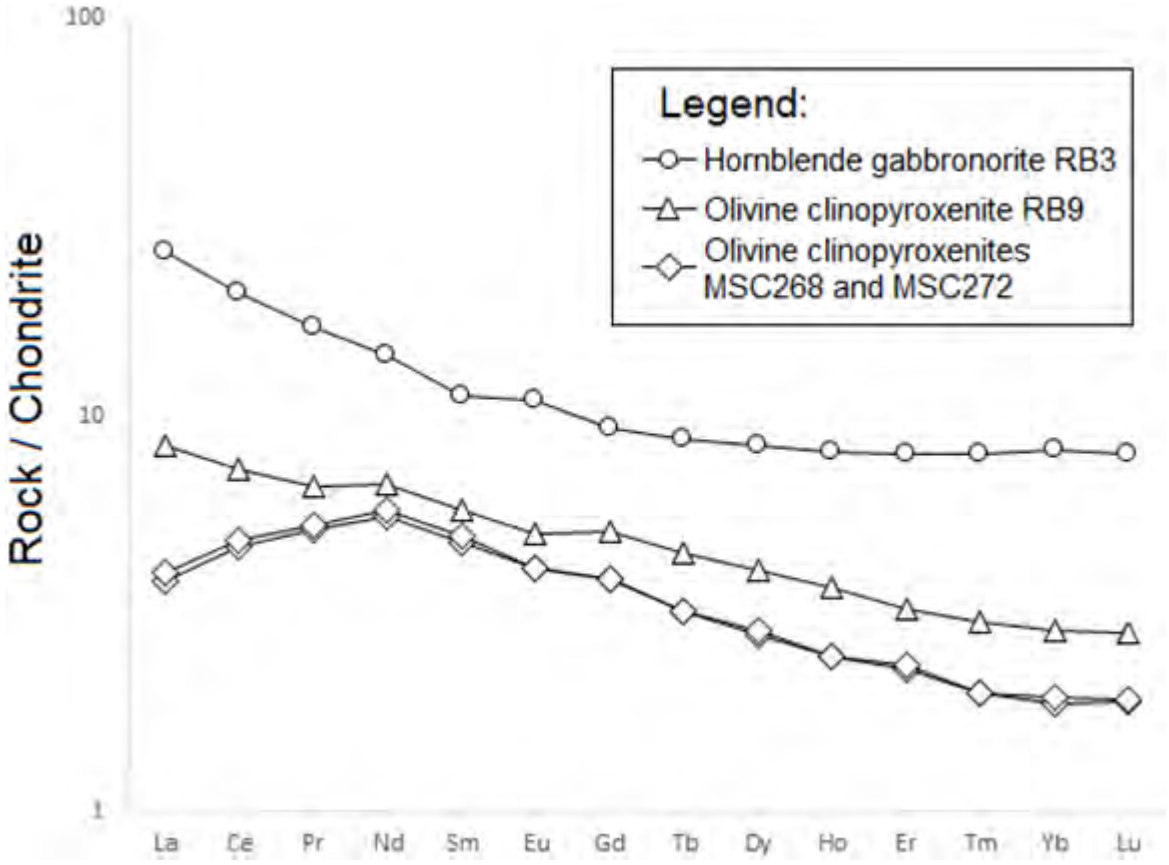

Figure 5.24: Chondrite-normalised REE patterns of rock samples from KC. Normalisation values are from the C1 chondrite of Sun and McDonough (1989).

prominent feature of samples MSC268 and MSC272's REE plots is the negative, concave upward slope from La_N to Nd_N.

The hornblende gabbronorite sample RB3 differs from the ultramafic rocks of this intrusion in terms of a higher $(La/Sm)_N$ value of 2.31 and a lower $(Tb/Yb)_N$ value of 1.06. This rock type's relatively steep slope in terms of its LREE and flat slope of HREE bears resemblance to the olivine-hornblende gabbronorite from Ww. However, in contrast to the diorite from Ww, a small positive Eu anomaly of 1.06 is recorded in the KC hornblende gabbronorite. REE concentrations for other rock types from KC are not available.

5.6.3 Rietfontein Complex

Significant variation in the REE patterns of RietC was observed for different sections and rock types of the intrusion. To aid in the presentation and discussion of the data, the rocks of RietC were divided into four groups that all have similar REE patterns (see Figure 6.25). These groups roughly correspond to the four textural groups as discussed in Chapter 4.

- Group 1

Group 1 includes the two samples of olivine-hornblende clinopyroxenite from the Lower Zone of RietC (CB1 and CB2) that have been analysed for REE. The two rocks show a large variation in their $(La/Sm)_N$ value (2.25 for CB1 and 1.42 for CB2) while very little variation is observed in terms of $(Tb/Yb)_N$ (1.56 for CB1 and 1.52 for CB2). CB1 is enriched in terms of its LREE compared to the HREE, while CB2 shows a similar but weakly developed enrichment pattern. Both samples display weakly developed Eu anomalies (0.90 for CB1 and 0.94 for CB2) due to the absence of plagioclase within the Lower Zone olivine clinopyroxenite.

- Group 2

Group 2 samples are primarily distinguished from the remainder of the intrusion on the grounds of an upwards curve from La to Nd on the chondrite-normalised REE diagram (similar to what is observed in some sample from KC). On average, Group 2 rocks have a low average $(La/Sm)_N$ value of 0.94 together with a low standard deviation of 0.06. $(Tb/Yb)_N$ values are even more consistent, with a standard deviation of merely 0.01 and an average of 1.72. This is a strong indication of a genetic relationship between these different samples. The only olivine diorite sample of Group 2 displays a positive Eu anomaly of 1.05 due to the presence of plagioclase, while the two olivine clinopyroxenite samples of this group both had negative Eu anomalies of 0.96 (which is once attributed to the low abundance of feldspar).

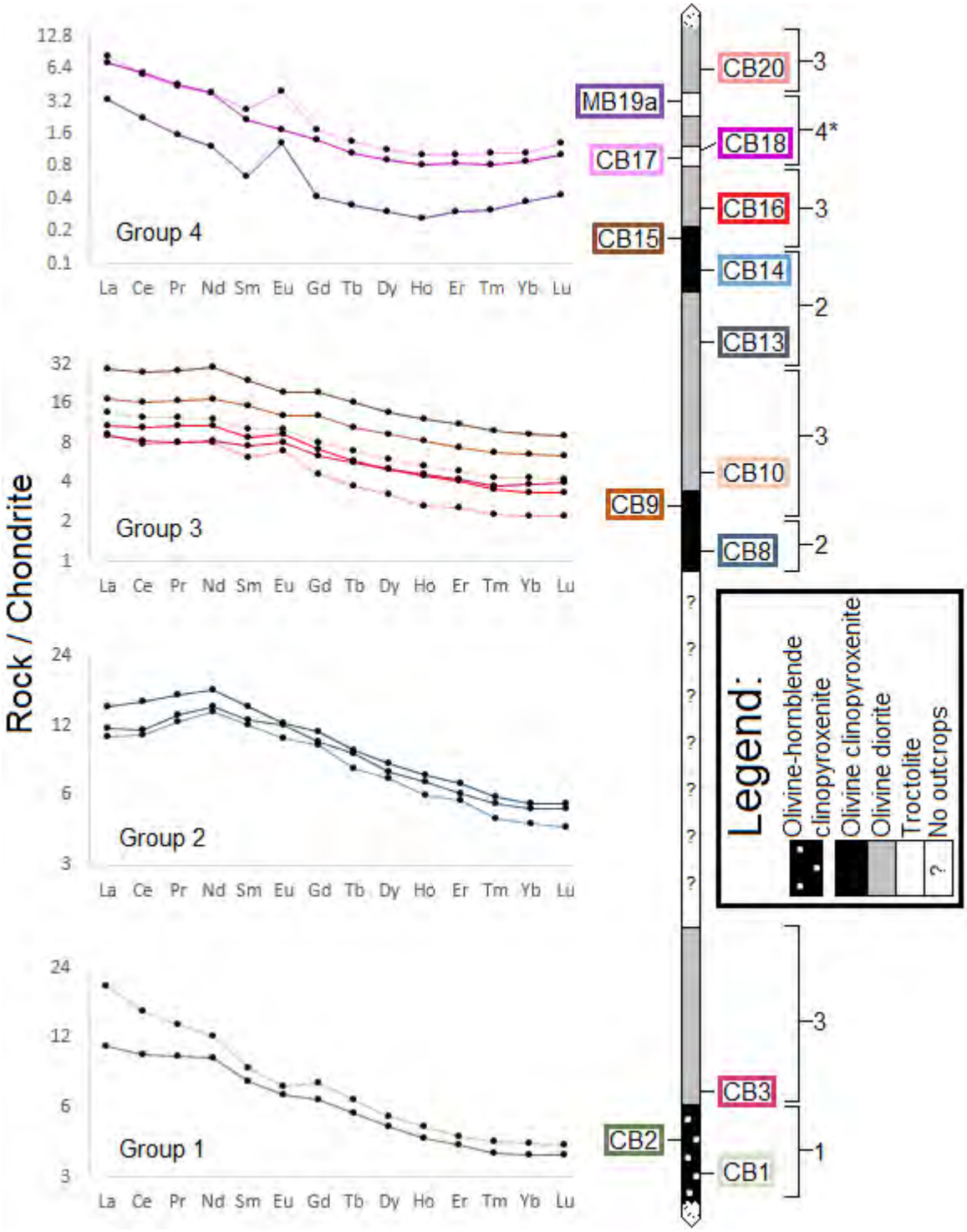

Figure 5.25: REE concentrations of RietC normalised to C1 chondrite. Normalisation values are from Sun and McDonough (1989). Localities of samples are marked according to colour on the stratigraphic column. Numbers on the right of the stratigraphic column indicate the group number that section of RietC belongs to. 4* = the layer of olivine diorite located between group 4 rocks belongs to group 3 and sample CB18 is magnetite-rich dunite.

- Group 3

In order to avoid extensive cluttering, not all Group 3 samples are plotted on Figure 5.25, but all other olivine diorite samples analysed for REEs from the RietC are included in this group. This group is characterised by relatively flat LREE slopes compared to the other groups. The average $(La/Sm)_N$ value is 1.31 and showed little variation with a standard deviation of 0.14. In terms of $(Tb/Yb)_N$ the average value recorded was 1.66 with a higher standard deviation of 0.10 in comparison with other groups and intrusions studied in this project. On average, the olivine diorite has an Eu anomaly of 1.19 ± 0.09, while the olivine clinopyroxenite has an average of 0.92. The positive Eu anomaly in the olivine diorite is attributed to the presence of plagioclase in this rock type, while the low abundance of this mineral in the olivine clinopyroxenite is responsible for the negative Eu anomaly.

- Group 4

All troctolite samples and the magnetite-rich dunite make up the Group 4 rocks. This group is characterised by the steepest LREE slopes with an average value of 3.85 for $(La/Sm)_N$ and a large standard deviation of 0.85. In contrast, the average $(Tb/Yb)_N$ value was very low (1.09) and also had a large standard deviation of 0.17. This group displays low concentrations of REE when compared to the rest of the intrusion (see Figure 5.25), with HREE dropping below chondritic values in the northern layer of troctolite in the Upper Zone. Another distinguishing feature of this group is the upward sloping curve produced from Ho to Lu on the chondrite-normalised REE diagram, which is especially apparent in the northern layer of troctolite. Both layers of troctolite display very large positive Eu anomalies that varied from 1.77 to 2.46 due to the accumulation of plagioclase within these layers. The sample of magnetite-rich dunite (CB18) has a slightly negative Eu anomaly of 0.97 due to its low abundance of feldspar.

CHAPTER 6

PETROGENESIS

Focus now shifts towards creating a petrogenetic model that is compatible with the mineralogical, petrographic, and geochemical data that has been presented in the previous chapters. Keary (2001) defines petrogenesis as the study of "all aspects of the formation of a rock". In the case of igneous rocks, this is taken to include magma genesis, magmatic crystallisation and differentiation, and deformation, which are all processes that contributed to the rock's appearance as seen today. This chapter also aims to answer the following questions introduced in the introductory chapter: are the Ww, KC, and RietC related to one another? If so, how are they related? And finally, are these intrusions comagmatic with the HITIS as originally proposed by De Waal *et al*. (2008)?

6.1 ORIGIN OF PRIMARY MAGMATIC TEXTURES

This section serves to shed light on the various processes at work during the crystallisation of the magmas responsible for the formation of Ww, KC, and RietC to produce the various textural features these rocks possess. It is divided into two subsections; the first deals with the origin of grain shapes and sizes, while the second subsection deals with the relative distribution and orientation of mineral grains. Refer back to Table 4.2 for a summary of the textural features of the different rock types distinguished in Ww, KC, and RietC.

6.1.1 Magmatic conditions responsible for grain shape and size

6.1.1.1 Equidimensional mineral shapes

Petrographic investigations revealed that olivine, augite, plagioclase, and enstatite are typically fine- to medium grained and exhibit equidimensional to elongated habits (section 4.2). The main factors controlling grain shapes in igneous rocks are (1) the degree of saturation of the melt in chemical elements needed to construct crystals, (2) crystal growth rate, (3) and the rate of diffusion of chemical elements (Vernon, 2004; Winter, 2010). If the degree of saturation is large (usually because of a large degree of undercooling), coupled with a high growth rate but slow diffusion of chemical elements, the resulting crystals typically have acicular or dendritic habits (Jafri & Charan, 1992; Lofgren & Russel, 1986; O'Driscoll *et al*., 2007; Vernon, 2004; Wick & Jones, 2012). If the magma experiences a relatively low degree of undercooling, the degree of saturation tends to be low while the rate

of diffusion tends to be faster than the growth rate. Under these conditions crystals usually grow with equal dimensions, producing grains with planar surfaces where in contact with other mineral grains (Vernon, 2004; Wick and Jones, 2012*)*.

Because of the more or less equidimensional shapes of the primary minerals in the rocks from Ww, KC and RietC, the magma is inferred to have undergone a low degree of undercooling. Magmatic crystallisation alone cannot explain the origin of the sutured grain contacts observed in Ww and the Lower Zone olivine-hornblende clinopyroxenite of RietC, and is discussed in section 6.3.

6.1.1.2 Irregular grain shapes of hornblende

Hornblende's interstitial nature, its occurrence as an oikocryst and mantle commonly surrounding pyroxenes (Figure 4.15) points to a relatively late time of formation. Oikocrystic hornblende with a similar texture was observed in the Ditrău Alkaline Massif in Romania, which was interpreted to form as an intercumulate mineral after accumulation of olivine and clinopyroxene (Pál-Molnár *et al*., 2015). Anderson (1980) has observed hornblende which had formed as a product due to a reaction between olivine and andesitic magma, and states that the two minerals commonly occur together in calc-alkaline, intermediate and mafic rocks. In rocks with a calc-alkaline affinity, mantles of hornblende are frequently seen around augite (Wilkinson, 1974). It thus seems likely that hornblende formed during a peritectic reaction between olivine and pyroxene in the presence of late magmatic H_2O-fluid after accumulation of these two mafic minerals. A peritectic reaction between augite and melt or residual magmatic fluids might also explain the occurrence of hornblende in clinopyroxene cleavage planes. Similar amphibole lamellae were observed in clinopyroxene and orthopyroxene by Veblen and Buseck (1981), which they attributed to late hydration of (or exsolution from) the single-chain inosilicates.

Another factor supporting a late time of formation for hornblende is the absence of simple twinning in this mineral (except twins that are inherited from pyroxene) (section 4.3.2). Mineral twins usually form because twinned nuclei are more stable in a melt; they are not as easily dissolved back into the magma as single nuclei. Viable nucleation might also occur when a mineral nucleates on a pre-existing surface (called heterogeneous nucleation), thereby decreasing the area of the nuclei exposed to the melt (Vernon, 2004). If hornblende nucleates directly on the pre-existing pyroxene, twinning would not be necessary to produce viable nuclei. This explains the absence of simple twinning in this mineral while simple twinning is common in primary, magmatic hornblende (Philpotts, 1989).

6.1.1.3 Interstitial nature of enstatite in Ww and the Lower Zone of RietC

The common occurrence of enstatite as an interstitial oikocryst (Figure 4.14) in Ww and the Lower Zone of RietC serves as an indication that it started to crystallise after olivine and augite (Vernon, 2004; Winter, 2010). If no heating of the magma occurs or a different primitive magma is added to the system, orthopyroxene cannot crystallise before olivine in a single cooling event (Gasparik, 2003; Winter, 2010). In addition, due to the low abundance of enstatite, it is expected that the melt will only become saturated in enstatite during the final stages of crystallisation.

6.1.1.4 Porphyritic texture in diorite sample WK36 from KC

Porphyritic textures are classically interpreted to form from a two-stage cooling event of a single magma. The first stage typically occurs within a subsurface magma chamber where large crystals are produced during slow cooling. This is followed by eruption of the magma on the Earth's surface and a fine matrix is developed under faster cooling conditions (Vernon, 2004; Winter, 2010). It is likely that the phenocrysts in WK36 were produced at a deeper level in the crust, while the matrix crystallised at a shallower region of the crust due to upward migration of the magma, producing the porphyritic texture. However, all other plagioclase-bearing rocks from KC have coarser grain sizes and are believed to have intruded at the same level, casting doubt on the validity of this explanation.

Swanson (1977) states that porphyritic textures in intrusive rocks may also come about during sudden dehydration of the magma. This leads to the formation of a fine-grained matrix surrounding earlier phenocrysts that formed under hydrous conditions. The presence of hornblende in the matrix of KC diorite (WK36) probably indicates that magmatic fluids were present during its crystallisation, rendering this explanation unlikely.

Vernon (2004) provides an explanation for the formation of intrusive porphyritic rocks that fits perfectly with what is observed in the diorite from KC. Initially, the magma cools slowly and multiple augite nuclei begin to form. At these conditions (a low degree of undercooling and saturation), the nucleation rate is slow and the growth rate is fast (conditions A on Figure 6.1), and large but few augite crystals begin to form. Components needed to construct augite crystals are extracted through the process of diffusion from the surrounding melt, preventing any further augite nuclei to form. In turn, the melt becomes progressively more saturated in plagioclase, but latent heat released during the crystallisation of augite also prevents plagioclase nucleation. When the latent heat dissipates, the melt may become highly oversaturated in plagioclase, leading to rapid nucleation and a slow rate of crystal growth for

this mineral (conditions B on Figure 6.1). Many small plagioclase grains are thus formed, causing the melt to become saturated with augite once more. Smaller grains of augite are thus formed during the final stages of crystallisation, producing the porphyritic texture observed in WK36 where augite phenocrysts are imbedded in a fine matrix of both plagioclase and augite.

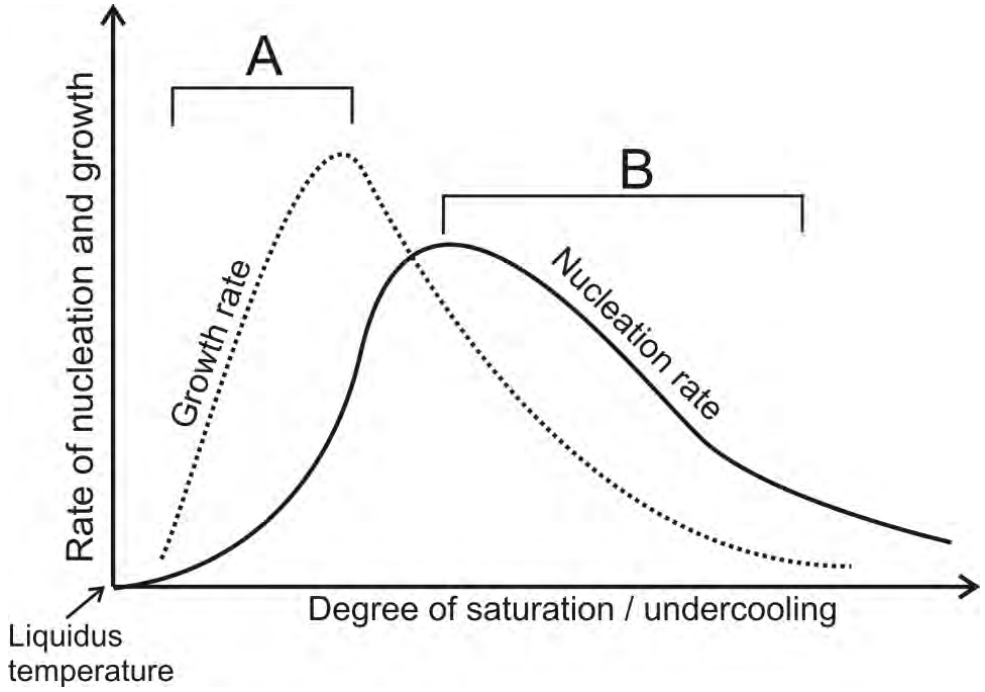

Figure 6.1: Generalised variation in the growth and nucleation rate of crystals in magma plotted against the degree of undercooling or saturation (modified after Vernon, 2004 and Winter, 2010). Magmas that crystallise under conditions labelled as A tend to produce a small amount of grains due to the low nucleation rate, but relatively large grains due to the fast growth rate. Under conditions B, relatively small but plentiful crystals are produced due to the fast nucleation but slow growth rate.

6.1.2 Grain distribution and orientation

6.1.2.1 Fish-net texture in wehrlite from KC

An explanation for the origin of the fish-net texture (Figure 4.18) has already been proposed by Bisschoff (1969) and is illustrated in Figure 6.2. During the development of this texture, it is thought that the melt initially becomes saturated in augite, leading to the formation of viable augite nuclei. As the augite crystals grow, the adjacent melt is depleted in the chemical constituents to build augite, and invariably enriched in the components necessary to crystallise olivine. After a certain degree of crystallisation, the melt in between the augite crystals become oversaturated in olivine, and olivine starts to crystallise. Eventually, olivine fills all the interstitial spaces between the augite crystals.

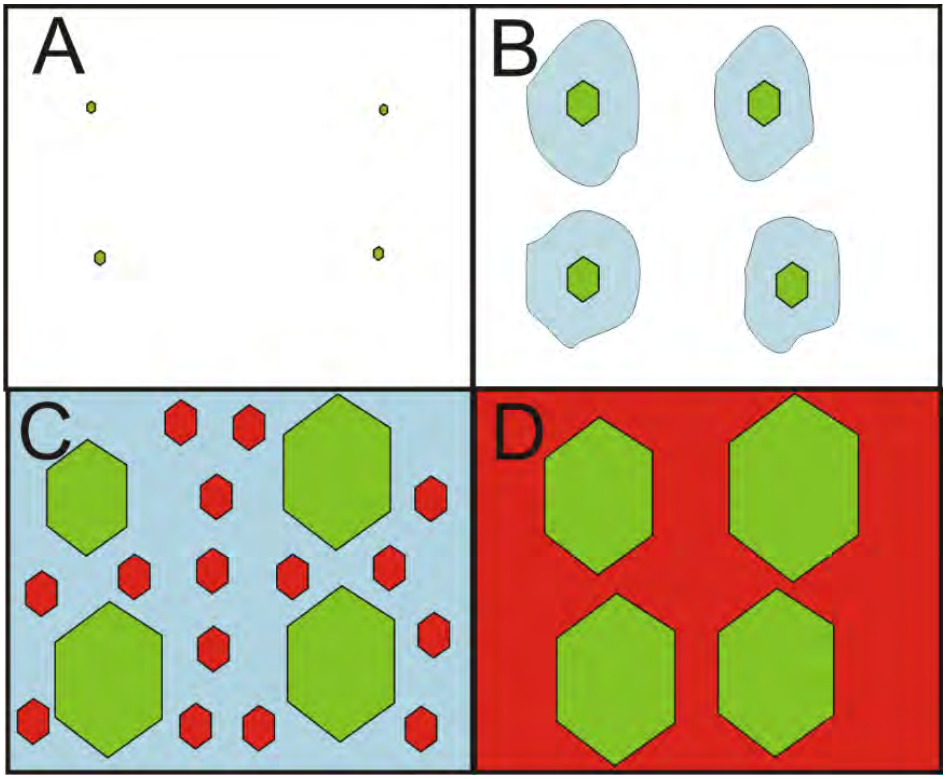

Figure 6.2: Diagram to illustrate the formation of a fish-net texture, where grains of augite are surrounded by grains of olivine (compare with Figure 4.17). A: Nucleation of augite crystals commence. B: As the augite crystals grow, the surrounding melt (indicated by the blue halo) is depleted in components needed to build augite crystals and more saturated in components needed to construct olivine. C: The melt becomes oversaturated in olivine, and olivine crystals begin to crystallise in between the augite crystals D: As the olivine crystals continue to grow, they fill the interstitial spaces between the augite grains.

6.1.2.2 Clustering of mineral grains

As mentioned in Chapter 4, separate clusters of mafic minerals and plagioclase are observed in olivine diorite from RietC and gabbronorite (sample RB3) from KC (sections 4.2.3, 4.2.5, and 4.2.7). In addition, clustering of augite to form a glomeroporphyritic texture is also observed in diorite (sample WK36) from KC (Figure 4.31).

Vernon (2004) proposes that new nuclei might find it easier to form on minerals with a similar composition. This might explain why clusters of olivine and augite are commonly observed together, as they are chemically more alike than to plagioclase. In addition, Vance and Gilreath (1967) has proposed that the clustering of similar minerals can occur through the process of synneusis, during which magmatic minerals drift together during the flow of the magma and become attached to one another due to molecular attraction between the crystal faces.

6.1.2.3 Sub-parallel alignment of plagioclase in RietC troctolite and KC diorite sample WK36

Parallel alignment of elongated magmatic minerals such as plagioclase has been observed in both extrusive (for example Sheth, 2016) and intrusive (see Higgins, 1994) igneous rocks and are both attributed to laminar flow of the magma. In addition, Vernon (2004) states that the alignment of plagioclase in intrusive rocks can also be a product of crystal settling and compaction, during which plagioclase crystals are aligned sub-parallel to the floor of the magma chamber. Both models are deemed plausible to explain the sub-parallel alignment of plagioclase in the troctolite from RietC (Figure 4.26). In the diorite from KC, magmatic flow serves as an elegant explanation for the sub-parallel alignment of plagioclase around augite glomerocrysts. If the glomerocrysts have indeed formed prior to the plagioclase (as discussed above), magmatic flow around the glomerocryst during plagioclase crystallisation would align the feldspar to the boundaries of the glomerocryst. An example of the proposed flow direction around a glomerocryst is shown in Figure 6.3.

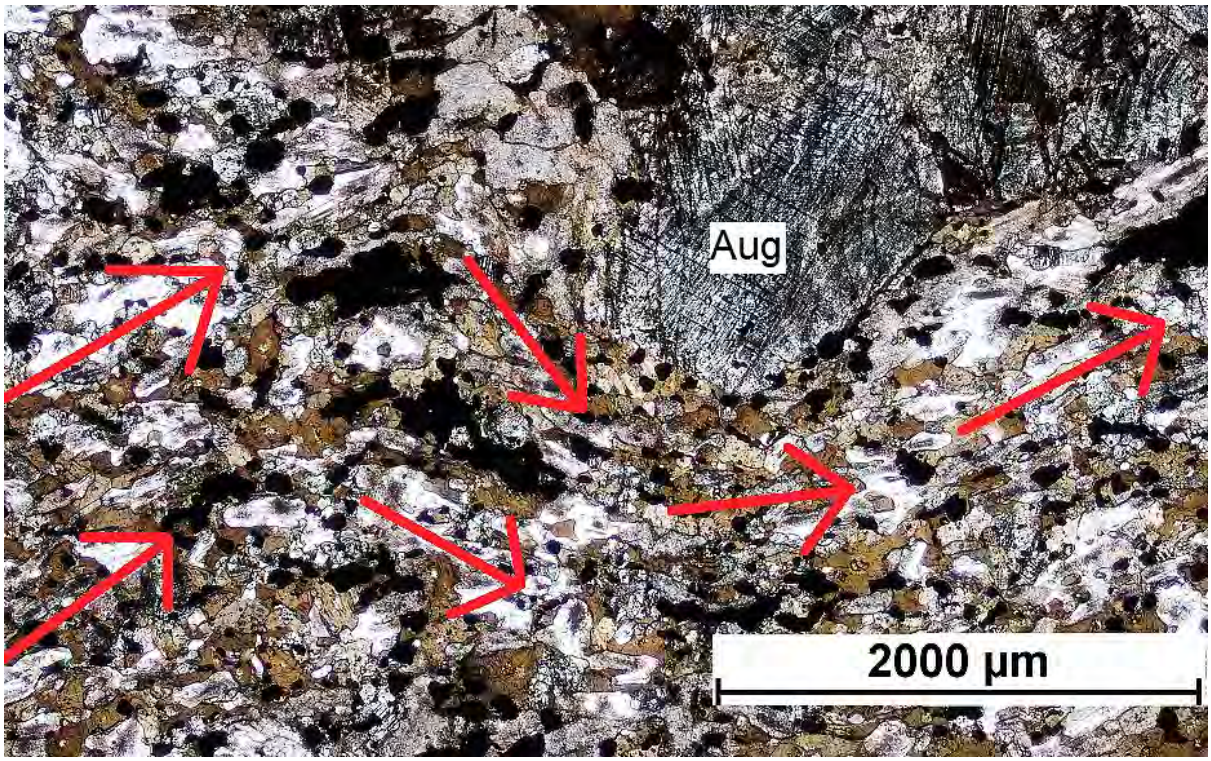

Figure 6.3: Photomicrograph to demonstrate the proposed direction of magmatic flow (red arrows) around an augite glomerocryst based on the orientation of the plagioclase grains in diorite from KC (sample WK36, PPL).

6.2 ORIGIN OF MINERALOGICAL AND GEOCHEMICAL VARIATIONS WITHIN THE INTRUSIONS

This section examines the Ww, KC, and RietC on a larger scale that the previous section. It serves to provide viable petrologic explanations for the observed variations in the mineralogy and geochemistry across the intrusive bodies that have arisen during magmatic crystallisation. It is split into three subsections; each dealing with the formation of Ww, KC, and RietC separately. Because the Ww is relatively uniform throughout its entire body (see sections 4.1.1 and 5.1), a relatively simple explanation is needed here. In the case of KC, this study primarily focusses on the ultramafic and mafic rocks of this intrusion, and its formation is dealt with in more depth by Boneschans (2017). On the other hand, RietC requires a much more lengthy investigation to decipher the origin of the igneous layering observed here.

6.2.1 Formation of the Winddam wehrlite

6.2.1.1 Olivine hornblende clinopyroxenite

Ww primarily varies in terms of its mineralogical content, while its geochemical composition varies little across the intrusive body. No good correlation could be found between the mineralogy and geochemical indicators of magmatic evolution such as Mg#, rendering the geochemistry of Ww unsuitable to unravel the processes responsible for the variation in its mineralogical content.

Given the great abundance of augite relative to olivine in some samples of Ww, a proposition is made that augite would start to crystallise prior to olivine. In order to test this hypothesis, the mineralogical composition in wt. % of Ww was plotted on the forsterite-diopside-silica system of Kushiro (1969) to compare it with the position of the forsterite-diopside eutectic. All modal hornblende was converted to augite for this comparison, as hornblende is primarily a result of hydration of magmatic augite.

Kushiro (1969) experimentally determined the position of the forsterite-diopside eutectic at both atmospheric pressure and at 20 kilobar. Based on the metamorphic assemblages observed in the core of the Vredefort Dome, Brink *et al*. (2005) estimated that Ww intruded at a depth of more than 30 km. The approximate pressure at which Ww intruded can be calculated using the formula:

$$P = ghp \qquad (6.1)$$

Where P refers to pressure in Pascal, g refers to gravitational acceleration (9.8 $m.s^{-2}$), h refers to depth in meters, and p refers to the density of the crust (2800 $kg.m^{-3}$). This corresponds to a lithostatic pressure of about 8.23 kilobar for Ww, meaning that the forsterite-diopside cotectic in the Ww magma chamber probably lies at an intermediate position between the two cotectic curves shown on Figure 6.4.

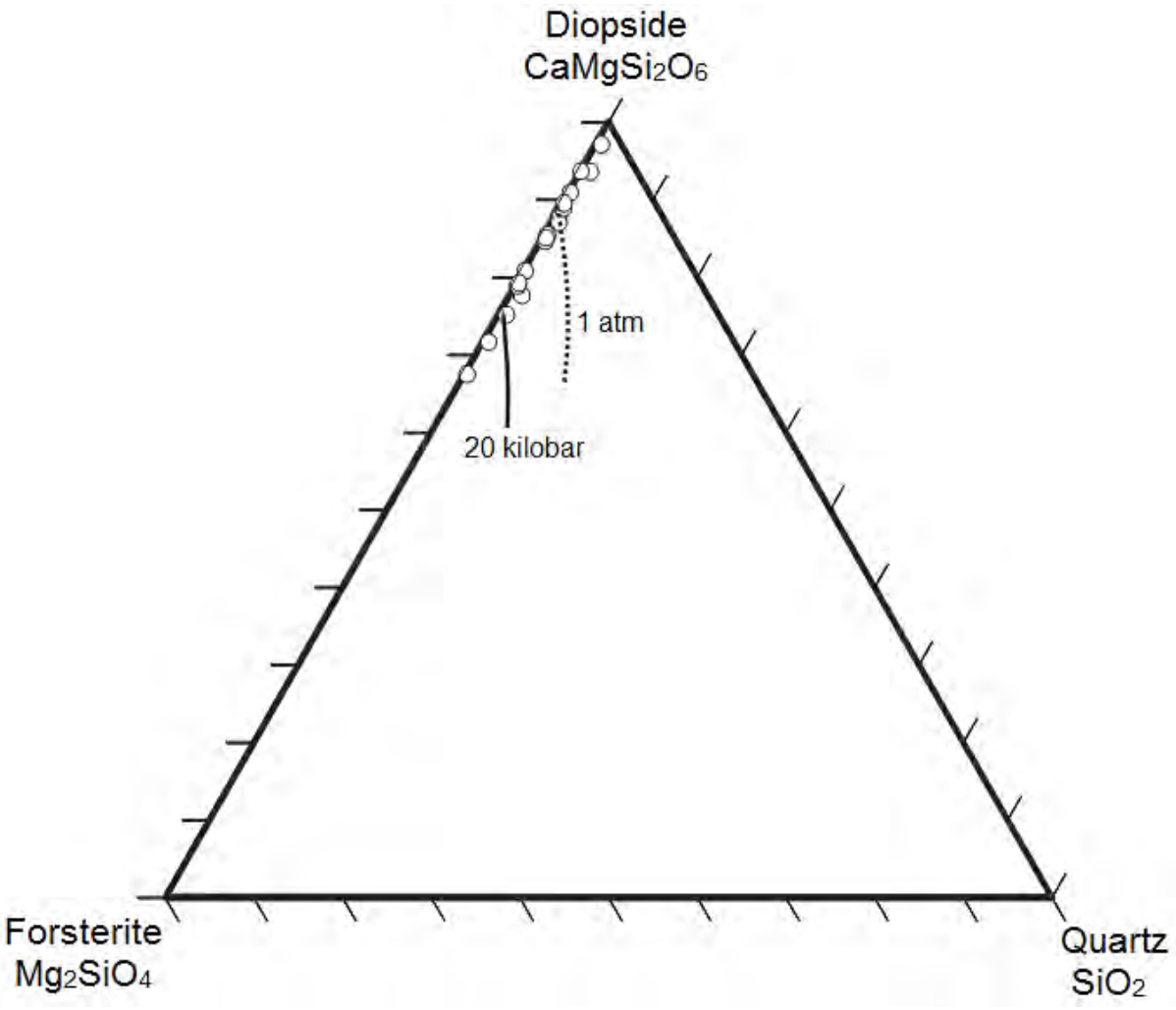

Figure 6.4: Samples from Ww plotted on a ternary diagram showing the position of the forsterite-diopside cotectic at atmospheric pressure (atm) and 20 kilobar in the system forsterite-diopside-silica (from Kushiro, 1969).

The fact that the majority of samples plot close to and above the 1 atm line indicates that augite was the first mineral to crystallise in most of the samples. Some samples plot in the forsterite field below the 20 kilobar cotectic, meaning that augite crystallisation could not have preceded the crystallisation of olivine throughout the entire intrusion. Similar grain sizes and densities of olivine and augite exclude the possibility that the modal variation is a product of varying settling velocities between these two minerals. The variation in the

mineralogical content is perhaps an indication of a spatially heterogeneous nature of the magma chamber in terms of its major elemental composition.

A process known to cause variations in a magma's chemical composition on a spatial scale is the preferred nucleation and/or growth of a certain mineral phase (Namur *et al*., 2015). A similar process is deemed responsible for variation in the modal abundance of plagioclase compared to mafic minerals in the Bjerkreim-Sonkdal layered intrusion in Norway (Namur *et al*., 2015). For example, the nucleation and growth of a diopside crystal would deplete the adjacent melt in both Mg and Ca. If the rate of depletion exceeds the rate of diffusion of chemical elements towards the depleted zone, this could inhibit diopside nucleation in the adjacent melt. As a consequence of Ca depletion, the composition of the adjacent melt would shift in the direction of the forsterite-diopside cotectic (see Figure 6.4). Latent heat released during the crystallisation of diopside can inhibit crystallisation of the adjacent melt (Namur *et al*., 2015), possibly causing the composition of the adjacent melt to cross the forsterite-diopside eutectic and into the forsterite field without any further crystallisation in the magma. As the adjacent magma starts to cool, olivine crystallisation will initiate in the depleted zone and the melt composition would shift back towards the diopside corner of the system. This process causes the melt to oscillate across the forsterite-diopside cotectic.

The variation in the abundance of hornblende in the intrusion is perhaps the product of a similar process. A high abundance of hydrous phases such as hornblende and biotite in a rock generally serves as evidence that the parental magma was rich in water (Barclay & Carmichael, 2004). Since hornblende only forms during the hydration of primarily augite, the water content of the magma is likely to affect how much hornblende would form. Because olivine and augite both exclude water during crystallisation, the melt surrounding regions of crystallisation is likely to be enriched in water. This could lead to the formation of higher modal abundances of hornblende in some regions of the magma chamber, while it is scarcer in others.

As discussed previously, enstatite likely formed during the later stages of magmatic crystallisation, and involves a peritectic reaction between olivine and magmatic silica. The modal abundance of enstatite is too low in this rock type to provide a sensible explanation for its variation in abundance across the intrusion.

6.2.1.2 The olivine-hornblende gabbronorite

The next step is to unravel the origin of the fine-grained, recrystallised olivine-hornblende (sample CB47) that forms part of the Ww outcrop. When its chemistry is compared to that of

the rest of Ww, it contains higher concentrations of incompatible elements such as Y, Zr, alkalis, P_2O_5 (Appendix D), and REE (Appendix G), hinting at a more evolved composition. Interestingly it contains very high Ni and Cr contents (898 ppm and 3042 ppm compared to an average of 395 ppm and 2076 ppm for the ultramafic rocks of Ww, respectively) implying that the intrusion is more primitive in terms of its geochemistry.

While fractional crystallisation of olivine and augite will raise the concentration of incompatible elements, it will also dramatically deplete the melt in Ni. This implies that olivine-hornblende gabbronorite CB47 is unlikely to be a product of fractional crystallisation from the magma responsible for the formation of ultramafic rocks from Ww. An alternative explanation is that this represents a chilled margin of the magma chamber in which Ww formed. Chilled margins typically have compositions that are much closer to the composition of the parental magma as their shorter cooling histories do not allow much fractionation to occur (they are emplaced adjacent to the cooler country rock and crystallise more rapidly). Thus, they are typically richer in incompatible elements and contain fewer compatible elements than the associated cumulates (Godel *et al*., 2011; Sen, 2014). This can explain the higher concentration of incompatible elements in olivine-hornblende gabbronorite CB47 and its finer-grained nature when compared to the ultramafic portion of Ww, but once again it fails to explain its higher Ni concentration. As discussed in section 5.6.1, this sample also displays a flatter HREE slope that is unmatched in the ultramafic rocks of Ww. All of this leads to the conclusion that CB47 might not be directly related to the remainder of Ww.

6.2.2 Formation of the Koedoesfontein Complex

6.2.2.1 Wehrlite-clinopyroxenite

These rocks primarily differ from one another in terms of the modal abundance of augite and olivine. In contrast to Ww, plotting olivine against common indicators of magmatic evolution (see Figure 6.5) reveals that olivine is typically more abundant when the rock has a more primitive composition. For example, the incompatible elements Zr and Y are less abundant when olivine is more common, while the Mg# tends to be higher when the olivine content is higher. In addition, when plotting the augite and forsterite content of the rock on the Fo-Di-Si system, the majority of samples lie at the forsterite side of the forsterite-diopside cotectic (see Figure 6.6). This implies that rocks from KC that contain more abundant olivine generally crystallised from a more primitive magma. Variations from this trend can be ascribed to oscillations across the cotectic, as described for Ww in section 6.2.1.1. Intercumulus plagioclase, observed in sample 304 (Figure 4.19 A), probably formed during

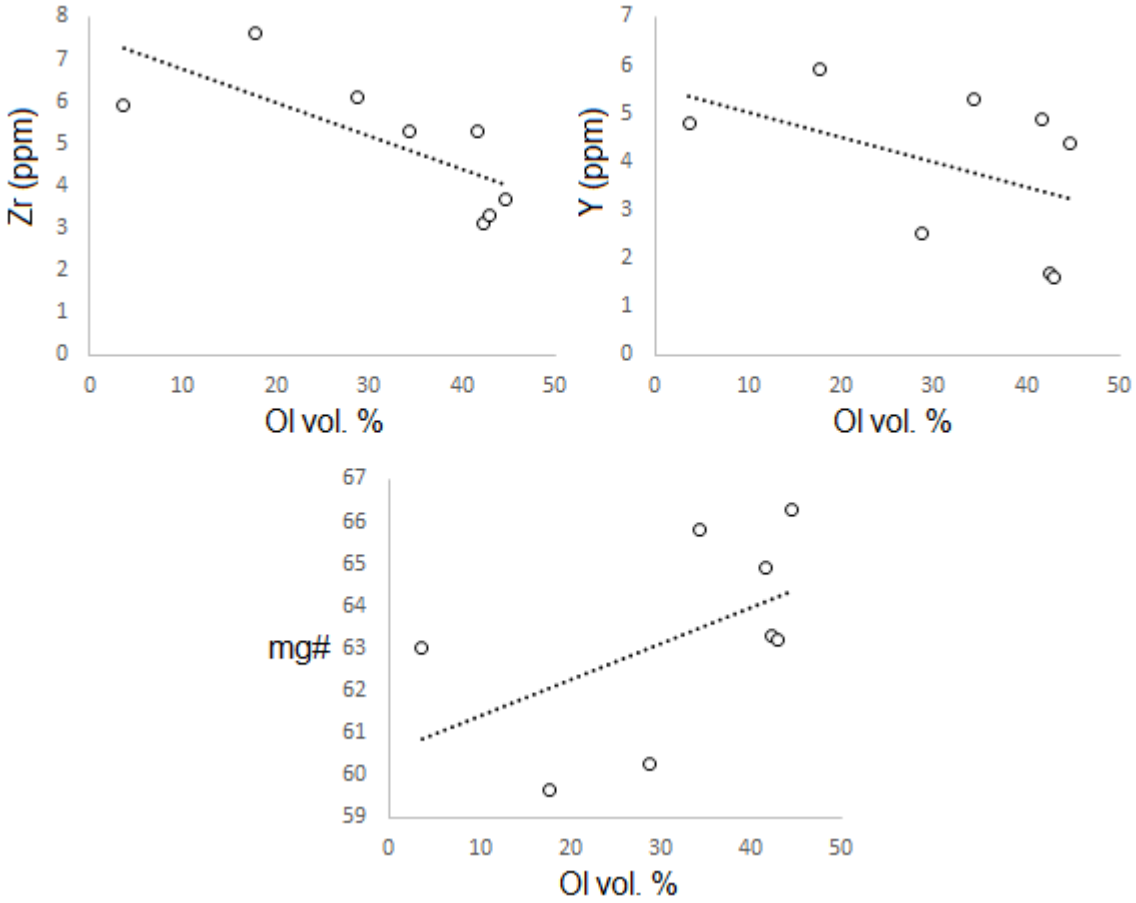

Figure 6.5: Olivine content of KC wehrlite-clinopyroxenite plotted against common indicators of magmatic evolution with associated trend lines.

the final stages of crystallisation after the melt became saturated in plagioclase during the formation of olivine and augite.

6.2.2.2 Enstatite-bearing samples RB3, RB20, and WK32

A question that remains to be answered is whether or not the enstatite-bearing rocks are related to the wehrlite-clinopyroxenite sill of KC. In the typical differentiation trend of tholeiitic magmas, olivine cumulates usually form during the early stages of magmatic crystallisation and is later replaced by orthopyroxene as the silica content of the system increases (Tegner *et al*., 1999; Winter, 2010). This would imply that the liquid responsible for the formation of the wehrlite-clinopyroxenite advanced along the forsterite-diopside cotectic (see Figure 6.6) until it reached the peritectic (point (a) on Figure 6.6), leading to the replacement of olivine during a reaction with magmatic silica. Plagioclase can join crystallisation if the magma becomes saturated in components necessary to construct plagioclase during crystallisation of the mafic silicates in the case of gabbronorite (RB3) and norite (WK32). The fact that

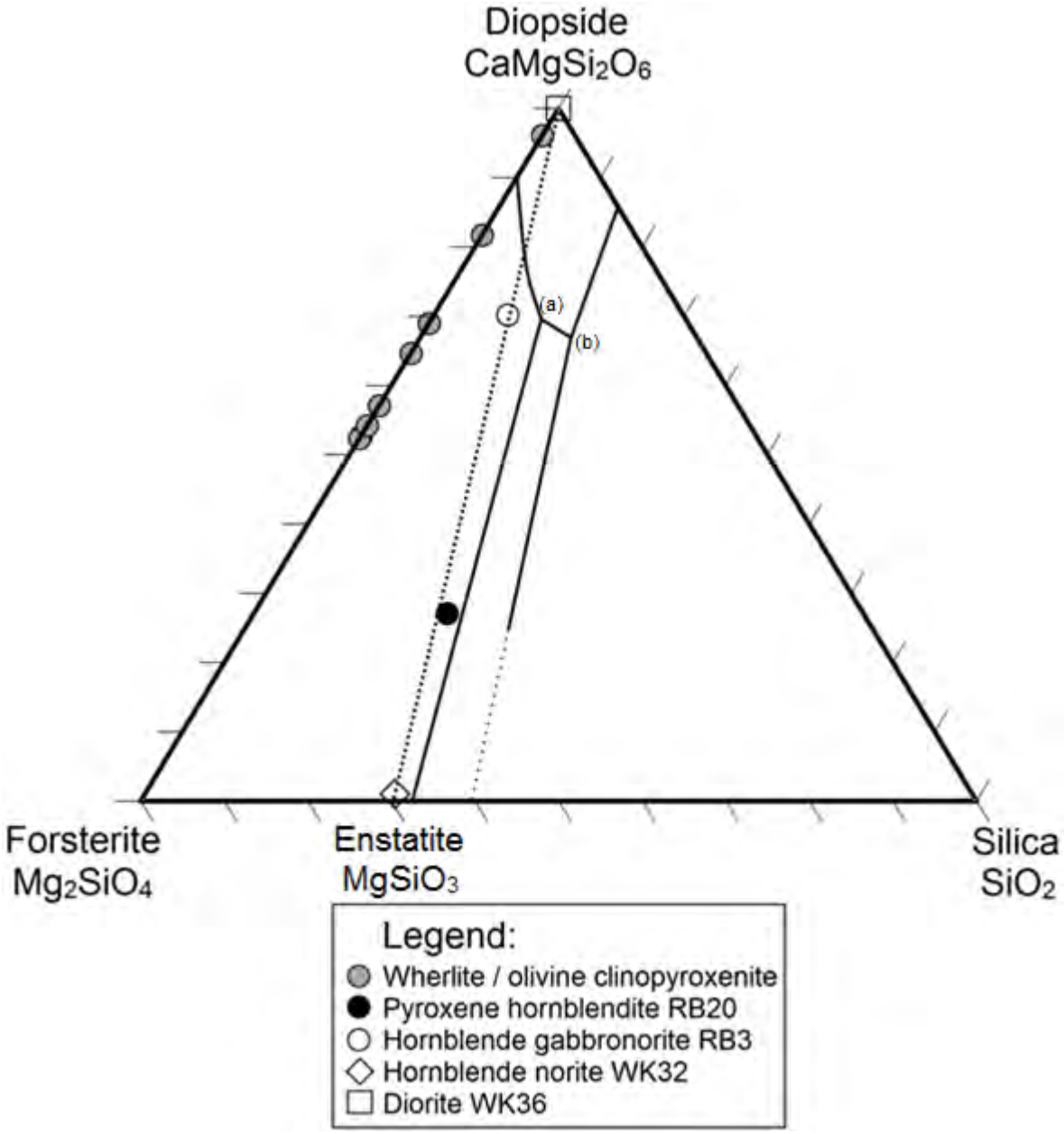

Figure 6.6: KC samples plotted on the forsterite-diopside-silica system of Kushiro (1972) at anhydrous conditions and atmospheric pressure. (a) Peritectic point; (b) Eutectic point.

gabbronorite (RB3) plots within the forsterite field indicates that olivine was probably one of the first minerals to crystallise, similarly to the wehrlite.

Further support for the proposition that these rocks formed from a differentiated magma responsible for the formation of the wehrlite-clinopyroxenite is the fact that they are generally enriched in incompatible elements and depleted in compatible elements. They do, however, show differences in terms of trace element ratios, with gabbronorite (RB3) and hornblendite (RB20) possessing positive Rb anomalies which is absent in the wehrlite-clinopyroxenite. Gabbronorite (RB3), hornblendite (RB20), and norite (WK32) also have a larger Zr/Y ratios of 1.57, 4.2, and 3.79 respectively, while this ratio varies between 0.84 and 1.30 in the

wehrlite-clinopyroxenite. In addition, gabbronorite (RB3) has a flatter HREE slope in comparison to the ultramafic rocks (section 5.6.2). If hornblendite (RB20) crystallised from the same magma that produced the wehrlite-clinopyroxene sill, some process other than fractional crystallisation would be required to shift the composition of the melt across the (a) peritectic towards the (b) eutectic on Figure 6.6 due to the presence of quartz in this sample.

In a study performed by Tegner *et al*. (1999) on the Hasvik Layered Intrusion in Norway, it was found that the assimilation of crustal materials can enhance the tholeiitic nature of basaltic magmas if the assimilated material is rich in silica. This has a tendency to decrease olivine and clinopyroxene content of the rock and increase orthopyroxene abundance. It is well known that the assimilation of crustal materials can lead to Rb, K, and Zr enrichment of the basaltic magma. Perhaps it is possible that mineralogical and chemical differences of the enstatite-bearing rocks and the wehrlite-clinopyroxenite are due to crustal assimilation.

The Hasvik Layered Intrusion consists of 21% assimilated material, and is considered one of the most contaminated layered intrusions in the world (Tegner *et al*., 1999). In spite of this, the Hasvik Layered Intrusion shows no significant variation in its Zr/Y ratio across different lithological units as is the case for KC. It thus seems unlikely that crustal contamination would have had such a large impact on the trace element composition of KC. It is thus concluded that the enstatite-bearing rocks from KC is not related to the wehrlite-clinopyroxenite sill, and represents a different magmatic lineage.

6.2.2.3 Diorite sample WK36

Diorite from KC had the most evolved composition in terms of its trace element concentrations. It also displays similar patterns on spider diagrams as the wehrlite-clinopyroxenite of KC, as discussed in section 5.5.2. Although it also contains an elevated Zr/Y ratio of 1.78, it does not possess a negative Zr anomaly as observed for the enstatite-bearing rocks. Thus, the diorite appears to be more closely related to the wehrlite-clinopyroxenite and might have formed from a similar, but more differentiated magma.

A problem associated with this viewpoint is the crystallisation sequence observed in the diorite versus the one observed in the wehrlite-clinopyroxenite. In the wehrlite-clinopyroxenite, olivine forms first followed by augite and then plagioclase. In the diorite, augite forms first followed by plagioclase while no olivine grains are observed. To form the glomeroporphyritic texture as described in section 6.1.1.4 requires oscilation across an augite-plagioclase cotectic (such as the one shown in Figure 6.7), while the wehrlite-clinopyroxenite has to be situated around a forsterite-diopside cotectic.

As described previously (section 6.2.1.1), in-situ crystallisation of a mineral (such as olivine) can inhibit the formation of this mineral in other parts of the magma chamber. Consider the composition of a magma located at the point of the red circle on Figure 6.7. It is not considered unlikely that the parental magma of the wehrlite-clinopyroxenite sill would lie in a similar position, as forsterite, diopside, and plagioclase are all observed in sample 304 (see Figure 4.19 A). Because the composition of the magma lies in the forsterite field, olivine would fractionate from the magma. As chemical elements needed to construct olivine are extracted from the magma, the adjacent magma is depleted in components necessary to construct olivine and it progresses along the blue line. If sufficient latent heat is released into the adjacent magma, it is possible that no crystallisation would occur until the composition of the magma lies close to the diopside-plagioclase cotectic (indicated by the blue circle). As the magma cools, crystallisation would commence and the melt would be able to oscillate across the diopside-plagioclase cotectic as described in section 6.1.1.4.

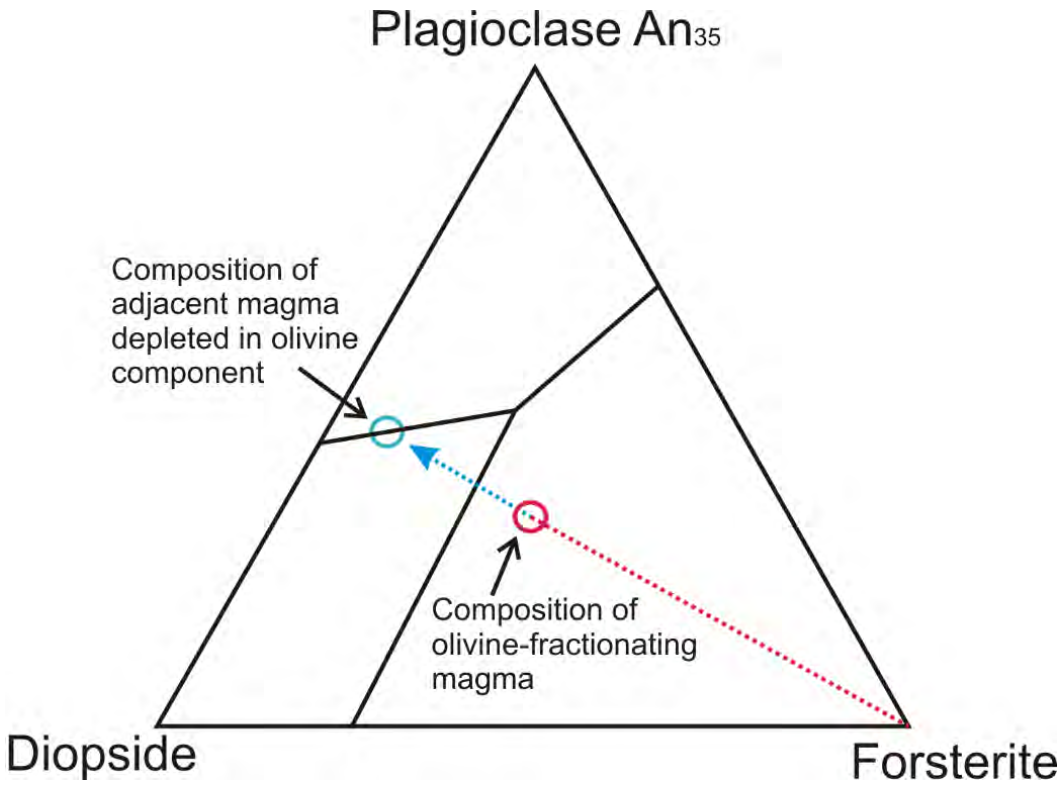

Figure 6.7: KC samples plotted on the Fo-Di-Si system of Kushiro (1972) at anhydrous conditions and atmospheric pressure (from Yoder & Tilley, 1962).

6.2.3 Formation of the Rietfontein Complex

Mineralogical and geochemical variations observed in RietC will be discussed in four subsections based on the four groups of REE patterns observed in this intrusion (section 5.6.3). Sample collection localities and the group to which the samples belong are shown on

Figure 6.8, along with the variation in their Mg#. The formation of Group 3 rocks have important implications for the formation of Group 2 rocks and, therefore, the formation of Group 3 rocks will be discussed before Group 2.

6.2.3.1 Group 1

Group 1 only includes the lowermost olivine-hornblende clinopyroxenite layer of RietC. Both samples have similar olivine contents, and primarily differ from each other in terms of their modal hornblende and augite abundances (CB1 and CB2). When plotted on the Fo-Di-An_{35} ternary diagram (see Figure 6.9), both samples plot on the diopside side of the forsterite-diopside eutectic, indicating that augite was probably the first silicate mineral to crystallise in this rock layer. Because the formation of hornblende entails the reaction of augite with water, the water content of the magma likely decreased upwards in the profile as the modal abundance of hornblende decreases from CB1 to CB2 (see Figure 4.10).

In terms of its geochemistry, Zr (Figure 5.10), K_2O, and P_2O_5 (Figure 5.5) declines and the En endmember content of augite and Fo endmember content of olivine increases (Figure 5.11) from olivine-hornblende clinopyroxenite sample CB1 to CB2, and points to a more primitive composition upwards in the profile. In addition, an increase in Mg# (Figure 6.8) and the rise in the Cr content of the augite (Figure 5.12) also support this notion. Although a small decrease in the Ni contents of olivine (Figure 5.12) goes against this trend, in general the geochemistry suggests that this layer of olivine-hornblende clinopyroxenite becomes more primitive higher up in the profile.

This might suggest that the magma that intruded to form olivine-hornblende clinopyroxenite CB1 mixed with one (or several) more primitive magmas later on to produce CB2. An alternative explanation is that the chemistry of olivine-hornblende clinopyroxenite CB1 was altered by equilibration with intercumulus liquid, a process inferred to have occurred in the ultramafic series of the Stillwater Complex (Raedeke & McCallum, 1984). Intercumulus liquid is typically depleted in compatible elements (such as Ni, Cr, and Mg) and enriched in incompatible elements (such as Zr, Y, and REE) because of the extraction of cumulate phases during magmatic crystallisation. Exchange between the cumulate minerals and the late magma can give them a more evolved composition. The magma in contact with the cooler floor of the magma chamber would crystallise faster and larger proportions of melt will

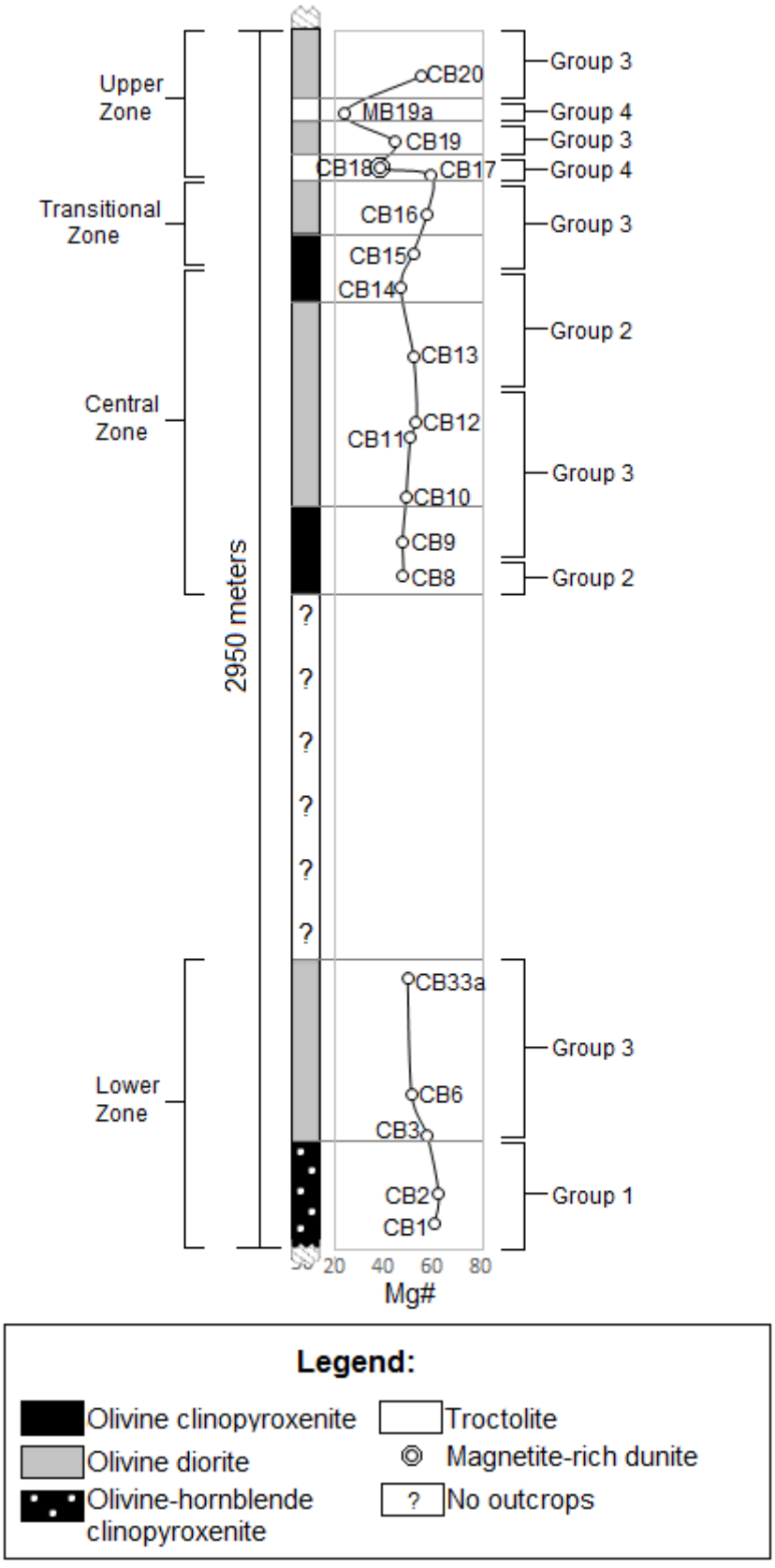

Figure 6.8: Variation in Mg# perpendicular to the layering of RietC.

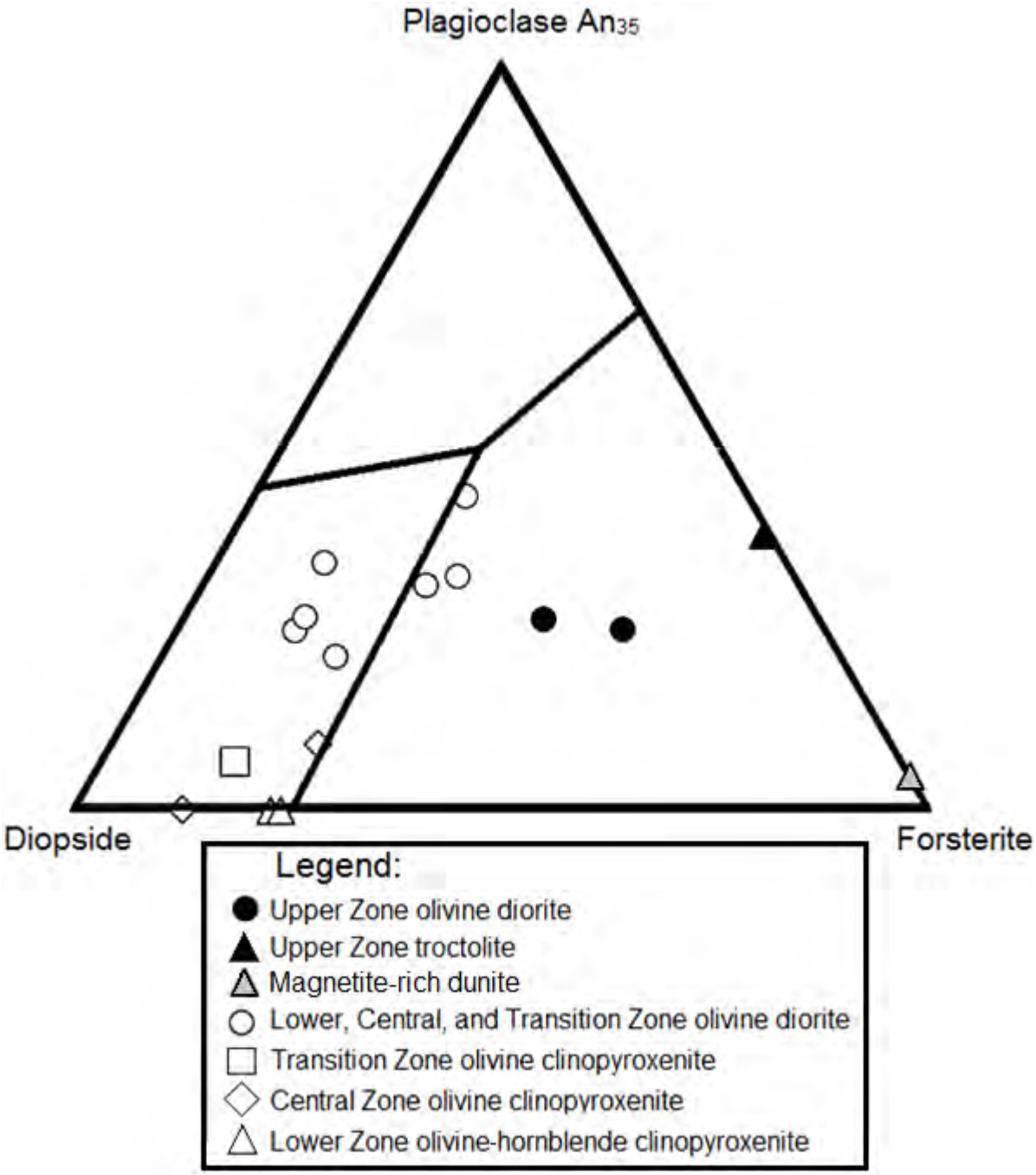

Figure 6.9: Samples of different rock types from RietC plotted on the forsterite-diopside-anorthite$_{35}$ ternary diagram to establish the order of crystallisation of olivine, augite, and plagioclase. An anorthite content of 35 mol. % is chosen to reflect the composition of the plagioclase from RietC (from Yoder & Tilley, 1962).

become trapped between the cumulates, resulting in a more evolved composition for the underlying rocks compared to those that are located higher up stratigraphically.

6.2.3.2 Group 3

With the exception of olivine diorite CB13, Group 3 contains all the olivine diorite samples from RietC and two olivine clinopyroxenite samples, namely CB9 and CB15. In terms of its petrography, no conclusive evidence was found to suggest the order of crystallisation in the olivine diorite. With the exception of olivine diorite from the Upper Zone, all olivine diorite samples from RietC plot in the vicinity of the diopside-forsterite cotectic (see Figure 6.9). However, due to the presence of forsterite, augite, and plagioclase in these rocks, the melt composition probably lies close to the Fo-Di-An_{35} eutectic. The fact that the samples plot towards the base of the diagram away from the eutectic implies that some crystallisation of augite and olivine preceded plagioclase crystallisation. Olivine was probably the first mineral to crystallise in the Upper Zone olivine diorite due to the fact that these samples plot deeply into the forsterite field.

Bisschoff (1969) proposed that olivine diorite from RietC formed from a more differentiated magma responsible for the formation of the olivine clinopyroxenite layers (section 2.5.3). If that is the case, one would expect the olivine diorite to be more evolved geochemically than the ultramafic layers. In order to test this possibility, the geochemical characteristics of olivine diorite samples will be compared to their underlying ultramafic layers.

In the Lower Zone, olivine diorite CB3 appears to be more primitive than the underlying olivine-hornblende clinopyroxenite CB2 in terms of an increase in the olivine's Fo endmember content (Figure 5.11), the Cr and Ni contents of the augite and olivine (Figure 5.12), respectively, and a decline in the contents of the incompatible elements Ce (Appendix H), Zr, Y (Figure 5.10) and Rb (Figure 5.9). The En endmember content of the augite (Figure 5.11) is inconclusive regarding the relative change in primitivity from CB2 to CB3. In contrast to the mineral chemistry, whole-rock Mg# (Figure 6.8) decreases slightly from CB2 to CB3, which is consistent with fractional crystallisation. However, the decrease of Mg# might simply be the product of a higher modal abundance of magnetite in olivine diorite CB3, and might not be indicative of a more evolved composition.

In the Central Zone, olivine diorite CB10 appears more primitive geochemically than the underlying olivine clinopyroxenite CB9 in terms of lower K_2O, P_2O_5 (Figure 5.5), Zr, Y (Figure 5.10) and Ce (Appendix H) contents, a higher Mg# (Figure 6.8), and higher Cr (Figure 5.12) and Fo endmember contents in olivine (Figure 5.11). Decreasing En endmember content (Figure 5.11) and Cr (Figure 5.12) of the augite along with a decrease in Ni concentration in olivine (Figure 5.12) goes against this observed trend, but the majority of the geochemical data supports a more primitive composition of the olivine diorite. The olivine diorite (CB16) of

the Transitional Zone is no exception, as a dramatic decrease is observed in Zr, Y (Figure 5.10), Ce (Appendix H), K_2O, and P_2O_5 (Figure 5.5) concentrations compared to the underlying olivine clinopyroxenite CB15. This is accompanied with an increase in whole-rock Mg# (Figure 6.8) and Fo endmember (Figure 5.11) and Ni content (Figure 5.12) of the olivine.

As a melt's magnesia content decreases and the silica content increases, trace elements generally tend to become more compatible with crystallising phases (Bèdard, 2005; 2007; 2014; Rollinson, 1993). This gives one plenty of reason to believe that the olivine diorite layers should have higher concentrations of incompatible trace elements than underlying ultramafic layers if it was simply produced by means of fractional crystallisation. According to partition coefficients compiled by Rollinson (1993), plagioclase also has a higher compatibility with Ce than olivine and pyroxene, although the olivine diorite still has a lower concentration of this trace element. Although the change in concentration of these elements are small in most cases, the possibility that olivine diorite crystallised from more primitive magmas than the underlying ultramafic layers has to be considered.

The more primitive nature of olivine diorite from the Lower Zone might be due to variations in the H_2O content of the melt. The abundance of hydrous phases (such as hornblende and biotite) in igneous rocks can give one an indication of the relative abundance of H_2O in the melt (Barclay & Carmichael, 2004). In magmas, water tends to inhibit the polymerisation of silicate tetrahedrons due to the replacement of O^{2-} by OH^- ions. This neutralises the charge of the tetrahedron and subsequently increases the difficulty of producing viable crystal nuclei. As a result, H_2O has a habit of lowering the temperature of the liquidus and eutectic point in silicate magmas (Vernon, 2004). Variation in the H_2O-content of melts has also been known to change the crystallisation sequence of basaltic melts (Berndt *et al*., 2005), and has produced cyclic mafic- and ultramafic layers that are geochemically indistinguishable from one another in the famous Oman ophiolite (Abily *et al*., 2011).

Berndt *et al*. (2005) have investigated the effect of water on the crystallisation sequence of synthetic MORB materials with variable chemical compositions (see Berndt *et al*., 2005 for details). These materials were subjected to melting and subsequent crystallisation under different H_2O contents and oxygen fugacity conditions. During cooling of the magma, olivine was usually one of the first phases to form, followed by simultaneous crystallisation of clinopyroxene and plagioclase. In the case of one of the relatively silica-rich synthetic MORB materials, clinopyroxene formed prior to plagioclase, while no olivine crystallisation occurred. In both cases, however, it was found that the formation of plagioclase was delayed at higher H_2O contents.

For example, consider a mafic magma with an H_2O content and temperature at point one on Figure 6.10. At these conditions, olivine will be the only phase to crystallise. During cooling of the magma at a constant H_2O content in the direction of point 2, clinopyroxene will start to crystallise at point X. If olivine and clinopyroxene sink to the bottom of the magma chamber, a layer of olivine clinopyroxenite might form. After the magma reaches point 2, consider the addition of a hotter, more primitive magma that has a lower H_2O concentration. This shifts it in the direction of point 3. When it crosses point Y, plagioclase start to crystallise, and an olivine diorite layer forms that is geochemically more primitive than the underlying olivine clinopyroxenite. Because the Lower Zone olivine clinopyroxenite contains much more hornblende than the olivine diorite, it probably also contained much more H_2O. This mechanism might, therefore, be responsible for the origin of layering in the Lower Zone of RietC. However, due to the low abundance of hydrous phases in the remainder of RietC, this mechanism is less likely to be responsible for the layering produced in the remainder of the Complex.

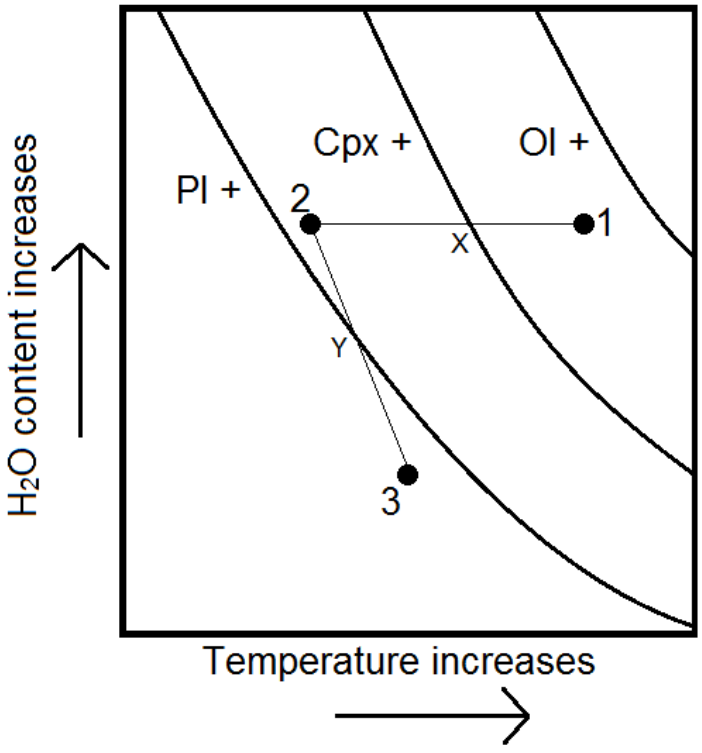

Figure 6.10: Generalised effect of temperature and H_2O content of the magma on the crystallisation of olivine, clinopyroxene, and plagioclase based on the experimental results of Berndt *et al*. (2005) to describe the formation of the Lower Zone of RietC. Minerals indicated on the diagram start crystallising on the left-hand side of the curved lines. See text for details.

An alternative mechanism that can explain the formation of olivine diorite throughout the entire intrusion is magma mixing. An interesting feature of Group 3 rocks is that their intra-REE ratios lie intermediate between those of Group 2 and 4 rocks. For example, when

mixing the REE contents of olivine clinopyroxenite CB8 of Group 2 and troctolite MB19a from Group 4 yields a more comparable REE pattern to that of Lower Zone olivine diorite CB3 (Figure 6.11). Because this theoretical hybrid magma contains a lower REE abundance than olivine diorite CB3, it might indicate that the hybrid magma might have undergone some crystal fractionation before it was emplaced to form the Lower Zone olivine diorite of RietC.

Using the REE values from olivine clinopyroxenite CB8 and mixing it with the REE values of troctolite MB19a in a 3:2 ratio, respectively, a very similar REE pattern to olivine diorite CB16 from the Transitional Zone is produced (see Figure 6.12 (a)). An exception is the absence of a Eu anomaly in the theoretical hybrid. This is because plagioclase accumulation has the ability to change the ratio of Eu relative to the other REE, while REE ratios generally stay constant during crystal fractionation. Little plagioclase is present in Group 2 olivine clinopyroxenite, thus preventing the formation of a Eu anomaly in the theoretical hybrid. Even more convincing results are produced for olivine diorite CB19 from the Upper Zone (see Figure 6.12 (b)). This time the theoretical hybrid was produced by mixing olivine clinopyroxenite CB14 with sample MB19a in a 1:2 ratio.

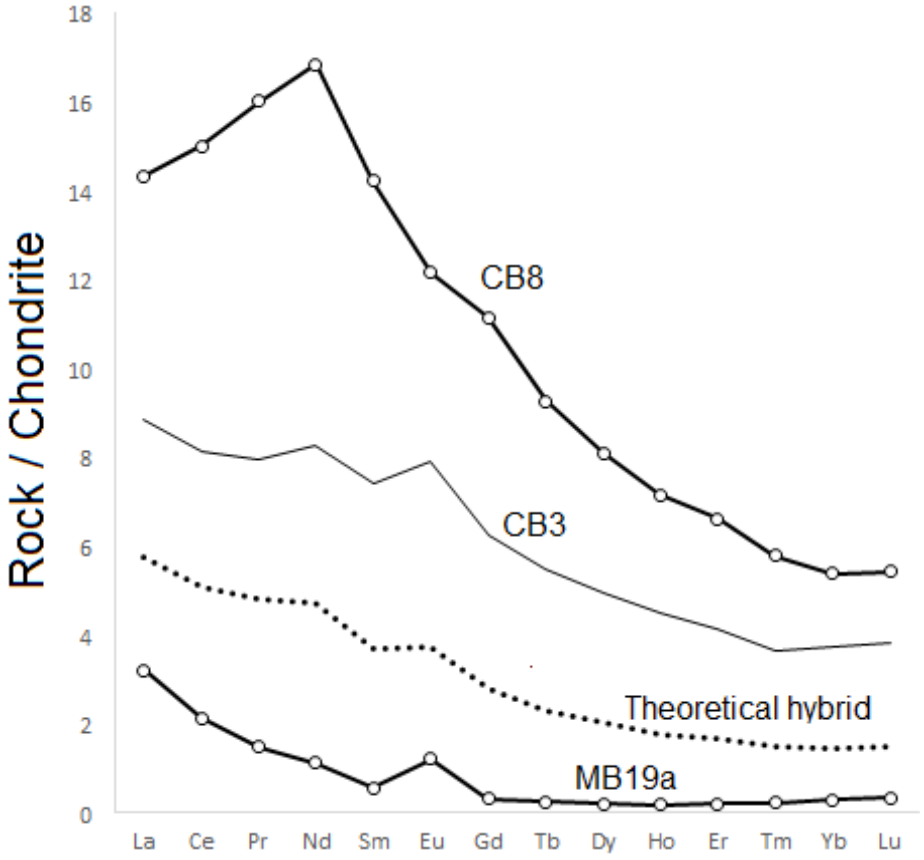

Figure 6.11: Chondrite-normalised REE diagram with samples olivine clinopyroxenite CB8, olivine diorite CB3, and troctolite MB19a and a theoretical hybrid consisting of 22.9 wt. % troctolite MB19a and 77.1 wt. % olivine clinopyroxenite CB8.

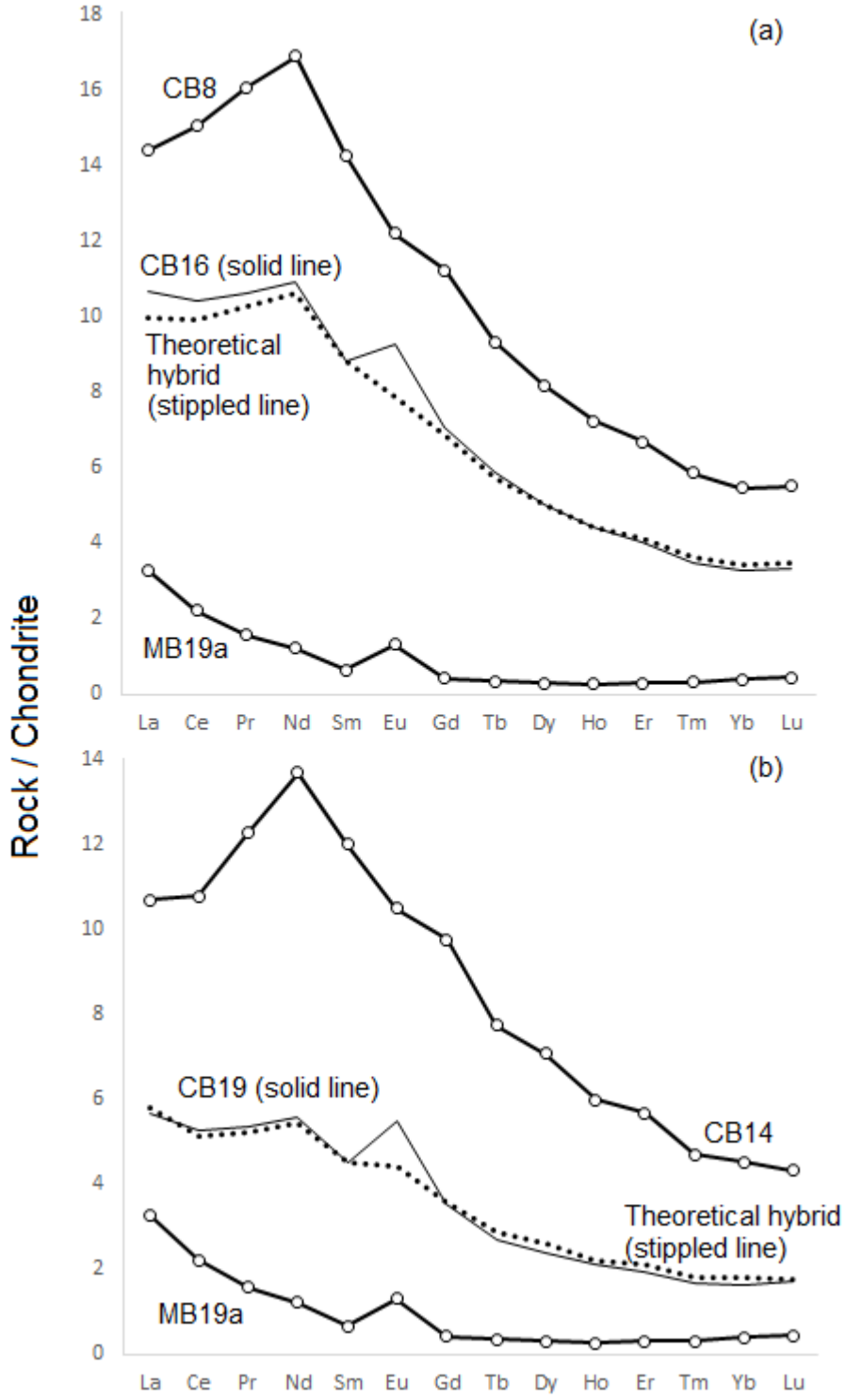

Figure 6.12: Chondrite-normalised REE diagram with (a) samples olivine clinopyroxenite CB8, olivine diorite CB16, and troctolite MB19a and a theoretical hybrid consisting of 22.9 wt. % troctolite MB19a and 77.1 wt. % olivine clinopyroxenite CB8.

Because Group 2 rocks primarily consist of olivine and augite, it is inferred that the magma crystallised along the forsterite-diopside cotectic on the Fo-Di-An ternary diagram, while the Group 4 troctolite would crystallise along the anorthite-forsterite cotectic as this rock

primarily consists of plagioclase and olivine (see Figure 6.13). When these two magmas mix, crystal mushes of olivine and augite from the Group 2 magma and olivine and plagioclase from the Group 4 magma could mix to produce an olivine diorite layer. In addition, the composition of the magma is likely to shift closer to the Fo-Di-An eutectic, meaning that simultaneous crystallisation of olivine, augite, and plagioclase will ensue shortly after the magma mixing has occurred (see Figure 6.13).

Not all Group 3 olivine diorite layers contain intermediate REE contents between Group 2 and 4 rocks like the examples shown in Figures 6.11 and 6.12 (compare the abundances of REE from Group 2 and 3 rocks on Figure 5.25). It is inferred that rocks with higher REE contents experienced additional fractional crystallisation (perhaps in a deeper-seated magma chamber) before being emplaced into RietC either before or after magma mixing has occurred.

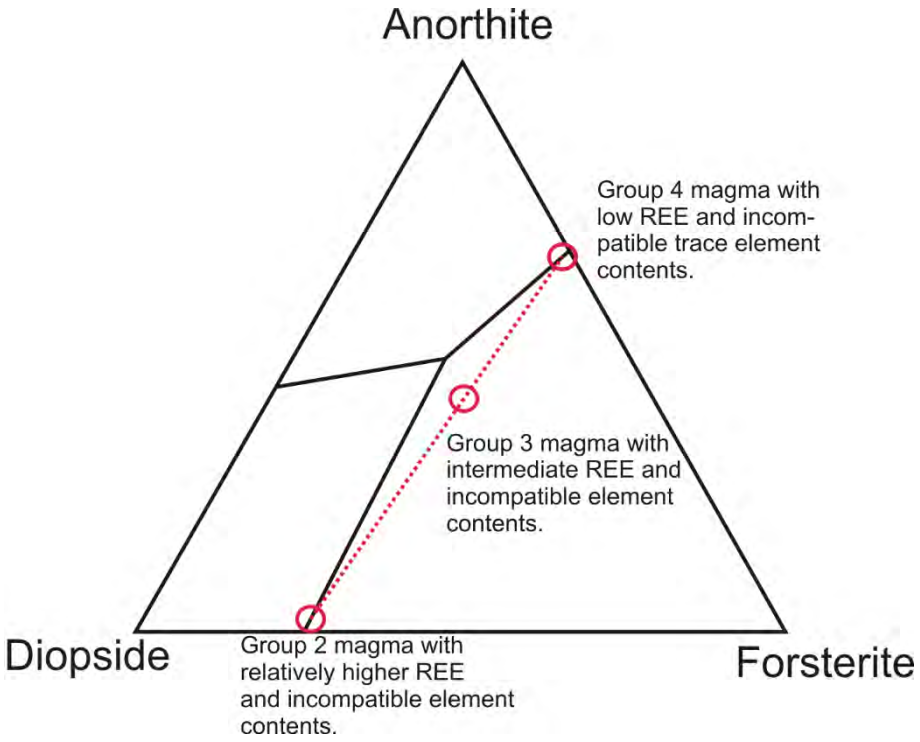

Figure 6.13: Forsterite-diopside-anorthite$_{35}$ ternary diagram which displays the inferred positions of the magmas deemed responsible for the formation of Group 2 and 4 rocks. When these two magmas mix, a hybrid will be produced with a composition located somewhere on the red line depending on the relative proportions of the two magmas. This can produce the Group 3 magma with a composition closer to the eutectic of the system. After the Group 3 magma has undergone some olivine fractionation, it will reach the eutectic and simultaneous crystallisation of olivine, augite, and anorthite will ensue, producing an olivine diorite layer.

This explanation is more problematic to apply to the olivine clinopyroxenite samples CB9 and CB15 that also belong to Group 3. Why would these rock layers possess ultramafic

mineralogical assemblages, while olivine diorite results when mixing Group 2 and 4 magmas? Perhaps the parental magma responsible for their formation simply consists of a larger fraction of Group 2 magma relative to Group 4. They do not, however, possess REE patterns that are more alike to Group 2 rocks than the Group 3 olivine diorite. An alternative explanation is that these rocks formed by mixing of Group 2 magma and a more differentiated Group 4 magma. If a differentiated Group 4 magma mixes with a primitive Group 2 magma, the composition of the hybrid is likely to fall somewhere on the forsterite-diopside cotectic, as shown in Figure 6.14. An olivine clinopyroxenite layer would thus be produced with an REE pattern similar to that of Group 3 rocks.

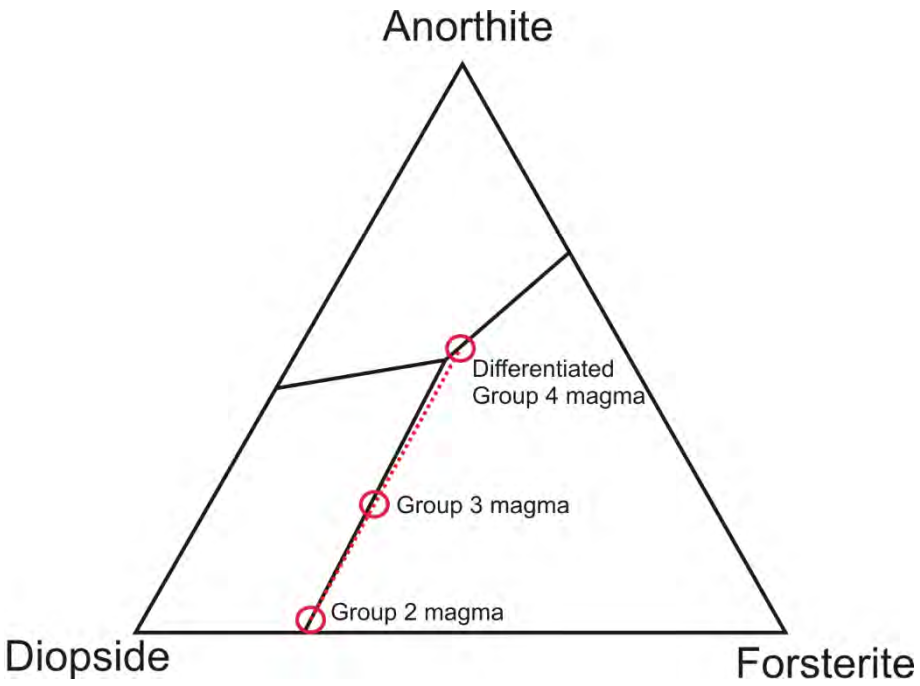

Figure 6.14: Forsterite-diopside-anorthite$_{35}$ ternary diagram which displays the inferred positions of a Group 2 magma and a differentiated Group 4 magma. When these two magmas mix, a hybrid (Group 3) will be produced with a composition located somewhere on the red line depending on the relative proportions of the two magmas. Because the hybrid lies on the forsterite-diopside cotectic, these two minerals would crystallise simultaneously to produce an olivine clinopyroxenite layer.

6.2.3.3 Group 2

The parental magma responsible for the formation of Group 2 rocks crystallised to form the basal layer of the Central Zone of RietC (sample CB8), as well as a portion of olivine diorite (CB13) and olivine clinopyroxenite (CB14) of the upper part of the Central Zone. The ultramafic rocks from Group 2 RietC follows a similar crystallisation sequence as the one described for the Lower Zone olivine-hornblende clinopyroxenite as they plot in a similar

position on Figure 6.9, with the exception of intercumulus plagioclase that starts to crystallise after the formation and settling of cumulus olivine and clinopyroxene.

In section 2.5.3 it is noted that Bisschoff (1969) proposed that the olivine clinopyroxenite layers of the Central Zone formed due to the intrusion of a more primitive magma at this stage that inhibited plagioclase crystallisation. Because no outcrops could be found directly south of the Central Zone, it is not possible to assess whether the southern olivine clinopyroxenite layer formed due to the addition of a more primitive magma. The northern olivine clinopyroxenite layer seems to become more evolved compared to the underlying olivine diorite in terms of decreasing En endmember content of augite (Figure 5.11), decreasing An content of plagioclase (Figure 5.11), decreasing Cr content of augite (Figure 5.12), and a decrease in the whole-rock Mg# (Figure 6.8). Although it does appear to become more primitive in terms of a decreasing Y (Figure 5.10) concentration and a small increase in the Fo endmember content of olivine (Figure 5.11), the majority of the geochemical data suggests that this rock layer is more evolved that the underlying olivine diorite.

The more evolved composition can be explained by considering the addition of Group 2 magma. This commences approximately at the point of olivine diorite sample CB13, which has an REE pattern characteristic of Group 2 rocks. This is met with a reduction of the plagioclase content at this section of RietC (Figure 4.10) as the composition of the melt moves away from the forsterite-diopside-plagioclase eutectic and onto the forsterite-diopside cotectic. Because the Group 2 parental magma typically contains higher concentrations of incompatible elements, this explains the more evolved composition of the Group 2 olivine clinopyroxenite compared to the surrounding diorite.

6.2.3.4 Group 4

All troctolite samples make up Group 4 of RietC. The appearance of troctolite CB17 overlying olivine diorite CB16 is consistent with the addition of more primitive Group 4 magma due to a decrease in K_2O, P_2O_5 (Figure 5.5), Zr, and Y (Figure 5.10), and an increase in Mg# (Figure 6.8). No mineralogical data is available across this boundary and could not be used to assess the relative primitivity of the troctolite layer. Although olivine diorite CB16 is considered to be a hybrid that formed during mixing of Group 2 and 4 magmas, an additional influx of Group 4 magma at the base of the Upper Zone finally shifted the composition of the magma away from the forsterite-diopside-plagioclase eutectic and into the forsterite field (see Figure 6.9), drastically reducing the sum of augite in the rock. After some fractionation of olivine, the melt would have reached the forsterite-plagioclase

cotectic. When plagioclase started crystallising along with olivine a troctolite layer formed. Due to the presence of a small modal abundance of oikocrystic augite, this mineral is inferred to have formed during the final stages of crystallisation when the melt reached the Fo-Di-An eutectic.

Soon after the formation of troctolite CB17, the magnetite-rich dunite (CB18) was deposited. This was accompanied by the formation of a large amount of modal magnetite. Not much geochemical information is available across the transition from troctolite CB17 to dunite CB18. A very small (perhaps insignificant) decrease in the K_2O and Zr concentrations are observed, while an increase is observed in the P_2O_5 content. Despite the fact that the dunite has a more primitive mineralogical composition, its relative primitivity could not be assessed geochemically with any certainty.

The formation of the northern troctolite sample MB19a atop the olivine diorite is consistent with the addition of more primitive Group 4 magma observed as a decrease in the K_2O, P_2O_5 (Figure 5.5), and Zr (Figure 5.10) concentrations. The dramatic decrease observed in the Mg# (Figure 6.8) is a product of the large amount of magnetite present in troctolite MB19a, and does not indicate a more evolved composition. No mineralogical data is available to assess the variation in the relative primitivity of the troctolite and the underlying olivine diorite.

- Origin of magnetite

In a study performed by Pang *et al*. (2008) on the lower section of the Panzhihua Intrusion in South-Western China, they found that magnetite-rich layers primarily form due to crystal settling. Magnetite was inferred to be one of the first phases to crystallise, and because of its high density, could sink relatively quickly in the magma and accumulate at the bottom to form economic Fe-Ti oxide deposits. Pang *et al*. (2008) also stated that crystal settling is likely to be the dominant mechanism responsible for the formation of magnetite layers in other intrusions throughout the world. If crystal settling is indeed responsible for the formation of magnetite deposits in RietC, one would need to explain why the underlying troctolite CB17, inferred to have crystallised from a similar magma as the magnetite-rich sample CB18, does not contain abundant magnetite. In the underlying Transitional- and Central Zone, the modal magnetite abundance as recorded in the thin sections never exceeds 3.2 vol. %. Unless the magnetite-rich dunite (CB18) was formed because of the addition of a magma that differs considerably from the one parental to troctolite CB17 that would crystallise a large amount of magnetite initially, some other process must be responsible for abundant magnetite crystallisation.

The crystallisation of magnetite could have occurred because of a variation in the oxygen fugacity (fO_2) of the magma. Increased oxygen content of magma has the ability to convert ferrous (Fe^{2+}) iron into ferric (Fe^{3+}) iron. While iron predominantly occurs in the Fe^{2+} oxidation state in silicates, both Fe^{2+} and Fe^{3+} is required to construct magnetite (Deer *et al*., 2013). Higher up in the Panzhihua Intrusion, variations in fO_2 has produced alternating layers of gabbros with varying contents of titano-magnetite that did not form due to crystal settling (Namur *et al*., 2015).

If a higher fO_2 is responsible for magnetite formation, what would be the source of the oxidising agent? The answer might lie in the country rock of RietC, namely the Chuniespoort Group dolomite (see section 2.5.3). When exposed to high temperatures, carbonate rocks are known to devolatise and release large quantities of CO_2 (Winter, 2010). The presence of calcite in some rocks of RietC (see section 4.4) does serve as an indication that the rocks were exposed to CO_2-bearing fluids. Bataleva *et al*. (2016) have found in experimental studies that ferrous iron has the ability to reduce CO_2, producing graphite (C) and ferric iron (Fe_2O_3) as products and can lead to significant magnetite crystallisation. Because the Panzhihua Intrusion is also located adjacent to carbonate rocks, Namur *et al*. (2015) has suggested that abundant magnetite has crystallised in some layers because of the injection of CO_2, causing fluctuations in the magma's fO_2. Dissolved CO_2 could have kept on increasing during the crystallisation of RietC until the fluid's concentration became high enough to initiate abundant magnetite crystallisation in the Upper Zone. The decrease in magnetite content in the olivine diorite that lies in between the magnetite-rich rocks might be due to the addition of Group 2 magma with a lower CO_2 content.

It is interesting to note that the two highest MgO and lowest FeO contents in olivine were recorded in samples CB18 and MB19a while it also contained the highest abundance of magnetite. The FeO/MgO ratio of silicate melts can be estimated using the following equation (Roeder & Emslie, 1970):

$$D_{olivine} = (FeO/MgO)_{olivine} / (FeO/MgO)_{melt}$$

Roeder and Emslie (1970) states that a $D_{olivine}$ value typically varies from 0.27 to 0.33 when using mole fractions. Using a $D_{olivine}$ value of 0.33 (which should give the highest FeO/MgO ratio for the melt), yields a $(FeO/MgO)_{melt}$ value of 1.26 for dunite CB18. This corresponds to a Mg# (in weight fractions) of the melt of 0.31. This is higher than the average for the RietC (0.29), despite the fact that the whole-rock contains much more iron. Perhaps this can be attributed to the presence of large quantities of ferric iron, which would more likely form part of a mineral with a spinel structure than being incorporated in olivine. This would, however,

imply that these rocks crystallised under exceptionally high fO_2 conditions that far exceed those anticipated for the majority of basaltic melts by Roeder and Emslie (1970).

An argument against high fO_2 conditions in the magma from which the magnetite crystallised is the size of the Eu-anomaly in the plagioclase-rich troctolite which is much larger compared to the olivine diorite samples (section 5.6.3). At high oxygen fugacities, Eu^{2+} is oxidised to Eu^{3+}, and the latter is incompatible with plagioclase (Bèdard, 2006; Weill & Drake, 1973). If a high oxygen fugacity is responsible for the formation of the magnetite, the Eu anomaly in plagioclase would likely be much smaller.

Liquid immiscibility is also known to cause crystallisation of iron-rich phases in magmas (Fischer *et al*., 2016; Jakobsen *et al*., 2005; Jakobsen *et al*., 2010; Lui *et al*., 2016; Velasco *et al*., 2016). Magmas that follow the tholeiitic trend of iron enrichment during crystal fractionation (section 5.3.2) can reach a point where the magma segregates in two immiscible liquids; one that is rich in iron and one that is rich in silica (Philpotts, 1978). The iron-rich separate usually occurs as small globules (Philpotts, 1978) that might be included in the silicate crystals (Velasco *et al*., 2016), while in other cases larger globules of the iron-rich magma can be attached to the side of a growing silicate mineral. As the silicate mineral attempts to grow around the iron-rich globule, lobate boundaries of the silicate arises (Philpotts, 1978). This process might explain the lobate boundaries of the plagioclase as observed in the magnetite-rich troctolite sample 52. However, hard evidence for liquid immiscibility is usually presented in the form of melt inclusions in minerals with contrasting compositions (some melt inclusions are rich in silica while others are rich in iron) (Fischer *et al*., 2016; Jakobsen *et al*., 2005, 2010; Lui *et al*., 2016; Velasco *et al*., 2016). No melt inclusions could be identified in the minerals from the magnetite-rich rocks from RietC. In spite of this, liquid immiscibility is considered the most likely mechanism responsible for the formation of abundant magnetite in RietC.

A summary of the processes considered responsible for the mineralogical and geochemical variations seen across RietC is given in Figure 6.15.

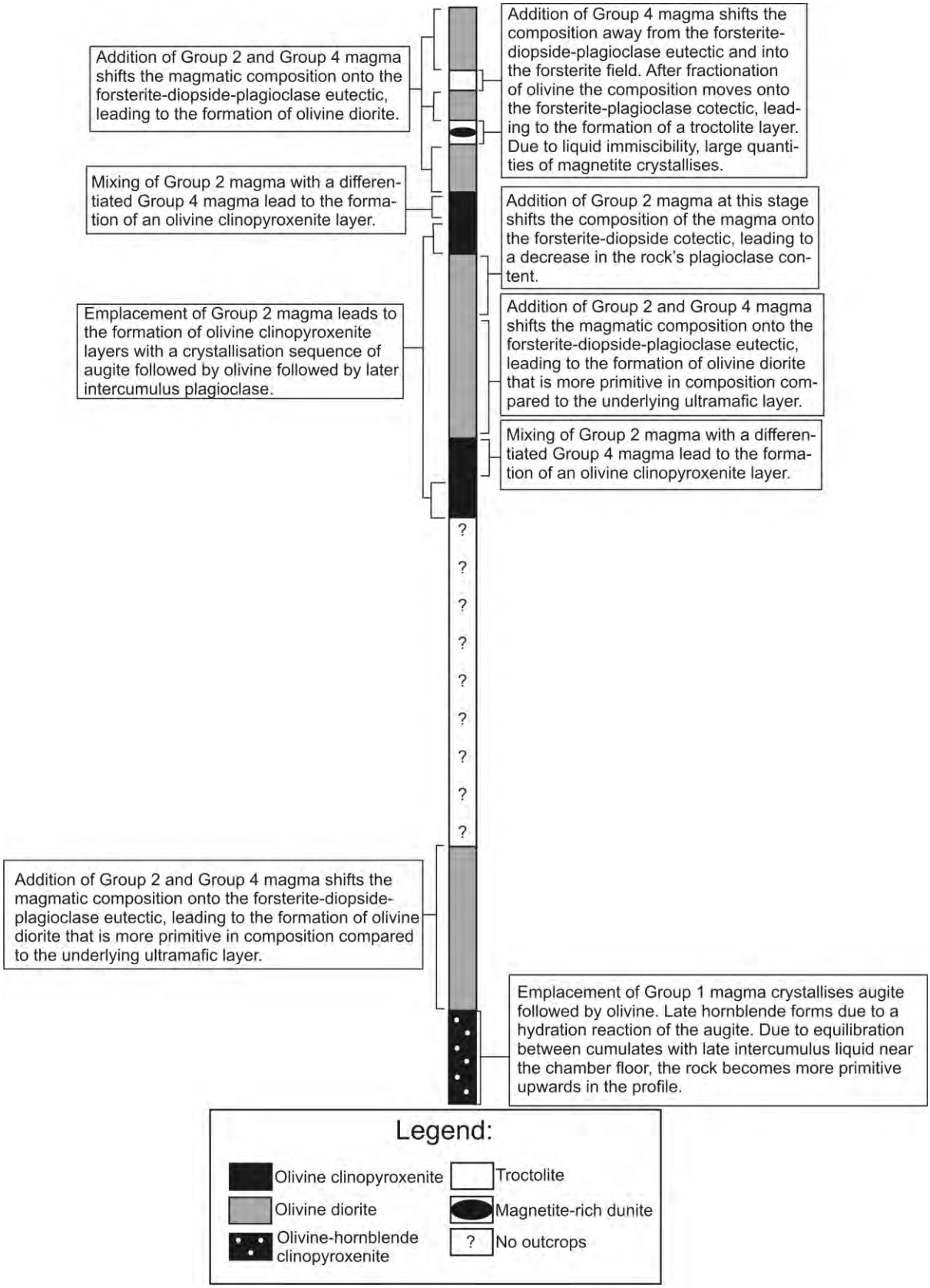

Figure 6.15: Summary for the processes deemed responsible for the variation in the mineralogical content across RietC.

6.3 DEFORMATION

Focus shifts to the deformation processes that had occurred after crystallisation. Deformation textures recorded during the petrographic analysis of Ww, KC, and RietC include grain boundary migration, fine-grained recrystallised olivine and hornblende with polygonal crystal shapes, deformation twins in hornblende and plagioclase, and PDFs in olivine from Ww. The latter two textures have already received attention in Chapter 4, and their means of formation will not be repeated here. In the final subsection, the possible cause for deformation is considered.

6.3.1 Sutured grain boundaries and grain boundary migration

A feature characteristic of the olivine-hornblende clinopyroxenite from Ww and the Lower Zone of RietC is the sutured nature of grain boundaries between augite grains (see Figures 4.11 and 4.12), the origin of which cannot be described by referring to magmatic crystallisation alone. Deformation processes after initial crystallisation can change grain shapes in igneous rocks long after sub-solidus conditions were reached (Vernon 2004). When a large amount of stress is applied to a rock body, changes will occur to reduce its strain and lower the total free energy of the system. One of these “strain reduction” processes that might occur is called “grain-boundary migration recrystallisation” (Vernon, 2004). While Suteanu and Kruhl (2002) state that this process is most commonly observed in quartz, they also mention that it can occur in any substance with a crystal structure. Deformed crystals typically contain a large number of dislocations in its crystal lattice (Bollinger *et al*., 2015; Piazolo *et al*., 2015) which increases the free energy of the system and thus its thermodynamic instability (Vernon, 2004).

During grain boundary migration, a grain of augite incorporates atoms into its own crystal structure from a neighbouring strained augite grain with a higher density of dislocations, therefore expanding its own boundary into that of the strained crystal (see Figure 6.16) (Suteanu & Kruhl, 2002; Vernon, 2004; Winter, 2010). The overall abundance of imperfections in the crystalline lattices is thus reduced during the process, and the free energy decreases. Vernon (2004) states that the movement path of the expanding crystals is unpredictable and apparently random, which leads to the uneven contacts observed in the minerals. This texture thus serve as an indication that stresses were applied on Ww and the Lower Zone of RietC sometime after its solidification to induce grain boundary migration.

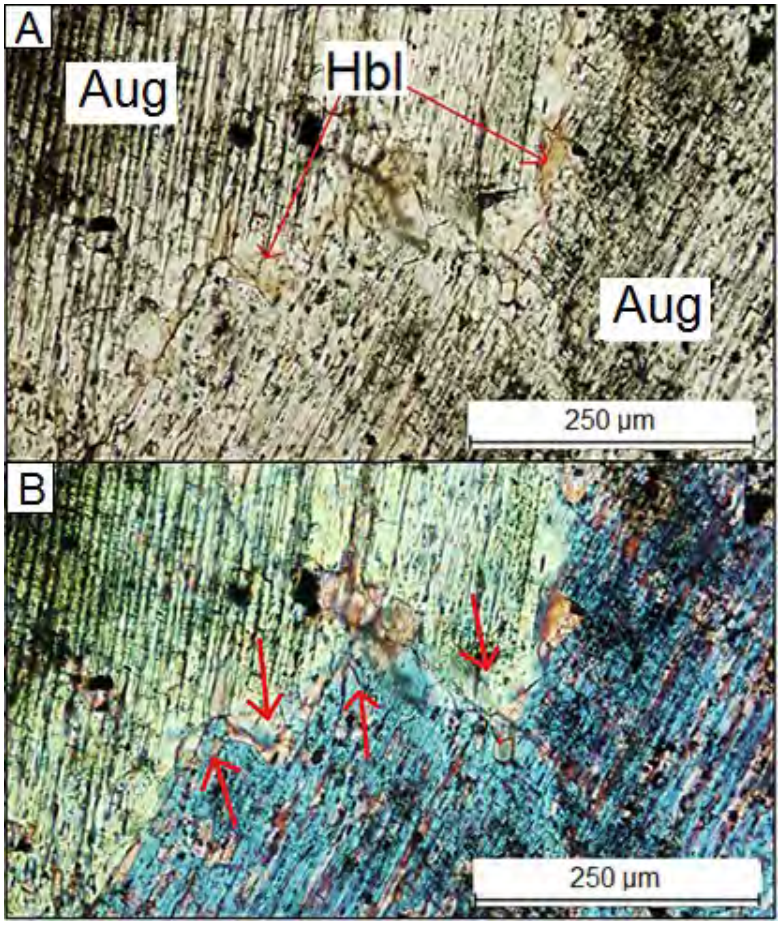

Figure 6.16: (A) Two augite grains with sutured grain contacts (sample W01). Notice the interstitial presence of brown hornblende between the two grains (PPL). (B) Same as A, using XPL. Red arrows indicate the assumed relative movement of the grain boundaries to produce the sutured texture.

High temperatures are required for a sutured texture to develop (Fitz Gerald & Stünitz, 1993; Suteanu & Kruhl, 2002), and the length of bulges that form during boundary migration increases with temperature (Suteanu & Kruhl, 2002). In addition, Vernon (2004) states that fluids present can greatly assist the grain boundary migration. Evidence of hydration of pyroxene can be seen as small fragments of hornblende in-between grain boundaries of the former mineral (see Figure 6.16), which indicate a hydration reaction of the pyroxene to form hornblende. This serves as evidence that some fluid was indeed trapped between clinopyroxene grains when the sutured texture developed.

6.3.2 Fine, polygonal mineral grains

As discussed in Chapter 4, some thin sections from Ww (Figure 4.16 and 4.32) and the troctolite from RietC (Figure 4.27) contained fine-grained granoblastic crystal aggregates with 120° degree triple-point grain boundary intercept angles. Vernon (2004) ascribes this

texture to recrystallisation, during which the mineral grains form planar, low-energy contacts. This texture is typical in ultramafic rocks, where the remaining heat after sub-solidus conditions are reached, can provide sufficient energy for recrystallisation to occur (Vernon, 2004). However, a different explanation must also account for the reduction in grain size. Tkalcec and Brenker (2015) described a similar texture in a deformed harzburgitic meteorite. They observed coarse-grained, rounded olivine grains in the harzburgite, while some patches contained finer olivine grains, with 120^{o} grain boundary intercept angles. The texture came about due to high stresses applied to certain areas in the rock that led to fracturing of the olivine, followed by recrystallisation to produce the polygonal grain shapes. It is thus inferred that some sections of RietC and Ww were fragmented by some deformational process, after which recrystallisation occurred.

6.3.3 Cause of deformation

Gibson *et al*. (2005) state that the presence of a granoblastic texture (similar to the one observed in Ww) has been observed in the ultramafic rocks from the drill core of borehole Beta-1. If, as proposed by Merkle and Wallmach (1997) (section 2.3.6), the Beta-1 ultramafic rocks are related to the BIC, the granoblastic texture had to arise after the formation of the BIC. Since a granoblastic texture has not been described in the Annas Rust dolerite (Bate, 1995; Coetzee *et al*., 1995), the texture had likely formed prior to this intrusion. This places the age constraint on the origin of the texture between 2053 Ma and 1000 Ma. According to Stepto (1990), the meteorite impact is the only deformation event that took place during this timeframe in this area of the Kaapvaal Craton. The conclusion is thus made that the granoblastic texture observed in both the Beta-1 ultramafic rocks and Ww arose during the meteorite impact event along with the PDFs observed in olivine (section 4.4.3). Therefore, the age of Ww can be placed before the meteorite impact event, and resolved the issue regarding the age discrepancy between Ww and RietC as pointed out by Stepto (1990) (see section 2.5.1).

6.4 RELATION BETWEEN THE WINDDAM WEHRLITE, THE RIETFONTEIN COMPLEX, AND THE KOEDOESFONTEIN COMPLEX

The next question that needs to be answered is whether or not a genetic relationship exists between Ww, KC, and RietC, and what exactly might the nature of that relationship be. Comparisons will only be made between the ultramafic rocks from the three intrusions. This is because, as discussed in the previous section, the hornblende gabbronorite, hornblende

norite, and diorite from KC and the olivine-hornblende gabbronorite from Ww contrasts with the chemistry of the ultramafic rocks from these intrusions. Olivine diorite from RietC is believed to have formed due to magma mixing, while the geochemistry of the troctolite is unique compared to all other rock types studied. In contrast, the geochemistry of the ultramafic rocks from the three intrusions all have similar patterns on spider diagrams (section 5.5), and typically show significant overlap on Harker diagrams (section 5.3).

6.4.1 Methodology: REE modelling

In order to assess a relationship between Ww, KC, and RietC, an REE modelling approach will be employed. To accomplishing this goal the REE composition of the parental melt of each intrusion has to be estimated. Theoretically, this can be achieved using partition coefficient (D) values (see equation 5.1) by means of the equation (Rollinson, 1993):

$$C_{melt} = C_{rock} / D_{rock} \qquad (6.1)$$

C refers to mass concentration of a particular trace element, while D_{rock} refers to its partition coefficient for the whole-rock. Assuming a rock consists of minerals A, B, and C, a particular D_{rock}-value for the whole-rock can be calculated using the formula:

$$D_{rock} = (M_A \times D_A) + (M_B \times D_B) + (M_C + D_C) \qquad (6.2)$$

where M refers to the mass concentration of a particular mineral in the rock and D is the partition coefficient of the mineral for a particular trace element. To convert modal mineralogy of each rock to mass fractions, average densities were used for each mineral (mineral densities are from Cairncross & McCarthy, 2015).

Another problem that needs to be overcome is selecting a set of D-values for modelling purposes. If D-values are to be calculated, especially for REE, it is best to obtain mineral chemistry via methods such as laser ablation ICP-MS (for example Godel *et al*., 2011), which is beyond the scope of the current study. A given set of D-values from Fujimaki *et al*. (1984) are used for olivine, clinopyroxene, and plagioclase, and Arth's (1976) values for hornblende in equilibrium with basaltic liquid. In the data set from both sources, D-values for Pr, Tb, Ho, and Tm are unavailable for the majority of minerals. For these elements, intermediate D-values of the two adjacent REEs on the periodic table were used, for D-values of REEs usually increase from left to right across the row of lanthanides (Rollinson, 1993; Winter, 2010). D-values used to perform REE modelling are given in Appendix N.

It is noted that D-values may vary greatly in different magmas, especially with varying temperature, pressure, and Si and Mg content (Bèdard, 2005; 2006; 2007; 2014; Rollinson,

1993; Winter, 2010). Despite these difficulties, a single set of D-values would be able to reflect the relative influence of the crystallisation of different phases on the composition of the magma. It is stressed that the results here should only be treated as semi-quantitative, and is only used to test the hypothesis that similar REE patterns of parental melts of rocks in this study can be produced via fractional crystallisation of more primitive melts.

Estimating the parental melt with varying Mg contents using a single set of D-values is likely to cause an overestimation in the difference between the REE contents of the two melts. This is because elements tend to become more compatible with decreasing Mg contents, implying the more evolved rock type would include more REEs during its crystallisation relative to the more primitive rock type. This invariably leads to an overestimation in the melt REE content of the evolved rock type relative to the more primitive rock type. Thus, the REE modelling performed here is likely to lead to overestimations in the amount of crystallisation that needs to occur to produce one melt type via fractional crystallisation of another.

After melt compositions are calculated using equations 6.1 and 6.2, changes in the melt composition during fractional crystallisation can be calculated using the following equation (Arth, 1976; Hanson, 1989; Janousek *et al*., 2014; Rollinson, 1993):

$$C_{melt} = C_{initial} \times F^{(D-1)} \qquad (6.3)$$

where $C_{initial}$ refers to the composition of the melt before fractionation, F refers to the fraction of liquid remaining, and D refers to the bulk partition coefficients of the fractionating phases (also calculated with equation 6.2). An example of calculations performed for the purpose of REE modelling is given in Appendix O.

Better results were obtained in all cases if the modal percentage of hornblende was reduced in the rocks. In a study performed by Oliver (1949) on Subdury norite from Canada, it was found that uralitisation has, with the exception of hydration, little effect on the whole-rock chemistry. In addition, Otamendi *et al*. (2016) have also noted that, when hornblende forms during the final stages of crystallisation, hornblende does not significantly alter the composition of the whole-rock. Because hornblende formed during a late-stage hydration reaction of primarily augite in all thin sections studied (section 6.1.1.2), it possibly did not participate in the removal of REE from the melt during its crystallisation. All modal hornblende is thus converted to clinopyroxene (*i.e.* augite) for modelling purposes.

6.4.2 Relation between KC and RietC

As discussed in Chapter 5, the ultramafic rocks of KC are more primitive in composition than those of RietC. Because of the similarity between the whole-rock REE patterns of Group 2 rocks of RietC (Figure 5.25) and olivine clinopyroxenite samples MSC268 and MSC272 of KC (see Figure 5.24), it is considered possible that the magma parental to Group 2 of RietC can be produced via fractional crystallisation of the KC magma. The estimated parental magma composition of RietC olivine clinopyroxenite (CB14) can be produced after 55% crystal fractionation of olivine and clinopyroxene in a 7:1 ratio from the estimated parental melt composition of KC olivine clinopyroxenite MSC272 (see Figure 6.17 (a)). A larger degree (60%) of fractionation can produce a close replica of CB8's estimated liquid composition by extracting olivine and clinopyroxene in a 2:1 ratio, respectively (Figure 6.17 (b)).

If both olivine clinopyroxenites CB8 and CB14 have arisen from the parental magma of olivine clinopyroxenite MSC272, an explanation is required regarding how different fractions of olivine and clinopyroxene would crystallise from the same magma. It is considered more likely that olivine clinopyroxenite CB8 would be the product of further fractional crystallisation of the magma parental to olivine clinopyroxenite CB14, and that it might not have originated directly from the differentiated KC magma. Nevertheless, both of these olivine clinopyroxenite layers appear to have a close relationship with KC and are probably crystallisation products from the same primary magma.

Because KC is located closer to the centre of the Vredefort Dome than RietC (see Figure 2.5), it had to intrude at a deeper level (see section 2.4.8). It is thus inferred that during the upward migration of the magma, it first crystallised to form the ultramafic rocks of KC, while the resulting, more differentiated magma moved further upwards to eventually produce a section of RietC.

The parental magma of KC sample MSC272 was also compared to the parental magma of Lower Zone olivine-hornblende clinopyroxenite CB1. In this case, fractional crystallisation of olivine and clinopyroxene delivered the best result in terms of Sm to Lu, but no ratio of minerals present in these rock types could produce the same REE pattern as observed for La to Nd of CB1. If some relation between CB1 and KC might exist, it is clear that some process other than fractional crystallisation altered the slope of the four lightest REE.

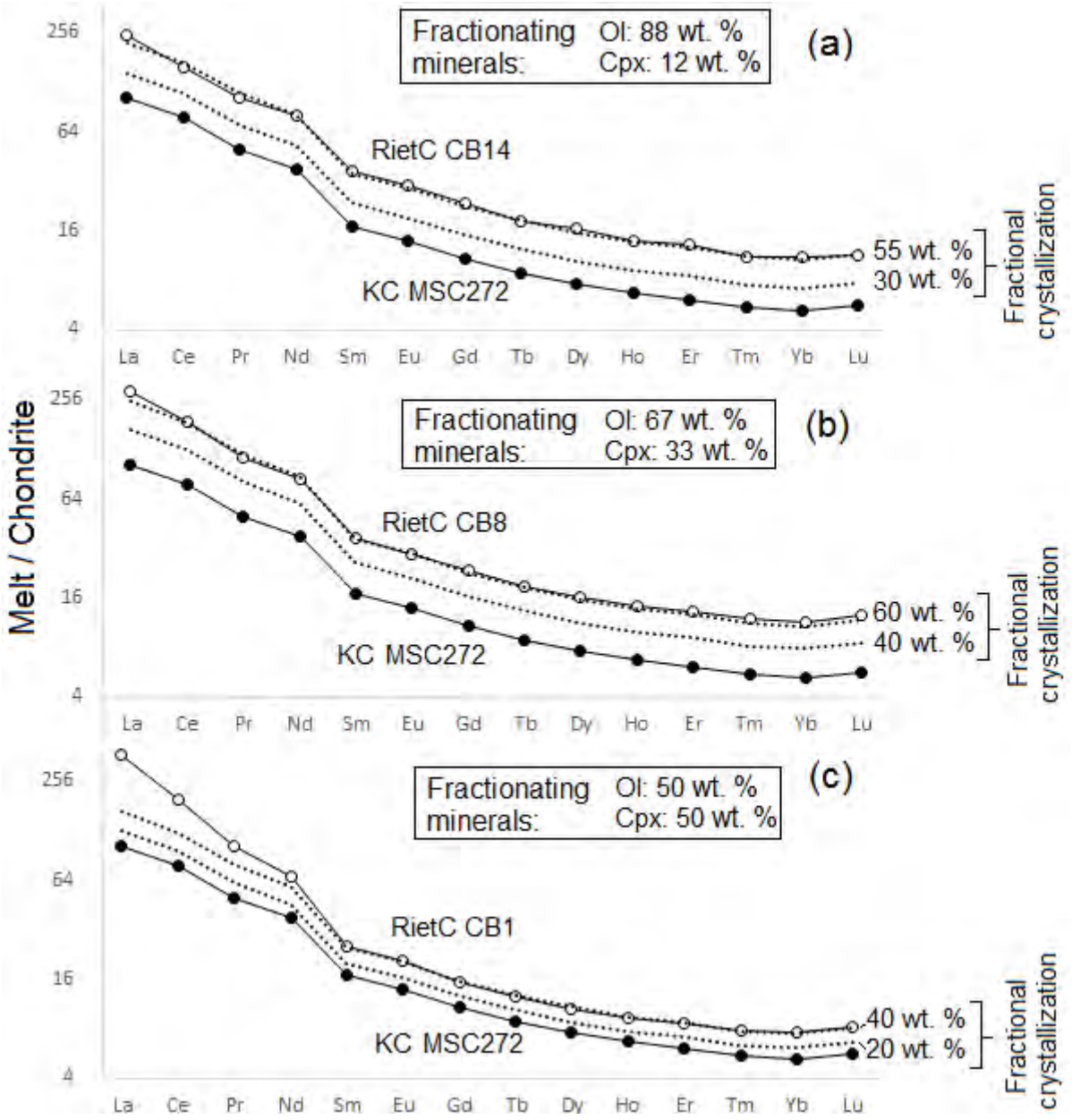

Figure 6.17: Estimated chondrite-normalised REE parental melt compositions for olivine clinopyroxenite (MSC272) of KC and olivine clinopyroxenite samples (a) CB14 (b), CB8, and (c) CB1 of RietC. Normalisation values are from Sun and McDonough (1989). Dashed lines indicate the change in the REE composition of the melt during fractional crystallisation of different proportions of olivine (Ol) and clinopyroxene (Cpx).

6.4.3 Relation between Ww and RietC

Due to the remarkable similarities between the Lower Zone olivine clinopyroxenite and the ultramafic rocks of Ww in terms of both petrographic, mineralogical and geochemical aspects, one would expect them to have originated from the same primary magma. However, this comparison is difficult to make, since samples from both intrusions show

significant variation in terms of their chondrite-normalised LREE patterns (see Figure 5.23 and 5.25).

When REE modelling is performed to produce the parental magma of Lower Zone olivine-hornblende clinopyroxenite CB1 from Ww samples, a good fit is produced in terms of Nd to Tb on the chondrite-normalised REE diagrams. However, because of the great variation in the ratios of the LREE, mismatches for these elements are produced in the majority of cases. An exception is olivine-hornblende clinopyroxenite samples CB49 and CB54, which produced a loose fit in terms of La to Tb, as shown on Figure 6.18. This is especially apparent with samples CB49 (from Ww) and CB1 (from RietC), since the best fit is obtained and the modal composition of the fractionating phases used are close to what is observed in both rock types (augite exceeds olivine). The lower values for $(Tb/Yb)_N$ in Ww are unmatched in any RietC samples, which produces the mismatch observed in Figure 6.18 and fractional crystallisation alone could not explain this variation.

Because the partition coefficient dataset used does not account for variations in pressure, temperature, and composition, the mismatch produced for the HREE could be attributed to erroneous partition coefficients. Since the HREEs have atomic radii that are smaller than the LREE, one can expect the D-values of the HREE to be higher relative to the LREE in melts that crystallise under greater pressures. This is because cation sites of crystals decrease when pressure increases, making it more difficult to accept larger cations into the crystal lattice. If this is the case, the heaviest REE would be more compatible with Ww than the other REE relative to RietC since Ww intruded at a greater depth in the Vredefort Dome (it lies closer to its structural centre). Because the same D-values are used to estimate the melt composition of both intrusions, this could lead to an overestimation of the HREE content of the parental magma of Ww relative to RietC.

The fact that Ww intruded at a deeper level in the crust does imply that it also crystallised at a higher temperature. Thermal expansion can diminish the compressional effect discussed above, and has the potential to render this explanation invalid. When comparing the D-values of olivine determined for surface basalt (Rollinson, 1993) versus those calculated for mantle peridotite (from Shaw, 2000), the trend described above does, however, become apparent (see Figure 6.19) (the difference in compatibility between heavier and lighter REE is much greater in mantle peridotite versus those in surface basalt). It is uncertain whether pressure alone is responsible for this variation, but in comparison to RietC, Ww would have formed from a melt with a higher Mg content, higher temperatures, and higher pressures, which are the same differences that exist between surface basalt and mantle peridotite.

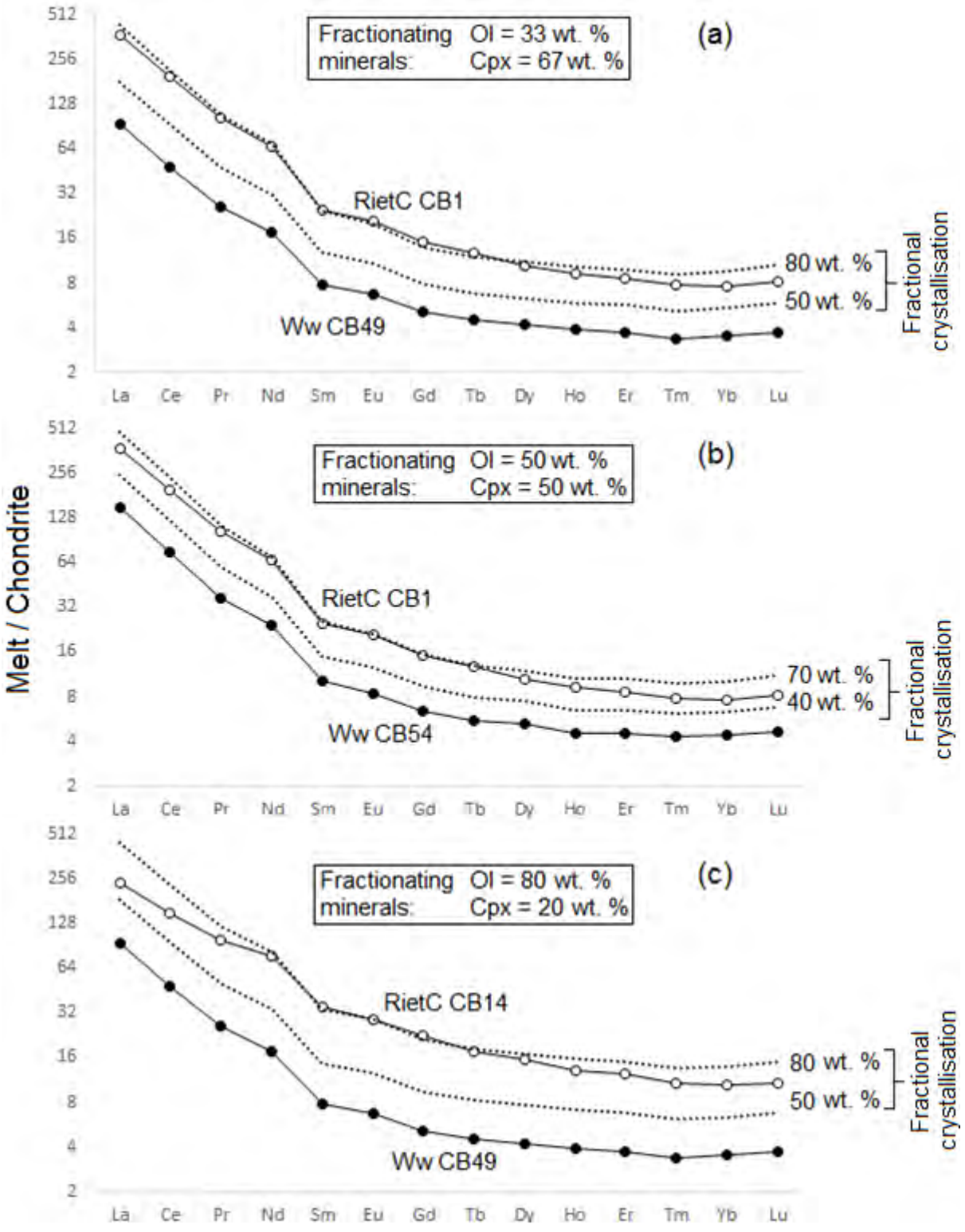

Figure 6.18: Estimated chondrite-normalised REE parental melt compositions for olivine-hornblende clinopyroxenite samples CB49 and CB54 of Ww and olivine clinopyroxenite samples (a) CB14 (b), CB8, and (c) CB1 of RietC. Normalisation values are from Sun and McDonough (1989). Dashed lines indicate the change in the REE composition of the melt during fractional crystallisation of different proportions of olivine (Ol) and clinopyroxene (Cpx).

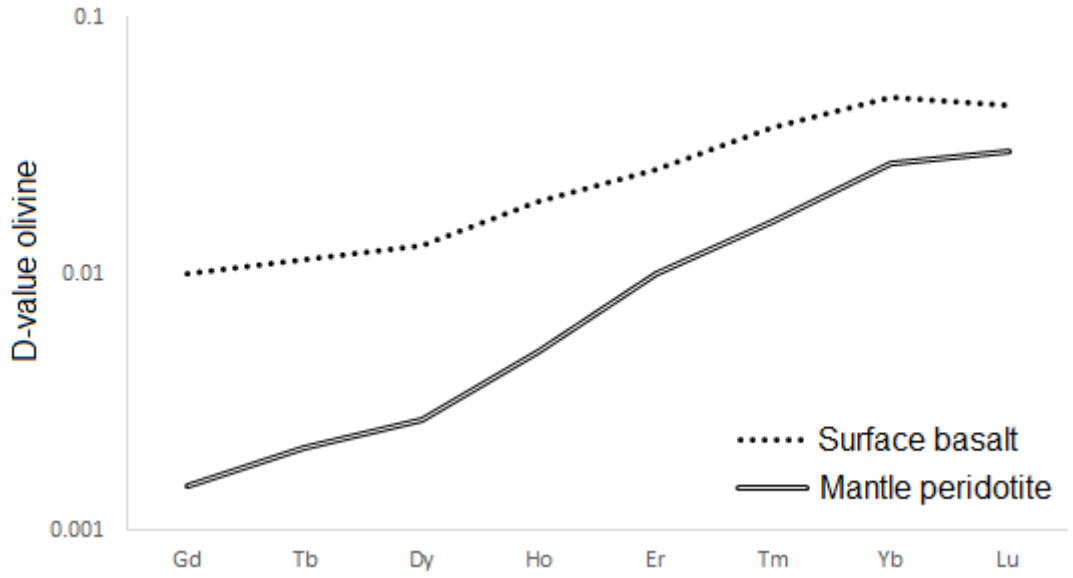

Figure 6.19: Variation in the partition coefficients (D) for the eight heaviest REE of surface basalt and mantle peridotite. D-values for surface basalt are from Rollinson (1993) and D-values for mantle peridotite are from Shaw (2000).

The parental magma of olivine clinopyroxenite CB49 is also compared to the parental magma of Central Zone olivine clinopyroxenite CB14 of RietC (see Figure 6.18 (c)). Once again, a relatively good match is produced in terms of Nd to Tb, while the ratios of the lighter and heavier REEs differ. However, poorer results are obtained than when comparing Ww to the Lower Zone of RietC, with which Ww also shares better mineralogical and petrographic similarities. It is thus concluded that Ww is closer related to the Lower Zone of RietC, while KC is more closely related to its Central Zone.

6.4.4 Relation between Ww and KC

As significant overlap occurs in the REE contents of ultramafic rocks occur from Ww and KC, fractional crystallisation is not required to prove their relation. The estimated melt composition of Ww shows slightly elevated LREE slopes and flatter HREE slopes in comparison with estimated melt compositions calculated for KC. An example is shown where the estimated parental melt composition of Ww olivine-hornblende clinopyroxenite W12 is compared to KC olivine clinopyroxenite MSC272 in Figure 6.20. The flatter HREE slope of the Ww sample can perhaps also be ascribed to the fact that Ww has intruded at a deeper level than KC as discussed in the previous section. Because Ww shows significant variation in its HREE slopes within the intrusion itself, the variation it displays when compared to KC is not indicative of a separate source of origin between the two intrusions. In addition, the argument is made that, because KC and Ww both consist of olivine (± hornblende)

clinopyroxenites, and because they show significant overlap on the majority of Harker diagrams and the AFM diagram, it is unlikely that they are not comagmatic products. Some process likely altered their REE slopes other than fractional crystallisation.

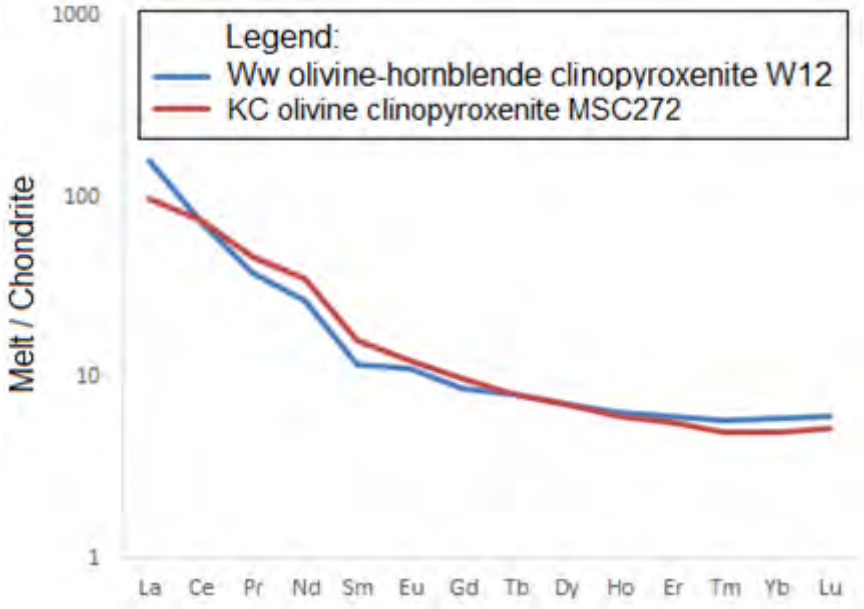

Figure 6.20: Estimated chondrite-nomralised REE melt compositions for olivine-hornblende clinopyroxenite W12 of Ww and olivine clinopyroxenite MSC272 of KC. Normalisation values are from Sun and McDonough (1989).

6.4.5 Conclusion

Ultramafic rocks from Ww, KC, and RietC all show comparable plots in terms of Nb to Tb on chondrite-normalised REE diagrams, which hints at a comagmatic relationship between the three intrusions. Central Zone Group 2 rocks from RietC had similar patterns in terms of all REEs when compared to the Central Zone olivine clinopyroxenite from KC, while Ww magmas produced a closer match to the Lower Zone olivine clinopyroxenite from RietC. Thus, Ww are closely related to the olivine-hornblende clinopyroxenite from the Lower Zone of RietC, while ultramafic rocks from KC are closely related to the ultramafic rocks from the Central Zone of RietC. Although Ww and KC are considered to be comagmatic products, some process other than fractional crystallisation likely caused some variation in their REE slopes. The findings of this section is summarised in Figure 6.21.

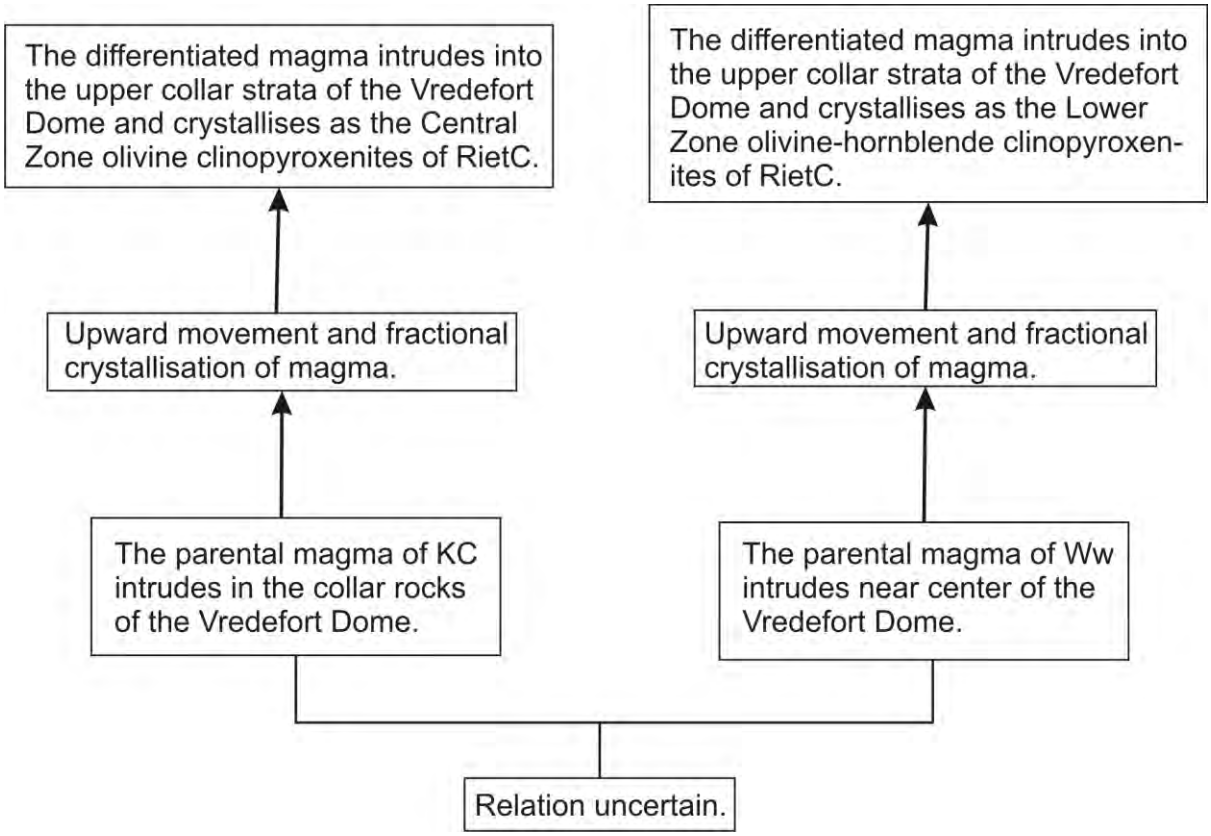

Figure 6.21: Flow diagram to demonstrate the relation between Ww, KC, and RietC as inferred from REE modelling.

6.5 RELATION WITH HITIS

One of the main hypotheses to be tested is the compatibility of Ww, RietC, and KC with the HITIS model proposed by De Waal *et al*. (2008). To recap, De Waal *et al*. (2008) suggest that RietC and KC would fall into stage D to E of the HITIS' liquid line of descent (see Figure 2.3) based on the type of cumulates observed in these rock types. Because of the chemical similarities between RietC and Ww (Stepto, 1990 and Chapter 5 of this dissertation) it is suggested that, if the HITIS model holds up, Ww might also be representative of stage D to E.

6.5.1 Comparison of whole-rock chemistry

One feature of Ww, KC, and RietC that stood out is their relatively primitive compositions as indicated by the high MgO content and low incompatible and high compatible trace element concentrations. It is thus decided to compare these intrusions to the most primitive rock type representative of the HITIS, namely the Marble Hall "primitive diorite" (MHPD) of De Waal *et*

al. (2000). If Ww, KC, and RietC prove to be more primitive than MHPD, it would be impossible for the intrusions to form part of stage D to E of Bu's evolutionary pathway.

In order to perform this comparison, one rock of each intrusion (RietC, KC, and Ww) with the highest magnesium number is selected and normalised to the composition of MHPD (Figure 6.22). Since the rocks with the highest magnesium number is ultramafic, it is decided to plot the most primitive olivine diorite sample (CB6) from RietC on the diagram as well, because its mineralogy is more comparable to the HITIS diorite. The composition of the most evolved olivine diorite from RietC (CB10) is also plotted on this diagram. In addition, the syenodiorite from the Lindequesdrift intrusion (LI) is plotted to allow for comparison with a rock type representative of stage D-E of HITIS. Elements used for normalisation on Figure 6.22 are divided into three groups; elements belonging to group A and C are expected to increase and decrease during magmatic evolution, respectively, while the geochemical behaviour during crystal fractionation of group B is more difficult to predict.

In terms of group A elements, all rock types of Ww, RietC, and KC appear to be more primitive in composition compared to MHPD. The only exception to the rule is the higher iron concentrations of RietC, which might be attributed to its greater abundance of magnetite. Compared to the LI syenodiorite, all rock types pertained to this study appears to have a more primitive composition, especially regarding the incompatible trace elements (Y, Zr, and Rb). The only exceptions are P_2O_5 (in which case RietC has higher concentrations) and FeO (higher concentrations are recorded in all the intrusions).

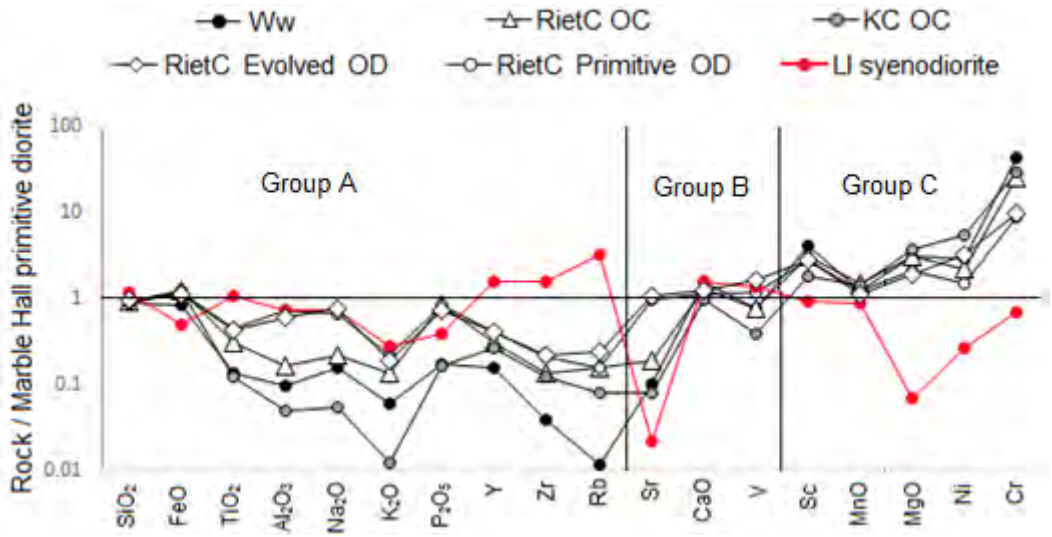

Figure 6.22: Visual presentation of various rock samples normalised to the most primitive rock type of the HITIS, namely the Marble Hall primitive diorite from De Waal & Armstrong (2000). Elements belonging to group A are expected to increase during magmatic evolution, while those belonging to C are expected to decrease. The geochemical behaviour of group B elements is difficult to predict during crystal fractionation. OC: Olivine clinopyroxenite. OD: olivine diorite. LI: Lindeques Drift intrusion

Normalisation patterns of group B elements can be explained with the aid of the mineralogical compositions of the different rock types. Sr is lower in the ultramafic rocks of all the intrusions because of the scarcity of plagioclase. CaO contents are almost identical for all rock types, while V is higher in those that contain more magnetite.

Group C elements show that RietC, KC and Ww clearly have more primitive compositions because all elements here display much higher concentrations than the HITIS intrusions. This is especially true regarding the Cr contents. Overall, it is clear that the most evolved rocks of the intrusions pertained to this study should not be considered as representatives of stage D-E on the HITIS' evolutionary pathway, as they have clearly formed from a magma with a more primitive composition than those that crystallised during stage A to B.

6.5.2 Comparison of chondrite-normalised REE plots

Despite the findings of the previous section, an attempt is made to assess if a genetic relationship exists between RietC, KC, Ww, and HITIS using chondrite-normalised REE patterns. A similar approach is used in this section as in the previous, whereby intrusions pertained to this study are compared to the MHPD and LI syenodiorite. This is done to accomplish two primary goals: to determine their stage of magmatic evolution relative to one another, and to compare the overall shape of their REE-normalised patterns.

Whole-rock chondrite-normalised REE plots of olivine-hornblende clinopyroxenite (CB1) from the Lower Zone of RietC, olivine-hornblende clinopyroxenite (CB54) of Ww, and olivine clinopyroxenite (MSC272) of KC, MHPD, and LI syenodiorite are all shown on Figure 6.23. RietC, KC, and Ww all appear to have a more primitive composition in comparison with MHPD, since they contain much lower REE abundances. It is perhaps important to keep in mind that REE depletion can also occur during magmatic evolution if a REE-compatible phase (for example monazite, see Stepanov *et al*., 2012) fractionates from the magma. Based on the findings in the previous section, it is deemed more likely that the lower REE concentrations are due to the primitive composition of the magma. The LI syenodiorite also appears to be more primitive compared to the MHPD, but finding reasons for this apparent depletion in REE lies outside the scope of this study.

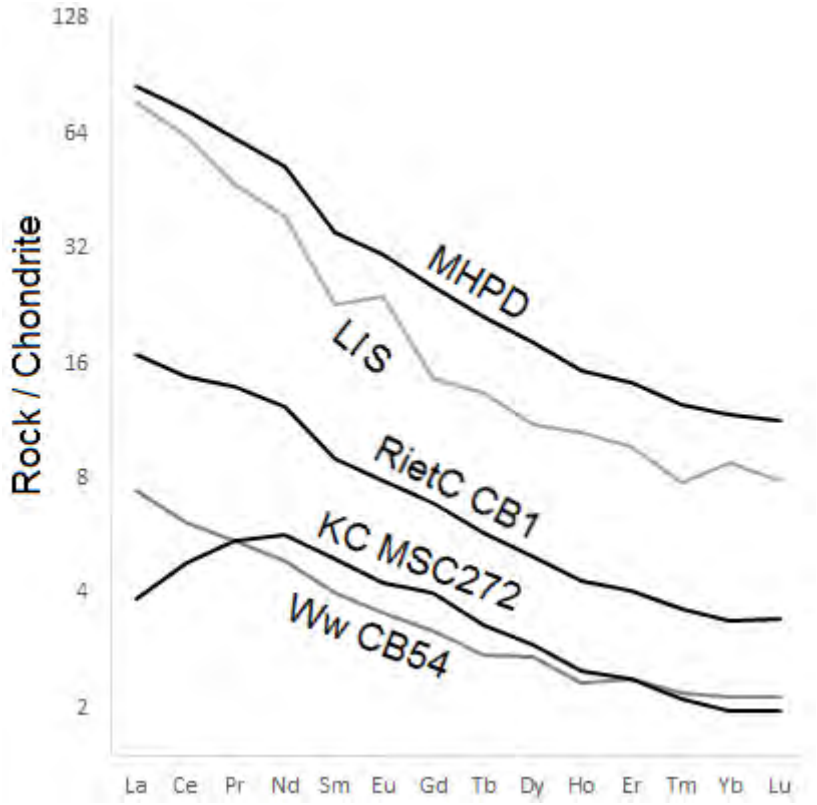

Figure 6.23: Whole-rock chondrite-normalised REE patterns of olivine-hornblende clinopyroxenite (CB1) from the Lower Zone of RietC, olivine-hornblende clinopyroxenite (CB54) of Ww, and olivine clinopyroxenite (MSC272) of KC, Marble Hall Primitive Diorite (MHPD), and Lindequesdrift intrusion syenodiorite (LIS).

The overall pattern of the REE is remarkably similar for RietC, Ww, and MHPD. Subtle similarities, like the increase in slope between Nd and Sm, as well as the decrease in slope between Ho and Er, serves as evidence that these intrusions are indeed related, as ratios between the REE tend to remain constant during crystal fractionation (Rollinson, 1993; Winter, 2010). While the LREE slope of KC differs considerably from that of MHPD, the two intrusions still show comparable HREE patterns. Thus, based on the evidence presented in this and the previous section, it is proposed that RietC and Ww indeed form part of the HITIS, but presents a more primitive composition than the rocks that belong to stage A of the Bu magma lineage.

6.5.3 From RietC to Marble Hall diorite: REE modelling

Because of the near-parallel REE patterns of the Lower Zone olivine-hornblende clinopyroxenite from RietC and MHPD, it is considered possible that MHPD could be formed by fractional crystallisation from a similar magma that produced the basal section of RietC. This is what this section aims to show using the same method described in section 6.5.1.

In case of MHPD, the exact modal mineral composition of the sample analysed is unknown. De Waal and Armstrong (2000) state that the plagioclase content of MHPD varies between 20 to 70 vol. %. Clinopyroxene and hornblende vary from 0 to 32 vol. % and 20 to 55 vol. %, respectively. To avoid any bias, it was decided to use equal proportions of the three minerals. Because De Waal and Amstrong (2000) state that hornblende also formed during a late hydration reaction of clinopyroxene in MHPD, all modal hornblende was converted to clinopyroxene here as well.

Extracting a mixture of olivine (46.8 wt. %), plagioclase (34.4 wt. %), clinopyroxene (6.3 wt. %), and hornblende (12.5 wt. %) from the estimated RietC magma produces a near-identical plot of REE as seen in the MHPD after 80 wt. % crystal fractionation (see Figure 6.24). The only exception is the mismatched produced for La, Ce, and Pr, of which higher concentrations are observed in the hypothetical melt.

6.5.4 From KC to Marble Hall diorite: REE modelling

In addition, the same method was applied to an estimated melt composition of KC olivine clinopyroxenite sample MSC272. Although the whole-rock LREE curves differ between KC and MHPD (Figure 6.23), converting them to liquid compositions yields much more comparable REE patterns (see Figure 6.25). In this case, 90 wt. % fractional crystallisation from the KC magma using a combination of olivine, clinopyroxene, and plagioclase in a 2:2:1 ratio produced an almost identical curve to that of MHPD. Using the KC magma as starting point eliminates the need to use hornblende as a crystallising phase to produce the MHPD pattern as is the case with RietC. If, as the petrographic evidence suggests, hornblende has arisen during the later stages of crystallisation due to the hydration of clinopyroxene (and did, therefore, not participate in the removal of REE from the melt), it is perhaps more likely that MHPD formed as a result of crystallisation of the KC magma. Because the parental magma of KC is also related to olivine clinopyroxenite of the Central Zone from RietC, this successfully links KC, RietC, and MHPD to one another. More primitive representatives of the Bu lineage have thus been discovered.

6.5.5 Implications of findings

As described in section 2.3.1, it is inferred that the HITIS Bu magma could have formed as a small fraction melt of the mantle from the same source as the Bushveld B3 magma. Since MHPD should no longer be considered the most primitive member of HITIS, this statement has to be re-evaluated.

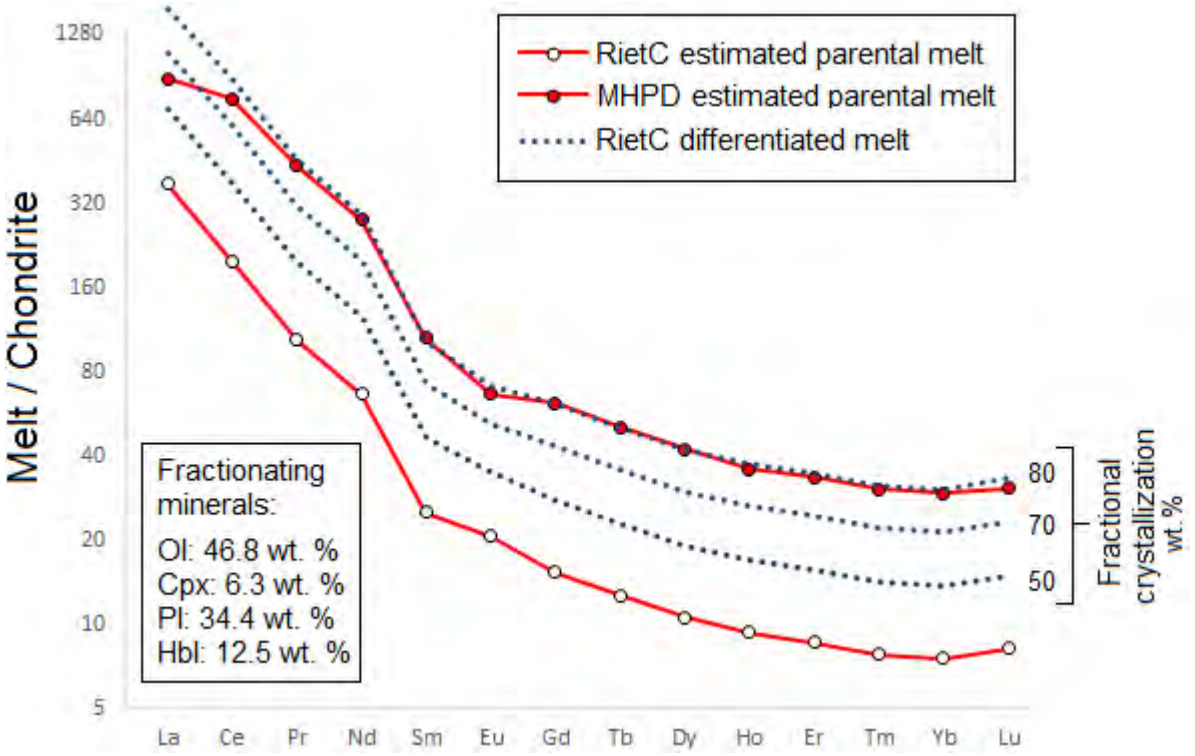

Figure 6.24: Estimated REE melt compositions of Lower Zone olivine-hornblende clinopyroxenite (CB1) of RietC and MHPD normalised to C1 chondrite of Sun and McDonough (1989). Dashed lines indicate the change in the REE composition of the melt during fractional crystallisation of the RietC parental magma.

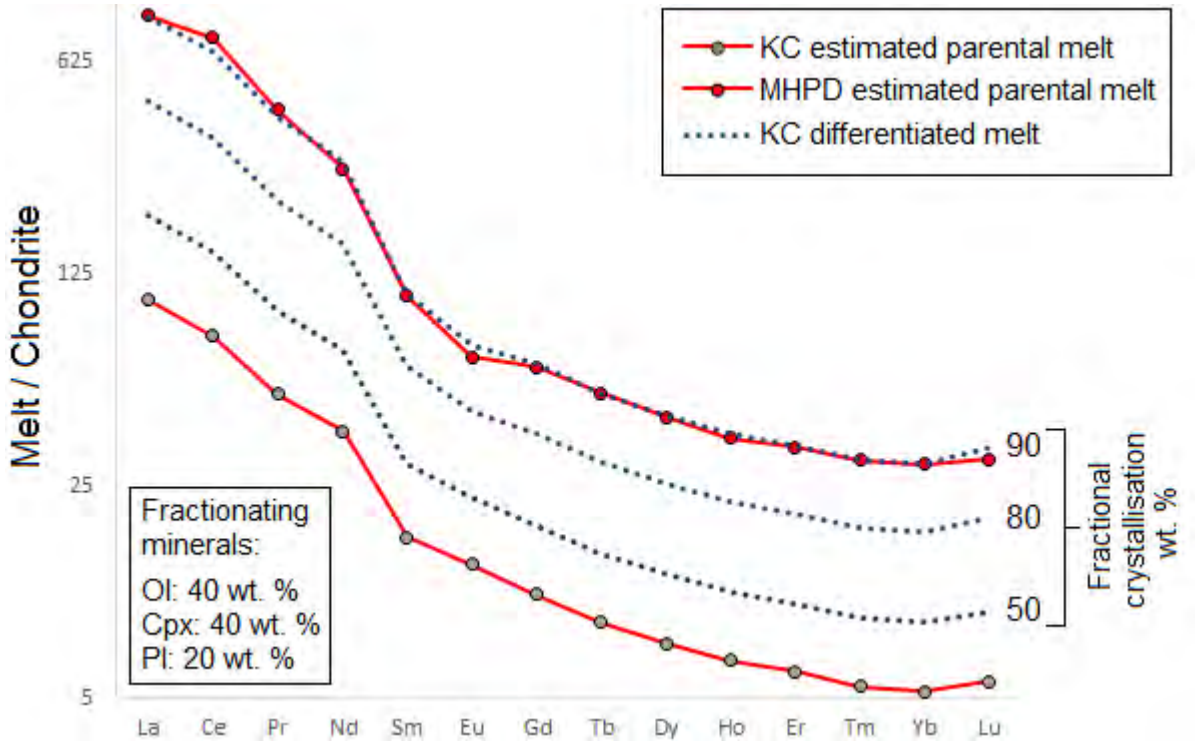

Figure 6.25: Estimated REE melt compositions of olivine clinopyroxenite (MSC272) of KC and MHPD normalised to C1 chondrite of Sun and McDonough (1989). Dashed lines indicate the change in the REE composition of the melt during fractional crystallisation of the KC parental magma (in weight fractions). See text for further details.

Furthermore the status of Bu as a high titanium magma has to be reconsidered. In a study performed by Lundgaard *et al.* (2006) on various localities of the MZ of the BIC, it was found that average TiO_2 concentrations in the clinopyroxene varies between 0.31 and 0.54 wt. %. Average TiO_2 concentrations in the relatively primitive olivine clinopyroxenite in the Lower Zone of RietC varies from 0.18 to 0.27 wt. %, which is lower than any average recorded by Lundgaard *et al*. (2006) in the MZ of the BIC. Although mineral chemistry of KC and Ww is not available, in terms of their whole-rock chemistry they contained even less TiO_2 than the ultramafic layer in the Lower Zone of RietC. This implies that the primary Bu magma (before any magmatic differentiation has occurred) was not as rich in titanium as originally proposed by De Waal *et al*. (2008). Alternatively, it is proposed in this study that the Bu magma was enriched in TiO_2 during fractional crystallisation of a Ti-incompatible phase such as plagioclase. This proposition is supported by the fact that a general trend of TiO_2 enrichment during crystal fractionation has been observed for Ww, KC, and RietC (see section 5.3.1). A lower mantle melt fraction is thus not necessary to explain the high titanium concentration as observed in many of the HITIS intrusions. However, this also implies that the relationship between the HITIS intrusions and the RLS has to be re-evaluated.

6.6 CHARACTERISTICS OF A COMMON MANTLE SOURCE

Contrary to what was originally believed, comparing Ww, RietC, and KC to HITIS do not shed any light regarding the origin of the three intrusions because they formed from a related, but more primitive magma. De Waal *et al*. (2008) were indecisive between assigning a spinel- or garnet lherzolite mantle as the source of the HITIS. This is because a garnet lherzolite source better explained the variation in REE concentrations between the Bu magma if it is inferred to have formed in the source in the mantle as the B3 magma responsible for the formation of the MZ of the RLS, while spinel lherzolite better explained the occurrence of hornblende in the MHPD (melts with higher water contents are typically formed from a spinel lherzolite source) (De Waal *et al*., 2008). Since more primitive rock compositions are now available, attempting to determine the mantle source of the HITIS might prove more fruitful. This is what this section aims to do; determine the origin of the primary magma that led to the formation of Ww, RietC, and KC.

6.6.1 Mantle mineralogy and degree of melting

Fertile mantle usually consists of lherzolite with four dominant mineral phases, namely clinopyroxene, orthopyroxene, olivine, and an Al-bearing phase, commonly spinel or garnet.

Spinel lherzolite typically occurs at depths of less than 60 km in the upper mantle, while garnet lherzolite occurs at greater depths (Foulger, 2010; Fumagalli & Klemme., 2015; Winter, 2010).

In order to discern between a spinel- and garnet bearing source, comparisons will be made between the $(La_N/Sm)_N$ and $(Tb_N/Yb)_N$ slopes of the parental melt of Ww and KC and melts produced during partial melting of both types of mantle material. Estimated parental melts of olivine-hornblende clinopyroxenite sample CB49 from Ww and olivine clinopyroxenite sample MSC272 from KC were used to perform the comparison. The decision is based on the low abundance of REE in these two samples and are thus less likely to have been affected by fractional crystallisation. In addition, because these melts are considered more primitive representatives of the melts that produced the ultramafic rocks in RietC, determining their mantle source characteristics will also help determine the mantle source characteristics of RietC.

Two models are generally used to estimate the trace element composition of magmas that arise during partial melting, called batch and fractional melting (Rollinson, 1993). Batch melting describes a single body of magma that remains in contact and equilibrium with the solid phase before its separation from the source as a single unit. In the case of fractional melting, small fractions of melt are periodically released from the source. In order to calculate the composition of a melt that arises during batch melting, the following equation is used from Rollinson (1993):

$$C_{melt} = C_{source} / [D_{rock} + F(1 - D_{rock})] \qquad (6.4)$$

Rollinson (1993) states that, because of their low viscosity, magmas with a basaltic composition are most likely to form according to the fractional melting model. The composition of a melt that forms during fractional melting can be calculated using the following equation (Rollinson, 1993):

$$C_{melt} = C_{source} / D_{rock} \times (1 - F)^{(1/Drock - 1)} \qquad (6.5)$$

In equations 6.4 and 6.5, C_{source} refers to the concentration of a trace element in the rock subjected to melting, C_{melt} to the concentration of the trace element in the melt, D_{rock} to the partition coefficient of the whole rock for that particular trace element, and F to the fraction of melt produced. It is important to note that these equations assume that mantle minerals are melted in their modal proportions. D-values for mantle minerals used for REE modelling are those compiled by Shaw (2000) and McKenzie and O'Nions (1991) (listed in Appendix P). The mineralogical composition of spinel lherzolite used here is 55.4 wt. % olivine, 25.2 wt. %

orthopyroxene, 17.3 wt. % clinopyroxene, and 2.1 wt. % spinel (from Shaw, 2000). For garnet lherzolite, the mineralogical composition is 59.8 wt. % olivine, 21.1 wt. % orthopyroxene, 7.6 wt. % clinopyroxene, and 11.5 wt. % garnet (from McKenzie & O'Nions, 1991).

For C_{source}, concentrations used are those of South African fertile peridotite nodules obtained from kimberlite for La, Ce, Nd, Sm, Eu, and Yb. The concentrations of these elements are from Nixon *et al*. (1981). Because the concentrations of the other REE elements are unknown in these samples, they were estimated based on the enrichment factor relative to the C1 chondrite from Sun and McDonough (1989). This enrichment factor tends to decrease from lighter to heavier REEs, and intermediate enrichment values are thus used to estimate the unknown concentrations. For example, in the fertile peridotite, Ce is 4.5 times more abundant that in the C1 chondrite, while Sm is enriched by a factor of about 3. The concentration of Pr is then estimated using an intermediate enrichment factor of 3.75, as it lies between Ce and Sm on the periodic table. The results for both models (batch and fractional melting) are shown in Figure 6.26.

In both melting models, garnet lherzolite produces greater $(La/Sm)_N$ and $(Tb/Yb)_N$ slopes than spinel lherzolite. This is in accordance with many examples in the literature (e.g. Ayalew *et al*., 2016; Ketchum *et al*., 2013; Khanna *et al*., 2013) that assign a spinel lherzolite source to basalts with flat $(Tb/Yb)_N$ slopes and a garnet lherzolite to basalts with higher $(Tb/Yb)_N$ slopes. Both slopes tend to decrease as the melt fraction increases.

Although the correlation is poor, the high $(La/Sm)_N$ slopes of both KC and Ww correspond with fractional melting of garnet lherzolite at low degrees of melting, while the relatively flat $(Tb/Yb)_N$ slope of Ww and KC is much closer to that produced during large degrees of batch melting of spinel lherzolite. However, because of the great variation observed in the LREE of Ww it is considered wise to base the decision regarding the mineralogy of the mantle source on the slope of the HREE. This produces a good fit for Ww if a spinel lherzolite source is considered after 15 wt. % melting for the fractional melting model and a relatively large melt fraction of 40 wt. % for the batch melting model (see Figure 6.26).

Variations in the LREE slopes of Ww samples could perhaps be a product of different melt fractions produced during a fractional melting process from the same mantle source. Varying the size of the melt fraction produced during a fractional melting process has a much greater influence on the LREE slope than on the HREE (see Figure 6.26). It is proposed that small melt fractions of mantle could intrude into the crust to produce Ww samples with a high LREE slope. If subsequent melts are produced in the mantle, they will have lower HREE

slopes. When these melts enter the Ww magma chamber, they can lead to variable slopes of the LREE observed across the intrusive body.

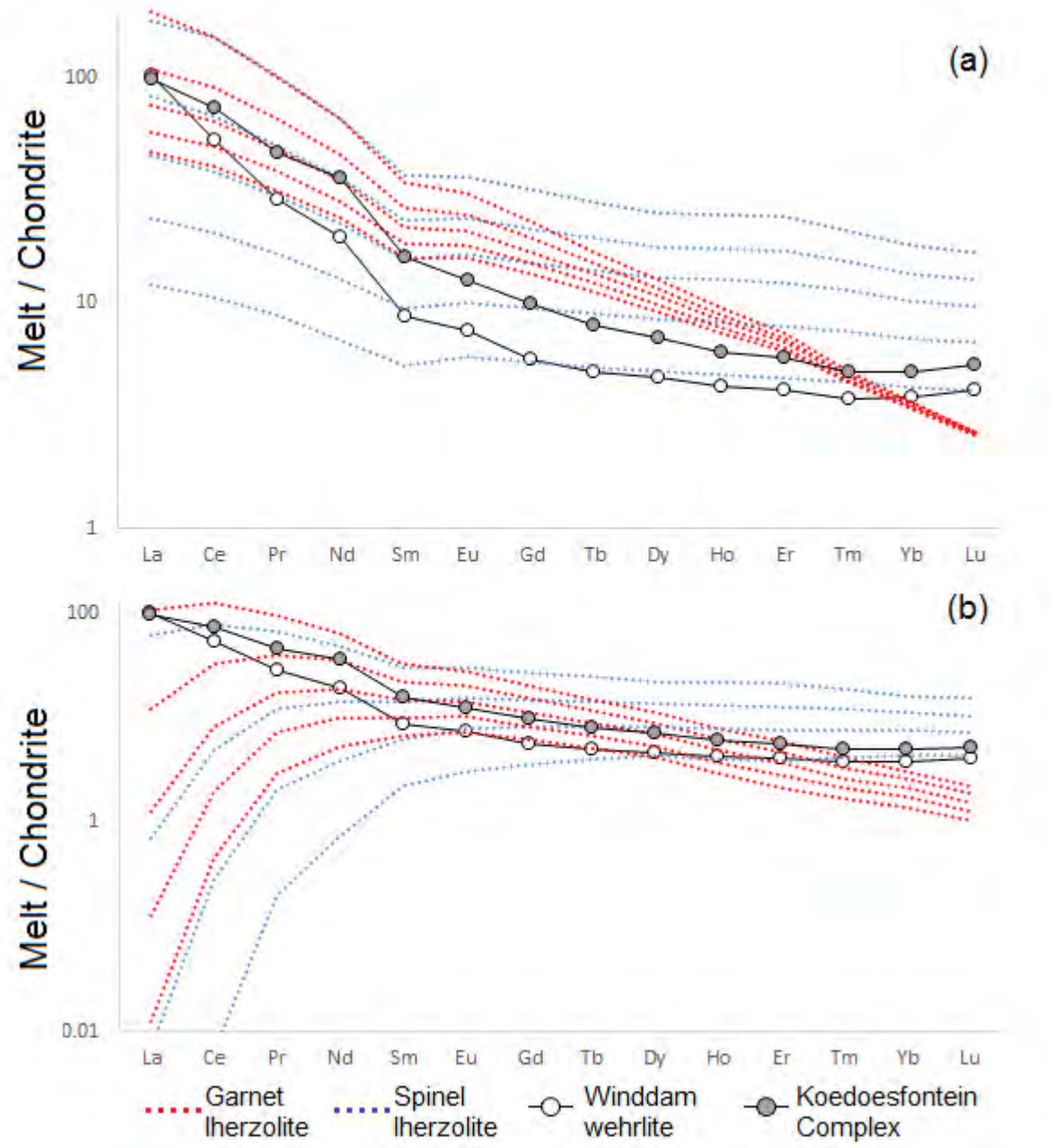

Figure 6.26: Estimated melt compositions during (a) batch and (b) fractional melting of spinel and garnet lherzolite compared to the estimated melt composition of Ww sample CB49 normalised to the C1 chondrite of Sun and McDonough (1989). Different lines indicate different melt fractions, with the uppermost lines for garnet lherzolite indicating a 2 wt. % melt fraction and the bottom line a 10 wt. % melt fraction. For spinel lherzolite, the uppermost lines for both models indicate a 1% melt fraction, and the bottom lines 15 wt. % for fractional melting and 40 wt. % for batch melting.

6.6.2 Chemical characteristics

In terms of its chemistry, the mantle source should be able to deliver a melt with the following characteristics as observed for the three intrusions studied: positive Ba and Pb anomalies, and negative U, Th, Nb, P, and Zr anomalies (see sections 5.6 and 5.7). However, crustal contamination could also be responsible for the development of positive Ba and Pb anomalies. In order to assess this possibility, spider diagrams for the ILG into which Ww is intrusive are constructed using data from La Grange (2004) (Figure 6.27). On this diagram, it is clear that the ILG also possess a negative P and Nb anomaly and a positive Pb anomaly. In contrast, however, the ILG generally shows positive Th and U anomalies, has a positive Zr anomaly, and a negative Ba anomaly. The ILG alone can, therefore, not be responsible for these chemical characteristics observed in Ww, and the mantle source is more likely responsible for the observed trends.

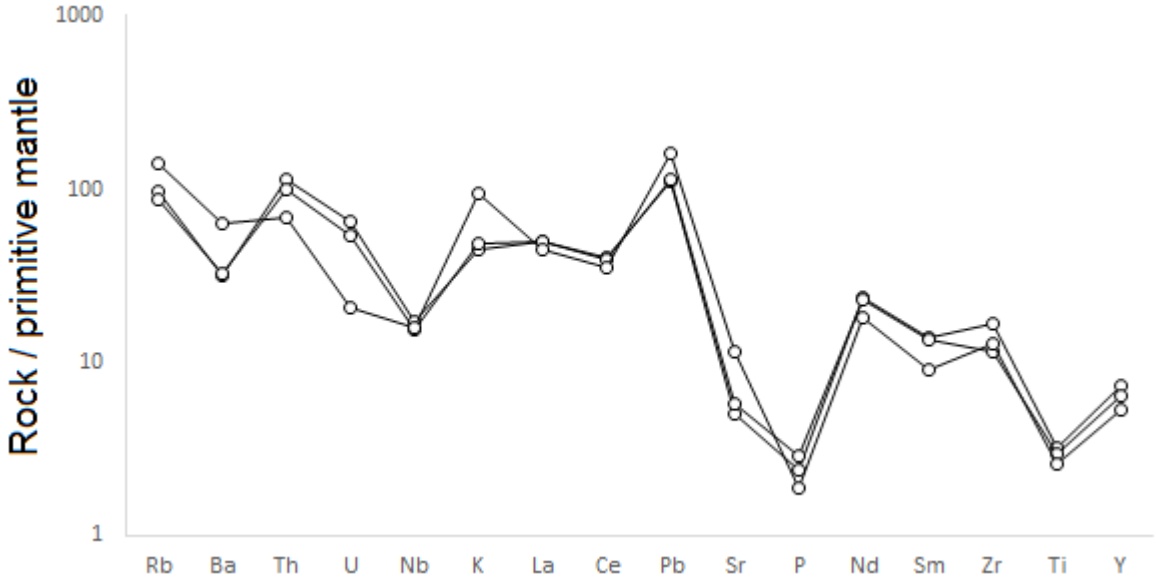

Figure 6.27: Spidergram for the ILG into which Ww is intrusive normalised to the primitive mantle (normalisation values from McDonough *et al*., 1992). ILG trace element compositions are from La Grange (2004).

Previous studies have shown that the mantle is typically enriched in mobile elements such as Ba (Zhang *et al*., 2016) and Pb (Ernst, 2014; Zhang *et al*., 2016) when exposed to subducting oceanic crust. This invariably leads to the relative depletion in the more immobile elements such as Nb (Ernst, 2014; Woo *et al*., 2014; Zhang *et al*., 2016), P, (Ernst, 2014), and Zr (Woo *et al*., 2014). All these chemical characteristics can be observed in the majority of samples reported here.

If the mantle has been enriched in mobile elements during subduction, one has to examine the history of the Kaapvaal Craton to determine when such enrichment could have taken place. Between the Kaapvaal and Zimbabwe cratons lies a belt that consists of granulite-gneiss that was metamorphosed at high pressures, referred to as the Limpopo metamorphic belt. The belt is thought to have formed during the emergence of the two, once separate cratons, possibly because of subduction that occurred at the northern end of the Kaapvaal craton approximately 2700 Ma ago (McCarthy & Rubidge, 2005; Nguuri *et al*., 2001; Tankard *et al*., 1982). This ancient, continental arc setting could be responsible for the enriched nature of the mantle underneath the Kaapvaal craton before the formation of the BIC and HITIS. Both the B1 and B2 magmas of the RLS display positive Pb and Nb anomalies (Godel *et al*., 2011), which could also be a result of mantle enrichment.

Samples display various amounts of enrichment or depletion in the different elements (especially Pb), while the relative patterns of rocks affected by mantle enrichment tend to remain consistent in related suite of rocks (for example Zhang *et al*., 2016; Woo *et al*., 2014). A combination of mantle enrichment and variable amounts of crustal contamination is thus considered responsible for the observed geochemical trends across Ww, KC, and RietC and within the intrusions themselves.

6.7 CHAPTER SUMMARY

Rocks from Ww, KC, and RietC are inferred to have crystallised under a low degree of undercooling resulting in the formation of medium-grained and approximately equal-dimensional mineral shapes.

The irregular, interstitial occurrence of hornblende and enstatite in Ww and the Lower Zone olivine-hornblende clinopyroxenite of RietC indicate that they formed during the later stages of magmatic crystallisation due to a reaction between late magmatic fluids and silica, respectively. The porphyritic texture in KC diorite is inferred to have come about due to preferred nucleation of augite to form augite glomerocrysts, followed by rapid nucleation of plagioclase, magnetite, and augite in the matrix due to supersaturation of these minerals. Preferred nucleation of augite is also responsible for the formation of the fish-net texture observed in wehrlite from KC, where augite crystals are surrounded by olivine that nucleate after the augite. Clusters of mafic minerals and plagioclase in mafic and dioritic samples from RietC and KC are believed to originate due to synneusis that involves attachment of like minerals during flow of the magma. Flow textures are recorded in the troctolite from

RietC and diorite from KC and is observable as the sub-parallel alignment of plagioclase laths.

The variation in the mode of augite versus olivine in Ww is inferred to have come about due to in-situ crystallisation of augite in some sections of Ww, causing enrichment of the adjacent melt in olivine component. This causes more olivine to crystallise in some sections of the magma chamber. More hornblende has formed in areas where H_2O has accumulated due to prior crystallisation of augite and olivine that reject H_2O in their crystal structures. Due to contrasting geochemical characteristics, the olivine-hornblende gabbronorite of Ww could not have formed directly from the same magma responsible for the formation of the ultramafic rocks of the intrusion.

Olivine is typically the first mineral to have crystallised in the wehrlite-clinopyroxenite sill, and more augite forms in areas where the melt has a more evolved composition as crystallisation proceeds on the olivine-augite cotectic. The enstatite-bearing rocks are inferred to have formed from a different magmatic lineage than the wehrlite-clinopyroxenite due to contrasting geochemical characteristics. The diorite from KC is believed to have arisen due to fractionation of the parental magma responsible for the formation of the wehrlite-clinopyroxenite sill.

RietC is believed to have originated from at least two magmatic lineages: one responsible for the formation of the olivine (± hornblende) clinopyroxenite and one responsible for the formation of the troctolite and dunite. Mixing of the two magmatic lineages has resulted in the formation of the olivine diorite as it displays intermediate REE ratios between those observed in the former two rock types.

The ultramafic rocks from Ww and KC (excluding the pyroxene hornblendite) are believed to be comagmatic products. Fractionation of olivine and augite and upward movement of the magma parental to Ww has produced the Lower Zone olivine-hornblende clinopyroxenite of RietC, while fractionation of the magma responsible for the formation of the wehrlite-clinopyroxenite of KC produced the olivine clinopyroxenite from the Central and Transitional Zones of RietC.

Further fractionation of olivine, augite, and plagioclase of the parental magma of Ww, KC, and RietC produces a nearly identical REE pattern observed in the MHPD. Fractionation also increases the alkali and TiO_2 content of the magma to produce the alkali and TiO_2-rich nature of the MHPD. This implies that Ww, KC, and RietC are comagmatic with the HITIS, but represent its most primitive members and do not fall into stage D-E of the Bu magma's

evolutionary pathway. The Bu magma was thus not originally a high Ti-magma, and cannot be produced by small fraction melting from the same mantle source as B3 of the RLS.

Ww, KC, and RietC are inferred to have formed by large fraction melting of a spinel lherzolite mantle source due to their flat HREE patterns and low REE contents. A fractional melting process of the mantle is deemed responsible for the variation observed in the LREE across the Ww intrusion. Due to exposure of the mantle wedge to a subducting oceanic plate during the convergence of the Kaapvaal and Zimbabwe cratons, the mantle was depleted in HFSE.

CHAPTER 7

CONCLUSION

The first two objectives of this study was to compile reports on the mineralogy, petrography, and geochemistry of Ww, KC, and RietC and the most important findings of these reports are given in the first section of this chapter. To avoid tedious descriptions of all the minor geochemical variations that occur between different samples, the descriptions given below are generalised. The major conclusions drawn regarding the petrogenesis of the three intrusions, their relation to one another, and their relation to the HITIS is given in the second section. In the two final sections of this chapter, the significance of this study is given followed by recommendations for future research.

7.1 SUMMARY OF FINDINGS

7.1.1 Mineralogy and petrography

The modal analysis of Ww revealed that it primarily consists of olivine-hornblende clinopyroxenite and one sample of olivine-hornblende gabbronorite. KC contains a sill of wehrlite, olivine clinopyroxenite, and clinopyroxenite, as well as mafic samples that classified as hornblende gabbronorite, hornblende norite, and a single sample of diorite. A unique sample from KC classifies as quartz-bearing pyroxene hornblendite. Ultramafic rocks from RietC consist of olivine-hornblende clinopyroxenite from its Lower Zone and olivine clinopyroxenite from its Central and Transitional Zone. Other rock types that form part of RietC include olivine diorite and magnetite-rich troctolite and dunite

All rocks from Ww, KC, and RietC are typically fine to medium grained. Ultramafic rocks from Ww and the Lower Zone of RietC are characterised by adcumulate textures, sutured grain contacts between augite, and late interstitial enstatite and hornblende. Ultramafic rocks from KC and the Central and Transitional Zones of RietC are similar petrographically, and contain augite and olivine with planar to curved grain boundaries, little hornblende, no enstatite, and intercumulus plagioclase in some samples.

Cumulate textures are absent in the olivine diorite from RietC and the hornblende gabbronorite from KC. The hornblende norite from KC is highly deformed and fractured. Diorite from KC is characterised by a glomeroporphyritic texture, with augite glomerocrysts and a matrix consisting of augite, plagioclase, and magnetite. The plagioclase laths in the KC diorite are aligned sub-parallel to one another, hinting at magmatic flow. The olivine-

hornblende gabbronorite from Ww has a granoblastic texture consisting of polygonal olivine, augite, hornblende, and plagioclase. Plagioclase laths in troctolite from RietC are aligned sub-parallel to one another and have irregular, lobate boundaries where in contact with abundant magnetite.

Deformation textures observed include sutured grain boundaries, fine-grained polygonal mineral aggregates, deformation twinning, and PDFs in the olivine from Ww. Serpentine, tremolite, calcite, iddingsite, saponite, sericite, and clay minerals are common as alteration products throughout the intrusions.

7.1.2 Geochemistry

The ultramafic rocks from Ww, KC, and RietC are characterised by low TiO_2 concentrations, very low incompatible trace element (such as Zr, Y, and Rb) contents, and high compatible trace element (such as Ni, Cr, and Co) contents. On Harker diagrams, they show significant overlap in terms of their geochemistry. On average, ultramafic rocks from RietC appear to be more evolved than ultramafic rocks from Ww and KC, while the latter two intrusions are more difficult to distinguish from each other. On multi-element spider diagrams, ultramafic rocks from all three intrusions show similar patterns, hinting at a comagmatic relationship. They typically possess positive Ba, Pb, and Ti anomalies, together with negative Th, U, Nb, P, and Zr anomalies. On chondrite-normalised REE diagrams, ultramafic rocks from Ww, KC, and RietC typically possess low HREE slopes and variable LREE patterns. Although some exceptions occur, they are generally fractionated in terms of LREE over HREE.

The olivine-hornblende gabbronorite from Ww has elevated compatible (Ni, Cr, and Co) and incompatible element (Rb, Zr, and Y) contents compared to ultramafic rocks from the same intrusion, casting uncertainty regarding whether or not is should be considered more evolved than the ultramafic rocks. While its LREE slope is indistinguishable from ultramafic samples from Ww, it has a significantly lower HREE slope.

The enstatite-bearing rocks of KC typically contain lower compatible (MgO, Ni, Cr, and Co) and higher incompatible (alkalis, Rb, Zr, and Y) element concentrations compared to the ultramafic rocks, pointing to a more evolved composition. They are also characterised by positive Rb, K, Sr, and Zr anomalies which are absent in the ultramafic rocks. In terms of REE, the hornblende gabbronorite differs from the wehrlite-clinopyroxenite in terms of a significantly higher LREE and lower HREE slope. The diorite generally shows dramatic depletion in terms of compatible element (Ni, Cr, and Co) concentrations compared to the enstatite-bearing rocks and the wehrlite-clinopyroxenite. With the exception of the absence

of a positive Pb anomaly in the diorite, it has a similar pattern on multi-element spider diagrams compared to the wehrlite-clinopyroxenite of KC.

On average, olivine diorite of RietC typically contain higher alkali concentrations and slightly lower incompatible trace element (Rb, Zr, and Y) concentrations and compatible element (Ni, Cr, and Co) concentrations compared to the ultramafic rocks. Their patterns on multi-element spiderdiagrams are similar to the ultramafic rocks, but they possess a positive Sr anomaly due to the accumulation of plagioclase feldspar. REE patterns of the olivine diorite differ from most of the ultramafic samples. The troctolite from RietC has higher compatible element concentrations compared to the ultramafic rocks and olivine diorite due to the abundance of magnetite. It also has the lowest incompatible element (Zr, Y, and Rb) concentrations. Its pattern on the multi-element spider diagram differs dramatically from the ultramafic rocks and olivine diorite of RietC, and displays negative Th, U, La, Ce, Pb, Nd, Sm, and Y anomalies, and positive Ba, Sr, and Ti anomalies. It generally has much lower REE contents compared to other rock types from RietC, and is characterised by higher LREE and HREE slopes.

7.2 MAJOR CONCLUSIONS

This section describes the conclusions made regarding the formation of Ww, KC, and RietC, their relation to one another, and their relation to HITIS in chronological order in which the events are inferred to have occurred.

1. The mantle underneath the Kaapvaal craton was relatively depleted in U, Th, Nb, P, and Zr, and relatively enriched in Ba and Pb due to subduction that had occurred related to the collision of the Kaapvaal craton with the Zimbabwe craton. Due to the dramatic variation in the Pb anomaly in all ultramafic samples, the mantle source alone could have attributed to this anomaly, and possible contamination of the crust might also be responsible for its occurrence.

2. Due to the low REE concentration and low $(Tb/Yb)_N$ of ultramafic rocks from Ww, KC, and RietC, the primary melt responsible for its formation likely formed due to large fraction batch melting of spinel lherzolite. This large melt fraction led to the formation of a tholeiitic magma with a low alkali content and a low TiO_2 concentration.

3. This magma moved upward and emplaced into Archaean granite and Witwatersrand strata that would later form part of the Vredefort Dome to form the ultramafic rocks of Ww and KC, respectively. A comagmatic relationship of the two intrusions is supported by their

similar mineralogies, overlapping plots on Harker diagrams, overlapping REE contents, and small variations between their HREE and LREE slopes.

4. Variation in the mode of ultramafic rocks in Ww are considered products of in-situ crystallisation of augite in some sections of the intrusion. This leads to the depletion of augite component in the adjacent melt, causing more olivine to crystallise in these adjacent areas. A similar process is deemed responsible for the mineralogical variation observed in the wehrlite-clinopyroxenite sill from KC, but olivine was generally the first silicate to nucleate followed by augite.

5. Due to conflicting geochemical characteristics of the enstatite-bearing rocks from KC and the olivine-hornblende gabbronorite from Ww when compared to the ultramafic rocks of these intrusions, it is concluded that these rocks formed from a different magma with a contrasting geochemical composition.

6. Crystal fractionation and further magmatic differentiation of the magma occurred after the formation of Ww and KC before it was emplaced into the Ventersdorp Supergroup and Chuniespoort Group to form the ultramafic rocks of the RietC. This is supported by the fact that extraction of olivine and augite from the parental melts of Ww and KC can produce near-identical REE patterns of the parental magma of ultramafic rocks from RietC.

7. Because the geochemical characteristics of the troctolite differ considerably when compared to the ultramafic rocks from RietC, the troctolite is also inferred to have crystallised from a contrasting magma type. The olivine diorite from RietC has intermediate REE slopes between some of the ultramafic rocks and troctolite from RietC, and is thought to have originated due to mixing of the two parental magmas responsible for the formation of the two latter rock types.

8. A differentiated magma was formed via fractional crystallisation of the same primary magma responsible for the formation of Ww, KC, and RietC. This led to the enrichment of Ti, alkalis, REE, and other incompatible elements. This magma was emplaced near the present day town of Marble Hall to form the Marble Hall primitive diorite of De Waal & Armstrong (2000), originally considered to be the most primitive member of the HITIS. This successfully links Ww, KC, and RietC to the HITIS. These three intrusions are now considered the most primitive members of the HITIS' magmatic line of descent.

9. Evidence of deformation in these intrusions are planar deformation features in olivine from Ww, pseudotachylite in some ultramafic samples from KC and RietC, granoblastic textures with polygonal mineral aggregates in Ww and troctolite in RietC, and sutured grain

boundaries between augite grains. The primary cause for these deformation textures is believed to be the meteorite impact event deemed responsible for the formation of the Vredefort Dome.

7.3 SIGNIFICANCE OF STUDY

The first in-detail report on the petrography of Ww was produced, along with in-depth reports regarding the geochemical characteristics of Ww, KC, and RietC that were not available before. New petrogenetic models were proposed to explain the formation of Ww, KC, and RietC that were based on both geochemical and mineralogical evidence in contrast to older models that relied on the mineralogy only. It also came to light that Ww, KC, and RietC are indeed part of the HITIS, but represent its most geochemically primitive members. Because of the low TiO_2, alkali, and REE contents of these intrusions, it was inferred that the Bu magma was produced by large fraction mantle melting. Tying the HITIS to the Bushveld magmatic event by suggesting it represents a lower fraction mantle melt from the same source where the B3 magma was produced is thus no longer plausible.

7.4 RECOMMENDATIONS FOR FUTURE RESEARCH

During the course of this project, the following issues came to light that requires further research to be resolved:

- The possible relationship between the Bushveld magmatic event and Ww, KC, RietC, and the remainder of the HITIS has to be determined.
- The origin of the enstatite-bearing rocks from KC and the olivine-hornblende gabbronorite from Ww has to be studied in detail, as fractional crystallisation alone could not establish a genetic relationship between these rocks and the ultramafic rocks from these intrusions.
- The chemistry of the inclusions trapped in the PDFs of olivine from Ww need to be determined to unravel their identity and origin.
- Determine the chemistry of the fine, opaque, rod-shaped exsolved phases from augite (Figure 4.34) observed in Ww, KC, and RietC to determine their identity.
- Determine the chemistry of the mineral present in the symplectite intergrowths observed in augite (Figure 4.40) from KC to assess its identity and means of formation.

REFERENCES

Abily, B., Ceuleneer, G. & Launeau, P. 2011. Synmagmatic normal faulting in the lower oceanic crust: evidence from the Oman ophiolite. *Geology*, 39:391–394.

Adachi, T., Hokada, T., Osanai, Y., Toyoshina, T., Baba, S. & Nakano, N. 2010. Titanium behaviour in quartz during retrograde hydration: occurrence of rutile exsolution and implications for metamorphic processes in the Sør Rondane Mountains, East Antarctica. *Polar Science*, 3:222-234.

Agangi, A., Hofmann, A., Rollion-Bard, C., Marin-Carbonne, J., Cavalazzi, B., Large, R. & Meffre, S. 2015. Gold accumulation in the Archaean Witwatersrand Basin, South Africa – Evidence from concentrically laminated pyrite. *Earth-Science Reviews*, 140:27-53.

Albarède, F. 2003. Geochemistry: an introduction. 1st ed. New York: Cambridge University Press.

Anderson, A.T. 1980. Significance of hornblende in calc-alkaline andesites and basalts. *American Mineralogist*, 65:837-851.

Armstrong, R.A., Compston, W., Retief, E.A., Williams, I.S. & Welke, H.J. 1991. Zircon ion microprobe studies bearing on the age and evolution of the Witwatersrand triad. *Precambrian Research*, 53(3-4):243-266.

Arth, J.G. 1976. Behavior of trace elements during magmatic processes – a summary of the theoretical models and their applications. *Journal of Research United States Geological Survey*, 4(1):41-47.

Ayalew, D., Jung, S., Romer, R.L., Kersten, F., Pfänder, J.A. & Garbe-Scönberg, D. 2016. Petrogenesis and origin of modern Ethiopian rift basalts: constraints from isotope and trace element geochemistry. *Lithos*, 258-259:1-14.

Baier, J., Audétat, A. & Keppler, H. 2008. The origin of the negative niobium tantalum anomaly in subduction zone magmas. *Earth and Planetary Science Letters*, 267(1-2):290-300.

Baratoux, D. & Reimold, W.U. 2016. The current state of knowledge about shatter cones: introduction to the special issue. *Meteoritics & Planetary Science*, 51(8):1389-1434.

Barclay, J. & Carmichael, I.S.E. 2004. A hornblende basalt from Western Mexico: water-saturated phase relations constrain a pressure-temperature window of eruptibility. *Journal of Petrology*, 45(3):485-506.

Barnes, S-J. & Maier, W.D. 2002. Platinum-group element distribution in the Rustenburg Layered Suite of the Bushveld Complex, South Africa. (*In* Cabri, L.J., *ed*. The Geology, Geochemistry, Mineralogy and Mineral beneficiation of platinum-group elements. Canadian Institute of Mining, Metallurgy and Petroleum, Special Volume 54, p. 431-458).

Bataleva, Y.V., Palyanov, Y.N., Sokol, A.G., Borzdov, Y.M. & Bayukov, O.A. 2016. Wüstite stability in the presence of CO_2-fluid and a carbonate-silicate melt: implications for the graphite/diamond formation and generation of Fe-rich mantle metasomatic agents. *Lithos*, 244:20-29.

Bate, M.D. 1995. Petrology of the Anna Rust dolerite sill, Vredefort Structure. Potchefstroom: PUCHO (Dissertation – MSc).

Bèdard, J.H. 2005. Partition coefficients between olivine and silicate melts. *Lithos*, 83:394-419.

Bèdard, J.H. 2006. Trace element partitioning in plagioclase feldspar. *Geochimica et Cosmochimica Acta*, 70:3717-3742.

Bèdard, J.H. 2007. Trace element partitioning coefficients between silicate melts and orthopyroxene: parameterization of D variations. *Chemical Geology*, 244:263-303.

Bèdard, J.H. 2014. Parameterization of calcic pyroxene – melt trace element partition coefficients. *Geochemistry Geophysics Geosystems*, 15(2):303-336.

Berndt, J., Koepke, J. & Holtz, F. 2005. An experimental investigation of the influence of water and oxygen fugacity on differentiation of MORB at 200 MPa. *Journal of Petrology*, 46(1):135-167.

Bisschoff, A.A. 1969. The petrology of the igneous and metamorphic rocks of the Vredefort Dome and the adjoining parts of the Potchefstroom Syncline. Pretoria: UP (Thesis – PhD).

Bisschoff, A.A. 1972. The dioritic rocks of the Vredefort Dome. *Transactions of the Geological Society of South Africa*, 75:31-45.

Bisschoff, A.A. 1973. The petrology of some mafic and peralkaline intrusions in the Vredefort Dome, South Africa. *Transactions of the Geological Society of South Africa*, 76(1):27-52.

Bisschoff, A.A. 1982. Thermal metamorphism in the Vredefort Dome. *Transactions of the Geological Society of South Africa*, 85:43-57.

Bisschoff, A.A. 1996. Note on the relative ages of the pseudotachylite and the basic granophyre in the Vredefort Dome. *South African Journal of Geology*, 99(1):89-92.

Bisschoff, A.A. 1999a. Vredefort Dome: Explanation of geological sheets 2627CA, CB, CC, CD, DA, DC and 2727AA, AB, BA (1:50 000). Pretoria: Council for geoscience.

Bisschoff, A.A. 1999b. The geology of the Vredefort Dome. Scale 1:50 000. Council for Geoscience, Pretoria.

Bjerga, A., Konopásek, J. & Pedersen, R.B. 2015. Talc-carbonate alteration of ultramafic rocks with the Leka Ophiolite Complex, Central Norway. *Lithos*, 227:21-36.

Bollinger, C., Merkel, S., Cordier, P. & Raterron, P. 2015. Deformation of forsterite polycrystals at mantle pressure: comparison with Fe-bearing olivine and the effect of iron on its plasticity. *Physics of the Earth and Planetary Interiors*, 240:95-104.

Boneschans, R.B, Coetzee, M.S. & Siebert, S.J. 2015. A geobotanical investigation of the Koedoesfontein Complex, Vredefort Dome, South Africa. *Australian Journal of Botany*, 63(3-4):324-340.

Boneschans R.B. 2017. The petrology and associated woody vegetation of the Koedoesfontein Complex in the Vredefort Dome, South Africa. Potchefstroom: NWU (Dissertation – MSc, in preparation.).

Brink, M.C., Waanders, F.B. & Bisschoff, A.A. 1997. Vredefort: A model for the anatomy of an astrobleme. *Tectonophysics*, 270:83-114.

Brink, M.C., Waanders, F.B., Bisschoff, A.A. & Coetzee, M.S. 2005. The impact structure of Vredefort, South Africa. Extended abstracts, Geocongress 2005, UKZN, July 2005, South Africa.

Buchanan, P.C., Koeberl, C. & Reimold, W.U. 1999. Petrogenesis of the Dullstroom Formation, Bushveld Magmatic Province, South Africa. *Contributions to Mineralogy and Petrology*, 137:133-146.

Buckley, V.J.E., Sparks, R.S.J. & Wood, B.J. 2006. Hornblende dehydration reactions during magma ascent at Soufrière Hills Volcano, Montserrat. *Contributions to Mineralogy and Petrology*, 151:121-140.

Cairncross, B. & McCarthy, T. 2015. Understanding minerals and crystals. 1st ed. Cape Town: Struik Nature.

Cawthorn, R.G., Eales, H.V., Walvaren, F., Uken, R. & Watkeys, M.K. 2009. The Bushveld Complex. (*In* Johnson, M.R., Anhaeusser, C.R. & Thomas, R.J., *ed*. Geology of South Africa. Johannesburg: The Geological Society of South Africa. p 261-281).

Cawthorn, R.G. & Walraven, F. 1997. The Bushveld Complex: a time to fill and a time to cool. Economic geology research unit. University of the Witwatersrand. Information circular No. 307.

Cawthorn, R.G. & Walraven, F. 1998. Emplacement and crystallisation time for the Bushveld Complex. *Journal of Petrology*, 39(9):1669-1687.

Clark-Halkett, C.R. 2010. An investigation into the formation of the lower Main Zone in the Eastern Limb of the Bushveld Complex, South Africa. Pretoria: UP (Dissertation – MSc).

Clemént, J-P., Caroff, M., Duboignon, P., Launeau, P., Bohn, M., Cotton, J., Blais, S. & Guille, G. 2007. A possible link between gabbros bearing high temperature iddingsite alteration and huge pegmatoid intrusions: the Sociaty Islands, French Polynesia. *Lithos*, 96(3-4):524-542.

Coetzee, M.S. 2001. 'n Petrologies-geochemiese ondersoek van ultramafies-mafiese indringings in die kraag- en kerngesteentes van die Vredefortstruktuur. Bloemfontein: UFS (Thesis - PhD).

Coetzee, M.S., Bate, M.D. & Elsenbroek, J.H. 1995. Flow differentiation – an explanation for the origin and distribution of plagioclase glomerocrysts in the Anna Rust dolerite sill, Vredefort Dome. *South African Journal of Geology*, 98:276-286.

Coetzee, M.S., Beukes, G.J., de Bruiyn, H. & Bisschoff, A.A. 2006. Geochemistry and petrogenesis of tholeiitic intrusions of possible Bushveld-age in the Vredefort Dome, South Africa. *Journal of African Earth Sciences*, 45:213-235.

Coetzee, H. & Kruger, F.J. 1989. The geochronology, Sr- and Pb- isotope geochemistry of the Losberg Complex, and the southern limit of the Bushveld Complex magmatism. *South African Journal of Geology*, 92(1):37-41.

Davies, G. & Cawthorn, R.G. 1984. Mineralogical data on a multiple intrusion in the Rustenburg Layered Suite of the Bushveld Complex. *Mineralogical Magazine*, 349(48):469-480.

Deer, W.A., Howie, R.A. & Zussman, J. 2013. An introduction to the rock-forming minerals. 3rd ed. London: The Mineralogical Society.

Delvigne, J.E. 1998. Atlas of micromorphology of mineral alteration and weathering. 1st ed. Ottawa: Mineralogical Association of Canada.

De Oliveira, G.J.G., Vasconcelos, M.A.R., Crosta, A.P., Reimold, W.U., Goes, A.M. & Kowitz, A. 2014. Shatter cones and planar deformation features confirm Santa Marta in Piaui State, Brazil, as an impact structure. *Meteoritics & Planetary Science*, 49(10):1915-1928.

De Waal, S. & Armstrong, R.A. 2000. The age of the Marble Hall diorite, its relationship to the Uitkomst Complex, and evidence for a new magma type associated with the Bushveld igneous event. *South African Journal of Geology*, 103(2):128-140.

De Waal, S.A., Graham, I.T. & Armstrong, R.A. 2006. The Lindeques Drift and Heidelberg Intrusions and the Roodekraal Complex, Vredefort, South Africa: comagmatic plutonic and volcanic products of a 2055 Ma ferrobasaltic magma. *South African Journal of Geology*, 109:279-300.

De Waal, S.A., Graham, I.T. & Phillips, D. 2002. Age and significance of the Marble Hall breccia, Bushveld Complex, South Africa. *South African Journal of Geology*, 105:227-240.

De Waal, S.A., Schweitzer, J.K., & Graham, I.T. 2008. A Bushveld-related high-Ti igneous suite (HITIS) derived from an alkali to transitional basaltic magma, South Africa. *South African Journal of Geology*, 111:201-224.

Dunn, T. 1987. Partitioning of Hf, Lu, Ti, and Mn between olivine, clinopyroxene and basaltic liquid. *Contributions to Mineralogy and Petrology*, 96(4):476-484.

Eales, H.V. 2000. Implications of the chromium budget of the Western Limb of the Bushveld Complex. *South African Journal of Geology*, 103(2):141-150.

Eales, H.V. 2002. Caveats in defining the magmas parental to the mafic rocks of the Bushveld Complex, and the manner of their emplacement: review and commentary. *Mineralogical Magazine*, 66(6):815-832.

Ernst, R.E. 2014. Large igneous provinces. 1st ed. Cambridge: Cambridge University Press.

Evans, C.A. & Baltuck, M. 1988. Low-temperature alteration of peridotite, hole 637. *Proceedings of the Ocean Drilling Program, Scientific Results*, 103:235-239.

Etheridge, M.A., Walls, V.J., Cox, S.F. & Vernon, R.H. 1984. High fluid pressures during regional metamorphism and deformation: Implications for mass transport and deformation mechanisms. *Journal of Geophysical Research*, 89:4344-4358.

Fagereng, A., Harris, C., La Grange, M. & Stevens, G. 2008. Stable isotope study of the Archaean rocks of the Vredefort impact structure, central Kaapvaal Craton, South Africa. *Contributions to Mineralogy and Petrology*, 155:63-78.

Fischer, L.A., Wang, M., Charlier, B., Namur, O., Roberts, J., Veksler, I.V., Cawthorn, R.G. & Holtz, F. 2016. Immiscible iron- and silica-rich liquids in the Upper Zone of the Bushveld Complex. *Earth and Planetary Science Letters*, 443:108-117.

Fitz Gerald, J.G. & Stünitz, H. 1993. Deformation of granitoids at low metamorphic grade. II: Granular flow in albite-rich mylonites. *Tectonophysics*, 221:299-324.

Fujimaki, H., Tatsumoto, M. & Aoki, K. 1984. Partition coefficients of Hf, Zr, and REE between phenocrysts and groundmasses. Proceedings of the fourteenth lunar and planetary science conference, part 2. *Journal of Geophysical Research*, 89(Supplement):B662-B672.

Fumagalli, P. & Klemme, S. 2015. Mineralogy of the Earth: phase transitions and mineralogy of the upper mantle. (*In*: Schubert, G., *ed*. Treatise on geophysics. 2nd ed. Vol 2. Oxford: Elsevier. p 7-31).

Foulger, G.R. 2010. Plates vs. plumes: a geological controversy. 1st ed. Oxford: Wiley-Blackwell.

Garde, A.A., McDonald, I., Dyck, B. & Keulen, N. 2012. Searching for giant, ancient impact structures on Earth: the Mesoarchaean Maniitsoq structure, West Greenland. *Earth and Planetary Science Letters*, 337-338:197-210.

Gauert, C.D.K., De Waal, S.A. & Wallmach, T. 1995. Geology of the ultrabasic to basic Uitkomst complex, eastern Transvaal, South Africa: an overview. *Journal of African Earth Sciences*, 21(4):553-570.

Gasparik, T. 2003. Phase diagrams for geoscientists: an atlas of the Earth's interior. 1st ed. Berlin: Springer-Verlag.

Gibson, R.L., Reimold, W.U. & Lana, C. 2005. Comment on: new PGE and Re/Os-isotope data from lower crustal sections of the Vredefort dome and a reinterpretation of its "crust-on-edge" profile. *South African Journal of Geology*, 108:309-313.

Graham, I.T., De Waal, S.A. & Armstrong, R.A. 2005. New U-Pb SHRIMP zircon age for the Schurwedraai alkali granite: Implications for pre-impact development of the Vredefort Dome and extent of Bushveld magmatism, South Africa. *Journal of African Earth Sciences*, 43:537-548.

Green, D.H. & Ringwood, A.E. 1967. The genesis of basalt magmas. *Contributions to Mineralogy and Petrology*, 15(104-105):159-167.

Godel, B., Barnes, S. & Maier, W.D. 2011. Parental magma composition inferred from trace element in cumulus and intercumulus silicate minerals: an example from the Lower and Lower Critical Zones of the Bushveld Complex, South Africa. *Lithos*, 125:537-552.

Goltrant, O., Doukhan, J., Cordier, P. & Courtillot, V. 1992. An investigation by transmission electron microscopy of planar deformation features in naturally shocked quartz. *Terra Nova*, 4(3):405-412.

Halim, A.H.A., Helmy, H.M., El-Rahman, Y.M.A., Shibata, T., Mahallawi, M.M.E., Yoshikawa, M. & Arai, S. 2016. Petrology of the Motaghairat mafic-ultramafic complex, Eastern Desert, Egypt: a high-Mg post-collisional extension-related layered intrusion. *Journal of Asian Earth Sciences*, 116:164-180.

Hallis, L.J., Anand, M. & Strekopytov, S. 2014. Trace-element modelling of mare basalt parental melts: implications for a heterogeneous lunar mantle. *Geochimica et Cosmochimica Acta*, 134:289-316.

Hanson, G.N. 1989. An approach to trace element modelling using a simple igneous system as an example. (*In* Lipin, B.R. & McKay, G.A., *ed*. Geochemistry and mineralogy of rare earth elements. Michigan: Mineralogical Society of America. p. 79-97).

Haraguchi, S., Ishizuka, H., Ishi, T., Fujioka, K., Yuasa, M. & Shibasaki, H. 2014. Low- and high-temperature alteration of volcanic rocks in the north-western Philippine Sea, and association with volcanic settings. *Island Arc*, 23:324-343.

Hargraves, R. 1961. Shatter cones in the rocks of the Vredefort ring. *Transactions of the Geological Society of South Africa*, 64:147-161.

Harlow, G.E. & Klimentidis, R. 1980. Clouding of pyroxene and plagioclase in eucrites: implications for post-crystallisation processing. *Lunar and Planetary Science Conference*, 2:1131-1143.

Harmer, R.E., Sharpe, M.R. 1985. Field relations and isotope systematics of the marginal rocks of the Eastern Bushveld Complex. *Economic Geology*, 80:813-837.

Harris, C., Fourie, D.S. & Fagereng, A. 2013. Stable isotope evidence for impact-related pseudotachylite formation at Vredefort by local melting of rocks. *South African Journal of Geology*, 116(1):101-118.

Hart, R.J., Andreoli, M.A.G., Smith, C.B., Otter, M.L. & Durrheim, R. 1990. Ultramafic rocks in the centre of the Vredefort structure (South Africa): Possible exposure of the upper mantle? *Chemical Geology*, 83(3-4):233-248.

Hart, R.J., McDonald, I., Tredoux, M., De Wit, M.J., Carlson, R.W., Andreoli, M., Moser, D.E. & Ashwal, L.D. 2004. New PGE and Re/Os-isotope data from lower crustal sections of the Vredefort Dome and a reinterpretation of its “crust on edge” profile. *South African Journal of Geology*, 107:173-184.

Hatton, C.J. 1995. Mantle plume origin for the Bushveld and Ventersdorp magmatic provinces. *Journal of African Earth Sciences*, 21(4):571-577.

Henderson, P. 1984. General geochemical properties and abundances of the rare earth elements. (*In* Henderson, P., *ed*. Rare earth element geochemistry. Amsterdam: Elsevier. P. 1-32).

Heinrich, E.W. 1965. Microscopic identification of minerals. 1st ed. New York: McGraw-Hill.

Hicks, L.J., Bridges, J.C. & Gurman, S.J. 2014. Ferric saponite and serpentine in the nakhlite martian meteorites. *Geochimica et Cosmochimica Acta*, 136:194-210.

Higgins, M.D. 1994. Numerical modelling of crystal shapes in thin sections: estimation of crystal habit and true size. *American Mineralogist*, 79:113-119.

Holler, F.J., Skoog, D.A. & Crouch, S.R. 2007. Principles of instrumental analysis. 6th ed. Belmont: Brooks/Cole.

Husen, A., Kamenetsky, V.S., Everard, J.L. & Kamenetsky, M.B. 2016. Transition from ultra-enriched to ultra-depleted primary MORB melts in a single volcanic suite (Macquarie Island, SW Pacific): implications for mantle source, melting process and plumbing systems. *Geochimica et Cosmochimica Acta*, 185:112-128.

Irvine, T.N. & Baragar, W.R.A. 1971. A guide to the chemical classification of the common volcanic rocks. *Canadian Journal of Earth Sciences*, 8:523-548.

Isaacs, A.M., Brown, P.E., Valley, J.W., Essene, E.J. & Peacor, D.R. 1981. An analytical electron microscopic study of pyroxene-amphibole intergrowth. *Contributions to Mineralogy and Petrology*, 77:115-120.

Jackson, M.C. 1994. Geochemistry and metamorphic petrology of Dominion Group metavolcanics in the Vredefort area, South Africa. *South African Journal of Geology*, 97:62-77.

Jafri, S.H. & Charan, S.N. 1992. Quench textures in pillow basalt from the Andaman-Nicobar Islands, Bay of Bengal, India. *Proceedings of the Indian Academy of Sciences – Earth Planet Sciences*, 101(1):99-107.

Jahn, A. & Riller, U. 2009. A 3D model of first-order structural elements of the Vredefort Dome, South Africa – Importance for understanding central uplift formation of large impact structures. *Tectonophysics*, 478:221-229.

Janousek, V.J., Moyen, J., Martin, H., Erban, V. & Farrow, C. 2014. Geochemical modelling of igneous processes – principles and recipes in R language: bringing the power of R to a geochemical community. 1st ed. Berlin: Springer.

Jakobsen, J.K., Tegner, C., Brooks, C.K., Kent, A.J.R., Lesher, C.E., Nielsen, T.F.D. & Wiedenbeck, M. 2010. Parental magma of the Skaergaard intrusion: constraints from melt inclusions in primitive troctolite blocks and FG-1 dykes. *Contributions to Mineralogy and Petrology*, 159:61-79.

Jakobsen, J.K., Veksler, I.V., Tegner, C. & Brooks, C.K. 2005. Immiscible iron- and silica-rich melt in basalt petrogenesis documented in the Skaergaard intrusion. *Geology*, 33:885-888.

Kamo, S.L., Reimold, W.U., Krogh, T.E. & Colliston, W.P. 1996. A 2.023 Ga age for the Vredefort impact event and a first report of shock metamorphosed zircons in pseudotachylitic breccias and granophyre. *Earth and Planetary Science Letters*, 144:369-387.

Keary, P. 2001. Dictionary of geology. 2nd ed. London: Penguin Reference.

Ketchum, K.Y., Heaman, L.M., Bennett, G. & Hugh, D.J. 2013. Age, petrogenesis and tectonic setting of the Thessalon volcanic rocks, Huronian Supergroup, Canada. *Precambrian Research*, 233:144-172.

Khanna, T.C., Sai, V.V.S., Zhao, G.C., Rao, D.V.S., Krishna, A.K., Sawant, S.S. & Charan, S.N. 2013. Petrogenesis of mafic alkaline dikes from the ≈2.18 Ga Mahbubnagar Large

Igneous Province, Eastern Dharwar Craton, India: geochemical evidence for uncontaminated intracontinental mantle derived magmatism. *Lithos*, 179:84-98.

Klein, C. 1994. Minerals and rocks: exercises in crystallography, mineralogy, and hand specimen petrology. Revised edition. New York: John Wiley 7 Sons.

Klein, C. & Dutrow, B. 2008. The 23rd edition of the manual of mineral science. 23rd ed. New Jersey: John Wiley & Sons.

Koeberl, C. 2002. Mineralogical and geochemical aspects of impact craters. *Mineralogical Magazine*, 66(5):745-768.

Koeberl, C., Reimold, W.U. & Shirey, S.B. 1996. Re-Os isotope study of the Vredefort Granophyre: Clues to the origin of the Vredefort Structure, South Africa. *Geology*, 24:913-916.

Krivolutskaya, N.A., Bryanchaninova, N.I. 2011. Olivines of igneous rocks. *Russian Journal of General Chemistry*, 81(6):1302-1314.

Kruger, F.J. 1990. The stratigraphy of the Bushveld Complex: a reappraisal and the relocation of the Main Zone boundaries. *South African Journal of Geology*, 93(2):376-381.

Kruger, F.J. 1994. The Sr-isotopic stratigraphy of the western Bushveld Complex. *South African Journal of Geology*, 97(4):393-398.

Kruger, F.J. 2004. Filling the Bushveld Complex magma chamber: lateral expansion, floor interaction, magmatic unconformities, and chromite and PGE deposits. Economic Geology Research Institute Hugh Allsop Laboratory. University of the Witwatersrand. Information Circular No. 377.

Kruger, W.A.J. 2014. Rietfontein Complex, Vredefort Dome: potential toxicity of vanadium to cattle. Potchefstroom: NWU (Mini-dissertation – Hons.)

Kushiro, I. 1969. The system forsterite-diopside-silica with and without water at high pressures. *American Journal of Science*, 267:269-294.

Kushiro, I. 1972. Effect of water on the compositions of magmas formed at high pressures. *Journal of Petrology*, 13:311-334.

Kushiro, I. 2001. Partial melting experiments on peridotite and origin of mid-ocean ridge basalt. *Annual Review of Earth and Planetary Sciences*, 29:71-107.

Lana, C., Reimold, W.U., Gibson, R.L., Koeberl, C. & Siegesmund, S. 2004. Nature of the Archaean midcrust in the core of the Vredefort Dome, Central Kaapvaal Craton, South Africa. *Geochemica et Cosmochimica*, 68(3):623-642.

Langenhorst, F. & Deutsch, A. 2012. Shock metamorphism of minerals. *Elements*, 8(1):31-36.

La Grange, M. 2004. A detailed petrographic and oxygen isotopic study of metamorphic rocks and Archaean basement complex gneisses from the Vredefort Dome, South Africa. Cape Town: UCT (Dissertation - MSc).

Latypov, R. 2015. Basal reversals in mafic sills and layered intrusions. (*In* Charlier, B., Namur, O., Latypov, R. & Tegner, C. Layered intrusions. Springer Geology. p 259-294).

Le Bas, M.J. & Streckeisen, A.L. 1991. The IUGS systematics of igneous rocks. *Journal of the Geological Society, London,* 148:825-833.

Lee, M.R., Tomkinson, T., Hallis, L.J. & Mark, D.F. 2015. Formation of iddingsite veins in the martian crust by centripetal replacement of olivine: evidence from the nakhlite meteorite Lafayette. *Geochimica et Cosmochimica Acta*, 154:49-65.

Le Roux, H., Reimold, W.U. & Doukhan, J. 1994. A TEM investigation of shock metamorphism in quartz from the Vredefort dome, South Africa. *Tectonophysics*, 230(3-4):223-239.

Lieger, D. & Riller, U. 2012. Emplacement history of Granophyre dikes in the Vredefort Impact Structure, South Africa, inferred from geochemical evidence. *Icarus,* 219:168-180.

Lofgren, G. & Russel, W.J. 1986. Dynamic crystallisation of chondrule melts of porphyritic and radial pyroxene composition. *Geochemica et Cosmochinica Acta*, 50(8):1715-1726.

Lotter, N.O., Bradshaw, D.J., Becker, M., Parolis, L.A.S. & Kormos, L.J. 2008. A discussion of the occurrence and undesirable flotation behaviour of orthopyroxene and talc in the processing of mafic deposits. *Minerals Engineering*, 21(12-14):905-912.

Low, P.C., Seaman, S.J., Karlstrom, K.E., Williams, M.L. 2009. Delicate oscillatory zoning in pyroxene preserved through variation in the clouding density of exsolved oxides: an insight into mafic-ultramafic chamber dynamics. Geological Society of America, 2009 Northeast Section Meeting- Abstracts with Programs, 41:31.

Liu, P., Zhou, M., Ren, Z., Wang, C.Y. & Wang, K. 2016. Immiscible Fe- and Si-rich silicate melts in plagioclase from the Baima mafic intrusion (SW China): Implications for the origin of

bi-modal igneous suites in large igneous provinces. *Journal of Asian Earth Sciences*, 127:211-230.

Lundgaard, K.L., Tegner, C., Cawthorn, R.G., Kruger, F.J. & Wilson, J.R. 2006. Trapped intercumulus liquid in the Main Zone of the eastern Bushveld Complex, South Africa. *Contributions to Mineralogy and Petrology*, 151:352-369.

Marsh, J.S. 2009. The Dominion Group. (*In* Johnson, M.R., Anhaeusser, C.R. & Thomas, R.J., *ed*. Geology of South Africa. Johannesburg: The Geological Society of South Africa. P. 149-154).

Marsh, J.S., Bowen, M.P., Rogers, N.W. & Bowen, T.B. 1989. Volcanic rocks of the Witwatersrand Traid, South Africa. II: Petrogenesis of mafic and felsic rocks of the Dominion Group. *Precambrian Research*, 44(1):39-65.

Martini, J.E.J. 1978. Coesite and stishovite in the Vredefort Dome, South Africa. *Nature*, 272:715-717.

Martini, J.E.J. 1991. The nature, distribution and genesis of the coesite and stishovite associated with the pseudotachylite of the Vredefort Dome, South Africa. *Earth and Planetary Science Letters*, 103(1-4):285-300.

Mayer, J.J. & Bate, M.D. 1994. The discovery of a shatter cone at the Rietfontein Complex and new data on the extent of the mafic portion of the complex. *South African Journal of Geology*, 97(2):225-227.

McCarthy, T. & Rubidge, B. 2005. The story of earth and life: a southern African perspective on a 4.6-billion-year journey. 1st ed. Cape Town: Struik Publishers.

McIntire, W.L. 1963. Trace element partition coefficients – a review of theory and applications to geology. *Geochimica et Cosmochimica Acta*, 27:1209-1264.

McDonough, W.F., Sun, S., Ringwood, A.E., Jagoutz, E. & Hofmann, A.W. 1992. K, Rb, and Cs in the earth and moon and the evolution of the earth's mantle. *Geochimica et Cosmochimica Acta*, 56(3):1001-1012.

McKay, G.A. 1989. Partitioning of rare earth elements between major and silicate minerals and basaltic melts. (*In* Lipin, B.R. & McKay, G.A., *ed*. Geochemistry and mineralogy of rare earth elements. Michigan: Mineralogical Society of America. p. 45-77).

McKenzie, D. & O'Nions, R.K. 1991. Partial melt distributions from inversion of rare earth element concentrations. *Journal of Petrology*, 32:1021-1091.

Mehdilo, A. & Irannajad, M. 2010. Applied mineralogical studies on Iranian hard rock titanium deposit. *Journal of Minerals & Materials Characterization & Engineering*, 9(3):247-262.

Merkle, R.K.W. & Wallmach, T. 1997. Ultramafic rocks in the centre of the Vredefort structure (South Africa): geochemical affinity to Bushveld rocks. *Chemical Geology*, 143:43-64.

Monroe, J.S., Wicander, R. & Hazlett, R.W. 2007. Physical geology: exploring earth. 6th ed. Belmont: Brooks/Cole.

Morrison, J.M., Goldhaber, M.B., Mills, C.T., Breit, G.N., Hooper, R.L., Holloway, J.N., Diehl, S.F. & Ranville, J.F. 2015. Weathering and transport of chromium and nickel from serpentinite in the Coast Range ophiolite to the Sacramento Valley, California, USA. *Applied Geochemistry*, 61:72-86.

Murphy, J.B. 2006. Igneous rock associations 7. Arc magmatism I: Relationship between subduction and magma genesis. *Journal of the Geological Association of Canada*, 33(4):145-168.

Naldrett, A.J., Wilson, A., Kinnaird, J. & Chunett, G. 2009. PGE tenor and metal ratios within and below the Merensky Reef, Bushveld Complex: implications for its genesis. *Journal of Petrology*, 50(4):625-659.

Namur, O., Abily, B., Boudreau, A.E., Blanchette, F., Bush, J.W.M., Ceuleneer, G., Charlier, B., Donaldson, C.H., Duchene, J.C., Higgins, M.D., Morata, D., Nielsen, T.F.D., O'Driscoll, B., Pang, K.N., Peacock, T., Spandler, C.J., Toramaru, A. & Veksler, I.V. 2015. Igneous layering in basaltic magma chambers. (*In* Charlier, B., Namur, O., Latypov, R. & Tegner, C. Layered intrusions. Springer geology. p 75-152).

Nesse, W.D. 2004. Introduction to optical mineralogy. 3rd ed. New York: Oxford University Press.

Nguuri, T.K., Gore, J., James, D.E., Webb, S.J., Wright, C., Zengeni, T.G., Gwavava, O. & Snoke, J.A. 2001. Crustal structure beneath southern Africa and its implications for the formation and evolution of the Kaapvaal and Zimbabwe cratons. *Geophysical Research Letters*, 28(13):2501-2504.

Nixon, P.H., Rogers, N.W., Gibson, I.L. & Grey, A. 1981. Depleted and fertile mantle xenoliths from southern African kimberlites. *Annual Reviews of Earth and Planetary Science*, 9:285-309.

O'Driscoll, B., Donaldson, C.H., Troll, V.R., Jerram, D.A., Emeleus, C.H. 2007. An origin for harristic and granular olivine in the Rum Layered Suite, NW Scotland: a crystal size distribution study. *Journal of Petrology*, 48(2):253-270.

Oliver, T.A. 1949. The effect of uralitization upon the chemical composition of the Sudbury norite. http://www.minsocam.org/ammin/AM36/AM36_421.pdf Date of access: 16 June 2016.

Onwualu-John, J.N. 2016. Positive anomalous concentrations of Pb in some gabbroic rocks of Afikpo basin south-eastern Nigeria. *Environmental Geochemistry and Health*, 38(4):1029-1035.

Otamendi, J.E., Tiepolo, M., Walker, B.A., Cristofolini, E.A., & Tibaldi, A.M. 2016. Trace elements in minerals from mafic and ultramafic cumulates of the central Sierra de Valle Fértil, Famatinian arc, Argentina. *Lithos*, 240-243:355-370.

Pál-Molnár, E., Batki, A., Almási, E., Kiss, B., Upton, B.G.J., Markl, G., Odling, N. & Harangi, S. 2015. Origin of mafic and ultramafic cumulates from the Ditrău Alkaline Massif, Romania. *Lithos*, 239(1-18).

Pang, K., Zhou, M., Lindsley, D., Zhao, D. & Malpas, J. 2008. Origin of Fe-Ti oxide ores in mafic intrusions: evidence from the Panzhihua Intrusion, SW China. *Journal of Petrology*, 49(2):295-313.

Papike, J.J., Ross, M. & Clark, J.R. 1969. Crystal-chemical characterization of clinoamphiboles based on five new structure refinements. *Mineralogical Society of America Special Paper*, 2:117-136.

Piazolo, S., Montagnat, M., Grennerat, F., Moulinec, H. & Wheeler, J. 2015. Effect of local stress heterogeneities on dislocation fields: examples from transient creep in polycrystalline ice. *Acta Materialia*, 90:303-309.

Pickersgill, A.E., Osinski, G.R. & Flemming, R.L. 2015. Shock effects in plagioclase feldspar from the Mistastin Lake impact structure, Canada. *Meteoritics & Planetary Science*, 50(9):1546-1561.

Philpotts, A.R. 1978. Textural evidence for liquid immiscibility in tholeiites. *Mineralogical magazine*, 42(324):417-425.

Philpotts, A.R. 1989. Petrography of igneous and metamorphic rocks. 1st ed. Long Grove: Waveland Press.

Raedeke, L.D. & McCallum, I.S. 1984. Investigations in the Stillwater Complex: part II. Petrology and petrogenesis of the ultramafic series. *Journal of Petrology*, 25(2):395-420.

Reimold, W.U. & Jourdan, F. 2012. Impact! – Bolides, craters and catastrophes. *Elements*, 8(1):19-24.

Reimold, W.U., Pybus, G.Q.J., Kruger, F.J., Layer, P.W. & Koeberl, C. 2000. The Anna's Rust Sheet and related gabbroic intrusions in the Vredefort Dome – Kibaran magmatic event on the Kaapvaal Craton and beyond? *Journal of African Earth Sciences*, 31:499-521.

Robb, L.J., Brandl, G., Anhaeusser, C.R. & Poujol, M. 2009. Archaean granitoid intrusions. (*In* Johnson, M.R., Anhaeusser, C.R. & Thomas, R.J. Geology of South Africa. Johannesburg: The Geological Society of South Africa. p 57-94).

Roeder, P.L. & Emslie, R.F. 1970. Olivine-liquid equilibrium. *Contributions to Mineralogy and Petrology*, 29:275-289.

Roelofse, F., Ashwal, L.D. & Romer, R.L. 2015. Multiple, isotopically heterogeneous plagioclase populations in the Bushveld Complex suggest mush intrusions. *Chemie der Erde – Geochemistry*, 75(3):357-364.

Rollinson, H. 1993. Using geochemical data: evaluation, presentation, interpretation. 1st ed. Edinburgh: Pearson.

Rooney, T.P., Riecker, R.E. & Ross, M. 1970. Deformation twins in hornblende. *Science*, 169(3941):173-175.

Sagy, A., Fineberg, J. & Reches, Z. 2004. Shatter cones: Branched, rapid fractures formed by shock impact. *Journal of Geophysical Research*, 109:1-20.

Saito, T., Uno, M., Sato, T., Fukisaki, W., Haraguchi, S., Li, Y., Sawaki, Y., Yamamoto, S. & Maruyama, S. 2015. Geochemistry of accreted metavolcanic rocks from the Neoproterozoic Gwna Group of Anglesey-Lleyn, NW Wales, U.K.: MORB and OIB in the Iapetus ocean. *Tectonophysics*, 662:243-255.

Schmitt, R.T. & Langenhorst, F. 1996. Planar deformation features in olivine from experimentally shocked H6 chondrite Kernouve. *Meteoritics and Planetary Science*, 31:124.

Schreyer, W. 1984. Metamorphism and fluid inclusions in the basement of the Vredefort Dome, South Africa: guidelines to the origin of the structure. *Journal of Petrology*, 24(1):26-47.

Scoates, J.S. & Friedman, R.M. 2008. Precise age of the platiniferous Merensky Reef, Bushveld Complex, South Africa, by the U-Pb zircon chemical abrasion ID-TIMS technique. *Economic Geology*, 103(3):465-471.

Scoon, R.N. & Mitchell, A.A. 2012. The Upper Zone of the Bushveld Complex at Roossenekal, South Africa: geochemical stratigraphy and evidence of multiple episodes of magma replenishment. *South African Journal of Geology*, 115(4):515-534.

Sen, G. 2014. Petrology: principles and practice. 1st ed. Berlin: Springer-Verlag.

Sharp, M.R. & Hulbert, L.J. 1985. Ultramafic sills beneath the Eastern Bushveld Complex: mobilized suspensions of early Lower Zone cumulates in a parental magma with boninitic affinities. *Economic Geology*, 80:849-871.

Shaw, D.M. 2000. Continuous (dynamic) melting theory revisited. *The Canadian Mineralogist*, (38):1041-1063.

Sheth, H. 2016. Giant plagioclase basalts: continental flood basalt-induced remobilization of anorthositic mushes in a deep crustal sill complex. *The Geological Society of America*, 128(5-6):916-925.

Slawson, W.F. 1976. Vredefort core: a cross-section of the upper crust? *Geochimica et Cosmochimica Acta*, 40(1):117-121.

Spudis, P.D., Martin, D.J.P. & Kramer, G. 2014. Geology and composition of the Orientale Basin impact melt sheet. *Journal of Geophysical Research: Planets*, 119:19-29.

Stepanov, A.S., Hermann, J., Rubatto, D. & Rapp, R.P. 2012. Experimental study of monazite/melt partitioning with implications for the REE, Th and U geochemistry of crustal rocks. *Chemical Geology*, 300-301:200-220.

Stepto, D. 1990. The geology and gravity field in the central core of the Vredefort structure. *Tectonophysics*, 171:75-103.

Stevens, G., Gibson, R.L. & Droop, G.T.R. 1997. Mid-crustal granulite facies metamorphism in the Central Kaapvaal Craton: the Bushveld Complex connection. *Precambrian Research*, 82:113-132.

Sumner, D.Y. & Beukes, N.J. 2006. Sequence stratigraphic development of the Neoarcean Transvaal carbonate platform, Kaapvaal Craton, South Africa. *South African Journal of Geology*, 109:11-22.

Sun, S.S. 1980. Lead isotopic study of young volcanic rocks from mid-ocean ridges, ocean islands and island arcs. *Philosophical Transactions of the Royal Society*, 297:409- 445.

Sun, S.S. & McDonough, W.F. 1989. Chemical and isotopic systematics of oceanic basalts: implications for mantle composition and processes. (*In*: Saunders, A.D. & Norry, M.J. (eds) Magmatism in ocean basins. Geological Society. London. Special publication p 313-345).

Suteanu, C. & Kruhl, J.H. 2002. Investigation of heterogeneous scaling intervals exemplified by sutured quartz grain boundaries. *Fractals*, 10(4):435-449.

Swanson, S.E. 1977. Relation of nucleation and crystal-growth rate to the development of granitic textures. *American Mineralogist*, 62:966-978.

Tankard, A.J., Jackson, M.P.A., Eriksson, K.A., Hobday, D.K., Hunter, D.R. & Minter, W.E.L. 1982. Crustal evolution of South Africa: 3.8 billion years of Earth history. 1st edition. New York: Springer-Verlag.

Tegner, C., Robins, B., Reginiussen, H. & Grundvig, S. 1999. Assimilation of crustal xenoliths in a basaltic magma chamber: Sr and Nd isotopic constraints from the Hasvik Layered Intrusion, Norway. *Journal of Petrology*, 40(3):363-380.

Tkalcec, B.J. & Brenker, F.E. 2015. Asteroidal processes recorded by polyphase deformation in a harzburgitic diogenite NWA 5480. *Journal of Structural Geology*, 77:138-150.

Torres-Alvarado, I.S., Pandarinath, K., Verma, S.P. & Dulski, P. 2010. Element mobility due to hydrothermal alteration in Los Azufres geothermal field, Mexico. Proceedings World Geothermal Congress, Bali, Indonesia, 25-29 April.

Vance, J.A. & Gilreath, J.P. 1967. The effect of synneusis on phenocryst distribution patterns in some porphyritic igneous rocks. *The American Mineralogist*, 52:529-536.

Van der Westhuizen, W.A., De Bruiyn, H. & Meintjes, P.G. 2009. The Ventersdorp Supergroup. (*In* Johnson, M.R., Anhaeusser, C.R. & Thomas, R.J. Geology of South Africa. Johannesburg: The Geological Society of South Africa. p 187-208).

Veblen, D.R. & Buseck, P.R. 1981. Hydrous pyriboles and sheet silicates in pyroxenes and uralites: intergrowth microstructures and reaction mechanisms. *American Mineralogist*, 66:1107-1134.

Velasco, F., Tornos, F. & Hanchar, J.M. 2016. Immiscible iron- and silica-rich melts and magnetite geochemistry at the El Laco volcano (northern Chile): evidence for a magmatic origin for the magnetite deposits. *Ore Geology Reviews*, 79:346-366.

Vernon, R.H. 2004. A practical guide to rock microstructure. 1st ed. New York: Cambridge University Press.

Vernon, R.H. & Clarke, G.L. 2008. Principles of metamorphic petrology. 1st ed. New York: Cambridge University Press.

Verwoerd, W.J. 2006. The Pilanesberg Alkaline Province. (*In*: Johnson, M.R., Anhaeusser, C.R. & Thomas, T.J. Geology of South Africa. Johannesburg: The Geological Society of South Africa. p 237-260).

Wang, S., Sun, F., Qian, Z. & Gao, P. 2014. Magmatic evolution and metal element enrichment during formation of the Niumaoquan magnetite ore deposit, Xingjian, China. *Ore Geology Reviews*, 63:64-75.

Weill, D.F. & Drake, M.J. 1973. Europium anomaly in plagioclase feldspar: experimental results and semiquantitative model. *Science*, 180:1059-1060.

White, R.S. 1997. Mantle plume origin for the Karoo and Ventersdorp flood basalts, South Africa. *South African Journal of Geology*, 100(4):271-282.

Wick, M.J. & Jones, R.H. 2012. Formation conditions of plagioclase-bearing type I chondrules in CO chondrites: A study of natural samples and experimental analogs. *Geochimica et Cosmochimica Acta*, 98:140-159.

Wilkinson, J.F.G. 1974. The mineralogy and petrography of alkali basaltic rock. (*In* Sørenson, H., *ed*. The alkaline rocks. London: John Wiley & Sons. P. 67-95).

Wilson, A.H. 2012. A chill sequence to the Bushveld Complex: insight into the first stage of emplacement and implications for the parental magmas. *Journal of Petrology*, 53(6):1123-1168.

Wilson, A.H. 2015. The earliest stages of emplacement of the Eastern Bushveld Complex: development of the Lower Zone, Marginal Zone and Basal Ultramafic Sequence. *Journal of Petrology*, 56(2):347-388.

Winter, J.D. 2010. Principles of igneous and metamorphic petrology. 2nd ed. New Jersey: Pearson.

Woo, Y., Yang, K., Kil, Y., Yun, S. & Arai, S. 2014. Silica- and LREE-enriched spinel peridotite xenoliths from the Quaternary intraplate alkali basalt, Jeju Island, South-Korea: old subarc fragments? *Lithos*, 208-209:312-323.

Yoder, H.S. & Tilley, C.E. 1962. Origin of basalt magmas; an experimental study of natural and synthetic rock systems. *Journal of Petrology*, 3(3):342-529.

Zhang, S., Zheng, Y., Zhao, Z. & Yuang, H. 2016. The extremely enriched mantle beneath the Yangte Craton in the Neoproterozoic: constraints from the Qichun pyroxenite. *Precambrian Research*, 276:194-210.

Zeh, A., Ovtcharova, M., Wilson, A.H. & Schaltegger, U. 2015. The Bushveld Complex was emplaced and cooled in less than one million years – results of zirconology, and geotectonic implications. *Earth and Planetary Science Letters*, 418:103-114.

APPENDICES

A: ROCK SAMPLE COLLECTION

A.1: Samples collected from the Winddam wehrlite along with sample rock type, coordinates, and type of analysis performed on each sample.

Sample number	Rock type	Sample coordinates	Thin section	XRF (Major- and trace elements)	Trace elements ICP-MS	REE ICP-MS
W01	Hornblende clinopyroxenite	26°59'58.1''S 27°30'30.8''E	Yes	Yes	No	No
W02	Olivine-hornblende clinopyroxenite	27°00'01.0''S 27°30'31.1''E	Yes	Yes	No	No
W03	Olivine-hornblende clinopyroxenite	27°00'04.6''S 27°30'31.3''E	Yes	Yes	No	No
W04	Olivine-hornblende clinopyroxenite	27°00'07.3''S 27°30'30.3''E	Yes	Yes	No	No
W05	Olivine-clinopyroxene hornblendite	27°00'10.9''S 27°30'29.0''E	Yes	Yes	No	No
W06	Hornblende clinopyroxenite	27°00'01.1''S 27°30'43.9''E	Yes	Yes	Yes	Yes

A.1 (continued): Samples collected from the Winddam wehrlite along with sample rock type, coordinates, and type of analysis performed on each sample.

Sample number	Rock type	Sample coordinates	Thin section	XRF (Major- and trace elements)	Trace elements ICP-MS	REE ICP-MS
W07	Hornblende clinopyroxenite	27°00'01.1''S 27°30'40.1''E	Yes	Yes	Yes	Yes
W08	Hornblende clinopyroxenite	27°00'01.2''S 27°30'36.6''E	Yes	Yes	No	No
W09	Olivine-hornblende clinopyroxenite	27°00'01.6''S 27°30'32.1''E	Yes	Yes	Yes	Yes
W10	Olivine-hornblende clinopyroxenite	27°00'01.6''S 27°30'29.4''E	Yes	Yes	No	No
W11	Olivine-hornblende clinopyroxenite	27°00'01.7''S 27°30'25.6''E	Yes	Yes	Yes	Yes
W12	Olivine-hornblende clinopyroxenite	27°00'02.8''S 27°30''22.2'E	Yes	Yes	Yes	Yes
W13	Olivine-hornblende clinopyroxenite	27°00'02.4'S 27°30'18.3''E	Yes	Yes	Yes	Yes
W14	Olivine-hornblende clinopyroxenite	27°00'03.2''S 27°30'14.8''E	Yes	Yes	Yes	Yes
W15	Hornblende-clinopyeoxenite	27°00'02.6''S 27°30'11.0''E	Yes	Yes	No	No

A.1 (continued): Samples collected from the Winddam wehrlite along with sample rock type, coordinates, and type of analysis performed on each sample. * = Mode of sample was not determined.

Sample number	Rock type	Sample coordinates	Thin section	XRF (Major- and trace elements)	Trace elements ICP-MS	REE ICP-MS
W16	Olivine-hornblende clinopyroxenite	27°00'02.4''S 27°30'03.2''E	Yes	Yes	Yes	Yes
W17	Olivine-hornblende clinopyroxenite	27°00'03.5''S 27°30'00.0''E	Yes	Yes	No	No
W18	Olivine-hornblende clinopyroxenite	27°00'04.6''S 27°29'54.2''E	Yes	Yes	Yes	Yes
CB44	Olivine and hornblende-bearing clinopyroxenite*	Unknown	Yes	Yes	No	No
CB45	Olivine and hornblende-bearing clinopyroxenite*	Unknown	Yes	Yes	No	No
CB47	Olivine-hornblende gabbronorite	Unknown	Yes	Yes	No	Yes
CB48	Olivine and hornblende-bearing clinopyroxenite*	Unknown	Yes	Yes	No	No
CB49	Olivine and hornblende-bearing clinopyroxenite*	Unknown	Yes	Yes	No	Yes

A.1 (continued): Samples collected from the Winddam wehrlite along with sample rock type, coordinates, and type of analysis performed on each sample. * = Mode of sample was not determined.

Sample number	Rock type	Sample coordinates	Thin section	XRF (Major- and trace elements)	Trace elements ICP-MS	REE ICP-MS
CB50	Olivine and hornblende-bearing clinopyroxenite*	Unknown	Yes	Yes	No	No
CB52	Olivine and hornblende-bearing clinopyroxenite*	Unknown	Yes	Yes	No	No
CB53	Olivine and hornblende-bearing clinopyroxenite*	Unknown	Yes	Yes	No	No
CB54	Olivine-hornblende clinopyroxenite	Unknown	Yes	Yes	No	Yes
CB55	Olivine and hornblende-bearing clinopyroxenite*	Unknown	Yes	Yes	No	No
CB56	Olivine and hornblende-bearing clinopyroxenite*	Unknown	Yes	Yes	No	No
CB57	Olivine and hornblende-bearing clinopyroxenite*	Unknown	Yes	Yes	No	No

A.1 (continued): Samples collected from the Winddam wehrlite along with sample rock type, coordinates, and type of analysis performed on each sample. * = Mode of sample was not determined.

Sample number	Rock type	Sample coordinates	Thin section	XRF (Major- and trace elements)	Trace elements ICP-MS	REE ICP-MS
CB58	Olivine and hornblende-bearing clinopyroxenite*	Unknown	Yes	Yes	No	No
CB59	Olivine and hornblende-bearing clinopyroxenite*	Unknown	Yes	Yes	No	No
CB61	Olivine and hornblende-bearing clinopyroxenite*	Unknown	Yes	Yes	No	No
CB62	Olivine-hornblende clinopyroxenite	Unknown	Yes	Yes	No	Yes
CB63	Olivine and hornblende-bearing clinopyroxenite*	Unknown	Yes	Yes	No	No
CB64	Olivine and hornblende-bearing clinopyroxenite*	Unknown	Yes	Yes	No	No
CB65	Olivine and hornblende-bearing clinopyroxenite*	Unknown	Yes	Yes	No	No

A.1 (continued): Samples collected from the Winddam wehrlite along with sample rock type, coordinates, and type of analysis performed on each sample. * = Mode of sample was not determined.

Sample number	Rock type	Sample coordinates	Thin section	XRF (Major- and trace elements)	Trace elements ICP-MS	REE ICP-MS
CB67	Olivine and hornblende-bearing clinopyroxenite*	Unknown	Yes	Yes	No	No
CB68	Olivine and hornblende-bearing clinopyroxenite*	Unknown	Yes	Yes	No	No

A.2: Samples collected from the Koedoesfontein Complex along with sample rock type, coordinates, and type of analysis performed on each sample. * = Mode of sample was not determined.

Sample number	Rock type	Sample coordinates	Thin section	XRF (Major- and trace elements)	Trace elements ICP-MS	REE ICP-MS
RB3	Hornblende gabbronorite	26°49'37.5" S 27°23'43.4" E	Yes	Yes	Yes	Yes
RB7	Wehrlite	26°49'36.2" S 27°23'46.6" E	Yes	Yes	No	No
RB8	Wehrlite	26°49'37.0" S 27°23'47.16" E	Yes	Yes	No	No
RB9	Olivine clinopyroxenite	26°49'37.0" S 27°23'46.6" E	Yes	Yes	Yes	Yes
RB10	Clinopyroxenite	26°49'35.3" S 27°23'49.7" E	Yes	Yes	No	No
RB20	Pyroxene hornblendite	26°49'37.3" S 27°23'43.4" E	Yes	Yes	No	No
304	Olivine clinopyroxenite	Unknown	Yes	No	No	No
MSC266	Wehrlite / olivine clinopyroxenite*	Unknown	Yes	Yes	No	No

A.2 (continued): Samples collected from the Koedoesfontein Complex with along with sample identity, sample coordinates, and type of analysis performed on each sample. * = Mode of sample was not determined.

Sample number	Rock type	Sample coordinates	Thin section	XRF (Major- and trace elements)	Trace elements ICP-MS	REE ICP-MS
MSC267	Wehrlite / olivine clinopyroxenite*	Unknown	Yes	Yes	No	No
MSC268	Olivine clinopyroxenite	Unknown	Yes	Yes	No	Yes
MSC270	Wehrlite / olivine clinopyroxenite*	Unknown	Yes	Yes	No	No
MSC271	Wehrlite / olivine clinopyroxenite*	Unknown	Yes	Yes	No	No
MSC272	Olivine clinopyroxenite	Unknown	Yes	Yes	No	Yes
WK32	Hornblende norite	26°49'37.9" S 27°23'46.0" E	Yes	Yes	No	No
WK34	Wehrlite	26°49'36.7" S 27°23'48.0" E	Yes	Yes	No	No
WK35	Olivine clinopyroxenite	26°49'36.0" S 27°23'49.3" E	Yes	Yes	No	No

A.2 (continued): Samples collected from the Koedoesfontein Complex along with sample rock type, coordinates, and type of analysis performed on each sample. * = Mode of sample was not determined.

Sample number	Rock type	Sample coordinates	Thin section	XRF (Major- and trace elements)	Trace elements ICP-MS	REE ICP-MS
WK34	Wehrlite	26°49'36.7" S 27°23'48.0" E	Yes	Yes	No	No
WK35	Olivine clinopyroxenite	26°49'36.0" S 27°23'49.3" E	Yes	Yes	No	No
WK36	Diorite	26°49'35.2" S 27°23'51.2" E	Yes	Yes	No	No
WK38	Olivine clinopyroxenite	26°49'36.2" S 27°23'52.4" E	Yes	Yes	No	No
WK39	Wehrlite	26°39'35.4" S 27°23'49.8" E	Yes	Yes	No	No

A.3: Samples collected from the Rietfontein Complex along with sample rock type, coordinates, and type of analysis performed on each sample. * = see Figure 3.1 for stratigraphic position.

Sample number	Rock type	Sample coordinates	Thin section	XRF (Major- and trace elements)	Trace elements ICP-MS	REE ICP-MS
CB1	Olivine-hornblende clinopyroxenite	Unknown*	Yes	Yes	Yes	Yes
CB2	Olivine-hornblende clinopyroxenite	Unknown*	Yes	Yes	Yes	Yes
CB3	Olivine diorite	Unknown*	Yes	Yes	Yes	Yes
CB5	Olivine diorite	Unknown*	Yes	Yes	No	Yes
CB6	Olivine diorite	Unknown*	Yes	Yes	No	No
CB7	Olivine diorite	Unkown	Yes	Yes	No	Yes
CB8	Olivine clinopyroxenite	Unknown*	Yes	Yes	No	Yes
CB9	Olivine clinopyroxenite	Unknown*	Yes	Yes	Yes	Yes
CB10	Olivine diorite	Unknown*	Yes	Yes	Yes	Yes
CB11	Olivine diorite	Unknown*	Yes	Yes	Yes	Yes
CB12	Olivine diorite	Unknown*	No	Yes	No	No
CB13	Olivine diorite	Unknown*	Yes	Yes	No	No

A.3 (continued): Samples collected from the Rietfontein Complex with along sample rock type, coordinates, and type of analysis performed on each sample. * = see Figure 3.1 for stratigraphic position.

Sample number	Rock type	Sample coordinates	Thin section	XRF (Major- and trace elements)	Trace elements ICP-MS	REE ICP-MS
CB14	Olivine clinopyroxenite	Unknown*	Yes	Yes	Yes	Yes
CB15	Olivine clinopyroxentie	Unknown*	Yes	Yes	Yes	Yes
CB16	Olivine clinopyroxenite	Unknown*	Yes	Yes	Yes	Yes
CB17	Troctolite	Unknown*	Yes	Yes	Yes	Yes
CB18	Plagioclase-poor, magnetite-rich troctolite	Unknown*	Yes	Yes	No	Yes
MB19a	Magnetite-rich troctolite	Unknown*	Yes	Yes	No	Yes
CB20	Olivine diorite	Unknown*	Yes	Yes	No	Yes
CB35	Olivine diorite	Unkown	Yes	Yes	Yes	Yes
CB37	Olivine diorite	Unkown	Yes	Yes	Yes	No
CB38	Olivine diorite	Unkown	Yes	Yes	No	Yes
CB39	Olivine diorite	Unkown	Yes	Yes	No	No

A.3 (continued): Samples collected from the Rietfontein Complex along with sample rock type, coordinates, and type of analysis performed on each sample. * = see Figure 3.1 for stratigraphic position.

Sample number	Rock type	Sample coordinates	Thin section	XRF (Major- and trace elements)	Trace elements ICP-MS	REE ICP-MS
CB33	Olivine-hornblende clinopyroxenite	Unkown	Yes	Yes	No	Yes
CB33a	Olivine diorite	Unknown*	Yes	Yes	No	Yes
CB34	Olivine clinopyroxenite	Unkown	Yes	Yes	No	Yes
CB40	Olivine diorite	Unkown	Yes	Yes	No	No
CB41	Troctolite	Unkown	Yes	Yes	No	Yes
51	Troctolite	Unknown*	Yes	Yes	No	No
52	Magnetite-rich troctolite	Unknown*	Yes	Yes	Yes	Yes
54	Plagioclase-poor, magnetite-rich troctolite	Unknown*	Yes	Yes	Yes	No

B: MODAL MINERALOGY

B.1: The modal mineralogy of selected rock samples from the Winddam wehrlite determined optically by means of point counting.

	Olivine (vol. %)	Augite (vol. %)	Enstatite (vol. %)	Hornblende (vol. %)	Opaque phases (vol. %)	Biotite (vol. %)
W01	8.0	68.6	1.9	20.8	0.8	0.0
W02	13.0	65.7	1.7	18.2	1.4	0.0
W03	10.4	65.2	1.1	22.5	0.8	0.0
W04	12.9	67.8	1.1	17.1	1.1	0.0
W05	21.8	37.1	0.0	40.7	0.3	0.0
W06	0.8	62.6	2.0	33.4	1.2	0.0
W07	5.9	79.6	0.1	13.2	1.2	0.0
W08	2.5	83.1	3.8	10.3	0.3	0.0
W09	9.5	67.6	0.7	22.0	0.2	0.0
W10	13.2	66.4	1.2	18.8	0.4	0.0
W11	19.3	58.6	0.8	20.8	0.6	0.0
W12	18.0	63.1	0.5	18.0	0.3	0.0

B.1 (continued): The modal mineralogy of selected rock samples from the Winddam wehrlite determined optically by means of point counting.

	Olivine (vol. %)	Augite (vol. %)	Enstatite (vol. %)	Hornblende (vol. %)	Opaque phases (vol. %)	Biotite (vol. %)
W13	25.3	50.6	2.1	21.3	0.7	0.0
W14	19.3	56.5	1.0	22.0	1.2	0.0
W15	9.3	81.2	1.4	7.7	0.4	0.0
W16	30.7	59.8	0.9	8.3	0.3	0.0
W17	16.7	63.9	4.4	11.8	0.1	3.1
W18	9.7	72.1	2.9	15.1	0.2	0.0
CB49	21.2	51.3	1.1	25.4	1.0	0.0
CB54	23.4	57.5	0.5	18.2	0.4	0.0

B.2: The modal mineralogy of selected rock samples from the Koedoesfontein Complex determined optically by means of point counting.

	Olivine (vol. %)	Augite (vol. %)	Enstatite (vol. %)	Hornblende (vol. %)	Plagioclase (vol. %)	Magnetite (vol. %)	Quartz
RB3	0.0	23.7	10.1	14.7	50.3	0.9	0.0
RB7	42.6	49.1	0.0	0.1	0.0	5.8	0.0
RB8	44.1	54.0	0.0	0.7	0.0	5.9	0.0

B.2 (continued): The modal mineralogy of selected rock samples from the Koedoesfontein Complex determined optically by means of point counting.

	Olivine (vol. %)	Augite (vol. %)	Enstatite (vol. %)	Hornblende (vol. %)	Plagioclase (vol. %)	Magnetite (vol. %)	Quartz (vol. %)
RB9	28.6	65.0	0.0	0.7	0.0	5.8	0.0
RB10	3.8	95.6	0.0	0.5	0.0	0.0	0.0
RB20	0.0	12.9	33.8	49.3	0.0	12.0	2.5
WK32	0.0	0.0	51.8	28.0	19.7	0.5	0.0
WK34	44.6	54.0	0.0	0.6	0.0	0.8	0.0
WK35	34.5	65.1	0.0	0.1	0.0	0.8	0.0
WK36	0.0	23.7	0.0	30.5	32.8	0.0	0.0
WK38	17.8	78.5	0.0	3.2	0.0	0.5	0.0
WK39	41.6	54.7	0.0	2.6	0.0	1.1	0.0
MSC272	36.2	62.5	0.0	0.0	0.0	1.2	0.0

B.3: The modal mineralogy of selected rock samples from the Rietfontein Complex determined optically by means of point counting.

	Olivine (vol. %)	Augite (vol. %)	Plagioclase (vol. %)	Hornblende (vol. %)	Magnetite (vol. %)	Biotite (vol. %)
CB1	22.3	50.1	0.0	26.8	0.5	0.0
CB2	23.5	60.8	0.0	15.0	0.5	0.0
CB3	23.6	40.4	33.8	0.0	1.1	0.3
CB6	12.3	56.3	26.5	0.0	4.3	0.0
CB33a	21.5	28.5	44.7	1.3	3.4	0.3
CB9	10.6	69.2	3.6	0.2	11.4	0.2
CB10	12.6	54.8	28.1	0.0	4.1	0.1
CB11	11.4	50.0	36.0	0.0	1.9	0.3
CB13	18.4	55.0	23.0	0.0	3.1	0.0
CB14	21.7	61.7	9.6	0.0	6.7	0.1
CB15	14.2	70.4	7.0	0.8	3.2	4.4
CB16	26.4	36.6	34.7	0.0	0.7	1.3
CB17	48.0	0.7	35.0	0.1	14.4	0.9

B.3 (continued): The modal mineralogy of selected rock samples from the Rietfontein Complex determined optically by means of point counting.

	Olivine (vol. %)	Augite (vol. %)	Plagioclase (vol. %)	Hornblende (vol. %)	Magnetite (vol. %)	Biotite (vol. %)
CB19	42.0	19.8	24.2	0.0	12.5	0.9
CB20	37.6	29.5	28.1	0.3	3.7	0.0
51	60.7	0.0	25.8	0.0	13.0	0.5
52	40.5	0.0	21.7	0.0	37.1	0.7
54	68.8	0.0	4.3	0.0	25.8	1.1

C: X-RAY FLUORESCENCE RESULTS FOR MSC SAMPLES

C.1: Major and trace element compositions of samples labelled as MSC from the Koedoesfontein Complex determined with XRF at the University of the Free State.

Sample	MSC266	MSC267	MSC268	MSC270	MSC271	MSC272
wt. %						
SiO_2	45.03	45.18	46.89	45.58	46.14	46.92
TiO_2	0.25	0.26	0.32	0.49	0.32	0.32
Al_2O_3	0.81	0.88	1.03	1.25	1.05	1.04
Fe_2O_3(t)	14.86	14.5	13.87	18.8	13.98	13.66
MnO	0.23	0.21	0.21	0.27	0.21	0.21
MgO	25.31	25.04	23.28	18.74	23.15	22.85
CaO	9.75	10.35	12.12	11.51	12.00	12.18
Na_2O	0.21	0.21	0.27	0.27	0.25	0.26
K_2O	0.01	0.01	0.01	0.03	0.02	0.02
P_2O_5	0.02	0.02	0.02	0.03	0.02	0.02
H_2O-	0.26	0.23	0.15	0.88	0.15	0.15
LOI	2.76	2.40	1.67	1.33	1.80	1.63
Total	99.5	99.29	99.84	99.18	99.09	99.26
ppm						
Cr	1721	1846	1738	1839	1572	1676
Ni	744	888	750	857	530	827
Co	116	108	91	124	104	98
V	100	101	122	182	117	116
Zn	89	83	78	115	81	89
Rb	2	2	2	5	3	3
Ba	21	b.d.l.	14	133	34	24
Sr	33	33	40	50	39	40
Zr	18	18	19	25	20	20
Y	5	4	5	9	6	7
Nb	6	6	6	9	7	6
Cu	18	15	15	32	11	19
Sc	26	31	27	33	28	32

LOI = Loss on ignition

b.d.l. = below detection limit

D: X-RAY FLUORESENCE RESULTS FOR CB AND MB SAMPLES

D.1: Major and trace element compositions of samples labelled as CB (CB1 to CB41 are from the Rietfontein Complex and CB44 to CB69 are from the Winddam wehrlite) and MB (Rietfontein Complex) determined with XRF by J.H. Elsenbroek, J. Trojak, A. Schoeman, H.C. Cloete, and J. Bednarik at the Council of Geoscience.

Sample	CB1	CB2	CB3	CB5	CB6	CB7	CB8	CB9
wt. %								
SiO_2	47.51	47.23	48.34	49.46	45.80	47.51	43.93	43.94
TiO_2	0.62	0.50	0.55	0.91	0.92	0.80	1.60	1.48
Al_2O_3	2.67	2.93	9.53	9.70	11.92	7.57	3.75	3.87
Fe_2O_3	2.87	2.69	2.53	4.04	3.30	3.95	8.61	8.49
FeO	10.59	10.37	9.37	8.26	9.82	9.91	10.83	9.83
MnO	0.24	0.24	0.21	0.18	0.20	0.22	0.28	0.25
MgO	20.67	21.45	16.09	12.98	13.66	15.80	17.37	16.03
CaO	12.97	13.10	10.93	11.86	11.44	12.43	12.17	12.94
Na_2O	0.87	0.76	2.41	2.75	2.60	1.75	0.77	0.83
K_2O	0.11	0.07	0.09	0.19	0.18	0.13	0.10	0.11
P_2O_5	0.10	0.08	0.05	0.10	0.10	0.07	0.10	0.09
H_2O-	0.06	0.06	0.09	0.06	0.07	0.11	0.26	0.24
LOI	0.94	1.05	1.16	1.06	0.40	0.98	1.57	1.47
Total	100.22	100.53	101.35	101.55	100.41	101.23	101.34	99.57
ppm								
Cr	1517	1575	576	664	522	747	1052	818
Ni	292	305	286	194	202	259	369	317
V	198	178	180	251	301	258	494	511
Zn	67	76	69	68	65	77	92	92
Rb	4	6	4	8	4	8	8	8
Ba	83	64	103	128	141	160	104	209
Sr	79	72	422	426	400	313	239	119
Zr	20	14	21	35	31	27	109	27
Y	6	6	6	8	8	8	12	11
Nb	5	4	3	4	4	4	5	4
Cu	89	51	6	33	26	26	65	59
Sc	44	44	33	42	39	43	51	54

LOI = Loss on ignition
b.d.l. = below detection limit

D.1 (continued): Major and trace element compositions of samples labelled as CB (CB1 to CB41 are from the Rietfontein Complex and CB44 to CB69 are from the Winddam wehrlite) and MB (Rietfontein Complex) determined with XRF by J.H. Elsenbroek, J. Trojak, A. Schoeman, H.C. Cloete, and J. Bednarik at the Council of Geoscience.

Sample	CB10	CB11	CB12	CB13	CB14	CB15	CB16	CB17
wt. %								
SiO_2	47.41	49.48	48.04	47.37	43.82	47.50	48.01	35.03
TiO_2	0.99	0.89	0.84	0.96	1.67	1.30	0.57	2.39
Al_2O_3	9.29	9.61	6.96	6.90	4.16	3.87	8.20	7.19
Fe_2O_3	3.94	3.38	3.24	3.69	8.12	4.48	2.22	11.31
FeO	9.39	8.75	11.11	11.29	11.02	11.01	10.93	18.36
MnO	0.20	0.18	0.22	0.23	0.25	0.26	0.20	0.26
MgO	12.63	12.35	16.24	16.12	16.41	16.40	17.69	19.80
CaO	11.87	12.13	12.03	12.15	13.06	14.15	10.57	2.18
Na_2O	2.41	2.96	2.12	1.96	1.20	1.50	2.30	2.07
K_2O	0.13	0.15	0.09	0.07	0.05	0.13	0.08	0.10
P_2O_5	0.06	0.09	0.07	0.06	0.05	0.13	0.06	0.05
H_2O-	0.08	0.03	0.03	0.04	0.18	0.13	0.03	0.20
LOI	1.09	0.40	0.66	0.26	0.34	0.32	0.43	1.46
Total	99.49	100.40	101.65	101.10	100.33	101.18	101.29	100.40
ppm								
Cr	597	563	847	877	774	751	523	1212
Ni	147	172	292	346	410	244	369	844
V	377	256	271	304	605	337	155	783
Zn	63	63	81	88	97	98	84	179
Rb	6	6	5	5	5	6	4	5
Ba	122	141	120	131	163	174	99	222
Sr	424	437	292	282	145	122	366	364
Zr	25	32	25	24	23	48	34	19
Y	7	8	8	9	9	14	8	b.d.l.
Nb	4	4	4	3	3	5	4	b.d.l
Cu	34	27	24	24	38	58	12	54
Sc	43	40	41	42	56	53	33	14

LOI = Loss on ignition
b.d.l. = below detection limit

D.1 (continued): Major and trace element compositions of samples labelled as CB (CB1 to CB41 are from the Rietfontein Complex and CB44 to CB69 are from the Winddam wehrlite) and MB (Rietfontein Complex) determined with XRF by J.H. Elsenbroek, J. Trojak, A. Schoeman, H.C. Cloete, and J. Bednarik at the Council of Geoscience.

Sample	CB18	CB19	MB19a	CB20	CB33	CB33a	CB34	CB35
wt. %								
SiO_2	27.45	39.57	23.48	45.72	41.33	47.55	50.92	45.21
TiO_2	3.47	1.98	5.59	0.69	2.49	0.90	1.23	1.69
Al_2O_3	2.18	6.38	5.23	7.20	3.34	11.07	7.19	5.04
Fe_2O_3	15.89	7.50	23.02	2.70	8.21	2.57	3.70	4.63
FeO	22.86	17.63	22.03	14.69	13.67	11.74	6.21	12.17
MnO	0.32	0.25	0.28	0.24	0.28	0.19	0.17	0.26
MgO	23.18	19.06	13.57	20.18	15.95	14.06	11.81	15.72
CaO	2.64	5.78	1.23	7.64	13.03	8.51	16.98	13.87
Na_2O	0.65	2.09	1.53	2.34	0.70	3.49	2.15	1.36
K_2O	0.09	0.04	0.04	0.04	0.06	0.25	0.01	0.10
P_2O_5	0.07	0.04	0.03	0.05	0.08	0.14	0.08	0.13
H_2O-	0.13	0.04	0.18	0.04	0.16	0.03	0.20	0.05
LOI	1.71	0.41	2.21	0.49	1.63	0.40	0.91	0.49
Total	100.64	100.77	98.42	102.02	100.93	100.90	101.56	100.72
ppm								
Cr	1961	743	2003	1704	725	260	676	588
Ni	1148	462	930	542	288	326	682	227
V	1175	608	2052	192	703	175	307	358
Zn	235	141	249	118	110	88	54	100
Rb	5	3	4	5	7	9	7	7
Ba	244	171	411	98	168	172	150	94
Sr	73	328	224	400	108	556	338	144
Zr	13	18	14	23	30	51	46	47
Y	b.d.l	b.d.l	b.d.l	b.d.l	11	7	12	14
Nb	4	4	5	3	8	8	7	9
Cu	97	46	125	11	51	48	21	67
Sc	14	24	21	27	36	16	41	34

LOI = Loss on ignition
b.d.l. = below detection limit

D.1 (continued): Major and trace element compositions of samples labelled as CB (CB1 to CB41 are from the Rietfontein Complex and CB44 to CB69 are from the Winddam wehrlite) and MB (Rietfontein Complex) determined with XRF by J.H. Elsenbroek, J. Trojak, A. Schoeman, H.C. Cloete, and J. Bednarik at the Council of Geoscience.

Sample	CB37	CB38	CB39	CB40	CB41	CB44	CB45	CB47
wt. %								
SiO_2	49.20	49.17	48.50	49.05	43.39	48.52	49.89	47.62
TiO_2	0.73	0.67	0.71	0.69	0.61	0.33	0.33	0.47
Al_2O_3	10.01	11.66	10.57	9.70	10.90	1.17	1.23	8.39
Fe_2O_3	1.81	2.18	2.17	2.01	6.73	3.48	2.57	3.01
FeO	8.61	7.29	10.39	6.59	12.03	6.84	6.05	7.97
MnO	0.17	0.16	0.18	0.16	0.22	0.23	0.20	0.19
MgO	14.33	13.25	14.55	13.48	18.12	20.40	20.14	21.27
CaO	12.49	11.82	9.58	14.23	4.15	15.51	16.87	7.92
Na_2O	2.86	3.26	3.11	2.68	2.67	0.65	0.66	1.52
K_2O	0.12	0.12	0.04	0.09	0.05	0.07	0.04	0.29
P_2O_5	0.09	0.09	0.08	0.06	0.05	0.08	0.06	0.06
H_2O-	0.04	0.04	0.01	0.07	0.24	0.16	0.16	0.16
LOI	0.33	0.51	0.34	0.27	0.87	1.26	1.30	0.24
Total	100.79	100.22	100.23	99.08	100.03	98.70	99.50	99.11
ppm								
Cr	341	304	273	382	358	1141	1116	3042
Ni	256	240	284	291	565	315	330	898
V	128	118	140	147	121	180	172	174
Zn	71	58	73	46	118	58	45	69
Rb	5	6	6	5	4	4	5	11
Ba	87	102	78	71	110	62	b.d.l.	115
Sr	501	557	534	429	625	49	47	78
Zr	38	37	34	32	18	5	6	29
Y	9	8	6	9	b.d.l.	b.d.l.	b.d.l.	12
Nb	7	7	7	7	6	5	5	5
Cu	17	18	26	b.d.l	b.d.l	900	709	48
Sc	27	21	19	33	5	43	40	27

LOI = Loss on ignition
b.d.l. = below detection limit

D.1 (continued): Major and trace element compositions of samples labelled as CB (CB1 to CB41 are from the Rietfontein Complex and CB44 to CB69 are from the Winddam wehrlite) and MB (Rietfontein Complex) determined with XRF by J.H. Elsenbroek, J. Trojak, A. Schoeman, H.C. Cloete, and J. Bednarik at the Council of Geoscience.

Sample	CB48	CB49	CB50	CB52	CB53	CB54	CB55
wt. %							
SiO_2	49.91	48.65	52.75	47.97	48.62	48.65	49.15
TiO_2	0.40	0.34	0.45	0.33	0.34	0.39	0.43
Al_2O_3	2.19	1.30	1.64	1.35	1.25	1.78	2.07
Fe_2O_3	2.71	2.90	2.39	3.22	2.59	2.70	2.74
FeO	5.86	6.89	6.89	7.22	7.03	6.89	7.97
MnO	0.19	0.21	0.22	0.26	0.21	0.20	0.22
MgO	19.27	22.49	19.05	22.66	21.15	20.75	20.83
CaO	15.39	14.09	15.82	14.01	14.88	14.45	14.25
Na_2O	0.84	0.72	0.93	0.68	0.68	0.78	0.88
K_2O	0.11	0.07	0.07	0.06	0.06	0.08	0.09
P_2O_5	0.12	0.06	0.09	0.07	0.06	0.08	0.07
H_2O-	0.24	0.24	0.20	0.28	0.24	0.20	0.18
LOI	1.79	1.34	0.44	1.25	1.55	1.88	0.76
Total	99.02	99.30	100.94	99.36	98.66	98.83	99.64
ppm							
Cr	3566	3298	2844	3071	3285	2797	2089
Ni	352	468	323	461	446	375	382
V	176	152	212	157	166	188	201
Zn	59	54	50	60	56	51	59
Rb	6	5	5	6	5	6	4
Ba	37	31	b.d.l.	82	69	20	10
Sr	82	55	76	51	54	75	84
Zr	12	7	11	6	6	12	12
Y	b.d.l.	b.d.l.	5	b.d.l.	b.d.l.	b.d.l.	6
Nb	5	5	6	5	4	5	5
Cu	535	378	456	428	548	233	482
Sc	41	36	40	42	42	41	44

LOI = Loss on ignition
b.d.l. = below detection limit

D.1 (continued): Major and trace element compositions of samples labelled as CB (CB1 to CB41 are from the Rietfontein Complex and CB44 to CB69 are from the Winddam wehrlite) and MB (Rietfontein Complex) determined with XRF by J.H. Elsenbroek, J. Trojak, A. Schoeman, H.C. Cloete, and J. Bednarik at the Council of Geoscience.

Sample	CB56	CB57	CB58	CB59	CB61	CB62	CB63
wt. %							
SiO_2	48.21	48.18	47.99	48.13	48.13	48.43	47.55
TiO_2	0.46	0.53	0.45	0.46	0.37	0.38	0.38
Al_2O_3	2.23	2.35	2.22	2.28	1.54	1.42	1.51
Fe_2O_3	3.57	3.72	3.72	3.53	3.68	3.33	3.42
FeO	7.82	8.28	8.46	7.73	7.28	7.91	8.88
MnO	0.23	0.23	0.29	0.25	0.23	0.25	0.26
MgO	20.46	20.36	20.12	20.71	21.45	20.38	20.73
CaO	13.39	13.37	13.55	13.28	13.84	14.67	13.97
Na_2O	0.96	0.96	0.85	0.89	0.74	0.67	0.67
K_2O	0.1	0.09	0.09	0.10	0.09	0.05	0.05
P_2O_5	0.08	0.09	0.10	0.11	0.14	0.08	0.08
H_2O-	0.24	0.16	0.22	0.22	0.16	0.14	0.12
LOI	1.14	0.82	1.10	1.35	1.30	1.26	1.38
Total	98.89	99.14	99.16	99.04	98.95	98.97	99.00
ppm							
Cr	2089	2000	1979	2177	2761	1638	2492
Ni	399	378	380	396	403	328	404
V	205	229	221	203	181	212	207
Zn	63	63	68	68	60	59	70
Rb	5	6	4	6	5	5	5
Ba	45	6	67	32	32	9	50
Sr	87	87	81	81	62	53	50
Zr	14	13	12	12	8	7	8
Y	6	5	b.d.l.	5	b.d.l	b.d.l.	b.d.l.
Nb	5	5	5	5	5	4	5
Cu	415	362	482	347	721	623	752
Sc	43	39	44	36	39	44	44

LOI = Loss on ignition
b.d.l. = below detection limit

D.1 (continued): Major and trace element compositions of samples labelled as CB (CB1 to CB41 are from the Rietfontein Complex and CB44 to CB69 are from the Winddam wehrlite) and MB (Rietfontein Complex) determined with XRF by J.H. Elsenbroek, J. Trojak, A. Schoeman, H.C. Cloete, and J. Bednarik at the Council of Geoscience.

Sample	CB64	CB65	CB67	CB68	CB69
wt. %					
SiO_2	48.20	48.48	51.10	46.85	50.09
TiO_2	0.43	0.39	0.31	0.59	0.42
Al_2O_3	1.91	1.78	0.91	1.53	1.80
Fe_2O_3	3.08	3.44	3.42	5.31	2.22
FeO	8.32	8.37	5.82	10.19	6.84
MnO	0.24	0.24	0.24	0.29	0.21
MgO	20.40	21.42	19.87	18.97	18.95
CaO	14.16	14.00	16.82	13.54	17.11
Na_2O	0.83	0.73	0.54	0.79	0.78
K_2O	0.08	0.06	0.02	0.06	0.03
P_2O_5	0.07	0.06	0.04	0.08	0.07
H_2O-	0.16	0.06	0.14	0.04	0.04
LOI	1.12	1.02	1.05	1.17	0.46
Total	99.00	100.05	100.28	99.41	99.02
ppm					
Cr	2275	2275	1626	1612	3797
Ni	377	377	300	358	274
V	210	210	180	349	209
Zn	60	60	46	81	50
Rb	5	5	5	6	4
Ba	7	7	b.d.l.	18	b.d.l.
Sr	69	69	40	66	54
Zr	10	10	b.d.l.	8	6
Y	b.d.l.	b.d.l.	b.d.l.	6	b.d.l.
Nb	5	4	4	5	4
Cu	555	463	909	1155	183
Sc	42	42	44	44	43

LOI = Loss on ignition
b.d.l. = below detection limit

E: X-RAY FLUORESCENCE RESULTS FOR WK SAMPLES

E.1: Major and trace element compositions of samples labelled as WK (Koedoesfontein Complex) determined with XRF by A.H. Wilson at the University of the Witwatersrand.

Sample	WK32	WK34	WK35	WK36	WK38	WK39
wt. %						
SiO_2	51.66	45.66	46.98	45.13	48.92	4682
TiO_2	0.42	0.28	0.34	2.30	0.47	0.33
Al_2O_3	10.24	0.92	1.12	10.7	1.34	1.06
Fe_2O_3*	1.12	1.46	1.38	2.00	1.45	1.42
FeO	9.07	11.85	11.16	16.23	11.77	11.49
MnO	0.18	0.22	0.21	0.28	0.24	0.20
MgO	16.69	25.84	23.80	7.04	19.28	23.59
CaO	7.48	10.67	12.38	10.12	15.05	12.04
Na_2O	1.66	0.34	0.39	3.55	0.51	0.37
K_2O	0.28	0.01	0.01	0.52	0.02	0.02
P_2O_5	0.06	0.03	0.03	0.54	0.02	0.02
LOI	1	2.56	2.09	0.8	0.71	2.56
Total	100.25	100.23	100.24	99.24	100.11	100.35
ppm						
Cr	2058.9	1788.7	1800.8	113.2	1663.9	2033.5
Ni	497.6	625.2	530.5	39.3	430.7	568.2
Co	106.1	156.3	137.0	128.2	148.3	183.2
V	161.3	107.6	138.0	442.1	188.1	133.4
Zn	74.1	82.6	71.5	149.0	79.9	75.9
Rb	6.0	0.3	0.6	6.2	0.0	b.d.l.
Ba	119.2	33.8	32.0	1392	48.8	58.4
Pb	3.9	0.7	6.1	b.d.l.	0.4	1.5
Sr	143.3	30.1	36.3	744.3	43.7	34.0
Zr	43.9	3.7	5.3	40.1	7.6	5.3
Y	11.6	4.4	5.6	22.5	5.9	4.9
Nb	1.9	1.4	1.1	9.9	1.1	1.9
Cu	b.d.l.	b.d.l.	b.d.l.	662.5	b.d.l.	b.d.l.
Sc	34.2	31.1	39.1	38.8	45.3	38.6

LOI = Loss on ignition
b.d.l. = below detection limit
*** = Fe_2O_3 calculated as 10 wt. % of total iron.**

F: X-RAY FLUORESCENCE RESULTS FOR W AND RB SAMPLES

F.1: Major and trace element compositions of samples labelled as W (Winddam wehrlite) and RB (Koedoesfontein Complex) determined with XRF by B. Venter at the North-West University, Potchefstroom campus.

Sample	WO1	WO2	WO3	W04	WO5	WO6	W07	W08	W09
wt. %									
SiO_2	44.79	43.73	42.95	42.81	43.05	43.49	44.21	42.72	43.68
TiO_2	0.39	0.36	0.35	0.33	0.34	0.38	0.28	0.32	0.31
Al_2O_3	1.80	2.04	1.96	1.73	2.09	2.37	1.60	1.86	1.75
Fe_2O_3(t)	10.74	10.75	11.69	11.86	11.17	11.94	9.89	12.16	10.27
MnO	0.24	0.23	0.22	0.22	0.20	0.22	0.20	0.23	0.20
MgO	18.33	19.45	20.30	19.57	20.31	19.35	20.35	22.42	20.80
CaO	15.64	14.98	13.98	14.19	13.81	13.91	15.43	12.82	14.56
Na_2O	0.63	0.73	0.70	0.67	0.82	0.84	0.63	0.69	0.72
K_2O	0.06	0.09	0.07	0.07	0.09	0.11	0.05	0.08	0.07
P_2O_5	0.02	0.02	0.03	0.02	0.04	0.04	0.02	0.03	0.02
LOI	5.79	6.18	6.46	6.95	6.26	5.78	6.52	5.13	6.21
Total	99.10	99.14	99.24	99.21	98.96	98.85	99.73	99.16	99.25
ppm									
Cr	1635.3	2086.8	2223.7	2264.7	2716.3	1772.1	2524.7	3113.2	2880.5
Ni	345.7	353.6	424.3	424.3	471.5	369.3	392.9	581.5	471.5
Co	109.8	123.9	132.4	120.6	119.4	163.5	122.3	130.6	121.1
V	224.2	218.6	224.2	224.2	213.0	207.4	201.8	168.1	196.2
Zn	68.3	56.6	65.7	54.7	84.2	84.3	52.5	63.1	60.0
Rb	1.6	2.4	1.2	1.1	1.00	1.6	0.3	0.8	0.7
Ba	23.4	52.4	18.9	14.9	34.1	90.9	29.8	16.9	20.8
Sr	53.7	76.2	56.1	44.1	123.3	46.4	42.4	38.3	51.0
Zr	9.0	10.1	8.2	5.7	15.2	7.8	5.7	2.6	8.2
Y	3.3	2.7	2.3	2.6	5.0	2.9	3.0	1.9	3.0
Nb	0.7	0.4	1.0	0.2	2.0	.08	0.4	b.d.l.	0.6
Cu	1030.5	399.4	223.7	982.6	407.4	175.7	191.7	215.7	399.4
Sc	50.7	46.2	42.1	50.7	49.1	45.5	57.8	55.8	50.6

LOI = Loss on ignition
b.d.l. = below detection limit

F.1 (continued): Major and trace element compositions of samples labelled as W (Winddam wehrlite) and RB (Koedoesfontein Complex) determined with XRF by B. Venter at the North-West University, Potchefstroom campus.

Sample	W10	W11	W12	W13	W14	W15	W16	W17	W18
wt. %									
SiO_2	44.59	41.12	43.48	43.70	43.25	42.89	41.33	44.11	44.90
TiO_2	0.38	0.74	0.35	0.33	0.32	0.38	0.70	0.59	0.33
Al_2O_3	1.72	3.53	2.12	1.73	1.83	1.59	3.53	1.94	1.47
Fe_2O_3(t)	9.11	15.22	11.58	10.27	11.35	13.09	15.29	14.19	10.88
MnO	0.20	0.24	0.22	0.20	0.24	0.24	0.24	0.28	0.26
MgO	18.85	18.00	20.18	20.61	21.03	18.78	18.02	18.19	17.88
CaO	16.59	12.34	14.14	14.64	13.86	14.87	12.36	12.86	16.31
Na_2O	0.66	1.22	0.76	0.70	0.69	0.63	1.21	0.58	0.57
K_2O	0.04	0.11	0.09	0.07	0.07	0.04	0.11	0.08	0.05
P_2O_5	0.02	0.06	0.03	0.02	0.03	0.01	0.06	0.02	0.01
LOI	6.29	6.43	5.48	6.33	6.00	6.24	5.89	6.00	6.35
Total	99.14	99.35	99.04	99.23	99.21	99.30	99.17	99.39	99.45
ppm									
Cr	2285.3	875.8	2257.9	2921.6	2381.1	1698.8	916.8	2004.7	643.2
Ni	345.7	353.6	424.3	416.5	440.0	337.9	377.2	353.6	227.9
Co	117.4	123.2	117.2	123.2	127.4	118.9	140.2	103.9	92.8
V	246.6	280.2	179.3	179.3	218.6	269.0	252.2	386.7	263.4
Zn	65.8	66.7	48.4	51.5	53.5	46.4	60.0	48.7	41.4
Rb	2.3	1.6	1.2	1.2	2.6	1.0	1.9	1.0	1.0
Ba	24.6	29.1	29.4	34.9	48.5	22.2	24.6	25.4	11.5
Sr	66.1	65.0	51.0	81.5	76.9	55.5	58.7	58.7	56.8
Zr	9.4	9.5	6.7	11.0	12.8	7.1	8.2	8.4	7.1
Y	2.8	3.7	2.1	2.0	3.0	2.3	2.6	3.0	3.4
Nb	1.0	0.2	0.9	1.0	1.1	1.0	1.7	1.0	0.6
Cu	639.1	295.6	375.5	359.5	303.6	583.2	343.5	407.4	958.6
Sc	49.6	48.4	47.1	43.7	45.4	46.8	40.0	44.1	50.8

LOI = Loss on ignition
b.d.l. = below detection limit

F.1 (continued): Major and trace element compositions of samples labelled as W (Winddam wehrlite) and RB (Koedoesfontein Complex) determined with XRF by B. Venter at the North-West University, Potchefstroom campus.

Sample	RB3	RB7	RB8	RB9	RB10	RB20
wt. %						
SiO_2	46.66	40.99	40.80	43.40	47.50	47.23
TiO_2	0.51	0.24	0.26	0.34	0.42	0.40
Al_2O_3	16.05	0.76	0.76	1.12	1.29	10.46
Fe_2O_3(t)	8.62	15.16	15.28	14.68	10.12	8.49
MnO	0.15	0.23	0.23	0.25	0.20	0.27
MgO	8.44	26.25	26.31	22.25	17.27	13.15
CaO	10.97	10.00	9.88	12.75	18.05	11.67
Na_2O	1.90	0.25	0.27	0.39	0.44	0.41
K_2O	1.31	0.01	0.00	0.03	0.03	1.05
P_2O_5	0.10	0.02	0.02	0.02	0.01	0.05
LOI	1.90	3.48	1.64	1.90	1.68	2.05
Total	96.86	97.76	95.99	97.50	97.63	95.42
ppm						
Cr	589.8	1588.4	1565.2	1752.0	1412.4	2008.3
Ni	134.3	592.5	608.1	461.7	277.4	386.4
Co	75.0	155.5	143.2	136.7	98.6	95.5
V	216.2	93.9	95.1	132.7	174.3	167.8
Zn	67.7	78.6	79.7	84.1	46.6	51.7
Rb	37.1	0.5	0.2	0.8	0.5	24.6
Ba	193.9	16.9	15.1	53.8	40.2	92.3
Sr	214.5	26.4	26.8	41.1	46.5	143.3
Zr	16.6	3.1	3.3	6.1	5.9	33.3
Y	10.0	1.7	1.6	2.5	4.8	7.9
Nb	1.4	b.d.l.	0.3	b.d.l.	b.d.l.	0.5
Cu	36.8	5.8	8.5	14.6	10.0	7.6
Sc	42.7	29.2	31.2	41.0	57.3	38.2

LOI = Loss on ignition
b.d.l. = below detection limit

G: REE ANALYSIS

G.1: REE analysis for samples labelled as CB (Rietfontein Complex) analysed by A. Späth at the University of Capte Town.

Sample	CB1	CB5	CB7	CB8	CB11	CB14	CB15	CB16	CB18	CB19
ppm										
La	3.97	3.55	2.68	3.42	3.33	2.54	5.22	2.53	1.75	1.34
Ce	8.93	8.48	6.92	9.37	7.91	6.71	13.5	6.47	3.67	3.27
Pr	1.24	1.21	1.06	1.53	1.17	1.17	2.04	1.01	0.44	0.51
Nd	5.56	5.94	5.25	7.91	5.66	6.41	10.4	5.1	1.79	2.61
Sm	1.32	1.51	1.39	2.19	1.46	1.84	2.71	1.35	0.33	0.69
Eu	0.44	0.57	0.52	0.71	0.6	0.61	0.86	0.54	0.1	0.32
Gd	1.36	1.58	1.48	2.31	1.53	2.01	2.89	1.46	0.29	0.73
Tb	0.21	0.23	0.22	0.35	0.23	0.29	0.42	0.22	0.04	0.1
Dy	1.21	1.42	1.36	2.08	1.4	1.8	2.5	1.28	0.23	0.61
Ho	0.24	0.28	0.26	0.41	0.28	0.34	0.48	0.25	0.046	0.12
Er	0.65	0.76	0.71	1.11	0.75	0.94	1.31	0.67	0.14	0.32
Tm	0.088	0.1	0.10	0.15	0.1	0.12	0.17	0.089	0.021	0.043
Yb	0.55	0.66	0.61	0.93	0.63	0.77	1.1	0.56	0.15	0.28
Lu	0.083	0.1	0.09	0.14	0.095	0.11	0.16	0.084	0.026	0.044

G.1 (continued): REE analysis for samples labelled as CB analysed by A. Späth at the University of Capte Town.

Sample	CB20	CB31	CB33	CB33a	CB34	CB35	CB38	CB41	MB19a
ppm									
La	2.21	3.2	3.30	5.96	6.51	5.48	3.61	2.09	0.78
Ce	4.86	7.89	9.45	13.3	12.7	14.5	9.21	3.90	1.38
Pr	0.76	1.21	1.52	1.66	2.44	2.28	1.44	0.47	0.15
Nd	3.7	6.1	7.85	7.14	11.7	11.5	7.24	1.93	0.57
Sm	0.93	1.55	2.13	1.55	2.90	3.01	1.88	0.39	0.10
Eu	0.40	0.58	0.70	0.59	0.92	0.94	0.71	0.28	0.076
Gd	0.94	1.64	2.33	1.47	2.91	3.08	1.83	0.35	0.085
Tb	0.14	0.24	0.35	0.21	0.43	0.46	0.27	0.05	0.013
Dy	0.81	1.43	2.07	1.20	2.51	2.72	1.61	0.29	0.076
Ho	0.15	0.28	0.40	0.23	0.48	0.53	0.31	0.057	0.015
Er	0.42	0.75	1.08	0.64	1.31	1.44	0.84	0.17	0.050
Tm	0.057	0.1	0.14	0.084	0.17	0.19	0.11	0.024	0.008
Yb	0.37	0.64	0.89	0.54	1.09	1.20	0.70	0.17	0.065
Lu	0.056	0.1	0.13	0.081	0.16	0.18	0.10	0.029	0.011

G.1 (continued): REE analysis for samples labelled as CB (Winddam wehrlite) and MSC (Koedoesfontein Complex) analysed by A. Späth at the University of Cape Town.

Sample	CB47	CB49	CB54	CB62	MSC268	MSC272
ppm						
La	4.38	1.08	1.75	0.96	0.91	0.95
Ce	9.85	2.37	3.69	2.44	2.89	2.99
Pr	1.24	0.34	0.49	0.36	0.49	0.50
Nd	5.42	1.63	2.21	1.84	2.59	2.69
Sm	1.41	0.46	0.59	0.54	0.73	0.76
Eu	0.44	0.16	0.20	0.19	0.24	0.24
Gd	1.56	0.50	0.63	0.62	0.79	0.79
Tb	0.27	0.082	0.10	0.10	0.12	0.12
Dy	1.79	0.53	0.66	0.63	0.71	0.73
Ho	0.37	0.11	0.13	0.13	0.14	0.14
Er	1.12	0.31	0.38	0.36	0.38	0.39
Tm	0.15	0.042	0.053	0.050	0.051	0.051
Yb	1.04	0.28	0.35	0.32	0.32	0.33
Lu	0.15	0.042	0.052	0.048	0.048	0.049

H: TRACE ELEMENT ANALYSIS

H.1: Trace element content of selected samples (CB – Rietfontein Complex; RB – Koedoesfontein Complex; W – Winddam wehrlite) determined via ICP-MS by A.H. Wilson at the University of the Witwatersrand.

Sample	CB1	CB2	CB3	CB9	CB10	CB13	CB15
ppm							
Li	4.482	4.423	4.758	13.471	6.106	3.299	6.241
P	410.455	125.166	140.585	317.696	193.556	129.032	421.376
Sc	38.209	54.116	21.482	53.97	19.584	25.6	60.094
V	236.974	227.277	276.363	569.651	489.524	360.136	414.58
Ga	6.03	5.468	11.929	10.148	12.431	10.763	9.543
As	0.026	0.068	0.116	0.084	0.092	0.179	0.23
Rb	2.567	5.107	2.906	7.367	3.765	1.512	5.581
Sr	80.211	73.895	385.832	117.905	422.185	319.26	117.338
Y	10.523	9.27	8.641	16.582	9.373	12.005	21.459
Zr	22.796	16.798	13.921	31.112	18.486	18.33	52.486
Nb	2.307	1.407	0.608	2.046	1.311	0.757	3.271
Ba	49.232	49.346	71.776	113.904	87.664	67.193	73.659
Sn	0.381	0.271	0.299	0.547	0.424	0.37	0.539
Cs	0.071	0.147	0.203	0.505	0.138	0.03	0.138
La	4.744	2.619	2.114	4.085	3.268	2.735	6.848
Ce	9.693	6.284	5.105	9.985	7.638	7.119	17.082
Pr	1.291	0.951	0.765	1.569	1.197	1.25	2.735
Nd	5.695	4.56	3.906	8.067	5.691	6.748	14.068
Sm	1.36	1.194	1.146	2.347	1.548	1.94	3.692
Eu	0.429	0.391	0.463	0.745	0.588	0.701	1.137
Gd	1.556	1.336	1.304	2.627	1.637	2.103	4.005
Tb	0.243	0.21	0.208	0.394	0.258	0.341	0.607
Dy	1.383	1.259	1.277	2.345	1.503	1.923	3.471
Ho	0.279	0.25	0.26	0.464	0.297	0.386	0.681
Er	0.745	0.683	0.697	1.211	0.802	1.01	1.822
Tm	0.108	0.097	0.095	0.17	0.11	0.14	0.252
Yb	0.709	0.629	0.654	1.102	0.735	0.897	1.574
Lu	0.104	0.094	0.1	0.161	0.106	0.133	0.231
Hf	0.664	0.513	0.51	0.979	0.575	0.663	1.587
Ta	0.111	0.071	0.034	0.11	0.071	0.042	0.18
W	0.035	0.109	0.036	0.036	0.028	0.019	0.052
Pb	1.247	0.775	1.263	1.85	1.325	1.215	0.811
Th	0.537	0.385	0.08	0.309	0.163	0.121	0.472
U	0.029	0.02	0.009	0.023	0.017	0.012	0.037

H.1 (continued): Trace element content of selected samples (CB – Rietfontein Complex; RB – Koedoesfontein Complex; W – Winddam wehrlite) determined via ICP-MS by A.H. Wilson at the University of the Witwatersrand.

Sample	CB17	52	RB3	RB9	WO6	WO7	WO9
ppm							
Li	4.994	4.889	30.005	3.366	6.046	5.286	9.033
P	177.38	125.81	540.972	105.296	126.072	63.535	142.396
Sc	7.21	7.221	59.263	60.919	50.835	66.61	56.647
V	862.129	1751.032	273.784	176.108	462.497	315.508	268.923
Ga	15.008	24.561	17.503	3.579	5.81	3.908	4.348
As	0.43	0.986	0.605	0.072	0.095	0.016	0.055
Rb	2.392	1.647	48.927	0.729	3.003	1.453	1.922
Sr	330.661	234.452	242.79	41.289	48.237	44.595	52.158
Y	2.047	1.021	15.517	6.805	6.808	7.299	7.098
Zr	16.998	17.094	24.359	7.988	8.721	6.399	9.233
Nb	1.891	2.415	4.455	0.254	1.076	0.685	0.988
Ba	103.89	65.104	243.726	17.343	30.354	14.707	27.055
Sn	0.676	1.057	1.133	0.163	0.281	0.19	0.267
Cs	0.033	0.019	1.299	0.018	0.251	0.137	0.2
La	1.981	1.303	6.138	1.996	1.483	1.046	1.529
Ce	3.562	2.162	12.656	4.522	3.309	2.647	3.557
Pr	0.425	0.256	1.583	0.632	0.481	0.419	0.526
Nd	1.766	1.009	6.591	3.146	2.325	2.061	2.493
Sm	0.415	0.219	1.715	0.883	0.695	0.696	0.767
Eu	0.23	0.135	0.63	0.29	0.25	0.242	0.277
Gd	0.364	0.186	1.915	1.05	0.884	0.879	0.916
Tb	0.05	0.024	0.324	0.169	0.151	0.156	0.158
Dy	0.285	0.138	2.145	1.03	0.971	1.01	1.038
Ho	0.058	0.029	0.456	0.207	0.203	0.214	0.213
Er	0.172	0.085	1.322	0.54	0.569	0.58	0.586
Tm	0.027	0.013	0.203	0.077	0.084	0.086	0.084
Yb	0.182	0.11	1.395	0.489	0.548	0.565	0.565
Lu	0.033	0.019	0.202	0.072	0.084	0.084	0.085
Hf	0.414	0.464	0.816	0.293	0.294	0.237	0.309
Ta	0.1	0.139	0.312	0.014	0.062	0.035	0.06
W	0.008	0.002	0.113	0.041	0.049	0.048	0.086
Pb	1.52	0.03	9.259	0.076	3.906	3.028	2.928
Th	0.129	0.072	0.86	0.107	0.12	0.086	0.131
U	0.012	0.007	0.159	0.006	0.012	0.008	0.014

H.1 (continued): Trace element content of selected samples (CB – Rietfontein Complex; RB – Koedoesfontein Complex; W – Winddam wehrlite) determined via ICP-MS by A.H. Wilson at the University of the Witwatersrand.

Sample	W11	W12	W13	W14	W16	W18
ppm						
Li	5.154	3.697	4.496	4.953	4.007	3.843
P	142.937	179.505	230.346	288.128	193.717	125.635
Sc	51.461	43.873	43.077	55.714	39.192	58.256
V	228.691	219	210.844	256.797	185.643	239.27
Ga	4.092	3.356	3.835	4.511	3.546	3.662
As	0.035	0.119	0.038	0.167	0.008	0.1
Rb	3.147	2.37	2.523	3.265	3.011	1.622
Sr	66.109	51.762	87.183	84.296	62.069	60.511
Y	8.035	5.53	5.814	7.168	6.058	7.115
Zr	11.114	7.34	12.432	14.723	9.26	7.895
Nb	1.253	0.978	1.967	1.92	1.226	0.788
Ba	38.206	32.631	35.123	62.516	32.928	21.814
Sn	0.181	0.122	0.196	0.202	0.164	0.19
Cs	0.154	0.059	0.113	0.089	0.071	0.154
La	2.072	1.683	2.926	3.308	2.313	1.746
Ce	4.763	3.244	5.178	6.345	4.572	4.151
Pr	0.707	0.463	0.64	0.864	0.64	0.663
Nd	3.485	2.258	2.823	3.87	2.919	3.337
Sm	0.963	0.638	0.747	0.989	0.841	0.957
Eu	0.357	0.241	0.265	0.362	0.289	0.339
Gd	1.15	0.789	0.893	1.152	0.952	1.122
Tb	0.189	0.134	0.143	0.184	0.154	0.191
Dy	1.152	0.824	0.866	1.093	0.95	1.144
Ho	0.24	0.168	0.177	0.228	0.192	0.231
Er	0.656	0.47	0.481	0.637	0.522	0.631
Tm	0.096	0.066	0.073	0.091	0.076	0.091
Yb	0.624	0.438	0.476	0.589	0.497	0.586
Lu	0.09	0.063	0.068	0.087	0.073	0.083
Hf	0.346	0.225	0.338	0.423	0.277	0.273
Ta	0.07	0.052	0.108	0.111	0.069	0.043
W	0.031	0.038	0.024	0.035	0.029	0.018
Pb	1.057	0.528	1.139	0.286	0.226	0.884
Th	0.181	0.201	0.129	0.352	0.133	0.119
U	0.018	0.019	0.012	0.03	0.012	0.012

I: MICROPROBE ANALYSIS OF MINERAL GRAINS

I.1: Mineral chemistry of olivine from the Rietfontein Complex analysed by L. Smuts with a JEOL electron microprobe at the Potchefstroom University of Christian Higher Education.

Sample	CB1	CB2	CB3	CB6	CB8	CB10	CB12	CB14	CB15	CB16	CB18	MB19a	CB20
wt. %													
SiO_2	37.01	37.64	37.37	36.93	37.11	37.61	36.8	37.57	36.05	37.18	37.4	37.55	37.3
TiO_2	0.02	0.04	0.09	0.03	0.03	0.03	0.04	0.05	0.04	0.03	0.05	0.06	0.03
Al_2O_3	0.11	0.02	0.12	0.01	0.03	0.04	0.07	0.06	0.05	0.01	0.05	0.05	0.01
FeO	28.55	27.09	25.94	29.51	28.13	27.63	28.86	27.83	31.09	27.31	26.4	25.67	27.25
MnO	0.47	0.35	0.45	0.42	0.4	0.43	0.39	0.39	0.45	0.37	0.33	0.31	0.37
MgO	33.85	35.13	35.98	33.12	33.66	34.33	33.3	34.12	31.35	35.08	35.46	35.98	34.72
CaO	0.03	0.03	0.03	0.05	0.08	0.06	0.04	0.07	0.06	0.05	0.14	0.09	0.05
Na_2O	0.07	0.05	0.04	0.02	0.03	0.01	0.03	0.02	0.07	0.01	0.01	0.03	0.02
K_2O	0.02	0.01	b.d.l.	b.d.l.	0.01	b.d.l.	0.01	b.d.l.	b.d.l.	0.01	0.01	b.d.l.	b.d.l.
NiO	0.1	0.08	0.09	0.07	0.07	0.04	0.08	0.08	0.05	0.09	0.08	0.08	0.09
Cr_2O_3	0.04	0.03	0.02	0.01	0.01	0.02	0.02	0.01	0.01	b.d.l.	b.d.l.	0.01	0.01
Total	100.27	100.47	100.13	100.17	99.56	100.2	99.64	100.2	99.22	100.14	99.93	99.83	99.85
Fo%	67.9	69.8	71.2	66.7	68.1	68.9	67.3	68.6	64.3	69.6	70.5	71.4	69.4

b.d.l. = below detection limit

I.2: Mineral chemistry of augite from the Rietfontein Complex analysed by L. Smuts with a JEOL electron microprobe at the Potchefstroom University of Christian Higher Education.

Sample	CB1	CB2	CB3	CB6	CB8	CB10	CB12	CB14	CB15	CB20
wt. %										
SiO_2	53.77	54.43	52.32	52.39	53.39	52.55	52.53	53.06	53.15	52.55
TiO_2	0.27	0.18	0.64	0.64	0.66	0.48	0.65	0.77	0.63	0.63
Al_2O_3	1.22	0.98	2.66	2.35	2.17	2.33	2.33	2.39	1.83	1.97
FeO	6.74	6.57	9.19	8.37	8.23	8.25	9.19	8.22	8.54	7.92
MnO	0.28	0.25	0.3	0.33	0.34	0.35	0.3	0.34	0.32	0.29
MgO	15.34	15.73	15.16	14.45	14.6	14.43	15.02	14.27	14.41	14.17
CaO	21.11	21.07	18.27	20.34	19.89	20.3	18.26	20.15	20.3	20.47
Na_2O	0.7	0.63	0.73	0.73	0.65	0.73	0.6	0.69	0.71	0.73
K_2O	b.d.l.	b.d.l.	0.01	b.d.l.	b.d.l.	0.02	0.01	b.d.l.	0.01	0.01
NiO	0.02	0.01	0.04	0.01	0.01	0.01	0.01	0.02	0.01	0.02
Cr_2O_3	0.18	0.65	0.71	0.32	0.23	0.21	0.47	0.17	0.1	0.33
Total	99.63	100.5	100.03	99.93	100.17	99.66	99.37	100.08	100.01	99.09
Wo	44.25	43.82	39.26	43.3	42.67	43.37	39.42	43.41	43.19	44.14
En	44.72	45.51	45.32	42.79	43.55	42.88	45.1	42.77	42.63	42.52
Fs	11.03	10.67	15.42	13.91	13.78	13.75	15.48	13.82	14.18	13.34

b.d.l. = below detection limit

I.3: Mineral chemistry of plagioclase from the Rietfontein Complex analysed by L. Smuts with a JEOL electron microprobe at the Potchefstroom University of Christian Higher Education.

Sample	CB3	CB4	CB5	CB6	CB7.1	CB7.2	CB10	CB14.1	CB14.2	CB14.3
wt. %										
SiO_2	59.65	59.26	59.72	59.63	59.14	59.19	61.23	61.26	61.32	61.64
TiO_2	0.08	0.06	0.08	0.10	0.07	0.08	0.06	0.10	0.08	0.07
Al_2O_3	25.13	24.97	24.68	24.71	24.91	25.03	24.10	23.94	23.82	23.80
FeO	0.24	0.18	0.24	0.31	0.24	0.18	0.22	0.15	0.24	0.25
MnO	0.07	0.01	0.01	0.02	b.d.l.	0.03	0.03	b.d.l.	0.02	0.04
MgO	0.07	b.d.l.	0.05	0.01	b.d.l.	0.26	0.01	b.d.l.	0.02	0.03
CaO	7.47	7.73	7.14	7.27	7.33	7.14	6.41	6.21	6.08	6.08
Na_2O	7.11	6.62	7.02	6.93	6.96	7.25	7.28	7.76	7.45	7.44
K_2O	0.45	0.42	0.61	0.58	0.55	0.41	0.62	0.59	0.72	0.78
SrO	0.15	0.01	0.26	0.27	0.58	0.19	0.14	0.35	0.26	0.15
BaO	0.01	b.d.l.	0.01	0.01	b.d.l.	0.01	0.02	b.d.l.	0.02	0.01
Total	100.43	99.26	99.81	99.84	99.81	99.77	100.11	100.36	100.03	100.29
An%	35.8	38.3	34.7	35.5	35.6	34.4	31.5	29.6	29.8	29.7
Ab%	61.6	59.3	61.7	61.2	61.2	63.2	64.8	67.0	66.0	65.8
Or%	2.6	2.5	3.5	3.4	3.2	2.3	3.6	4.2	4.2	4.5

b.d.l. = below detection limit

I.3 (continued): Mineral chemistry of plagioclase from the Rietfontein Complex analysed by L. Smuts with a JEOL electron microprobe at the Potchefstroom University of Christian Higher Education.

Sample	CB12.1	CB12.2	CB12.3	CB15	CB16	CB18	CB20	MB19a
wt. %								
SiO_2	60.92	61.30	60.06	63.19	59.40	60.95	60.47	60.92
TiO_2	0.10	0.09	0.10	0.12	0.08	0.10	0.08	0.11
Al_2O_3	24.81	24.90	24.24	23.43	25.15	24.90	24.51	24.31
FeO	0.17	0.27	0.21	0.15	0.22	0.18	0.16	0.18
MnO	0.01	b.d.l.	b.d.l.	0.02	0.04	b.d.l.	0.04	0.05
MgO	0.02	0.05	0.02	b.d.l.	b.d.l.	b.d.l.	b.d.l.	b.d.l.
CaO	6.93	6.60	6.79	5.10	7.48	6.77	6.82	6.58
Na_2O	6.00	5.78	7.50	7.14	7.07	6.85	7.31	7.49
K_2O	0.47	0.62	0.50	0.88	0.54	0.31	0.41	0.27
SrO	0.28	0.12	0.04	0.11	b.d.l.	b.d.l.	0.18	0.1
BaO	b.d.l.	0.01	0.01	0.01	b.d.l.	0.01	b.d.l.	0.01
Total	99.71	99.74	99.47	100.15	99.97	100.07	99.98	99.92
An%	37.8	37.1	32.4	26.7	35.8	34.7	33.2	32.2
Ab%	59.2	58.8	64.8	67.8	61.2	63.5	64.4	66.3
Or%	3.1	4.1	2.8	5.5	3.1	1.9	2.4	1.6

b.d.l. = below detection limit

J: X-RAY DIFFRACTION ANALYSIS

J.1: XRD diffractogram of olivine-hornblende gabbronorite sample CB47 from Ww. Analysis performed by B. Venter at the North-West University, Potchefstroom campus.

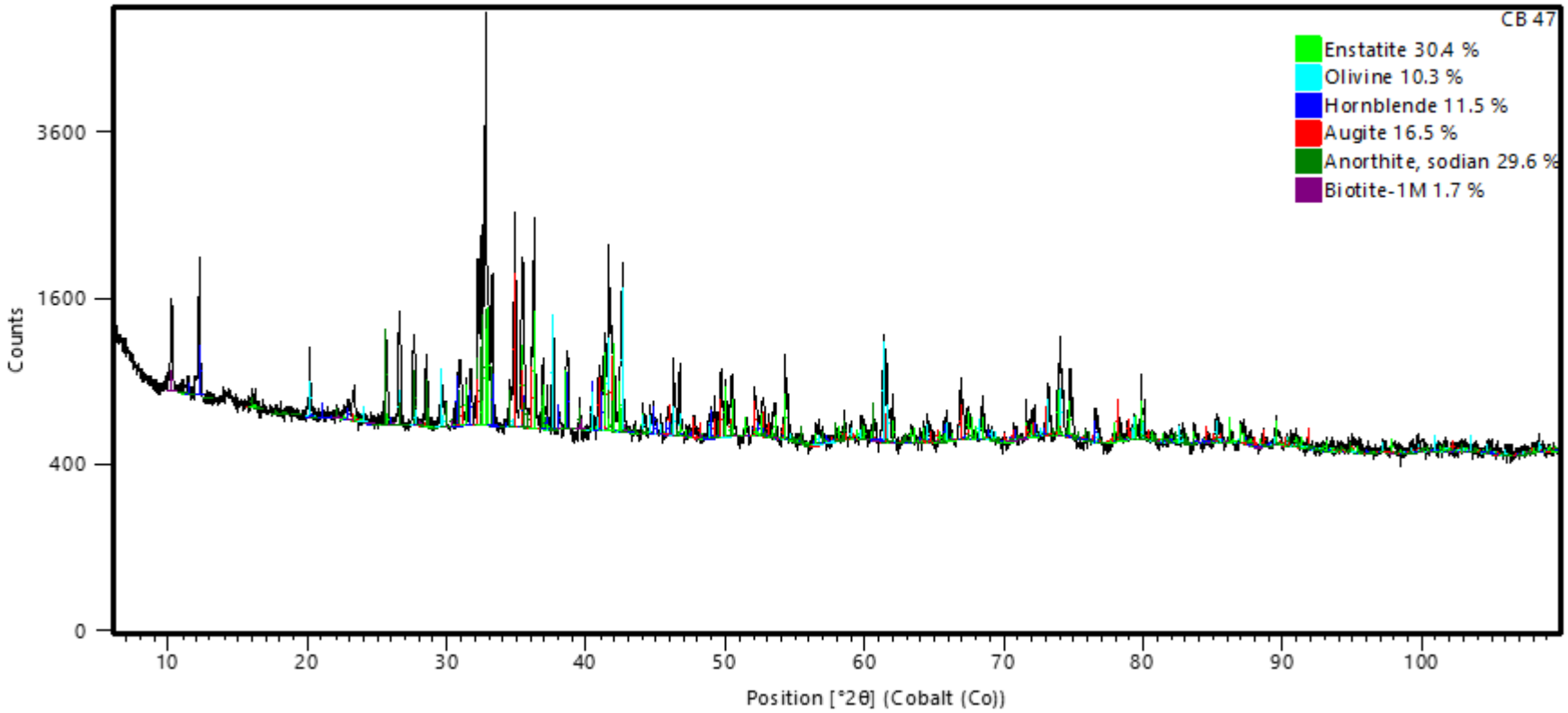

K: VALUES USED FOR NORMALISATION OF MULTI-ELEMENT SPIDER DIAGRAMS

K.1: Trace element concentration of the primitive mantle from McDonough *et al*. (1992).

Element	Concentration (ppm)
Rb	0.635
Ba	6.99
Th	0.084
U	0.021
Nb	0.713
K	240
La	0.708
Ce	1.833
Pb	0.071
Sr	21.1
P	92
Nd	1.366
Sm	0.444
Zr	11.2
Ti	1280
Y	4.55

L: REE CONCENTRATIONS USED FOR NORMALISATION ON CHONDRITE-NORMALISED REE DIAGRAMS

L.1: REE contents of C1 chondrite from Sun and McDonough (1989).

Element	Concentration (ppm)
La	0.237
Ce	0.621
Pr	0.095
Nd	0.467
Sm	0.153
Eu	0.058
Gd	0.2055
Tb	0.0374
Dy	0.254
Ho	0.0566
Er	0.1655
Tm	0.0255
Yb	0.17
Lu	0.0254

M: $(La/Sm)_N$, $(Tb/Yb)_N$, AND Eu-ANOMALY VALUES OF INDIVIDUAL SAMPLES

M.1: $(La/Sm)_N$, $(Tb/Yb)_N$, and Eu-anomaly values of samples from the Winddam wehrlite.

	WO6	WO7	WO9	W11	W12	W13	W14	W16	W18	CB47	CB49	CB54	CB62
Eu-anomaly	0.97	0.95	1.01	1.04	1.04	0.99	1.03	0.98	1.00	0.90	1.01	1.00	1.00
$(La/Sm)_N$	1.38	0.97	1.29	1.39	1.70	2.53	2.16	1.78	1.18	2.01	1.52	1.91	1.15
$(Tb/Yb)_N$	1.25	1.26	1.27	1.38	1.39	1.37	1.42	1.41	1.48	1.18	1.33	1.30	1.42

M.2: $(La/Sm)_N$, $(Tb/Yb)_N$, and Eu-anomaly values of samples from the Koedoesfontein Complex.

	RB3	RB9	MSC268	MSC272
Eu anomaly	1.06	0.92	0.96	0.94
$(La/Sm)_N$	2.31	1.46	0.80	0.81
$(Tb/Yb)_N$	1.06	1.57	1.70	1.65

M.3: $(La/Sm)_N$, $(Tb/Yb)_N$, and Eu-anomaly values of samples from the Rietfontein Complex.

	CB1	CB2	CB3	CB5	CB8	CB9	CB10	CB11	CB13	CB15	CB16	CB17	CB18	CB19	CB20	52
Eu-anomaly	0.90	0.94	1.15	1.12	0.96	0.91	1.12	1.22	1.05	0.90	1.17	1.77	0.97	1.37	1.29	1.99
$(La/Sm)_N$	2.25	1.42	1.19	1.52	1.01	1.12	1.36	1.47	0.91	1.20	1.21	3.08	3.42	1.25	1.53	3.84
$(Tb/Yb)_N$	1.56	1.52	1.45	1.58	1.71	1.63	1.60	1.66	1.73	1.75	1.74	1.25	1.21	1.62	1.72	0.99

N: PARTITION COEFFICIENTS USED FOR REE MODELLING DURING FRACTIONAL CRYSTALLISATION

N.1: Partition coefficients for REE between the common silicates observed in RietC, KC, and Ww and basaltic melt. D values for olivine, clinopyroxene, and plagioclase are from Fujimaki *et al*. (1984), while D values for hornblende are from Arth (1976). Shaded D values are estimated via linear interpolation.

	Clinopyroxene	Plagioclase	Hornblende	Olivine
La	0.056	0.19	0.25	0.0067
Ce	0.092	0.111	0.2	0.006
Pr	0.161	0.1005	0.265	0.00595
Nd	0.23	0.09	0.33	0.0059
Sm	0.445	0.072	0.52	0.007
Eu	0.474	0.443	0.4	0.0074
Gd	0.556	0.071	0.63	0.01
Tb	0.57	0.067	0.635	0.0115
Dy	0.582	0.063	0.64	0.013
Ho	0.5825	0.06	0.595	0.0193
Er	0.583	0.057	0.55	0.0256
Tm	0.5625	0.0565	0.52	0.03735
Yb	0.542	0.056	0.49	0.0491
Lu	0.506	0.053	0.43	0.0454

O: AN EXAMPLE OF CALCULATIONS PERFORMED FOR REE MODELLING DURING FRACTIONAL CRYSTALLISATION

The REE-modelling example explained here is from section 6.5.4 where it is shown that differences in the REE contents and patterns of the magma parental to the ultramafic rocks of KC and the parental melt of MHPD can be explained via fractional crystallisation.

First the mode of olivine clinopyroxenite sample MSC272 and the MHPD is converted to mass using the following equation:

$$M_{mineral} = V_{mineral} \times \rho_{mineral} \qquad (8.1)$$

where M refers to mass, V refers to volume, and ρ refers to density. To obtain V from point count determinations, it is assumed that the total volume of the rock is equal to 100 cm^3. This implies that, if a mineral occupies 50 vol. % of a rock, its total volume would be 50 cm^3.

Sample MSC272 consists almost entirely of augite and olivine and the following calculations are made:

For olivine:

$M_{olivine} = 36.2\ cm^3 \times 3.32\ g.cm^{-3}$

$M_{olivine} = 120.184\ g$

For augite:

$M_{augite} = 62.5\ cm^3 \times 3.2\ g.cm^{-3}$

$M_{augite} = 200.00\ g$

The steps are repeated for MHPD, which consists primarily of plagioclase and augite:

For augite:

$M_{augite} = 66\ cm^3 \times 3.2\ g.cm^{-3}$

$M_{augite} = 211.20\ g$

For plagioclase:

$M_{plagioclase} = 33\ cm^3 \times 2.68\ g.cm^{-3}$

$M_{plagioclase} = 88.44\ g$

Now that the mineral mass has been determined, the mass fraction of each individual mineral has to be calculated. This is done with the following equation:

$$MF_{mineral} = M_{mineral} / M_{total} \quad (8.2)$$

where MF refers to mass fraction.

For sample MSC272, the calculation has to be performed for both olivine and augite:

For olivine:

MF_{augite} = 120.184 g / 320.184 g

MF_{augite} = 0.38 w/W

For augite:

MF_{augite} = 200.00 g / 320.184 g

MF_{augite} = 0.62 w/W

The same calculations are performed for MHPD:

For augite:

MF_{augite} = 211.20 g / 299.64 g

MF_{augite} = 0.70 w/W

For plagioclase:

$MF_{plagioclase}$ = 88.44 g / 299.64 g

$MF_{plagioclase}$ = 0.30 w/W

The calculated mineral mass fractions (expressed as w/W) enabled the calculations of whole rock D-values for a particular trace element using equation 6.2. In order to perform REE modelling, the D-value is calculated for each REE separately. Only the calculations performed to obtain the whole-rock D-value for Tb is shown here.

For MSC272:

$D_{Tb} = (0.0115 \times 0.38 w/W)_{olivine} + (0.57 \times 0.62 w/W)_{augite}$

D_{Tb} = 0.36

For MHPD:

$D_{Tb} = (0.57 \times 0.70 w/W)_{augite} + (0.067 \times 0.30 w/W)_{plagioclase}$

$D_{Tb} = 0.42$

Using the D-values calculated above, the Tb content of the parental melt of each sample can be estimated using equation 6.1.

For MSC272:

$C_{Tb\ melt} = 0.12\ ppm / 0.36$

$C_{Tb\ melt} = 0.33\ ppm$

For MHPD:

$C_{Tb\ melt} = 0.8\ ppm / 0.42$

$C_{Tb\ melt} = 1.90\ ppm$

Because the parental melt of MSC272 has the lowest Tb content, it is deemed the most primitive and is used as the starting composition for REE modelling. Changes in the REE content during fractional crystallisation can be calculated using equation 6.3. In order to perform this calculation, the composite D-value of the fractionating phases need to be calculated. Using olivine, augite, and plagioclase in a 2:2:1 ratio, the best result is obtained for all REE when comparing a differentiated MSC272 parental magma to the parental magma of MHPD. The selection of the fractionating phases and their ratios is based on trial and error until a good fit is obtained for a particular degree of fractionation. To calculate the composite D-value of the fractionating phases, equation 6.2 is employed once more:

$D_{Tb} = (0.0.0115 \times 0.40\ w/W)_{olivine} + (0.57 \times 0.40 w/W)_{augite} + (0.067 \times 0.20 w/W)_{plagioclase}$

$D_{Tb\ =} 0.25$

The composite D_{Tb} value can then be substituted into equation 6.3. A degree of fractionation of 90% is used as this delivered the best results, giving an F-value of 0.1. The calculation is shown below:

$C_{melt} = 0.33 \times 0.1^{(0.25-1)}$

$C_{melt} = 1.89$

The calculated value (1.89) is almost identical to the Tb content of the parental melt of MHPD (1.90).

P: PARTITION COEFFICIENTS USED FOR REE MODELLING DURING MANTLE MELTING

P.1: Partition coefficients of REE for common mantle minerals used to estimate the composition of melts produced duriong melting of the mantle. Parition coefficients for olivine, clinopyroxene, orthopyroxene, and spinel are from Shaw (2000) while the partition coefficients for garnet are from McKenzie and O'Nions (1991).

	Olivine	Clinopyroxene	Orthopyroxene	Spinel	Garnet
La	0.0000053	0.0536	0.000044	0.00002	0.01
Ce	0.000105	0.0858	0.00014	0.00003	0.021
Pr	0.000251	0.137	0.00033	0.0001	0.054
Nd	0.000398	0.1873	0.00052	0.0002	0.087
Sm	0.00065	0.291	0.0016	0.0004	0.217
Eu	0.0008	0.329	0.0033	0.0006	0.32
Gd	0.0015	0.367	0.005	0.0009	0.498
Tb	0.0021	0.405	0.0067	0.0012	0.75
Dy	0.0027	0.442	0.0084	0.0015	1.06
Ho	0.005	0.415	0.0127	0.0023	1.53
Er	0.01	0.387	0.017	0.003	2
Tm	0.016	0.409	0.025	0.0038	3
Yb	0.027	0.43	0.033	0.0045	4.03
Lu	0.03	0.433	0.041	0.0053	5.5

Q: REE COMPOSITION OF FERTILE MANTLE NODULES FROM SOUTH AFRICAN KIMBERLITE

Q.1: REE contents of fertile South African mantle nodules from Nixon *et al*. (1981). Shaded values are estimated via linear interpolation according to the enrichment factor relative to C1 chondrite from Sun and McDonough (1989).

Element	Concentration (ppm)
La	1.16
Ce	2.72
Pr	0.345
Nd	1.35
Sm	0.35
Eu	0.145
Gd	0.493
Tb	0.0868
Dy	0.5698
Ho	0.1225
Er	0.3453
Tm	0.0512
Yb	0.33
Lu	0.0476